SCATTERING PROPERTIES OF SUSPENDED PARTICLES

by

Emlyn John Davies

A thesis submitted to the University of Plymouth
in partial fulfillment for the degree of

Doctor of Philosophy

School of Marine Science and Engineering,
Faculty of Science

Tuesday 18th June, 2013

Copyright Statement

Abstract

Scattering Properties of Suspended Particles
Emlyn Davies

Effective monitoring and modelling of the marine environment is of importance to both the general public and the scientific community, but relies on the ability to obtain accurate measurements of suspended particle characteristics. Many instruments for measuring particles rely on optical and acoustic scattering from the particles and use this information to infer a particle size and concentration. However, assumptions such as spherical particles of a known composition are widely used, both in measurement technology and in numerical modelling. Various imaging techniques have shown great variability in the shape, size and composition of marine particles when measured within their natural environment. Subsequently, there is substantial uncertainty in the response of light scattering instruments to this diverse range of particles.

In this study, a holographic camera was modified to simultaneously record in-focus images of marine particles with their forward angle scattering characteristics. This was achieved by combining both laser scattering and transmissometry with digital holography. The results from this system were compared with theoretical models of scattering from spherical particles within the intended size range of both instruments (15-500 μm), with particle size information from both techniques agreeing well during these idealised conditions. The combined holographic and light scattering system was then used to investigate the response of the LISST-100 (Sequoia Scientific Inc.) to spherical particles with diameters extending beyond that intended by the instrument (250 μm for type-B and 500 μm for type-C derivatives), but that have been observed *in-situ* with imaging methods. This revealed an aliasing of single large particles into multiple smaller particles during the inversion of LISST-100 scattering into a particle size distribution. For spheres greater than the type-C instrument range, the inversion of scattering produces particle volume distributions that peak at varying sizes between 250-400 μm. This key finding highlights the need for care to be taken when interpreting particle size distributions from the LISST-100 when there is potential for particles outside of its range limit. Natural particles, extracted from coastal waters, were then recorded by the combined

laboratory system. These complex particles produced highly variable scattering properties which were contaminated by asymmetrical features within the azimuthal plane. This observation of strong azimuthal asymmetry is of concern for both measurements and models of optical properties that assume a symmetrical scattering function for natural particle populations. The azimuthal asymmetry in scattering contributed to additional variability in the response of the instrument in comparison to the holographic camera, which was also subjected to apparent particle break-up via segmentation during image processing. A discussion of holographic imaging and laser diffraction for characterising particles *in-situ* forms the final part of this thesis, which utilises data from a magnified holographic system that covers the same size range of the LISST-100. This final analysis demonstrated the need for future technology to accurately measure size distributions over a much larger range of sizes than is currently possible (e.g. $< 2\,\mu m$ to $1000\,\mu m$).

In summary, three key factors were identified to cause an increase in the apparent number of small particles reported by the LISST-100: 1) contamination from scattering of particles larger than the intended size range of the instrument; 2) a decrease in refractive index (particle composition); 3) additional scattering from small sub-components of particle geometry. The standard holographic camera systems are capable of accurately obtaining particle size and concentration measurements that are comparable to other techniques such as the LISST-100. However, in situations where background illumination is poor, errors in the image processing routines can cause an apparent particle break-up due to incorrect binarisation. Despite this, the holographic method provides a unique and powerful mechanism that enables images of particles to be analysed within the context of their *in-situ* environment.

Contents

List of Figures

Acknowledgements

I am hugely grateful for the generous and extensive time that Alex Nimmo Smith has given me since starting at Plymouth University. His support and guidance has enabled me to learn a great deal about tackling the variety of problems facing a 'wannabe' scientist like me. I hope that I can try to repay some of these favours in future work together. Alex Souza, Yogi Agrawal and David Huntley have also provided me with invaluable guidance in tackling this investigation. George Graham has put-up with a huge amount of me pestering him for help with all sorts of issues and problems, regardless of their relevance - thank you very much for your patience. The people who have withstood the annoyance of me in the office (Bob, Ed, Ellie, Emma, Emma, Jaimie, Sam, Sola, Tom), also deserve a thanks for their patience. Jaimie and Ed have also prompted numerous lengthy discussions which have inspired many ideas that have been incorporated in this work - thank you very much for your time guys. David McKee and Dave Bowers have stimulated some very interesting debates while on fieldwork, and have provided me with many new ideas that I have tried by best to implement. I would also like to thank my parents and family for their support and for encouraging me with my studies.

Throughout the course of this work Sequoia Scientific Inc. have provided all the technical support I could ever have wished for on anything 'LISST' (especially Chuck and Ole). Wayne Slade has sacrificed a great deal of his time in helping me understand how to properly compute Mie scattering, and his 'fastmie' programme was exceptionally useful to me. Again, I would like to thank Yogi's generous time in helping me get to grips with optics, allowing me to spend time with the guys at the factory, and loaning me parts.

I would like to thank the reviewers of the papers and conference abstracts that I have submitted, as well as my examiners, all of whom have provided generous and constructive comments that have helped improve my work. Thank you also to the Natural Environment Research Council (NERC) for funding this work (NE/H525070/1) along with the support of the National Oceanography Centre (NOC, Liverpool), Plymouth University and Sequoia Scientific Inc.

Authors Declaration

At no time during the registration for the degree of Doctor of Philosophy has the author been registered for any other University award without prior consent of the Graduate Committee. Scientific seminars and conferences were attended, at which work from this thesis was presented, and three published journal articles contain material produced by the author during this study (references for these are under: "*Outputs and publications*"). There are 29000 words.

Signed:

Emlyn Davies

Date:

Outputs and publications

Peer Reviewed:

George W. Graham, **Emlyn J. Davies**, W. Alex M. Nimmo-Smith, David G. Bowers, and Katherine M. Braithwaite, (2012), "Interpreting LISST-100X measurements of particles with complex shape using Digital In-line Holography", Journal of Geophysical Research - Oceans. http://dx.doi.org/10.1029/2011JC007613 (Appendix C)

Emlyn J. Davies, W. Alex M. Nimmo-Smith, Yogesh C. Agrawal, and Alejandro J. Souza, (2012), "LISST-100 response to large particles", Marine Geology, Available online 3 April 2012, ISSN 0025-3227. http://dx.doi.org/10.1016/j.margeo.2012.03.006 (Appendix B)

Emlyn J. Davies, W. Alex M. Nimmo-Smith, Yogesh C. Agrawal, and Alejandro J. Souza, (2011), "Scattering signatures of suspended particles: an integrated system for combining digital holography and laser diffraction", Opt. Express 19, 25488-25499. http://www.opticsinfobase.org/oe/abstract.cfm?URI=oe-19-25-25488 (Appendix A)

Conference Abstracts:

Emlyn J. Davies, W. Alex M. Nimmo-Smith, Yogesh C. Agrawal, and Alejandro J. Souza, (2012), "Evaluating the LISST-100 Response to Complex Marine Particles", Particles in Europe (PiE), Barcelona, Spain. (Extended abstract & oral presentation)

Emlyn J. Davies, W. Alex M. Nimmo-Smith, Yogesh C. Agrawal, and Alejandro J. Souza, (2012), "Interpreting Forward Scattering from Complex Marine Particles", Ocean Optics, Glasgow, UK. (Extended abstract, oral presentation & poster)

George W. Graham, W. Alex M. Nimmo-Smith, David McKee, David G. Bowers, Robert MacDonald, **Emlyn J. Davies**, (2012), "Inconsistencies Between Theoretical Particle Abundance and In-Situ Observations in the Sea", Ocean Optics,

Glasgow, UK. (Oral presentation & poster given by George Graham)

Emlyn J. Davies, W. Alex M. Nimmo-Smith, George W. Graham, (2012), "Sequoia's LISST-HOLO: Results from a bedframe deployment in the Menai Strait, Wales", Oceanology International, London, UK. (Demonstration & poster).

Emlyn J. Davies, George W. Graham, W. Alex M. Nimmo-Smith, (2012), "Towards understanding particle size distributions derived from laser diffraction", AGU/ASLO/TOS Ocean Sciences Meeting, Salt Lake City, Utah, USA. (Oral presentation)

Emlyn J. Davies, W. Alex M. Nimmo-Smith, Yogesh C. Agrawal, and Alejandro J. Souza, (2010), "An integrated System for testing laser diffraction", Particles in Europe (PiE), Villefranche-sur-Mer, France. (Extended abstract & oral presentation)

Emlyn J. Davies, W. Alex M. Nimmo-Smith, Yogesh C. Agrawal, and Alejandro J. Souza, (2010), "Scattering signatures of suspended sediments", Challenger Conference for Marine Sciences, Southampton, UK. (Oral presentation)

Chapter 1

Introduction

Particles in the marine environment affect many vital processes, including radiative transfer, primary productivity, sound propagation, dispersal of pollutants, sediment transport, and fluxes of particulate organic carbon (Gentien et al., 1995; Irigoien and Castel, 1997; Jackson et al., 1997; Perillo, 1995; Proctor et al., 2003; Richards et al., 1996). For all these cases it is crucial to have an accurate measurement of suspended particle concentration and size to effectively model, monitor and understand the constantly changing global environment.

Accurate measurements of suspended particles are difficult to obtain due to their delicate and complex nature. Particles must be measured within their natural environment to avoid changing their shape and size which determine the rate at which they are transported through water. The measurement of suspended particles often requires a knowledge of the light or sound scattering patterns that are produced by the particles. This is an area that is relatively well understood for simple particles of homogeneous composition and spherical in shape (Bohren and Huffman, 1998). However, scientific understanding of the scattering characteristics of complex particles present in the natural marine environment is severely limited. As a result, instruments that rely on scattering by marine particles are constrained by a number of assumptions that have an unknown accuracy when applied to these complex particles. Previous studies have utilised various imaging techniques to aid assessments of the reliability of particle measurements using laser diffraction (Mikkelsen, 2001; Mikkelsen et al., 2005; Karp-Boss et al., 2007; Agrawal et al., 2008; Agrawal and Mikkelsen, 2009), but simultaneous measurements of the same sample had not been conducted during these assessments. The aim of this study is to:

Investigate the optical scattering characteristics of marine particles, with the objective of improving measurements of their size and concentration.

This aim is targeted at enhancing the appreciation of the errors associated with *in-situ* measurements of particles using laser diffraction in the marine environment. In addition, this study will provide contributions that will further the understanding of the influence of complex particles on the optical properties of water.

To address the aim of the project, a series of laboratory experiments have been conducted using a novel holographic camera and LISST-100X (Laser *in-situ* Scattering and Teansmissometer) type-c system, configured to allow simultaneous imaging of particles and measurement of their forward-angle scattering characteristics. The relationships between optical forward scattering from marine particles and their size and shape were then investigated. Laboratory experiments were conducted to allow control over the type of particles being examined, enabling progression of measurements from simple particles of a specific size, shape and composition, to more complex particles such as flocs. Finally, *in-situ* data was used to explore the relationship between the holographic cameras and LISST-100 sizing techniques in a variety of water masses. Knowledge gained from laboratory tests was applied to aid the analysis of the differences observed in the natural environment.

Following this introductory chapter, Chapter 2 presents a summary of the current state of research in the field of marine particle measurement, including: an introduction to marine particle types and dynamics, key concepts in optical scattering by particles in seawater, and a review of the techniques used for measuring marine particles and their optical properties. Chapter 3 contains explanations of the underlying principles of the chosen techniques for this study, in addition to the presentation of the combined LISST-100 and holographic camera system that has been developed. The laboratory system is then used to assess the response of the LISST-100 to particle sizes greater than the intended measurement range in Chapter 4. Chapter 5 further utilises the laboratory system to explore the relationship between size measurements from the LISST-100 and holographic camera when subjected to complex flocculated particles extracted from the Menai Strait, Wales, during the summer of 2011. This illustrates the response of the two instruments to particles typically found within the natural marine environment. The findings of Chapters 2-5 are then applied to *in-situ* comparisons of the two instruments when deployed alongside each other at various coastal locations within the UK continental shelf, and presented in Chapter 6. Finally, Chapter 7 discusses the main research findings of the study and presents recommendations for future work.

Chapter 2

Scientific Background

2.1 Aquatic particles

Particles in the marine environment vary in size from sub-micron colloids to flocculated aggregates of the order of millimetres (Jackson et al., 1997). Planktonic particles usually have sizes upwards of $4\,\mu m$, and larger flocculated particles may be several centimetres in size. The definition of 'particle' subsequently varies depending on the topic of interest. Jonasz and Fournier (2007) suggested that in the subject of optical properties of marine waters, particles are usually considered to be between 0.01 and $1000\,\mu m$. Within the remit of this work an 'aquatic particle' is considered as any entity with a longest axis greater than $0.01\,\mu m$. This includes particles of several millimetres in length and covers the size range in which optical scattering is expected to be influenced.

2.1.1 Particle types

Aquatic particles are mainly sourced from either terrestrially derived mineral grains, such as clays and sand, or from primary production of organic matter, such as microbes and plankton. The concentration of these particles therefore varies depending on the distance from their origin and the transport mechanisms that they are subjected to. In addition, as particles move, they interact with their surroundings and other particles, causing variability in their size, shape and composition through time and space.

Flocculated particles form from cohesive sediments which have compositions consisting of a combination of mineral grains and biogenic matter. The biogenic matter, combined with anaerobic decomposition of the organic material, causes the sediment to become cohesive. Cohesive sediments often form the majority of particulate matter in estuarine and coastal environments. The majority of particulates in the open ocean are of organic origin, such as phytoplankton. The concentration of inorganic particles increases in near-shore regions due to discharge of clays, silts and sand

from rivers (Bowers and Binding, 2006; Hill et al., 2000; Perillo, 1995). As a result, the ratio of organic to inorganic content would be expected to increase with distance offshore. This is likely to enhance flocculation as the surfaces of organic particles have convoluted chains of sticky polymers that, when brought into contact with another organic particle, bond together to form a larger floc. As a result, the average particle size will increase and the floc shape will become more complex. This increases the settling velocity of the particle, causing it to be more likely to fall out of suspension. However, the density of these flocs is relatively low and as a result, the settling velocity is less than that of a typical inorganic particle of the same size (Dyer and Manning, 1999). Once a distance offshore is reached where the concentration of inorganic material is so low, flocs no longer form and the majority of particles become dominated by plankton (Bowers and Binding, 2006).

The size of a suspended particle changes as other particles attach to one another through the process of flocculation, or sections break off (floc breakup). Flocculation occurs mostly as a result of the cohesive properties of organic polymers such as Extracellular Polymeric Substances (EPS). EPS are polymers that adhere to the edges of organic particles and play a key role in the flocculation process. The inter-particular bridging model describes how EPS allows particles to flocculate. Electrostatic charges on the surfaces of particles (Dyer and Manning, 1999) and salinity (Fugate and Friedrichs, 2003) are also factors that affect flocculation in environments with low salinities (such as river-estuary transition zones), but are less likely to be influential above about 5-10 PSU (Krone, 1963). For flocculation to occur, particles must first be brought together: often via Brownian motion, differential settling or turbulent shear.

Brownian motion causes particle collisions through random vibration of molecules which is dependent on temperature and dynamic viscosity, and is only influential for small particles of less than $0.2\,\mu m$. In general, flocs formed by Brownian motion are very fragile and have irregular shapes. Differential settling is the process in which larger particles settle faster onto smaller ones. Again, the low stress imposed on the particles during the collision results in fragile flocs. The differential velocities in turbulent shear cause particles to collide when an overtaking particle hits a slower moving one. The frequency of collisions therefore increases as turbulent shear increases. Flocs formed under this mechanism are often relatively strongly bonded. As well as bringing particles together, turbulent shear can also cause floc break-up of larger aggregates if there is a shear across the particle. The size of turbulent eddies (Kolmogorov microscale) is therefore thought to have an effect on the size of flocs (Fugate and Friedrichs, 2003).

2.1.2 Transport of suspended particles

Currents and turbulence

In addition to variations in nutrient concentrations and photosynthetically available radiation, the distribution of particles is affected by water motion. An understanding of the fluxes of suspended sediment is important for determining sediment budgets for a region, and subsequently predicting deposition or erosion rates. Assuming that particles suspended in the water move at the same speed as the water, the flux of sediment through a cross-section is equal to the multiple of water velocity and suspended sediment concentration. The movement of water is influenced by a combination of many factors, including: river discharge (in estuarine and coastal environments), water density, sediment input, tidal flows, waves, and large scale ocean currents (in offshore regions).

Stemmann et al. (2002) and Fugate and Friedrichs (2003) have shown that the amount of mixing within the water column has an important effect on the vertical distribution of suspended particles. Jackson et al. (1997) suggested that this may be, in part, due to the different physical processes that affect particles of different sizes. For instance, small particles are influenced more heavily by molecular diffusion and large particles may be affected more by turbulent shear.

Fugate and Friedrichs (2003) studied the relationship between turbulence and particle size in three estuaries with different amounts of TKE (Turbulent Kinetic Energy), using a profiling acoustic Doppler velocimeter. It was found that surface particle dynamics were affected by irregular advection events. In mid-depth, high TKE conditions, small Kolmogorov micro-scales reduced particle size due to floc breakup. Stratified, low TKE regions allowed differential setting to increase particle size. Suspended sediment distribution in mid-depth regions of the lower TKE areas was controlled by irregular re-suspension and trapping at the pycnocline. Re-suspension was found to be the main control on suspended particle size and distribution within the bottom layers of the three estuaries. It is, however, important to note that these measurements of suspended particles were made using a LISST-100 in conditions where the instrument is known to have uncertainties in its accuracy of measurement. Work such as that of Fugate and Friedrichs (2003) is vital in sediment transport studies. It is therefore crucial for the measurement of suspended particle characteristics to be accurate, highlighting the need for increased understanding of the performance and accuracy of instruments such as the LISST-100.

Settling velocity

Settling velocity is an important property of a suspended particle because it determines the length of time a particle remains in suspension and is used in models of

particle fluxes. The measurement of floc settling velocity is difficult due to their fragile nature and complex density structure. As a result, settling velocities can only be obtained accurately using *in-situ* techniques (Dyer and Manning, 1999; Mikkelsen, 2001).

Stoke's Law can be used to calculate a settling velocity (W_S) of spherical particles, from the diameter (D_M) and mean effective density ($\Delta\rho$) of a particle:

$$W_s = \frac{D_M^2 \Delta\rho g}{18\eta} \tag{2.1}$$

where g is the acceleration due to gravity and η is the molecular viscosity of water.

Because flocs are groups of particles bound together by EPS, they often have large gaps between the individual particles that make them up, and therefore have a density that is not always directly proportional to particle size. The mean effective density ($\Delta\rho$) is the difference between the floc density and the water density. This Stoke's Law approximation of settling velocity assumes spherical particles, which (as mentioned previously) is likely to be inaccurate in the marine environment. There have been a number of attempts at increasing the accuracy of the settling velocity prediction by including particle shape effects. For example, Dietrich (1982) introduced the Corey shape factor (Corey, 1949) into a settling velocity equation.

It is crucial that an accurate recording of particle size and shape is made when measuring suspended particles. The use of light scattering techniques to quantify particle shape is not a common topic amongst the literature. However, the distortions of scattering signatures due to shape effects has been considered by many authors in the field (Agrawal et al., 2008; Agrawal and Mikkelsen, 2009; Chami et al., 2006a; Chiappetta, 1980; Schuerman, 1979). This is discussed in more detail in Section 2.2.4.

2.1.3 Physical characterisation of particles

The classification of particles by way of their size, relies on the assumption that the shape of the particle can be expressed using a single metric. This means that particle shape must be quantified - a problem that becomes much harder for irregularly shaped particles of varying orientation, common in the marine environment. There have been many attempts to remove the effect of particle shape to allow a single variable to represent a size. The most commonly used definitions, are summarised in Table 2.1.

Each of the definitions described in Table 2.1 will result in inaccuracies in the expression of the size of non-spherical particles. As marine particles often have complex structures, the characterisation of particle shape is important for many aspects of suspended particle dynamics within the marine environment such as settling velocity (Section 2.1.2).

Table 2.1: Commonly used definitions of particle size (Jonasz and Fournier (2007)).

Particle size type	**Definition**
Equivalent spherical diameter (ESD)	Diameter of a sphere with volume equal to that of the particle.
Equivalent circular diameter (ECD) (Heywood diameter)	Diameter of a circle with area equal to that of the particle projection onto a plane.
Maximum chord diameter (major axis length)	Length of the longest chord of the particle projection onto a plane.
Minimum chord length (minor axis length)	Width of an ellipse fitted around a particle's projected area (perpendicular to the major axis).
Hydrodynamic diameter (Stokes diameter)	Diameter of a sphere having the same settling velocity as that of the particle.
Feret diameter	Length of the longest chord of the particle projection onto a plane with the chord aligned parallel to an arbitrary axis.
Martin diameter	Length of a chord of the particle projection onto a plane with the chord aligned parallel to an arbitrary axis and measured at the middle point of the Feret diameter measured along a perpendicular axis.

The size parameter (x) is commonly used to describe particle size in relation to the wavelength of the incident radiation:

$$x = kr = \frac{2\pi r}{\lambda} \tag{2.2}$$

where r is typically the radius of the particle, and λ is the wavelength of the incident radiation.

Refractive index

As light passes from one medium to another its speed changes according to the density of the medium that it passes through. This is because there is a greater concentration of scatterers in a more dense medium and therefore the optical path length of the light is extended due its numerous forward and backward scattering before it is re-emitted. The ratio of the speed of light in a vacuum to the speed of light in the medium through which it propagates is expressed as a refractive index.

Absorption causes the amplitude of the propagating waves to be reduced. This effect can be included by making the refractive index a complex number, with the imaginary part (n'') being the damping of the wave due to absorption (Jonasz and Fournier, 2007). In a homogeneous medium the absorption coefficient (a) is related to the imaginary part of the refractive index through the following equation:

$$a = \frac{4\pi}{\lambda} n'' \tag{2.3}$$

where λ is the wavelength of the light in a vacuum.

The refractive index of the particle relative to water may therefore be expressed as a complex number:

$$n \;\; = \;\; n' - n'' \tag{2.4}$$

where n' is the real part (ratio of the speed of light between the two media) and n'' is the imaginary part (absorption effect) (Jonasz and Fournier, 2007).

As discussed previously, the marine environment consists of many varying types of particle, each with a different size, shape and composition. Therefore it is difficult to predict how groups of particles within the water column will scatter light. This is partly due to the effects of multiple scattering, which occurs when the scattered light from one particle influences the scattering of light by other particles in the same area, and partly due to the refractive index of the particles being unknown.

The use of a single value for refractive index makes the assumption that the particle is homogeneous in composition. Heterogeneous particle structure has been classified by Schuerman (1979) into the following categories: *shell structure* - a particle with a core of one material surrounded by a mantle of a different material;

raisin pudding - aggregated particles containing clusters of various materials that are not close to each other; *aggregates* - the distribution between the aggregated particles are comparable with particle sizes; *birefringence* - particles that have a different refractive index for different directions of polarization.

Fractal structure

It is possible to classify the morphology of flocculated particles and obtain information on the method of flocculation by using fractal theory (Logan and Wilkinson, 1990). This is because the composition of a floc depends on the process by which it has been formed. Kranenburg (1994) summarised fractal structure by explaining that primary particles form flocs, which join together to form a larger floc, which join further to form larger flocs, and so on. Fractal theory was first applied to flocs in the marine environment by Krone (1963), who showed that floc density, strength and viscosity depend on the order of aggregation. A conclusion of this work was that the order of aggregation increases as the floc density decreases, and that the shear strength also decreases with increasing orders of aggregation.

Suspended flocs are also considered to be *self-similar* - a fractal structure which was explained by Kranenburg (1994), by considering a *basic element* of a fixed structure, formed by m_1 number of primary particles. A floc can form by connecting m_1 of these basic elements in such a way that the geometry of the elements is the same as the particle positions in the basic element. This action can then be repeated to form larger flocs. During each step, the size of the floc will increase by a factor m_2. As a result, the total number (N) of particles that make up a floc of size R_a is:

$$N \sim [\frac{R_a}{R_\rho}]^D \tag{2.5}$$

where R_ρ is the size of the primary particles, and D is the fractal dimension.

Values for fractal dimensions of varying particle types have been reported by Logan and Alldredge (1989), who calculated a three-dimentional fractal dimension D_3 for flocculating diatoms of 1.52 ± 0.19. Logan and Wilkinson (1990) compared the use of the porosity equations with settling velocity data for obtaining D_3 of marine snow and produced results of 1.39 ± 1.05 and 1.26 ± 0.06 respectively.

2.2 Optical scattering and absorption in seawater

The first stage in understanding light scattering by particles is to solve the 'direct' problem described by Bohren and Huffman (1998), which is to calculate the light scattering signature created by a particle of specified characteristics (shape, size and composition). However, instruments that measure marine particles need to be able to determine particle characteristics based on their light scattering signature

(the 'inverse' problem), and this is much harder to solve. To solve these problems it is necessary to have an understanding of what light is and how it interacts with material at the molecular level.

Quantum electrodynamics (QED) describes the interactions between light and matter by considering electrons and photons. In QED, light is considered to travel over all possible paths as a stream of particles (photons). Matter is composed of discrete electric charges which can be excited by the oscillating magnetic field of light. The charges on the matter then oscillate, and oscillating charges radiate electromagnetic waves, which is the scattered light. The original incident waves will interact with the scattered light so that the superposition of these waves is what is observed (Bohren and Clothiaux, 2006). This description of light scattering relies on sufficient distance between these scatterers to avoid scattered light from one molecule becoming the incident light on another molecule. A 'particle' is a collection of tightly-packed molecules, so the overall scattering signature that is produced is the superposition of the scattering from all molecules that make up the particle. The phase relations of the scattered waves depend on the scattering direction, size and shape of the particle. Therefore changes in particle size and shape will change the phase relations of the scattered waves causing differences in the observed scattering pattern.

For particles that are small compared to the wavelength of the incident light, all of the scattered light will be approximately in phase, so there is little variation in scattering intensity over changing angles. For particles larger than the wavelength of the incident light, the number of possibilities for constructive or destructive interference of the secondary waves increases. This means that larger particles have more peaks and troughs in their scattering pattern (Bohren and Huffman, 1998). The amplitude of the scattered wave is dependant on the composition of the particle which can be quantified (in optical terms) using the refractive index (Section 2.1.3).

2.2.1 Volume Scattering Function

The volume scattering function (VSF) is a measure of how light is scattered in different directions. The VSF of seawater is the sum of the VSF of pure water, the VSF of particulates and the VSF due to turbulent interactions with density interfaces. The scattering signature produced by water is the same in both forward and backward directions (due to a dominance of non-directional, Rayleigh scattering), whereas the scattering by particles is much stronger in the forward direction than the backward direction (Lee and Lewis, 2003). The contribution to the total VSF by particles is often the dominant factor in determining the overall VSF of water and may be modelled using optical scattering theories such as Mie Theory (Section 2.2.2). The VSF of particles depends on their size, shape and refractive index. The contribution due to turbulence has been explored by Bogucki et al. (1998) & Bogucki

et al. (2004) and the role of seawater constituents by Stramski et al. (2004). The VSF is expressed as $\beta(\theta)$, with θ being the angle of scattered light.

The scattering coefficient b (m^{-1}) may be derived by integrating the VSF (β) over all angles, as per Agrawal (2005):

$$b = 2\pi \int_0^{\pi} \beta(\theta) sin(\theta) d\theta \tag{2.6}$$

In situations where both scattering and absorption occur, an attenuation coefficient (c) is used to combine the absorption (a) and scattering (b) coefficients $(c = a + b)$.

Measurements of the volume scattering function

A volume scattering meter (VSM) was used in the work of Chami et al. (2006b) to measure the VSF from 0.6° to 177.3° with an angular resolution of 0.3°. By examining the ratio of the VSF to the scattering coefficient, it was found that the angular dependency of the VSF was strongly affected by the absorption and size distribution of particles. An extension of this work investigated the influence of the angular shape of the VSF and multiple scattering on remote sensing reflectance (Chami et al., 2006a). They found that the contribution of multiple scattering to radiance reflectance increased exponentially as the water became more turbid. This is as expected because the more turbid the water, the shorter the distance between particles, meaning that multiple scattering is more likely. Spinrad et al. (1978) compared Mie Theory with small-angle light scattering for a range of sizes of spherical particles in water. Their results agreed with theory for angles of $0.2 - 0.7°$. Further examples of measurements of the volume scattering function are those of Berthon et al. (2007a) & Berthon et al. (2007b) who used a multi-spectral volume scattering meter (MVSM) instrument to measure the VSF between 0.5° and 179° with an angular resolution of 0.3°. They found that the Fournier-Forand (FF) functions provided a good description of the measured VSF, which contradicts the conclusions of Chami et al. (2006a), who found differences between the FF functions and the VSF. The Fournier-Forand functions provide a theoretical description of the VSF, and are commonly used in radiance transfer models such as HYDROLIGHT (Berthon et al., 2007a; Chami et al., 2006a,b; Slade and Boss, 2006).

Agrawal (2005) and Slade and Boss (2006) described methods that allow the volume scattering function within the near-forward angles to be measured *in-situ* using the LISST-100 (Section 2.3.4). This is done by accounting for the optical power distribution and area of each of the 32 angular scattering detectors of the LISST-100 and is described in more detail in Section 2.3.4.

2.2.2 Computational methods for scattering and absorption

Mie Theory predicts scattering and absorption for a particle of pre-determined characteristics. It is based on Maxwell's electromagnetic field equations and is limited by the assumptions that the particles must be a perfect sphere, homogeneous in composition and the refractive index must be known. The concentration of particles must also be dilute enough for there to be no multiple scattering (Bohren and Huffman, 1998). The intensity of the scattering pattern is governed by the difference in refractive index between the particle and the dispersion medium.

The scattering coefficients, a_n and b_n, which are superimposed to provide an angular scattering distribution (S_1 & S_2), can be calculated with the following equations in accordance with Bohren and Huffman (1998):

$$a_n = \frac{\mu m^2 j_n(mx)[xj_n(x)]' - \mu_1 j_n(x)[mxj_n(mx)]'}{\mu m^2 j_n(mx)[xh_n^{(1)}(x)]' - \mu_1 h_n^{(1)}(x)[mxj_n(mx)]'} \tag{2.7}$$

$$b_n = \frac{\mu_1 j_n(mx)[xj_n(x)]' - \mu j_n(x)[mxj_n(mx)]'}{\mu_1 j_n(mx)[xh_n^{(1)}(x)]' - \mu h_n^{(1)}(x)[mxj_n(mx)]'} \tag{2.8}$$

where m is the refractive index of the sphere relative to the ambient medium; $x = 2\pi a/\lambda$ is the radius of the sphere); μ_1 is the magnetic permeability of the sphere; μ is the magnetic permeability of the ambient medium; j_n and h_n are spherical Bessel functions.

The angular scattering distribution for each polarisation are represented by S_1 and S_2:

$$S_1 = \sum_n \frac{2n+1}{n(n+1)}(a_n\pi_n + b_n\tau_n) \tag{2.9}$$

$$S_2 = \sum_n \frac{2n+1}{n(n+1)}(a_n\pi_n + b_n\pi_n) \tag{2.10}$$

where π_n and τ_n are functions that describe the angular scattering patterns of the spherical harmonics used to describe S_1 and S_2:

$$\pi_n = \frac{2n-1}{n-1}\cos\theta.\pi_{n-1} - \frac{n}{n-1}\pi_{n-2} \tag{2.11}$$

$$\tau_n = n\cos\theta.\pi_n - (n+1)\pi_{n-1} \tag{2.12}$$

The combination of the S_1 and S_2 scattering distributions may then be applied as follows:

$$S_{11}(\theta) = \frac{1}{2}|S_1(\theta)|^2 + \frac{1}{2}|S_2(\theta)|^2 \tag{2.13}$$

The S_{11} scattered power distribution is normalised by its scattering coefficient to

retrieve the phase function, $\widetilde{\beta}(\theta)$:

$$\widetilde{\beta} = \frac{S_{11}}{2\pi \int_0^{\pi} S_{11} \sin(\theta) d\theta} \tag{2.14}$$

The volume scattering function may then be calculated by integrating over the particle size distribution $N(D)$:

$$\beta_{Mie} = \int_0^{\infty} N \widetilde{\beta} C_{sca} dD \tag{2.15}$$

where N (m^{-3}) is the number of particles of diameter, D, and C_{sca} is the scattering cross-section (Slade and Boss, 2006).

Bohren and Clothiaux (2006) and Bohren and Huffman (1998) explain the computation of scattering patterns from particles in more detail and Wriedt (2009) explores advantages and disadvantages of various computer codes that are commonly used to calculate light scattering. Some extensions of Mie Theory, that include non-sphericity parameters, are also discussed. Figures 2.1 & 2.2 show Mie Theory predictions of scattering intensities for particle sizes between 1 and 100 μm. It is clear from Figure 2.1 that the scattering pattern is symmetrical either side of 0°. As a result, it is only necessary to calculate scattering angles between 0-180° to calculate the scattering at all angles. Scattering in the direction of 0° is in the forward direction and scattering at 180° is in the backward direction.

Figure 2.2 shows Mie predictions for small angle forward scattering between 0-10° - similar angles to those measured by a LISST-100 (type C) (see Section 2.3.4). There are distinctive peaks and troughs in the predicted scattering patterns. The first peak is often referred to as the principle diffraction lobe (PDL). As particle size increases, the angle to the PDL, decreases. Figure 2.3 shows that the refractive index controls the number of peaks and troughs in the scattering pattern, but is has more effect at larger angles. The PDL remains largely unaffected above refractive indices of approximately 1.1. It is worth noting that Figure 2.3 shows only relative scattering intensities and therefore the effect of refractive index on the magnitude of the scattering is not represented.

Figure 2.4 shows that as the incident wavelength increases, the angle to the PDL, increases. The relative angles between consecutive peaks and troughs are maintained at all the wavelengths plotted.

Geometrical optics approximation

The geometrical optics approximation is valid for particles with a radius that is much greater than the wavelength of the incident light ($a >> \lambda$). More specifically, Kokhanovsky and Macke (1997) stated that the geometrical optics approximation gives sufficiently accurate results for spheroids with size parameters greater than

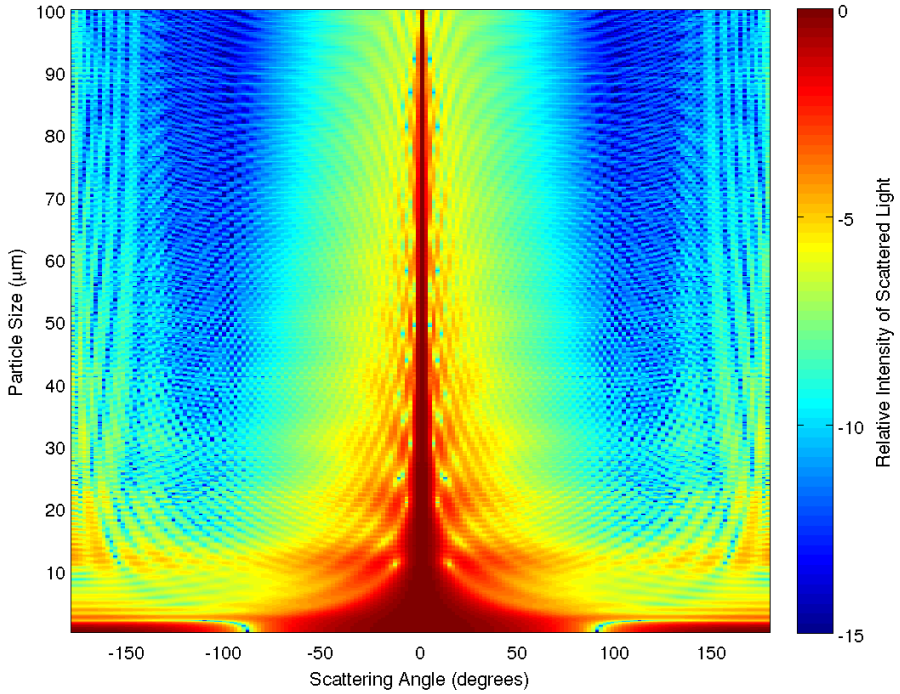

Figure 2.1: The effect of changing particle size on scattering angle at a constant wavelength, as predicted by Mie Theory.

60 (particle sizes larger than about $5\,\mu m$). This is because the wavelength of light is so small compared to the particle that the sphere surface can be considered to be approximately flat and therefore the principles of Snell's Law may be applied (Velesco et al., 1997). Kokhanovsky and Zege (1995) derived analytical solutions for the geometrical optics approximation for clusters of spherical particles of varying sizes. In doing this they simplified the approximation to allow for easier computation and introduced new parametrisation for edge effects. When comparing this adapted geometrical optics approximation to results from Mie Theory, they agreed within 5-8 %. However, this was using wavelengths of $2.25\,\mu m$ (within the infra-red wavelengths) and water cloud molecules, not suspended particulates in oceanic water. This approximation is therefore very difficult to apply to particles such as flocs, which consist of complex shapes and varying refractive indices. However, it can be applied successfully in some oceanographic situations, for example Bogucki et al. (1998) used the geometrical optics approximation to calculate light scattering from turbulence.

2.2.3 Scattering from collections of particles

Single scattering occurs when the number of particles is small enough and the separation between them is large enough so that the scattered light from a particle is not re-scattered by another particle. Multiple scattering, therefore, occurs when collections of particles produce scattering signatures that are different from single particles (Bohren and Huffman, 1998). Sediment concentrations in most coastal

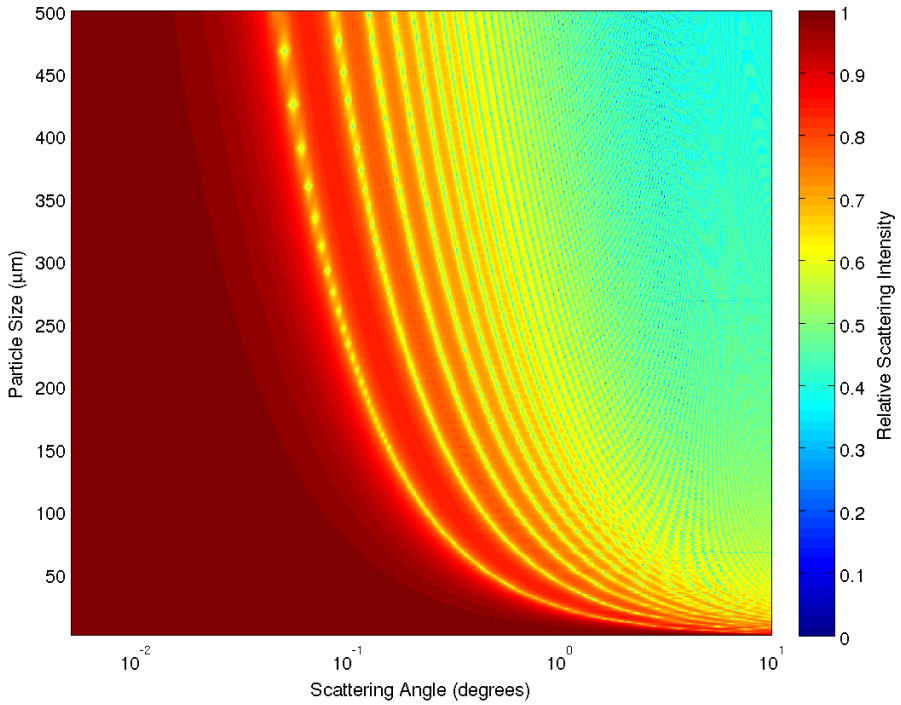

Figure 2.2: The effect of changing particle size on small angle forward scattering at a constant refractive index and incident wavelength, as predicted by Mie Theory.

waters are of a level high enough for multiple scattering to be significant. The simplified case of scattering by clusters of spherical particles of a constant size was investigated by Okada and Kokhanovsky (2009). The size parameter (x) used was 4, which corresponds to particles of 0.35 μm for an incident wavelength of 550 nm, and the densities of the particle clusters were between 0.1-30 %. Chiappetta (1980) described a method for calculating extinction, absorption and scattering cross-sections for particles in a multiple scattering environment. Using particle sizes similar to the wavelength of incident radiation, the numerical application to spheres agreed with Mie Theory.

The problems associated with multiple scattering from clusters of particles create a subsequent change in light attenuation through the water column in relation to spherical equivalent particles (Baker and Lavelle, 1984; Moody et al., 1987). There is a linear relationship between the light attenuation coefficient and particle concentration (Moody et al., 1987). However, despite this clear relationship, Moody et al. (1987) stated that because of potential changes in particle characteristics over time, the relationship between the light attenuation coefficient and particle concentration may vary. Baker and Lavelle (1984) claimed that calculations of light attenuation, based on scattering by spherical particles, underestimate observed attenuation by factors of 2-4. This is because the optical diameter of natural particles, which are non-spherical and have rough surfaces, is larger than the optical diameter of their volume equivalent spheres (Baker and Lavelle, 1984; Moody et al., 1987).

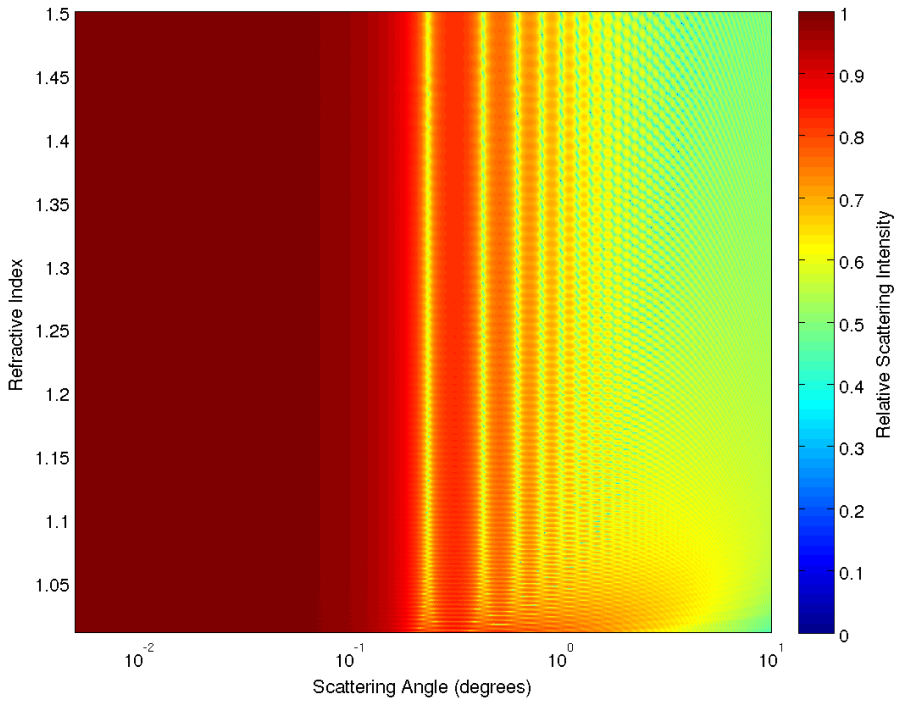

Figure 2.3: The effect of changing Refractive Index on small angle forward scattering for a 50 μm particle with a constant incident wavelength, as predicted by Mie Theory.

2.2.4 Scattering by non-spherical particles

Since the late 1980s there has been an increasing interest in scattering by non-spherical particles. This has resulted from more advanced computing capabilities, the knowledge that most particles within natural environments are non-spherical (Jonasz, 1987) and an increasing awareness of the errors associated with the assumption of spherical particles when predicting scattering patterns. A review of the electromagnetic theory of scattering by non-spherical particles is given by Mishchenko (2009). Various shape parameters may be used to simplify the problem for particles in the marine environment. The non-sphericity parameter is the ratio of the average projected area over all orientations of a particle, to the projected area of a volume equivalent sphere. Jonasz (1987) used a scanning electron microscope to conclude that the non-sphericity parameter of marine particles increases with particle size. Model results of scattering by Chebyshev particles (mathematically-derived deformed spheres) of varying shapes was published in a series of three papers: Mugnai and Wiscombe (1986), Wiscombe and Mugnai (1988) & Mugnai and Wiscombe (1989). Using 23 different shaped Chebyshev particles, they found that non-sphericity increases backscattering and that the concavity of the particle plays a key role in how it scatters light. Their models also showed that non-sphericity increases the absorption efficiency for size parameters greater than about 10 ($x \gtrsim 10$). Jonasz (1987) stated that non-sphericity causes an underestimation of the projected area of a particle when calculated using an equivalent sphere. The differences between measured and theoretical light scattering reported in work such as Agrawal et al.

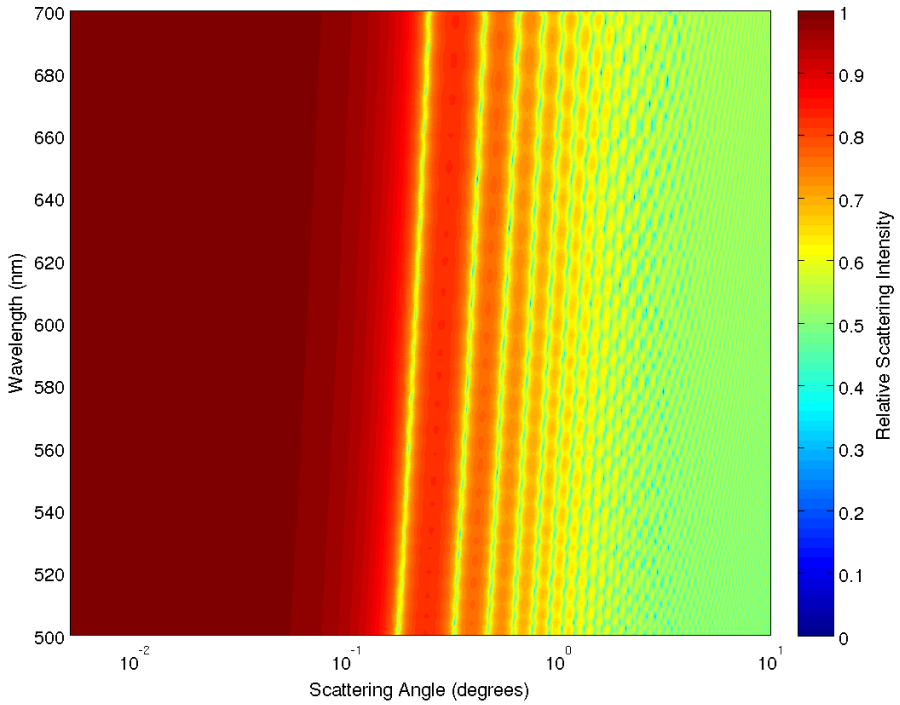

Figure 2.4: The effect of changing incident wavelength on small angle forward scattering for a 50 μm particle at a constant refractive index, as predicted by Mie Theory.

(2008), Kocifaj (2009), Kokhanovsky and Macke (1997) & Mikkelsen et al. (2005) could be, in part, due to this underestimation of the non-sphericity parameter.

Boss et al. (2009) performed an assessment of the differences between the beam attenuation of aggregates and the beam attenuation from their component parts. They applied a model proposed by Latimer and Wamble (1982) for approximating scattering by aggregates of blood platelets. This approach models aggregate scattering using a coated sphere approach which is demonstrated by Bohren and Huffman (1998). The volume and refractive index used for the coat was that of the primary particles (blood platelets) and the volume and refractive index of the core were representative of the spaces in between the primary particles. Latimer (1985) attempted to test this approximation experimentally and concluded that the lack of ability to accurately resolve aggregates with microscopy limited the degree to which the model could be reliably tested but it did show agreement "to a first approximation". The model presented by Boss et al. (2009) developed the coated sphere approach further by attempting to include the effects of non-sphericity through adding scattering predictions for an ellipsoid rotated through all orientations. This proved to be an effective approximation for beam attenuation for aggregates, but did not include any predictions of angular scattering functions, and is therefore not suitable for predicting the LISST-100 response to aggregates.

Comparisons of results using volume equivalent spheres and non-spherical particles have been considered in a variety of papers (Kocifaj, 2009; Kokhanovsky and Macke, 1997). Kokhanovsky and Macke (1997) obtained approximate equations for

the cross sections and asymmetry parameters of large, non-spherical particles. When the equations were applied to randomly oriented spheroids and hexagonal cylinders at different values of shape parameters and absorption, the error was found to be less than 20 % for the hexagonal cylinders. The effects of non-sphericity are also key for studies such as Gordon and Du (2001) who investigated the light scattering by *Emiliania huxleyi* (coccolithophore) and found that the backscattering cross section was strongly dependent on particle morphology due to multiple reflections within the particle. This highlights the importance of a knowledge of the refractive index of a particle, as well as the non-sphericity parameter when determining particle characteristics using light scattering. The results from these works allow for a strong argument for the development of a general theory of non-spherical scattering that considers both the deviation from a spherical equivalent and the concavity of the particle.

There has been a large amount of interest in improving the shape parametrisations when using Mie Theory for the calculation of particle characteristics. For example, Kokhanovsky and Macke (1997) explored analytical formulae for asymmetry parameters and absorption cross sections of non-spherical particles. Agrawal et al. (2008) discussed the limitations of Mie Theory when calculating a particle size distribution from a VSF when random shaped particles are present. They state that instruments such as the LISST-100 (see Section 2.3.4) could over-estimate size when assuming spherical particles due to a shift in the scattering pattern by approximately one scattering detector. The work of Agrawal et al. (2008) and Agrawal and Mikkelsen (2009) produced empirical data as an alternative to Mie Theory for random shaped particles of $1.09 - 21.39\,\mu m$ to improve the calculation of particle size distributions from *in-situ* observations of the VSF.

As well as a consideration of particle shape, it is also important to account for the orientation of a non-spherical particle. Asano and Sato (1980) simplified this problem by studying light scattering by randomly oriented, identical spheroidal particles. It was found that the scattering cross section, single scattering albedo, and asymmetry factor of spheroids tend to be larger than those for volume equivalent spheres. More specifically, the angular scattering pattern from spheroids was found to be very different from spheres for the side scattering and backscattering directions. This could suggest that the effect of particle shape is less of a problem for instruments that use forward angle scattering. In addition to these relatively simple non-spherical particles Latimer (1984) considered the difference between scattering by a homogeneous sphere with radial projections and a smooth homogeneous sphere. Both spheres had an equal refractive index (1.05 relative to the surrounding medium) and volume, and the size parameters used were between 0.03 and 1200 (approximately 0.5-100 μm). It was found that the radial projections caused a decrease in total scattering for small particles ($x < 45$) and increased scattering for

particles with size parameters greater than 45 (approximately 5 μm).

2.3 Instruments for measuring particles and their optical properties

A large number of methods have been used for the determination of particle characteristics. Some involve *in-situ* measurements, while others require further laboratory analysis of water samples. For example, Konert and Vandenberghe (1997) compared laser grain size analysis with pipette and sieve analysis and Jackson et al. (1997) used a variety of *in-situ* measurements, such as photographic camera systems and various video techniques. The fragile nature of marine particles, especially micro-organisms and cohesive sediments that have the potential to flocculate, means that reliable *in-situ* measurements are vital for the accurate representation of particle characteristics (Bale and Morris, 1987; Bale, 1996; Eisma and Kalf, 1996).

2.3.1 Acoustic scattering

Acoustic scattering may also be used to retrieve information on mean particle size and concentration (Thorne and Hanes, 2002). However, as mentioned previously, it is important for an accurate particle size distribution to be recorded and currently this is not possible using acoustic technology, which is limited to estimations of median particle size for a population. An advantage of acoustic measurements of particle characteristics is that a near-instantaneous profile of a water column is possible - a result that is not achievable using optics. A comparison of acoustic backscatter and laser diffraction measurements was investigated in the work of Thorne et al. (2007), who showed that measurements of mean grain size were consistent between the instruments, but there were discrepancies when measuring particle concentration.

2.3.2 Optical scattering

Optical backscatter sensors

Optical Backscatter Sensors (OBSs) are commonly used in determining concentrations of suspended particles within the water column. Various errors associated with using sensors of this nature were studied by Bunt et al. (1999) and include the shape and roughness of particles, which caused significant over-estimations of particle concentration. Particle size, flocculation and air bubbles were found to increase the response of the OBS by up to two times, and plankton increased the response of the OBS by four times. Unfortunately this technique is limited to concentration

measurements and so particle size distributions are currently unable to be retrieved from such a method.

2.3.3 Electrical Impedance

Coulter Counter instruments adopt a particle sizing technique that is reliant on changes in the levels of electrical resistivity caused by particles passing through a narrow aperture. The change in resistivity is proportional to the particle volume. Wider apertures allow for measurements of larger particles (up to about $600\,\mu m$) and narrower apertures enable measurements of less than $1\,\mu m$. Unfortunately this method is restricted to laboratory use and the size range is heavily dependant on the aperture width used. In addition to concerns of particle break-up due to shear forces generated through the aperture (Jonasz and Fournier, 2007), measurements informed through multiple aperture configurations encounter difficulties when splicing multiple distributions (Reynolds et al., 2010).

2.3.4 Laser diffraction

Laser particle sizing is now a commonly used method for determining an *in-situ* particle size distribution and concentration. This is because of its ability to measure particle characteristics *in-situ*, at a high sample rate and with minimal computational processing requirements. Konert and Vandenberghe (1997) compared laser grain size analysis with pipette and sieve analysis and concluded that laser diffraction is only accurate if the entire grain size range is considered and the sediment does not flocculate. This issue has been explored by Agrawal et al. (2008) in an attempt to improve the shape parametrisation in the processing of LISST-100 data (see Section 2.2.4). Karp-Boss et al. (2007) assessed the response of the LISST-100 to plankton, and found that various sub-components of a particle's geometry contributed to peaks in volume distributions from the LISST. These peaks corresponded to the sizes of various features within the particle. They concluded that the LISST response was a combination of equivalent diameters from the all-encompassing spheroid of the particle and the equivalent diameters of the sub-components such as the main body and appendages (Figure 2.5).

The LISST-100 is able to estimate the particle size distribution by inverting measurements of forward-angle scattering (Agrawal and Pottsmith, 2000), the principles of which are described in Chapter 3. Within the instrument collimated laser light passes through the sample volume onto a receiving lens. A specially made array of 32 detectors, positioned at the focal plane of the receiving lens, receives an intensity distribution of scattered light from the particles within the sample volume. As discussed in Section 2.2.2, the angle at which light is scattered is proportional to the size of the scattering particle. The optical power distribution on the ring detector gives

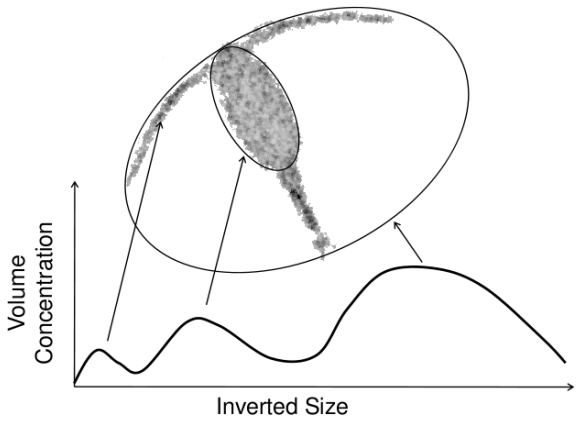

Figure 2.5: Illustration of the features of LISST-100 volume concentrations from multiple components of plankton geometry, as suggested by Karp-Boss et al. (2007).

the essential information on particle size distribution within the sample volume. For example, large particles are expected to cause a peak in optical power at small angles. The inversion of power distribution sensed by the rings produces an area distribution of particles. The volume distribution of particles is obtained from the area distribution by multiplying the area in any size class by the median diameter in that size class. The total volume concentration in the sample can then be obtained by summing the volume distribution. A known limitation of this technique is that it assumes spherical particles when calculating sizes (Lynch et al., 1994). Agrawal et al. (2008) has addressed this problem by producing a new kernel matrix for random shaped particles, as discussed in Section 2.2.4. A study by Mikkelsen et al. (2005) compared the use of LISST instruments with a particle imaging system and found that the LISST had a tendency to underestimate sizes. The application of *in-situ* measurements made by LISST instruments and other laser techniques has been investigated in a number of studies, including those of Bale and Morris (1987) and Law. et al. (1997).

The work of Konert and Vandenberghe (1997) concluded that for laser diffraction techniques to be reliable, particles must not flocculate. However, Agrawal and Pottsmith (2000) state that particle composition, and therefore refractive index, does not determine scattering characteristics received by the LISST-100 for particles larger than a few microns. This is due to small angle scattering being dominated by diffraction as opposed to refraction for large particles, as per Van-De-Hulst (1957). An evaluation of the effect of particle composition and refractive index on the reliability of inverting LISST-100 scattering into a particle size distribution was made by Andrews et al. (2010). They concluded that in most cases the original, mineral-like inversion matrix presented by Agrawal and Pottsmith (2000) performed well, and in specific cases of phytoplankton populations other custom-build matrices performed better. Unfortunately the validation of the size distribution inverted by the LISST-100 was achieved by comparison with microscope images, leading to uncertainty as

to whether discrepancies were a result of particle disturbance, concentration scaling errors resulting from the microscope sample preparation, artefacts arising from the set-up of the LISST-100 used, or from the LISST-100 inversion itself. The need for a carefully developed methodology that minimises these discrepancies is necessary for an accurate comparison of measurements techniques such as this.

2.3.5 Imaging

A comparison of particle size measurements from a Coulter Counter, LISST-100 and imaging was conducted by Reynolds et al. (2010). They found all three techniques reported generally good estimates of average particle size when known spherical standards were used. The performance of the LISST-100, when subjected to size distributions with features such as narrow peaks, was noted as less accurate than that of the Coulter Counter. This is as expected, given the angular resolution of the LISST scattering detectors, resulting in relatively broad size bins in comparison to a Coulter Counter. Mikkelsen et al. (2005) conducted a comparison of the LISST-100 in relation to standard imaging methods and concluded that the imaging technique used in their study had a tendency to report particle sizes larger than that of the LISST-100, but that a generally good agreement was apparent within the size ranges in which both instruments overlap. This lead to their suggestion that particle size distributions from both instruments could be spliced to provide information over a size range spanning from $2.5\,\mu m$ to several millimetres. A number of techniques that collect images of particles *in-situ* have been used to try and quantify accurate floc characteristics (Knowles and Wells, 1996; Dyer et al., 1996; Eisma and Kalf, 1996; VanLeussen and Cornelisse, 1996; Maldiney and Mouchel, 1996; Milligan, 1996; Syvitski and Hutton, 1996; Mikkelsen et al., 2005; Benson and French, 2007), most of which use video cameras and digital image processing to measure particle size and shape.

Electron microscopy is a well established method of retrieving nano-scale resolution of particles. Unfortunately, the preparation and treatment of particles needed causes severe disruption to any delicate particles and, in some cases, a shrinkage of size due to loss of water (Jonasz and Fournier, 2007). These necessary preparations remove all possibility of *in-situ* measurements of marine particles with electron microscopy. However, the accuracy of electron microscopes does make the technique a valuable tool for assessing the quality of particle standards when validating and testing other sizing instruments.

The application of in-line holography has recently become a topic of interest for the measurement of marine suspended particles. Owen and Zozulya (2000) and Graham and Nimmo-Smith (2010) describe how digital in-line holography can be used to measure marine particle size, shape and settling velocity. One of the main advantages of digital holography is that the hologram of the sample volume can be

reconstructed at any depth, allowing for an accurate measurement of any particle within the sample volume without errors due to depth of field and focussing which are a problem in standard imaging techniques and microscopy. A disadvantage of this technique is the relatively large amount of computational resources that are required for reconstructing and processing the holograms. It is often the case that imaging techniques are not used due to additional processing requirements, especially for long time-scale data-sets. The amount of data required for instruments such as the LISST-100 to retrieve an estimate of a PSD is much less than that of imaging and may subsequently be deployed with relative ease for long periods of time at relatively high sample rates.

2.3.6 Measuring optical properties of the water

Petzold (1972) presented ground-breaking measurements of the full volume scattering function *in-situ* from selected water masses. The work has been continually used as a proxy for the VSF in many radiative transfer models since (Mobley, 1994). However, temporal and spatial variability was observed, and is discussed by Agrawal (2005), who used the LISST-100 to measure variations in the near-forward angles of the VSF. It is well understood that the variability in the volume scattering function is controlled primarily by changes in the particle size distribution and total particle concentration, with particle size dominating variations in the forward angles.

The method presented by Agrawal (2005) and adopted by Slade and Boss (2006), accounts for the relationship between the optical power distribution and area of each of the LISST-100 angular scattering detector rings as follows:

$$\beta_{i,p}(\theta) = [P_{i,p}/P_0]e^{c_w L}/[\pi\phi L(1-\rho^{-2})\rho^{2i}\theta^2_{min} \tag{2.16}$$

where P_i is the optical power on each ring, P_0 is the laser power entering the water, ρ represents the ratio of the outer to inner radius of any ring, and L is the window separation (i.e. sample volume width).

Both studies reported close agreement between Mie Theory and the observed scattering for spherical particles, the main differences being a reduction in the number of fine-scale peaks and troughs due to the angular resolution of the scattering detectors (Figure 2.6). This effect can be easily accounted for by integrating the scattering intensities over the angular range of each detector, as demonstrated by Agrawal et al. (2008).

Scattering and absorption coefficients of samples of water may be measured using instruments such as the WetLabs ac-s, which estimates these bulk optical properties over many wavelengths at a spectral resolution of approximately 4 nm. Despite this useful *in-situ* technology, the sample is required to be pumped into the scattering tube before measurements may be taken, resulting in substantial disruption to the

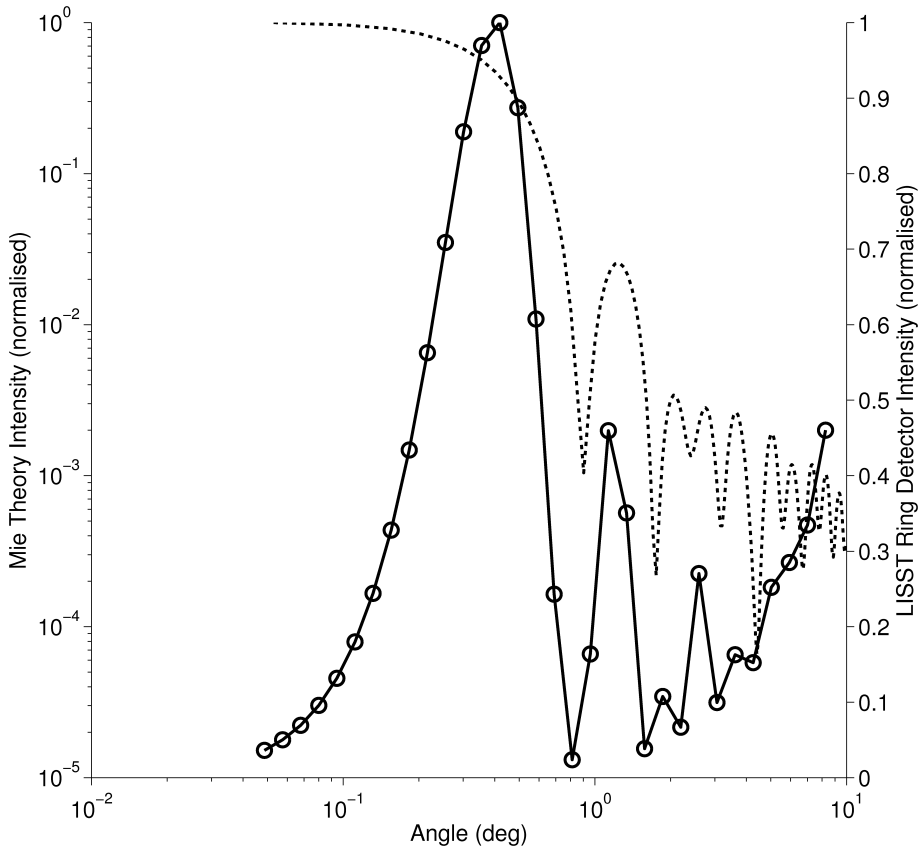

Figure 2.6: Mie Theory predictions of scattering from a 25 micron particle (dotted line), and the associated LISST-100 ring detector intensities (solid line, with circles indicating the centre of each ring detector). Adapted from Agrawal et al. (2008).

sample and potential floc break-up. Direct measurements of the scattering and absorption coefficients provide an easy assessment of the optical properties of the water, but do not give any information on the directional dependence of scattering, which is provided by the volume scattering function.

2.4 Summary

- There are many different types of marine particles of varying shapes, sizes and composition. There is no single method of representing particle characteristics, as each method fulfils a different purpose. It is therefore important to have a knowledge of the characteristics of suspended marine particles to predict their movement - a topic that is necessary for the modelling of the marine environment, for example, in pollutant dispersal and determining components of the Carbon Cycle. As a result it is vital to accurately measure marine particle characteristics *in-situ*.

- Light scattering theories vary in their complexity and computational demands. Mie Theory is based on Maxwell's electromagnetic field equations and is an exact solution for scattering of light by spherical particles and forms the basis of most light scattering models.

- Other models have been developed to take into account shape effects (such as the T-matrix) and multiple scattering. However, the reviewed literature does not highlight a single, widely used technique that accurately predicts light scattering from clusters of particles of any size, shape or composition.

- The publications that appear to hold the most weight have been ones which present results of light scattering and characterise specific situations, rather than attempt to formulate accurate predictive models.

- Marine particles can be measured using acoustic backscatter, optical backscatter, optical forward scattering and imaging techniques. Each of these techniques have specific advantages and disadvantages depending on particle composition, size, concentration and sampling rates.

- Optical forward scattering is the technique used in the popular LISST-100 instrument, which is based on optical scattering theory (Mie Theory) to invert a recorded VSF into a particle size distribution. However the knowledge of the accuracy of this method, when used with marine particles of complex structures such as flocs and zooplankton, is limited.

Chapter 3

Methods

Material in this chapter contains material that has been expanded from the following publication:

Emlyn J. Davies, W. Alex M. Nimmo-Smith, Yogesh C. Agrawal, and Alejandro J. Souza, (2011), "Scattering signatures of suspended particles: an integrated system for combining digital holography and laser diffraction", Opt. Express 19, 25488-25499. (Appendix A)

This chapter presents a novel, integrated system, which combines both digital in-line holography and a LISST-100 type-c. It is capable of simultaneously recording in-focus images of artificial or natural particles, with their small-angle forward scattering signature from within an identical sample volume.

One of the most widely used techniques for measuring the particle size distribution *in-situ* is that of laser diffraction. This technique is adopted by the LISST series of instruments (developed by Sequoia Scientific Inc.). The method for determining a particle size distribution (PSD) in this way relies on inversion algorithms based either on scattering theory or empirical measurement, and is described in this chapter. However, the available inversion algorithms perform at different accuracies, depending on the type of particles under investigation. For a thorough understanding of the response of LISST instruments to the many complex particles found in the marine environment, detailed information on both particle size and shape needs to be captured, and may be achieved using imaging. Standard imaging techniques encounter problems associated with limited depth-of-field in large sample volumes and, as a result, in-line holography is a preferred method for obtaining in-focus and high resolution particle images, regardless of their position within the sample volume.

The combined laboratory system described in this chapter is utilised throughout the work presented in subsequent chapters of this thesis, to help aid scientific understanding of scattering by complex marine particles, and the associated reliability

of particle size measurements using laser diffraction. Basalt spheres were used to validate the combined laboratory system through models and observations of scattering intensities and the associated particle size measurements inferred from digital holography and laser diffraction.

In addition to the introduction of the combined holographic camera and LISST-100 laboratory system, this chapter also describes the underlying principles of particle measurements using laser diffraction and digital holography. A detailed explanation of the holographic reconstruction and image processing software used for analysis of digital holograms is also presented.

3.1 Principles of laser diffraction and the LISST-100

The LISST-100 uses a custom 32-ring detector to measure the angular distribution of light scattering from particles using a wavelength of 670 nm for incident light (Agrawal and Pottsmith, 2000). The instrument consists of a collimated laser beam with a width of 6 mm that passes through the sample volume onto a receiving lens. The 32 ring detectors are positioned at the focal plane of the receiving lens. This configuration allows scattering intensities to be recorded at varying angles with larger angles being focused onto the outermost rings of the detector (Figure 3.2). Each ring detector covers scattering angles of logarithmically increasing ranges. The rings cover angles of 0.05-10° for the type-c (2.5-500 μm particle diameters) and 0.1-20° for the type-b (1.25-250 μm particle diameters), with each ring covering 1/6 of a circle in the azimuthal plane (Figure 3.1). As particle size increases, the angles of the principal peaks in the scattering function, recorded by the LISST, reduce and their scattering intensity increases, as illustrated in Figure 4.1(a). In addition, as the number of particles increases, the scattering intensity also increases. Therefore, the intensity distribution of the scattered light recorded by the LISST is related to both the size and concentration of particles present. This principle means that the recorded light intensities on each of the 32 rings may be inverted, using an appropriate inversion matrix, to predict the associated size distribution of the particles that produced the scattering. The concentration is then scaled, according to a calibrated conversion constant, to bring the inverted size distribution to a 'true' concentration. For the standard LISST-100 instruments the laser is on constantly at approximately 1 mW, leaving the ring detectors exposed to the incident light at all times. Each scattering measurement from the rings is representative of an integration time of just under 100 ms, leading to more accurate readings when particles in the sample volume are homogeneously distributed throughout this integration time. Varying instrument configurations have been adopted by Sequoia Scientific Inc. to enable measurements over different size ranges. The same array of ring detectors are used,

but with different focal length lenses, to allow for varying collection angles on the rings.

Figure 3.1: Diagram of the LISST-100 ring detector configuration. The shaped photo-detectors are shown by the black areas.

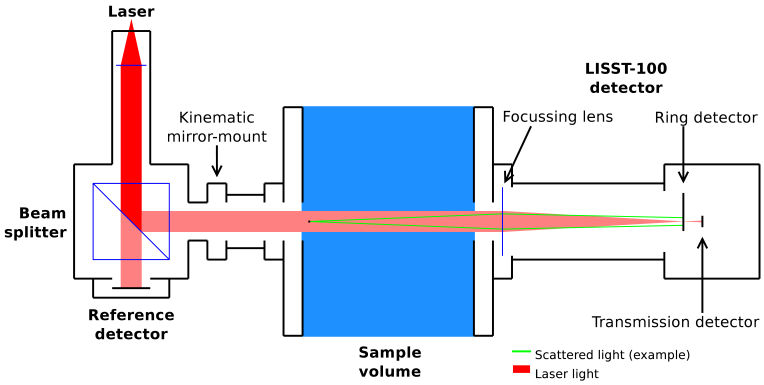

Figure 3.2: Schematic illustration of the LISST-100 instrument. A light ray scattered at any angle from the laser beam is focused to a position on the ring detector, allowing for a measure of the angular distribution of scattered light. The focused beam passes through a 75 μm hole at the centre of the ring detectors, behind which is a transmission detector for the calculation of beam attenuation.

The angular distribution of light scattered in the forward direction is primarily affected by the size of the particle. Using Mie Theory, it is possible to predict the intensity of light that would be recorded by each of the 32 ring detectors of the LISST-100, by integrating the theoretical VSF over the angle ranges covered by each of the rings. Figure 3.3 shows how the predicted intensities on each of the 32 detectors change with particle size. As particle size increases, the angle of the principal diffraction lobe (the largest peak in intensity at each size) decreases.

Substantial assumptions in the inversion of a VSF to an associated size distribution are that the particles in the sample volume are spherical and of a known refractive index. Agrawal et al. (2008) began to address these problems by producing an alternative kernel matrix for the inversion of scattering by random shaped particles, through empirical measurements of sand and ground coffee grains (Agrawal et al., 2008). However, unknown errors remain in the inversion when the LISST-100 is exposed to the wide range of complex particles and flocs that are common in marine environments. A number of studies have compared the performance of the LISST-100 with other particle sizing techniques, for example Mikkelsen et al. (2005)

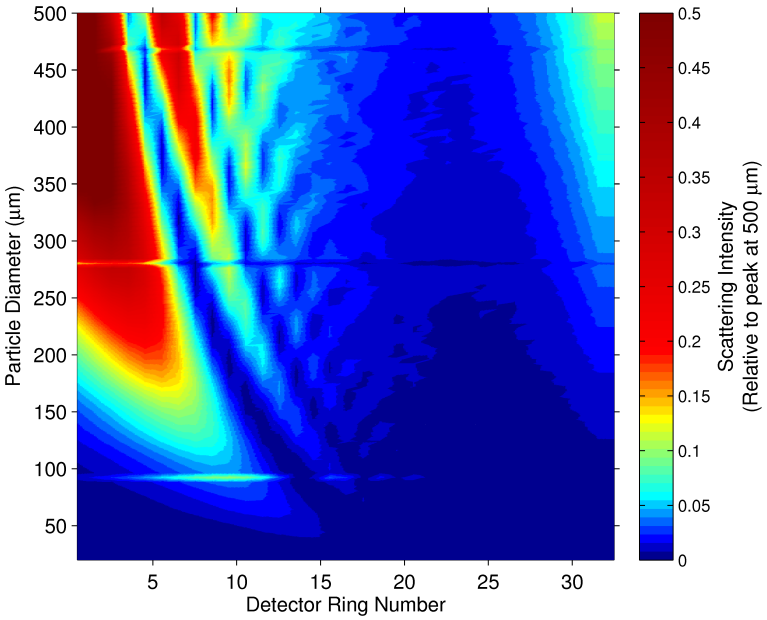

Figure 3.3: Predicted scattering intensities from Mie Theory for each of the 32 ring detectors of the LISST-100 type-c, for particle diameters of $20 - 500\,\mu m$ (size range covered by both the holographic camera and the LISST-100 type-c).

and Reynolds et al. (2010), both of which report comparable results between the LISST and other techniques. However, in regions in which large flocs were present, problems such as an overestimation of the volume of particles in the largest size bin were highlighted.

3.1.1 Correction of scattering

The LISST-100 measures the total scattering from both the water and the particles ($scat$). To retrieve scattering information from just the particles ($cscat$), a correction from a background water measurement ($zscat$) and attenuation (τ) is applied, and then corrected to account for the areas of each ring detector ($dcal$):

$$cscat = \left(\frac{scat}{\tau} - zscat \right) dcal \tag{3.1}$$

where τ it the percentage light transmission through the sample.

3.2 Digital in-line holography

A digital hologram takes the form of an interference pattern recorded by the CCD (Charge-Coupled Device) of a camera. This interference pattern is produced from constructive and destructive interference between coherent background light (laser light) and the scattered light from particles within the sample volume (Figure 3.4). The resulting hologram can be numerically reconstructed to produce in-focus images of every particle recorded, eliminating the problems associated with depth-of-field

and focussing that occur when using conventional imaging methods. The details of holographic reconstruction are explained by Owen and Zozulya (2000) and Graham and Nimmo-Smith (2010), the main principles of which are explained in subsequent sections of this chapter.

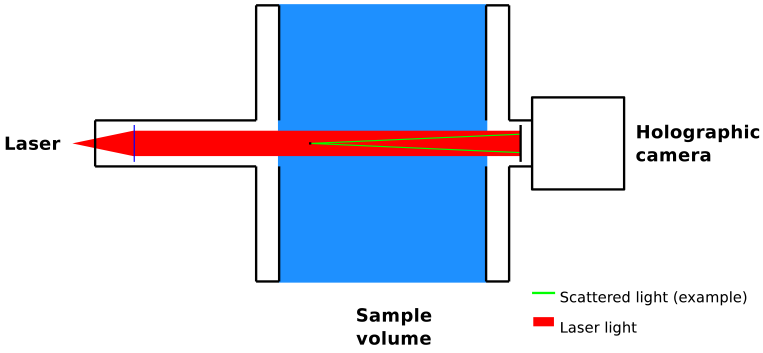

Figure 3.4: Schematic illustration of the optical set-up of the holographic camera. A collimated laser beam passes through the sample volume and is recorded by the CCD of the camera, positioned on the far side of the volume. Scattering of light from within the beam interferes with the incident light of the initial beam, creating an interference pattern (hologram) on the holographic camera.

The raw hologram ($I(x, y)$) is an image containing interference between the beam created from scattering by particles (E_0) and the incident laser light (E_r), as illustrated in Figure 3.5.

$$I(x, y) = |E_0(x, y, L)exp(ikL) + E_r exp(ikL)|^2 \tag{3.2}$$

where x, y is a position within the field, L is the distance to the CCD of the camera from the object and $k = (2\pi)/\lambda$.

It is demonstrated by Owen and Zozulya (2000), that the real image can be retrieved at any point within the sample by numerically propagating light back through the interference pattern ($I(x, y)$) using the routine summarised as follows:

1. Transform $I(x, y)$ into the Fourier domain:

$$\hat{E}(f_1, f_2) = \frac{1}{(2\pi)^2} \int\int dxdy I(x, y) exp(-if_1 x - if_2 y) \tag{3.3}$$

   where f_1, f_2 is a position within the Fourier domain.

2. Remove the zero frequency (DC) component (the part of the beam that is not diffracted):

$$\hat{E}(0, 0) = 0 \tag{3.4}$$

3. Multiply the Fourier harmonics by an appropriate phase factor to propagate back to a distance from the CCD to the location of the real image (z):

$$\hat{E}'(f_1, f_2, z) = \hat{E}(f_1, f_2) exp(-if^2 z/2k) \tag{3.5}$$

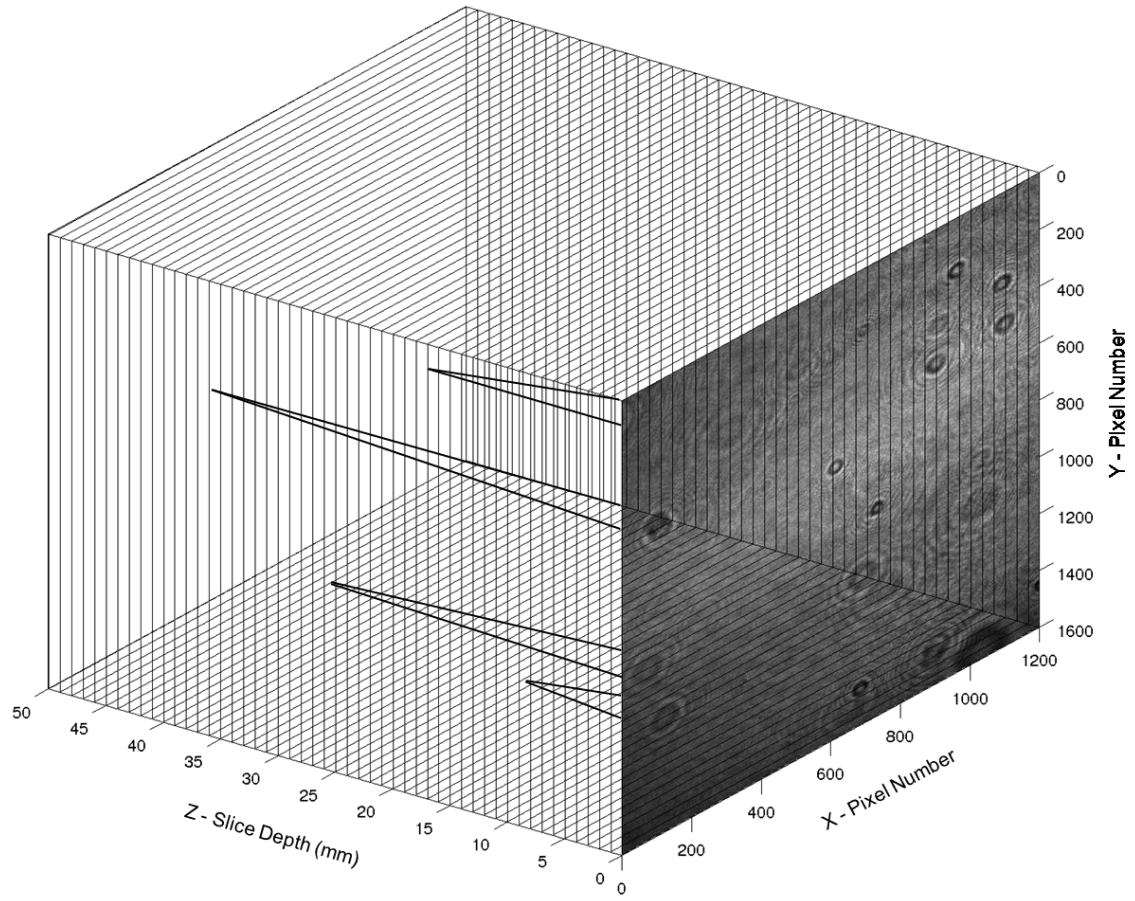

Figure 3.5: Illustration of the holographic camera sample volume and interference patterns.

where $f = \left(\frac{\pi}{PixelSize}\right)|f_1 + f_2|$

4. Obtain the real image by applying the inverse Fourier transform of $\hat{E}'$:

$$E(x, y, z) = \left| \frac{1}{2\pi} \int \int df_1 df_2 \hat{E}'(f_1, f_2, z) exp(i f_1 x + f_2 y) \right|^2 \tag{3.6}$$

Software to autonomously reconstruct, identify and size particles from a raw hologram using the above method has been developed from that of Graham and Nimmo-Smith (2010) during the process of this study. The first stage of the processing is to correct for deviations in the background intensity of the raw images and also attempt to remove stationary objects that may be present on the optical components. This is achieved by subtracting a clean background image (either from clear water or an average of a number of images) from the raw hologram. The holograms recorded using the combined LISST-100 and holographic camera system cover a large proportion of the Gaussian incident laser beam. In contrast, the images obtained from *in-situ* images capture a small portion of a much larger diameter beam. The differences in intensity across these two images are illustrated in Figure 3.6 and are important for governing the accuracy of the binerisation of particles.

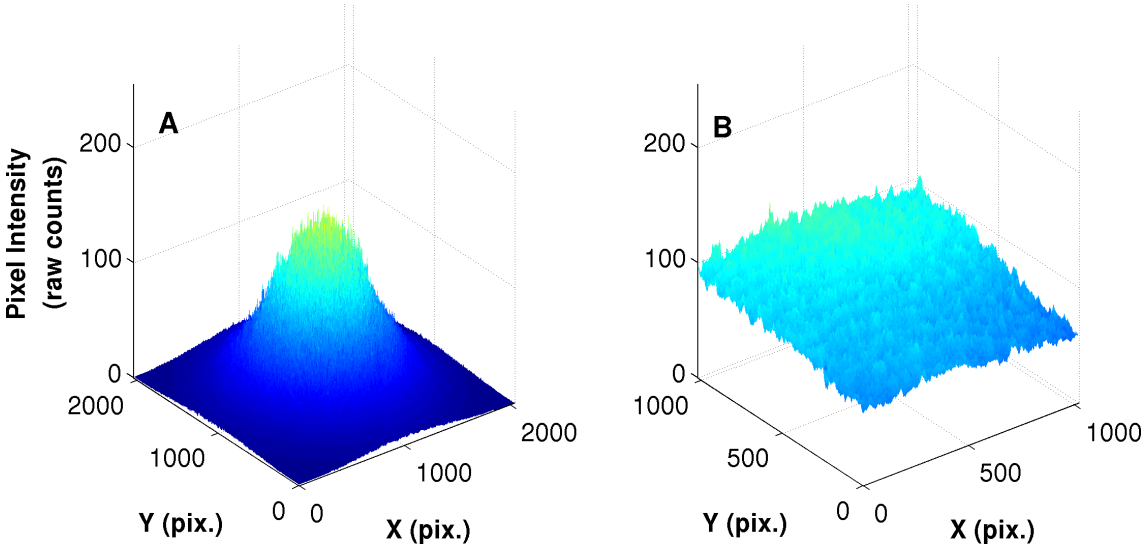

Figure 3.6: Examples of the beam intensity distribution used for: A, the combined holographic camera and LISST-100 system; and B, the stand-alone holographic camera systems used *in-situ*.

The holographic images shown in Figure 3.7(a) and 3.7(b) show a bright centre and dark edges, created from the Gaussian beam of the combined LISST-100 and holographic camera laboratory system. The reason for the chosen beam diameter, and resulting dark areas in the holograms, was to allow the holographic camera to capture the entire sample volume recorded by the LISST-100 when combining both instruments (Section 2). The background image of Figure 3.7(b) was subtracted from the raw image (a) in order to remove any stationary objects and

reduce noise. An example of the resulting clean image is shown in Figure 3.7(c). This is a similar process to the *zscat* (background scattering data) which is subtracted from LISST-100 data before analysis. Once a clean holographic image was calculated, the reconstruction procedure explained by Owen and Zozulya (2000) was then implemented, producing a stack of reconstructed images. Following this, each particle within the reconstructed image stack was manually focused and binarised to allow for errors in the automatic focusing and thresholding to be reduced, and for overlapping or poorly resolved particles to be excluded from the analysis. This procedure resulted in a binary image of all in-focus particles in the sample volume. Each particle in the binarised image was then analysed independently to return their geometrical properties, such as equivalent spherical diameter, perimeter and major axis length.

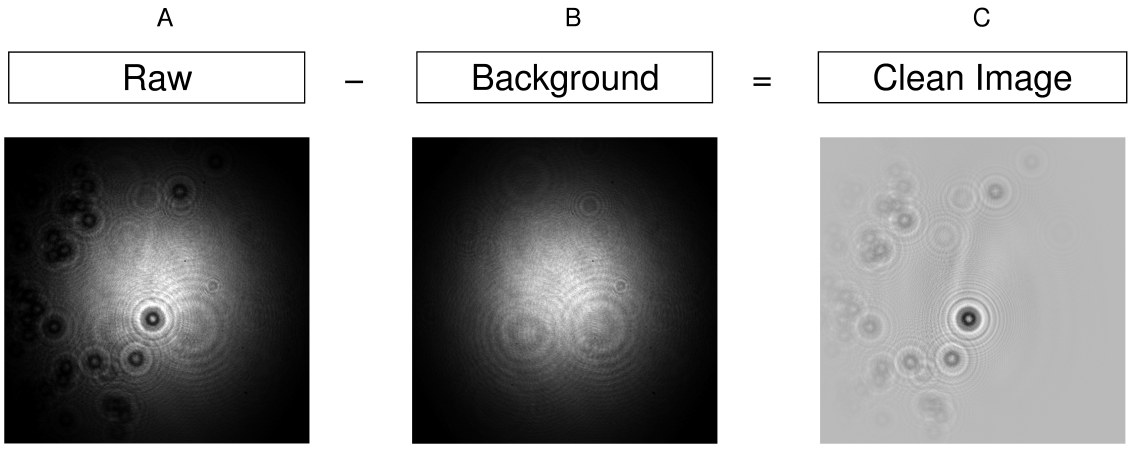

Figure 3.7: A: Example of a raw hologram containing basalt spheres. B: Example of a background image. C: Example of a clean image after background removal.

Following the correction of the raw image it is then numerically reconstructed, as per Owen and Zozulya (2000), to produces an array of real images ($E(x, y, z)$), focussed at different positions through the sample volume. Examples of two reconstructed images at different z distances are shown in Figure 3.8.

Particles are located by finding regions of high standard deviations ($\sigma(x, y)$) through the stack of real images returned by the reconstruction:

$$\sigma(x,y) = \left(\frac{1}{n-1} \sum_{i=1}^{n} \left(E(x,y,i) - \bar{E}(x,y) \right)^2 \right) \tag{3.7}$$

where n is the number of z real images that have been reconstructed and $\bar{E}$ is the mean of E through all z planes:

$$\bar{E}(x,y) = \frac{1}{n} \sum_{i=1}^{n} E(x,y,i).$$

For each of the identified particles (p) at locations within ranges specified by

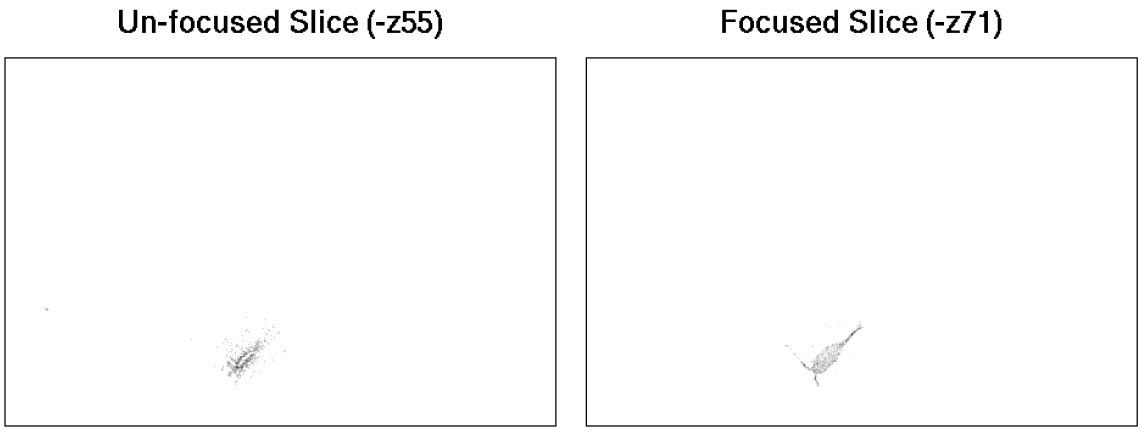

Figure 3.8: Examples of reconstructed holographic images at different depths through the sample.

x_p (of length n') and y_p (of length n''), may then be focussed to a position (z_F) at which the maximum total intensity of $E(x_p, y_p)$ is found in the stack of real images:

$$z_F(p) = \arg\max_z \sum_{i=1}^{n'} \sum_{j=1}^{n''} E(x_p(i), y_p(j), z) \tag{3.8}$$

Each focussed particle image ($E(x_p, y_p, z_F(p))$) may then be binarised, and the pixels counted, to enable the retrieval of geometrical statistics for the binary particle in the image.

Information on particle geometry is retrieved automatically using the reconstruction routine described here, when processing holographic data used in Chapters 5 and 6. Data analysis from Chapters 3 and 4 was performed using manual focussing and binerisation of particles. This was due to difficulties in automatically focussing perfectly spherical particles, leading to errors in their binerisation which are less problematic for non-spherical particles.

3.3 Combined LISST-100 and holographic camera laboratory system

The combination of digital holography and a LISST-100 should allow for a greater understanding of how forward scattering signatures are affected by various types of particle. This is because the system simultaneously records in-focus images of particles and their light scattering signature from within the same sample volume. Further development of a reliable alternative to Mie Theory, when using laser diffraction for the *in-situ* measurement of complex suspended particles, will then be possible. The new laboratory-based system allows for the forward-angle VSF, recorded by the LISST-100, to be compared with an accurate measurement of particle characteristics obtained with holographic imagery. The system consists of a purpose-built settling

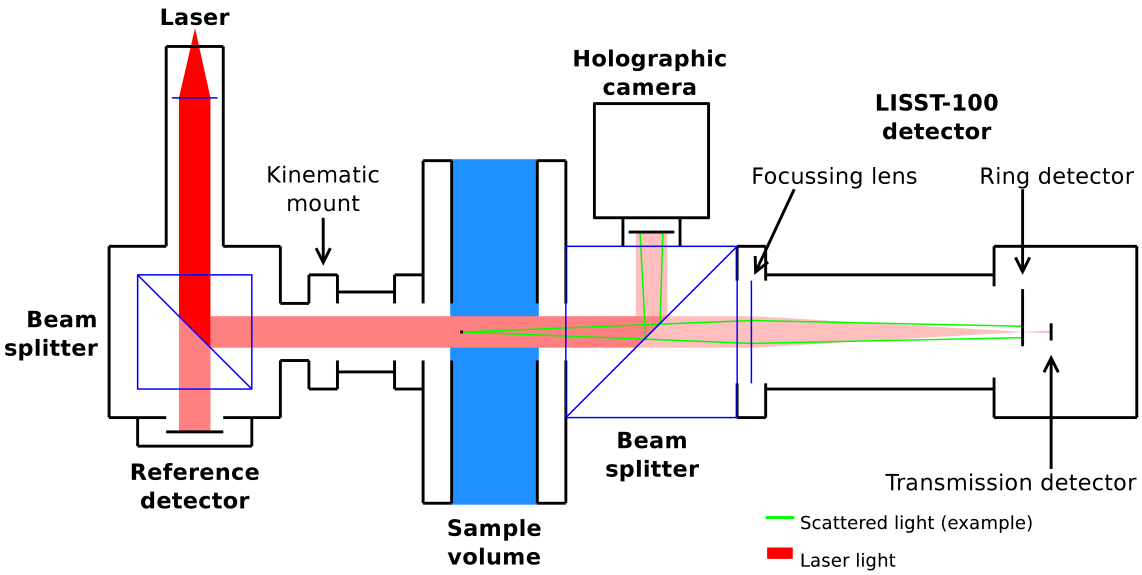

Figure 3.9: Schematic illustration of the combined LISST-100 and holographic camera laboratory system.

column that allows for a collimated laser beam (658 nm wavelength) to be passed through the sample volume, and for measurements to be taken simultaneously by the LISST-100 ring detectors and a holographic camera. This is achieved using a beam splitter positioned on the far side of the settling column, between the two instruments. A schematic illustration and photograph of the system are shown in Figures 3.9 and 3.10 respectively. The collimated laser beam is first passed through a beam splitter to allow for a reference of laser power to be measured. A kinematic mount is positioned between this beam splitter and the sample volume to allow for precise alignment of the laser to the LISST-100 ring detector. Once light has passed through the settling column it is split again with a larger beam splitter. The purpose of this is to enable the holographic camera to record images of the interference pattern, while simultaneously allowing the LISST-100 focusing lens to receive the same light and record the VSF.

The use of a 35 mm beam splitter and a sample volume length of 20 mm, allowed for a gap of 3.9 mm between the 10 degree scattering angle and the outer-most edge of the focusing lens of the LISST-100. This gave reassurance that there was no vignetting, whilst recording LISST-100 scattering measurements, within the angle ranges covered by the type-c instrument. A schematic illustration of the triggering cycle used for the two instruments is shown in Figure 3.11. The LISST-100 measurement is an average of the scattering by particles in the laser beam over a period of approximately 100 ms. In contrast, the holographic camera takes a near-instantaneous snapshot of the particles in the sample. In order to accurately quantify the particles that are recorded during the integration period of the LISST-100, two holograms are recorded - one at the start of the LISST-100 exposure (i.e. when the laser is turned on), and one at the end of the LISST-100 integration period (when

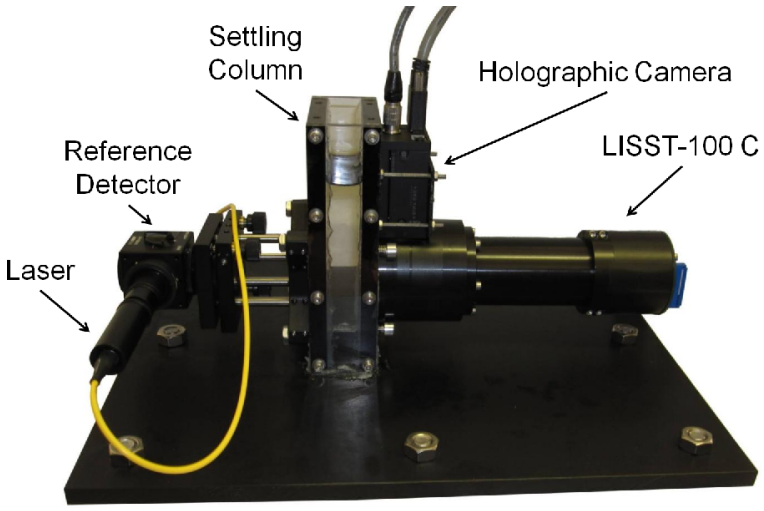

Figure 3.10: Photograph of the combined LISST-100 and holographic camera laboratory system.

the measurement is taken). After this period the laser is turned off until the LISST-100 ring detectors reset to zero. This ensures that each cycle obtains data restricted to the period in which that laser was switched on. The resulting sequence allows for a time series to be recorded, during which samples of particles may be introduced into the settling column and passed through the sample volume. Faster sampling is possible but is limited by the time taken for the LISST-100 rings to reset and the camera speed, which requires a minimum of 67 ms between consecutive holograms. A frame length of 0.2 seconds was used for this work.

3.4 Instrument validation

To validate the accuracy of measurements taken using the combined holographic camera and LISST-100 samples of basalt spheres were used, ranging from 90 to 500 μm in diameter. They were sieved into $\frac{1}{4}\phi$ size ranges to reduce the width of the particle size distribution of each sample that was measured. The first method for validation was a cross-comparison between the adapted LISST-100 (type-c) in the combined system, and a standard LISST-100 (type-c). Secondly, a comparison between scattering predictions, informed through measurements of particle sizes from the holographic camera, were compared with the LISST-100 scattering.

The optical configuration of the system does not interfere with the principles of measuring the angular scattering of light that are adopted by commonly used LISST-100 instruments described in Section 3.1. However, the wavelength of the laser used for the combined holographic camera and LISST-100 system was 658 nm as opposed to 670 nm adopted by a typical LISST-100. Figure 3.12 demonstrates that the 12 nm difference in wavelength between the two instruments was near-indistinguishable in both the scattering predicted by Mie Theory and the associated

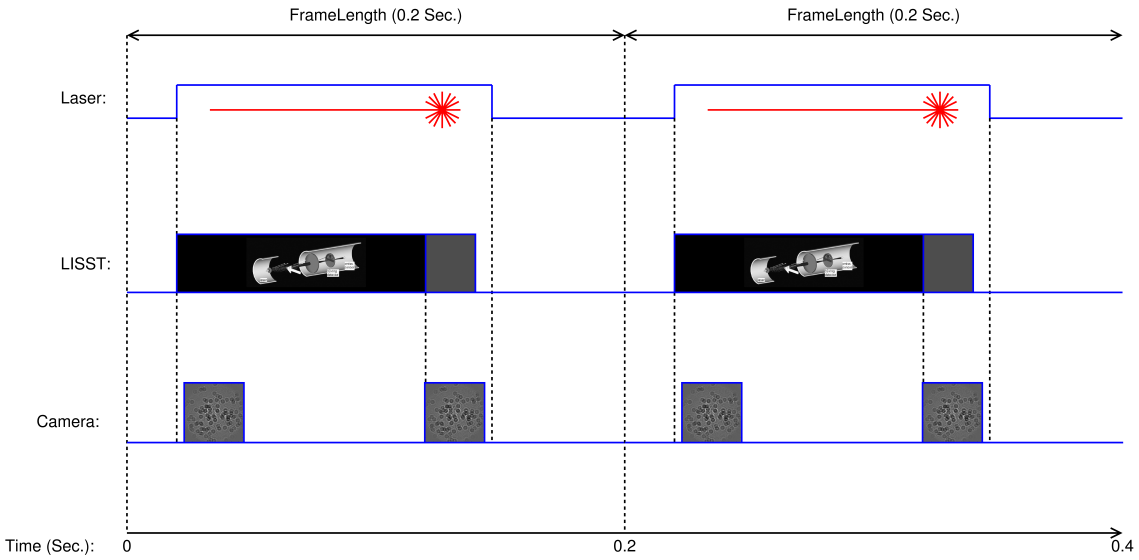

Figure 3.11: Schematic illustration of the triggering sequence of the laser, LISST-100 and holographic camera. Two frames are shown in this example, which includes two LISST scans and four holograms.

inverted volume distribution.

For reassurance that the LISST-100 scattering from the combined system was representative of a standard LISST-100, tests were carried out using the same samples of basalt micro-spheres used in subsequent tests. An example of the agreement between the two LISST instruments is shown in Figure 3.13(a). Some deviations between the two characteristic scattering functions that were recorded are present, and are as expected from slight changes in the width of the particle size distributions between the two sub-samples used. When comparing median sizes (D_{50}) from the holographic camera with the D_{50} from the inverted LISST-100 scattering, a near 1:1 fit is observed (Figure 3.13(b)). It was possible to account for small deviations below the 1:1 line by comparing the observed results with inverted numerical predictions of scattering from Mie Theory, and comparing the size used in the calculation of scattering with the D_{50} from the inverted size distribution (solid line of Figure 3.13(b)). The width of each of the LISST-100 ring detectors and associated size bins resulted in slight oscillations in the predictions of D_{50}, which were amplified in the larger size classes (with larger size ranges). The observations shown in Figure 3.13 illustrate the reliability of the combined laboratory system for reproducing both observations of a VSF and inverted particle sizes that are within close agreement with those of a standard LISST-100.

3.5 Combined system results

The data used for background removal for both the LISST-100 and holographic camera was taken from the region at the start of each time series before particles

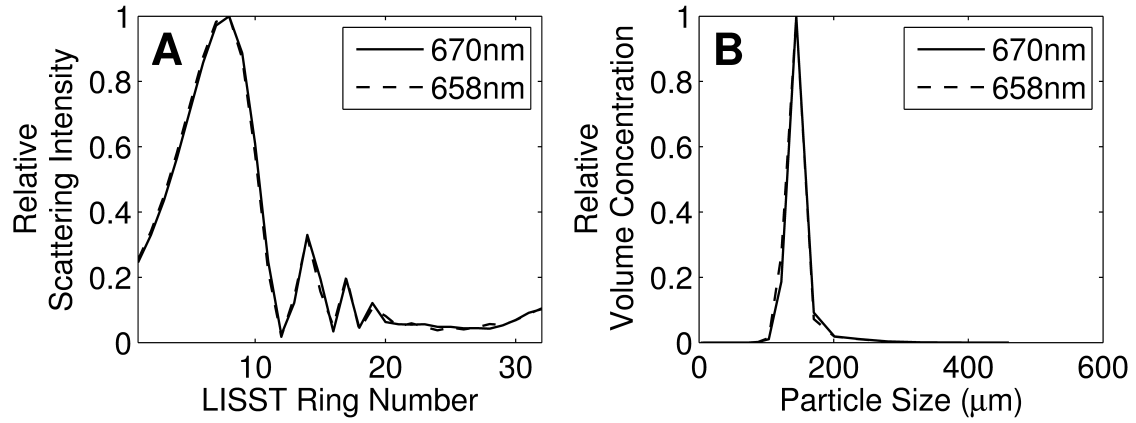

Figure 3.12: A: Mie scattering, integrated over the angle ranges of the LISST-100 (type-c) rings, at 670 nm (solid line) and 658 nm (dashed line). B: Inverted volume distributions from the scattering shown in A. The particle diameter used for these calculations was 137.5 μm.

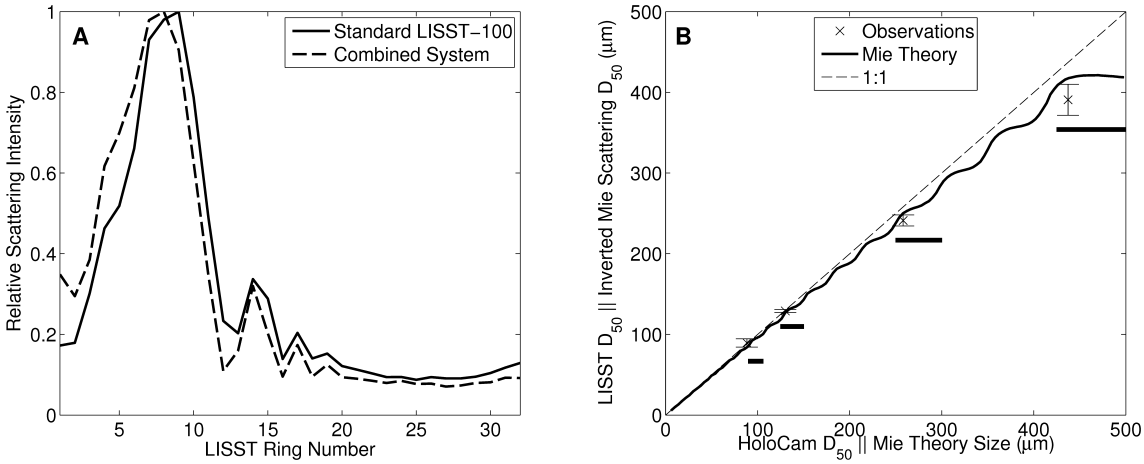

Figure 3.13: A: Comparison of scattering from basalt spheres of $125-150\,\mu m$ from a standard LISST-100 type-c (solid line) measurement and observation from the scattering recorded by the combined system (dashed line). B: Comparisons of calculated D_{50} (median size) values between the holographic camera and inverted LISST-100 scattering from the combined system. Observations are marked by crosses, with error-bars representing ± one standard deviation about the mean. The filled rectangles represent the limits of the sieved ranges for each sample. Numerical predictions from Mie scattering and the associated inverted PSD (calculated every 2 microns) are shown by the solid line.

were introduced into the sample volume. For the LISST-100, the *zscat* was taken from the frame containing the highest transmission value (i.e. the cleanest frame). The background image used for correction of the holograms was taken as the average of frames that were used to find the *zscat* values.

This background image was subtracted from each hologram before processing to reduce background noise, as per Figure 3.7. Data from each time series were filtered to leave only the frames that contained enough particles to produce a clear scattering response on the LISST-100 detectors, and few enough particles to allow for reliable reconstruction of holograms. This allowed for a comparison between the VSF measured by the LISST-100 and the PSD measured by the holographic camera. Multiple scattering is likely to contaminate the LISST scattering measurement with transmissions less than 40 %. All data analyzed here contained transmissions greater than 80 %, and is therefore unlikely to be contaminated with multiple scattering. To predict the scattering intensities recorded by the LISST-100 it was first necessary to calculate scattering from every particle recorded by the holographic camera using Mie Theory and integrating the Mie scattering intensities across the angle ranges covered by each of the 32 ring detectors of the LISST-100. The predicted scattering intensities of each particle were then scaled relative to the average pixel intensities of the background image from the same location in which the particle was recorded. This is illustrated by Figure 3.14, where the intensities of each of the particles in the binary image have been scaled according to the intensity of the background image in the same location. This scaling of scattering intensities accounted for the differences in scattering due to the particle location within the Gaussian beam. For example, particles in the centre of the beam will scatter more intensely than particles towards the edges. This was an important effect to consider due to the near-instantaneous sample time for each hologram: a problem that is removed through averaging during the LISST-100 sampling time. Predicted scattering intensities for each frame are then calculated from the sum of the predicted scattering from each particle, as predicted by Mie Theory. This 'predicted scattering function' can then be compared with the recorded scattering from the LISST-100 from the same point in time.

The progression from Figures 3.15(a) to 3.15(d) shows that as particle size increases, the angle of the principal diffraction lobe (PDL) decreases. The relative scattering intensities recorded by the LISST-100 fit closely to intensities of the predicted scattering function from Mie Theory, informed by the particle size information from the digital holography. Scattering from the basalt spheres also shows well-resolved peaks and troughs at angles larger than the PDL - a pattern that is expected from spherical particles. An examination of an electron micro-graph of the basalt spheres (Figure 3.16) reveals that some of the particles have variations in their surface roughness, suggesting that many of the deviations between predictions

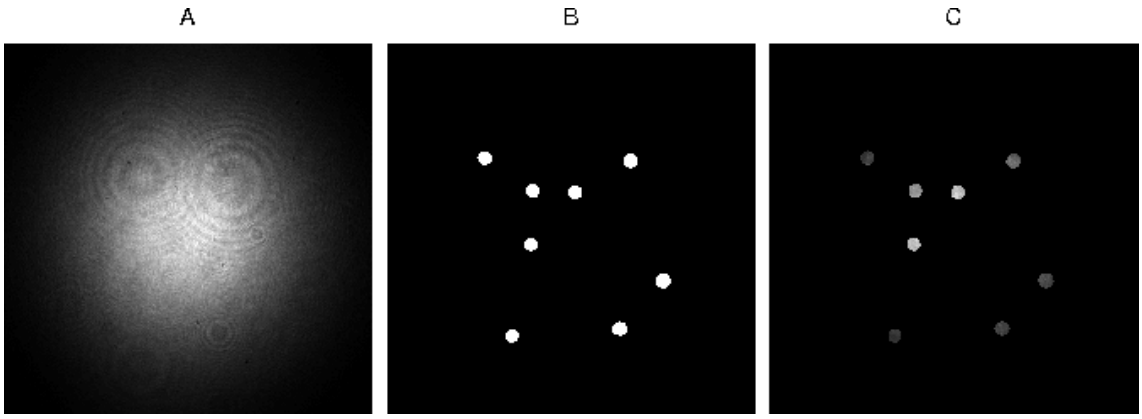

Figure 3.14: A: Background image. B: Binary image of basalt spheres. C: Binary image scaled to the background image to account for the Gaussian beam.

of scattering using Mie Theory and the observed scattering is likely to be due to these slight deviations from perfect spheres. The relative amplitude of the second and third peaks and troughs in the scattering was resolved very well by the predicted scattering function described earlier in this section. A single Mie Theory prediction (integrated over the angles of each of the LISST-100 ring detectors) using only the mean particle size, consistently overestimates the amplitudes of these second and third peaks and troughs in the scattering. This is due to the slight smoothing of the scattering signature caused by the width of the particle size distribution.

The problem of a known particle refractive index is also clear in Figure 3.15. The rising tail at larger angles of the scattering function (ring numbers greater than 22), typical of particles with refractive properties such as sand (evident in Figure 10 of Agrawal and Mikkelsen (2009)), was not resolved with the basalt spheres. This was due to the relatively high refractive index of basalt (1.95 relative to air). Because forward angle scattering is dominated by diffraction, a variable refractive index only affects the shape of the scattering function at larger angles, and therefore the predicted position of the PDL is not affected.

Finally, the LISST-100 scattering data was inverted into a PSD and compared with the PSD obtained from the holographic camera. This allowed for a comparison between sieving, imaging and laser diffraction, as shown in Figure 3.17. The "sharpen" option was used in the Sequoia Scientific Inc. inversion of scattering data because of the narrow ranges in size distributions that were used. The particle volume information from the holographic camera was binned into equivalent size classes to the LISST-100 (type-c) for a reliable comparison. For each of the size ranges, the peak in volume distribution obtained from both holography and the inverted LISST-100 scattering is clearly within the sieved ranges. The shapes of the size distributions matched well from the 90-106 μm (a), 125-150 μm (b) and 180-212 μm (c) samples, although a consistent underestimation of particle volumes from the LISST-100 is observed in the coarse tails of the distributions (i.e. sizes greater than the sieved ranges) when compared to that from the holographic camera. This

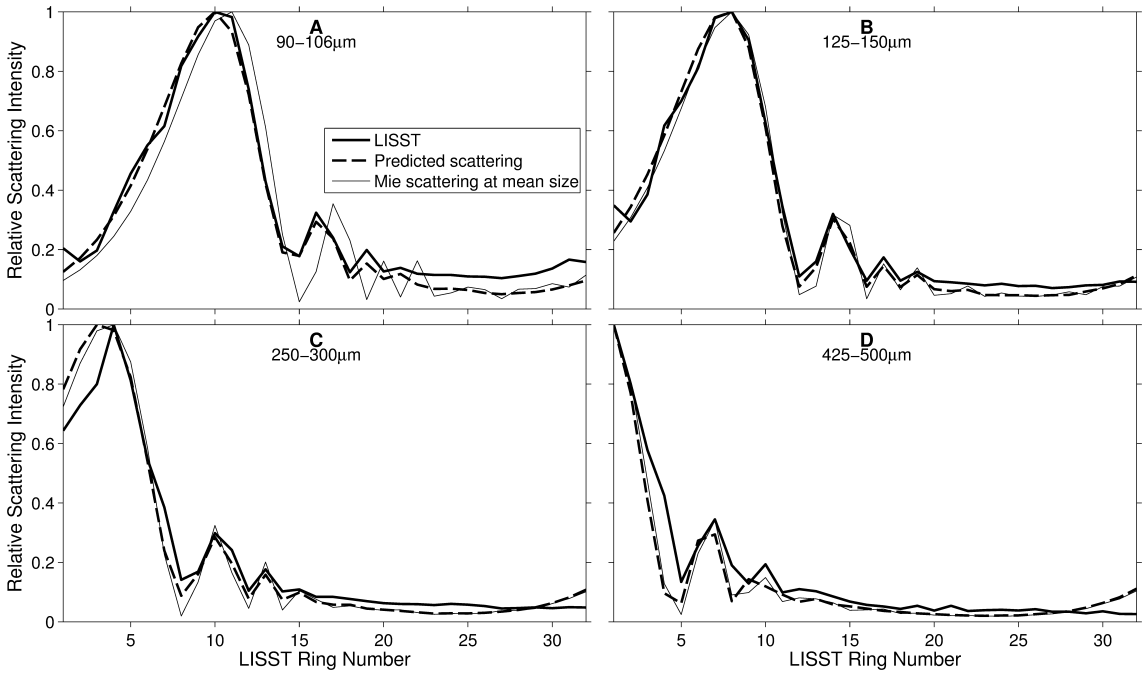

Figure 3.15: Comparison of observed scattering function (thick line) from basalt spheres, predicted scattering function informed by the holographic camera (dashed line), and Mie theory at the mean particle size recorded by the holographic camera (thin line). A: 90-106 μm; B: 125-150 μm; C: 250-300 μm; D: 425-500 μm.

Figure 3.16: An example scanning electron microscope image of a basalt particle used for the data shown in Figure 3.15. Scale bar is 70 μm.

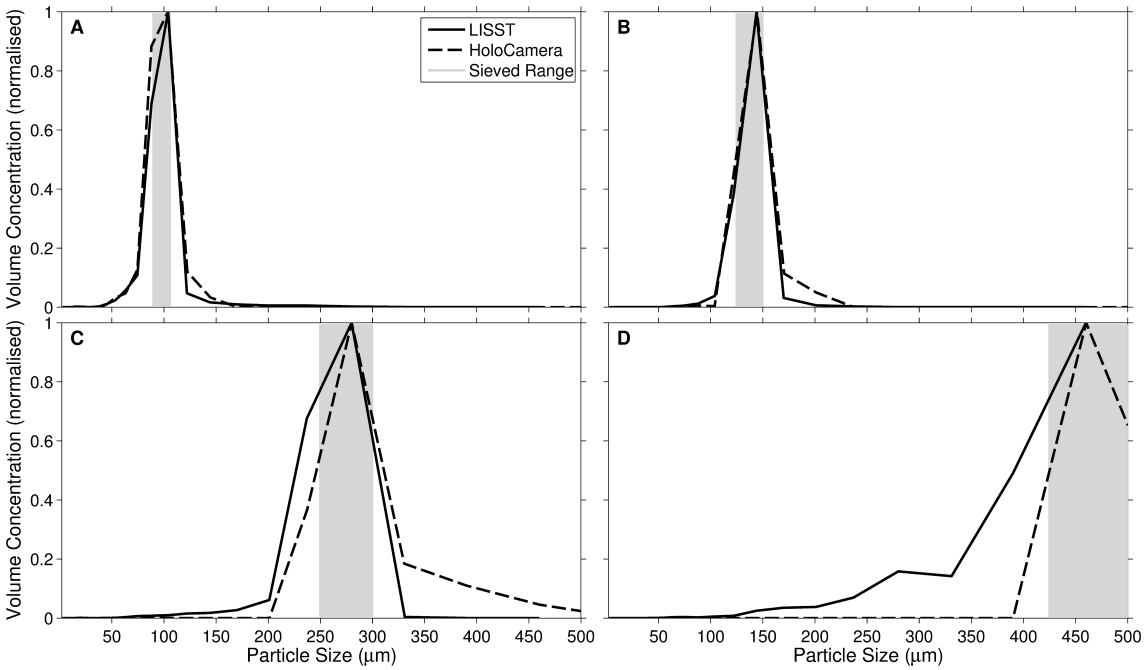

Figure 3.17: Volume distributions of basalt spheres from the inverted LISST-100 scattering data show in Fig. 11 (solid line) and holographic camera (dashed line). The shaded area represents the sieved range of each sample. A: 90-106 m; B: 125-150 m; C: 180-212 m; D: 250-300 m.

is possibly a result of a slight over-sharpening during the inversion of the LISST-100 scattering. While the peak in volume distribution for the sample of 425-500 μm spheres (d) is correctly placed in the correct size bin of both instruments, there is, however, a substantial increase in the number of smaller particles ($< 400\,\mu m$) inverted by the LISST-100.

As the focus of this work is to compare the determination of particle size measurement using a holographic camera and the LISST-100, the distributions in scattering intensities presented are relative to their peak, and are subsequently independent of total particle concentration. With a mono-dispersed sample of varying numbers of particles, the intensity of scattered light recorded by the LISST is proportional to the concentration of particles present. This allows the inversion of scattering from the LISST to give an estimate of particle concentration, in addition to particle size. However, the conversion of the inverted size distribution to a true volume concentration requires calibration of the LISST-inverted distribution using a known concentration of particles. The performance of the inversion for obtaining accurate particle concentrations will be assessed in Chapter 6. In addition, the effect of particles which are larger than the intended measurement range will be assessed in Chapter 4, in an attempt to understand how large aggregated particles may be interpreted by the inversion before assessing the response to natural particles in Chapter 5.

3.6 Summary and conclusions

- The new system, comprising of a combination of digital in-line holography and a LISST-100 type-c, is able to simultaneously record in-focus images of particles and their small-angle forward scattering signature. This is achieved using an additional beam splitter, positioned on the detector-side of the sample volume. The beam splitter allows for both the LISST-100 and holographic camera to simultaneously receive scattering data from particles within the sample.

- The combination of the LISST-100 and holographic camera will allow for an accurate measure of particle geometry to be compared with the forward angle light scattering signature recorded by the LISST-100.

- Comparison between scattering recorded by the combined system and that of a standard LISST-100 shows good agreement. It can therefore be assumed that accurate scattering measurements are possible using the adapted LISST-100 set-up described.

- When results from spherical particles recorded by the system are compared with Mie Theory, a very good agreement is clear between the theoretical predictions of scattering, informed by the holographic camera, and observed scattering from the LISST-100.

- When ranges of particle sizes are present the use of Mie Theory at only the mean particle size is not sufficient to accurately resolve the relative amplitudes of the peaks and troughs in scattering. It is therefore necessary for scattering to be predicted for each particle recorded in the holographic images before an accurate comparison can be made.

Chapter 4

LISST-100 Response To Large Particles

To further the assessment of the instrument size measurements from laser diffraction and holography presented in Chapter 3, the validation of the responses to spherical particles was extended to cover the larger size found in environments where flocs and large planktonic particles are present. The LISST-100 range of instruments determine the distribution of particle sizes *in-situ* using laser diffraction, but are limited to specific size ranges governed by the instrument configuration. As such, the effects of increasing the size of spherical particles beyond the range of the LISST-100 inversion was investigated. This Chapter utilises numerical predictions of scattering and the observational system (described in Chapter 3) to examine the response of the LISST to particles of up to 2000 μm.

Material in this chapter has been expanded from the following publication:

Emlyn J. Davies, W. Alex M. Nimmo-Smith, Yogesh C. Agrawal, and Alejandro J. Souza, (2012), "LISST-100 response to large particles", Marine Geology, 307-310, pp117-122, 10.1016/j.margeo.2012.03.006. (Appendix B)

4.1 Introduction

Restrictions apply to the inversion from a scattering function to an associated PSD. For example, an inversion matrix based on Mie Theory is restricted to spherical particles of a known refractive index and homogeneous composition, and inversions using the random shape kernel, developed by Agrawal et al. (2008), are limited by the size and range of particle shapes considered when producing an inversion matrix. These restrictions have prompted studies into the LISST response to both varying types of particle and varying PSDs. Primarily these studies have concentrated on the

effect of particles smaller than the LISST size limit (e.g. Reynolds et al., 2010), and on the effect of particle shape (e.g. Karp-Boss et al., 2007). However, the LISST is often used for measurements of a PSD in estuarine and coastal waters where large flocs and biological particles are present. These particles have been measured using imaging techniques at sizes ranging up to the order of millimetres in diameter (Eisma, 1986; Milligan, 1996; Graham and Nimmo-Smith, 2010). As the upper size limit of the LISST type-c is $500\,\mu m$, there is potential for these flocs to reach sizes outside the instrument range. Reynolds et al. (2010) reported an increased response in the smallest size bins of the LISST due to particles below the lowest limit of the instrument size range. This was in line with previous thoughts that particles outside the instrument range (either smaller than or larger than) would be contained within the outermost size bins (Agrawal and Pottsmith, 2000). Mikkelsen et al. (2005) reported that particles greater than $500\,\mu m$ resulted in the LISST overestimating the volume of particles in the largest size bin. However, no studies have systematically examined the effect of these large particles on the entire LISST size distribution using both observations and numerical predictions. In an attempt to understand how scattering from these flocculated particles is interpreted by the LISST, the response of the instrument to spheres of diameters from 2-2000 μm has been investigated, to cover the full size-range of sizes reported from *in-situ* imagery.

4.2 Methodology

Both numerical predictions from Mie Theory and observations from a novel system that combines digital holography and the LISST type-c were used. The observational system is described by Davies et al. (2011) and has been fully tested and validated against standard LISST instruments using spherical particles within the type-c size range. It uses a beam splitter on the detector-side of a settling column to allow scattered light from particles to be recorded simultaneously in the form of an angular intensity distribution (LISST type-c), and in the form of a digital hologram, as per Graham and Nimmo-Smith (2010). The holographic images were recorded twice per LISST measurement and manually focussed and binarised to enable high-precision particle size measurements. The background scattering for the LISST and background image for the holographic camera were taken from filtered water at the start of each sample collection run, and samples of particles were introduced to filtered water to allow for a clean background. Each sample was analysed independently, using the mean scattering from the LISST and associated particle statistics from the holographic camera. To remove uncertainties due to non-sphericity, sieved samples of basalt spheres were introduced into the combined LISST and holographic camera system. As in chapter 3, the use of basalt as opposed to other materials such as glass, was chosen to overcome the difficulties in focussing images of perfect spheres

with high transparency when using the holographic camera.

Numerical predictions of scattering functions from particles of single sizes were calculated using Mie Theory, and the result integrated over the angle ranges covered by each ring of the LISST type-c detectors. This gives a prediction of light intensities on each of the LISST ring detectors that matches that of spheres, as demonstrated by Agrawal et al. (2008) and Davies et al. (2011). These predictions of scattering were calculated for particle diameters at the mid-points of each bin of the LISST type-c detector, as well as from 2-1000 μm in steps of 4 μm, and from 1000-2000 μm in steps of 20 μm. For each size, a refractive index of 1.95, 1.55 and 1.45 (relative to air) was used. The use of a high refractive index of 1.95 was to suit that of the basalt spheres used for observations of scattering; 1.55 was chosen to represent mineral grains; and 1.45 as an estimate of samples containing a mix of phytoplankton and mineral grains (Aas, 1996). All predictions of scattering intensities were normalised by the peak intensity at 500 μm. Both predictions and observations of scattering were inverted into a LISST (type-c) derived PSD, using the standard Mie-based inversion provided by Sequoia Scientific Inc. (Agrawal and Pottsmith, 2000). To demonstrate the applicability to the LISST type-b, the predictions of scattering were integrated over the angle ranges covered by each of the type-b detectors using a refractive index of 1.55.

4.3 Results and discussion

4.3.1 Scattering predictions

Results from predictions of scattering from spheres are shown in Figure 4.1(b-d). As particle size increases the total intensity of scattered light increases in accordance with Mie Theory, and the angular position (and hence ring number) of the dominant peak in scattering decreases until reaching the inner-most ring at about 500 μm. For particle sizes greater than this the principal peak moves off the inside of the inner ring detectors. This results in the secondary peak becoming dominant and, due to increasing size, becoming progressively intense. This effect is repeated again at 1400 μm, where the secondary peak moves off the detectors, leaving the scattering from the third peak to become dominant on the rings. The change in refractive index across the three plots shows that the principal peak is largely unaffected by refraction. This is because the primary scattering peaks in the forward direction are dominated by diffraction, and are therefore controlled primarily by particle size. Despite this, there is a clear increase in scattering intensities on the outer rings caused by the lower refractive index of 1.45.

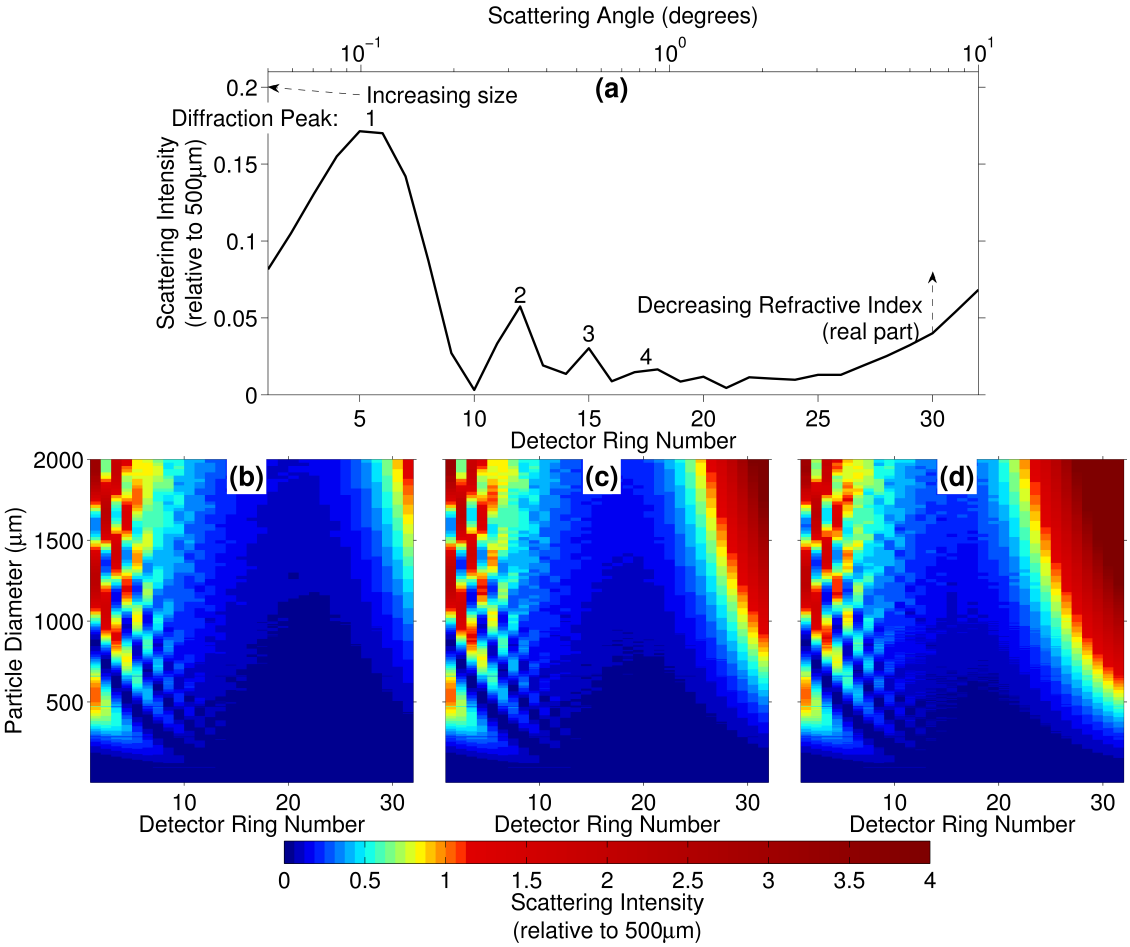

Figure 4.1: Schematic demonstration of Mie scattering from a 200 μm sphere as recorded by the LISST type-c (a). Mie predictions of scattering intensities on each ring of the LISST for diameters of 2-2000 μm, using a refractive index of (b) 1.95, (c) 1.55 and (d) 1.45.

4.3.2 Consequences for particle size measurement

The inversions of predicted scattering functions (Figure 4.1(b-d)), applied across the entire 2-2000 μm range, are shown in Figure 4.2(a-b). Both volume and number distributions are shown to illustrate the different emphasis that each one places on the PSD. The identical number of particles used in the calculation of predicted scattering for each size results in an increase in the volume of larger particles. The volume distributions of Figure 4.2(a) therefore show less emphasis on smaller particles than that of the number distributions (b). Within the LISST type-c size range, a good 1:1 fit is demonstrated between the sizes used in Mie predictions and the associated inverted size distributions. For particles larger than that allowed for in the LISST type-c inversion matrix, the inverted PSD is populated across multiple size classes.

Figure 4.2(c-d) show three examples of the predicted scattering and inverted volume distributions. The scattering from the 300 μm diameter particle was inverted into a wider distribution than that of the 150 μm particle. This is due to the angular range of the ring detectors and their associated size bins, which become increasingly wide for increasing size classes. The positions of the inner-most diffraction peaks have the most influence on the size of the inverted volume distribution. The 300 μm and 800 μm particles are therefore inverted into distributions that peak at similar sizes. The high scattering intensity of the 800 μm particle results in the secondary peak (ring 4) being similar to the intensity of the principal peak from a 500 μm particle. This results in the inverted distribution having a greater total volume concentration than that of the 300 μm particle.

Figure 4.2(e-f) show observed scattering and inverted volume distributions from a 250-300 μm sample of basalt spheres, compared with an 800-1000 μm sample. The prominent second and third peaks and troughs in the scattering function of the 250-300 μm sample are as expected from distributions of spheres with a narrow size distribution. However, in distributions with a wider range of sizes, these peaks and troughs become smoothed, leaving a scattering function that has only one primary peak - a shape which appears similar to the observed scattering from the 800-1000 μm sample. The smoother shape of the recorded scattering from the 800-1000 μm sample is therefore inverted into a broader distribution of particle sizes than the 200-300 μm sample.

The D_{50} (median size) from the inverted LISST distribution was compared with the particle sizes used for the calculation of scattering. This comparison was performed across the 2-2000 μm size range, and compared with the observations of scattering from basalt spheres (Figure 4.2(g)). Observations compliment the numerical prediction of a good 1:1 fit within the size range covered by the instrument. At 425 μm the D_{50} of the LISST plateaus before reducing again as particle size increases. The reduction in inverted D_{50} reaches a trough at 750 μm, where the reported median size from the LISST is 230 μm. This is caused by the primary peak

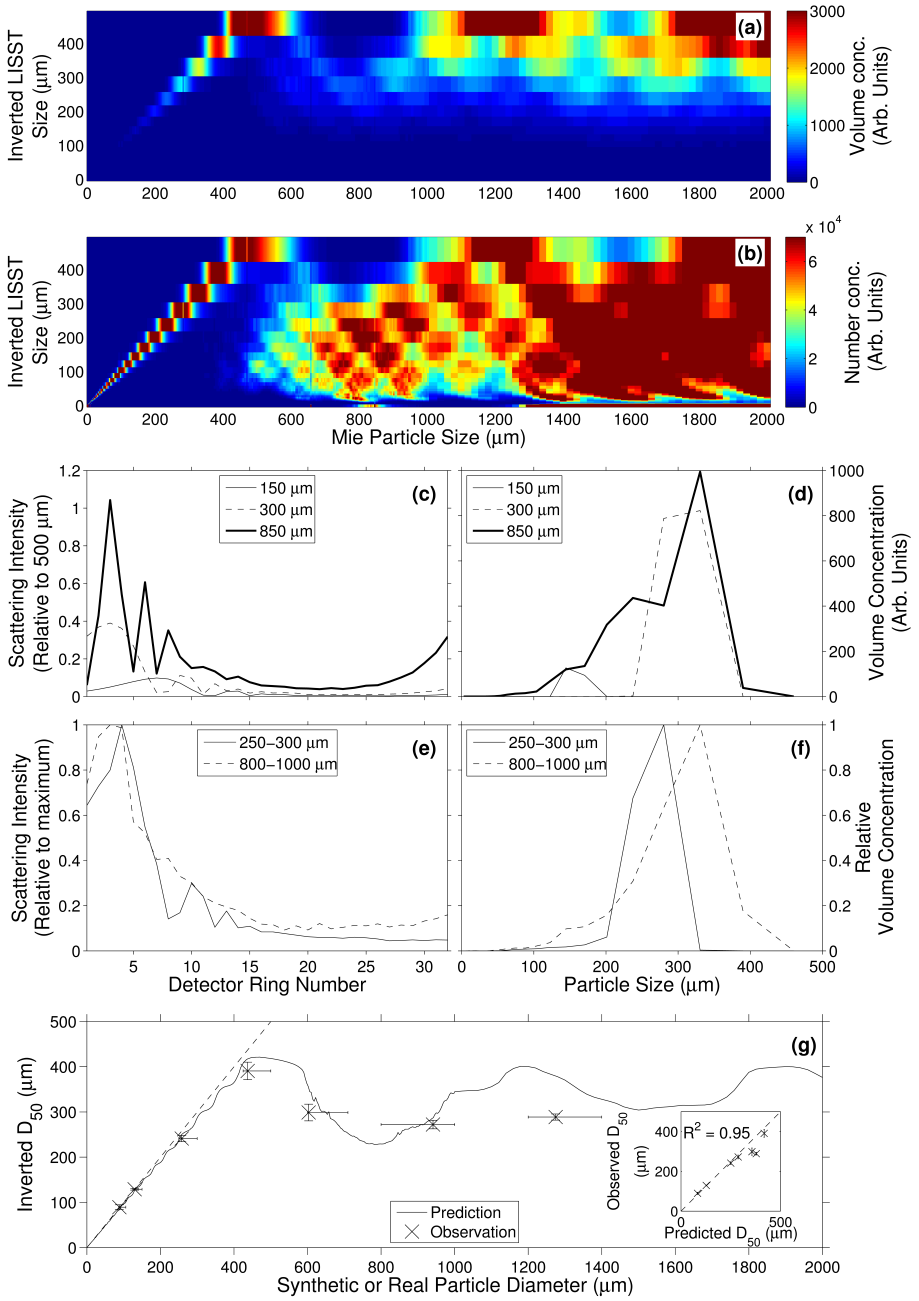

Figure 4.2: Inverted volume and number distributions from the scattering predictions of Figure 4.1(b) are shown in plots a and b respectively. Examples of predicted scattering (c) and inverted size distribution (d) are shown for 150 μm (thin line), 300 μm (dashed line), and 850 μm (thick line) particles. Examples of observed scattering (e) and inverted volume distributions (f) are shown for samples of basalt spheres of 250-300 μm (solid line) and 800-1000 μm (dashed line). A comparison of the D_{50} interpreted by the LISST type-c and the size of the scatterers is shown in g. Crosses mark the observed values from the holographic camera (x-axis) and the D_{50} from the inverted LISST scattering (y-axis). Horizontal error bars illustrate the sieved range of each sample. Vertical error bars are ± 1 standard deviation of the D_{50} measurements from the LISST. The inverted D_{50} values from observations and predictions are compared in the inserted plot.

in the scattering pattern moving off the inside of the inner-most ring of the detector, leaving the second peak in the scattering to be interpreted as the first during the inversion process, as shown in Figure 4.2(a-f).

The observations of scattering from samples above the LISST type-c range match closely with the predictions from Mie Theory, with the exception of the largest size sampled (1200-1400 μm). This deviation from the numerical prediction is likely to be due to the increased sensitivity of the LISST ring detectors to the alignment of the laser with the detectors. Accurate observations of scattering were therefore extremely difficult for particles so far outside the intended range of the instrument, and as a consequence, no observations were made for spheres larger than those contained within the 1200-1400 μm sample. The holographic images, on the other hand, remained largely unaffected by the increase in particle size and an accurate measurement was possible, showing a good match with the sieved ranges for each sample. This highlights the importance of an appropriate measurement technique based on the nature of the particle population under investigation.

The high correlation coefficient ($R^2 = 0.95$) from the predicted and observed D_{50} values over a wide range of particle sizes gives reassurance that the numerical predictions were an accurate representation (insert of Figure 4.2(g)). The second oscillation in D_{50} from the numerical predictions between 1200 and 1900 μm does not return such a large trough when compared to the second reduction in median size between 700 and 900 μm. This is due to the primary diffraction peak being much larger in amplitude than the subsequent peaks and troughs. It would be expected for the oscillations to continue to reduce in amplitude as size increases beyond 2000 μm due to a reduction in amplitude of adjacent peaks and troughs at angles larger than the primary diffraction peaks.

The contamination of the LISST size distribution due to the effects of particles larger than the intended size range is applicable to both the type-c and type-b instruments. This is because both detector configurations and inversion matrices rely on the primary diffraction peak of the scattering function falling within the angle range covered by the detectors. Predictions show that the same misinterpretation of the second and third scattering peaks is apparent on the LISST type-b, only occurring at the 250 μm size limit as opposed to 500 μm.

4.3.3 Refractive index effects

It is shown in Van-De-Hulst (1957) (page 71) that at small angles Mie Theory is dominated by diffraction, while at large angles, there is a transition to geometrical optics, causing refractive effects to become more influential. As particle size increases, this transition from diffraction to geometrical optics occurs at increasingly smaller angles. As a result, the effects of refraction become increasingly important as size increases, because diffraction dominates a reducing angle range over which the

LISST scattering is recorded. The rising tail at angles greater than these primary peaks typically becomes brighter and covers a larger proportion of the LISST angle range as size increases. Figure 4.3(a) shows three examples of predicted scattering from Mie Theory for spheres of identical size but different refractive index. When using a refractive index of 1.55, spheres above 800 μm produce scattering with a rising tail that is brighter than the primary diffraction lobes at smaller angles, and is apparent across a wider range of angles (rings 22-32) than the rising tail from the same size particle with a refractive index of 1.95. Figure 4.3(b) shows that this is interpreted as many small particles by the LISST when the inversion is applied - a problem which would be highlighted if using a number distribution. A sharp increase in apparent volume concentration in the smallest 5 size classes is initiated as soon as particle size exceeds the LISST range. The results from a refractive index of 1.45 show an increase in reported volume concentration in the smallest 5 size classes that is apparent over all sizes above 100 μm. This is of concern if using the LISST in environments where large flocculated particles are present, as their complex composition and low effective density (Graham and Nimmo-Smith, 2010) leads to an unpredictable refractive index. This would cause the rising tail at large angles of the scattering function to play a greater role in the inverted size distribution, resulting in greater uncertainty in the volume and number concentration of small particles returned by the inversion.

4.3.4 Application to particle size distributions

The importance of the spurious results from large spheres reported so far is dependent on the shape of the size distribution in question. For example, a Junge-like power-law distribution (where $n(D) \propto D^m$ when n is the number of particles of diameter D, and $m = -4$ (Morel and Maritorena, 2001)) would result in very few large particles, and a dominance in small sizes, leaving a reduced likelihood of contamination by large scatterers. However, as the exponent m increases towards zero, the chance of contamination by large particles increases. Using the same numerical predictions validated in Figure 4.2(g), tests of different power-law size distributions were conducted to establish the impact of contamination from large scatterers. The use of power-law distributions is to represent a simple size distribution, similar to that which would be expected from a typical *in-situ* LISST-derived PSD. These tests were not able to be performed using *in-situ* samples due to uncertainties in refractive index and particle shape effects on the inversion. For simplicity, these numerical simulations are therefore an illustration of a 'best-case' scenario if all particles match the conditions of Mie Theory.

We start with a constant volume of particles across all sizes, represented by the dashed lines in Figure 4.3(c-d), and demonstrate the apparent volume and number concentrations inverted by the LISST type-c, represented by the solid lines. The

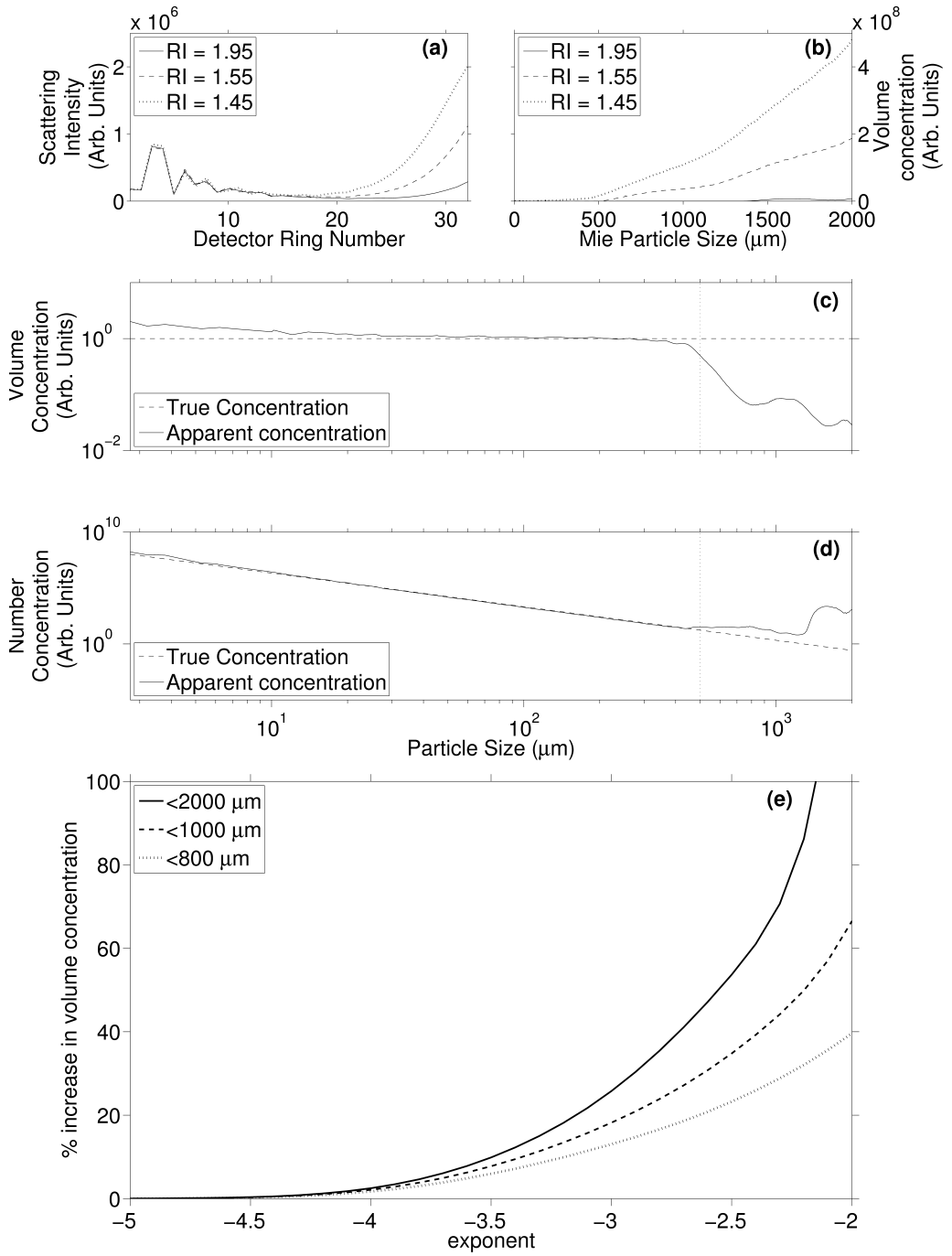

Figure 4.3: (a): Scattering functions from 800 μm spheres with a refractive index of 1.95 (solid line), 1.55 (dashed line) and 1.45 (dotted line). (b): Total volume concentration from the smallest 5 size classes ($< 6\,\mu m$) inverted from Mie scattering of $2-2000\,\mu m$ spheres using a refractive index of 1.95 (solid line), 1.55 (dashed line) and 1.45 (dotted line). (c): LISST volume concentration response (solid line) to particle sizes ranging from 2-2000 μm with equal volume concentration (dotted line) and a refractive index of 1.95. The associated number concentrations are shown in d. Percentage increase in total volume concentration due to particles larger than this LISST size range with varying m exponents of the power-law distribution is shown by e. The solid line shows the percentage increase when the size distribution is extended up to 2000 μm, the dashed line up to 1000 μm, and the dotted line up to 800 μm. The refractive index used for scattering calculations was 1. 55.

response of the LISST to particles within the operating range produces volume and number concentrations that closely match those which would be expected with a constant volume concentration. Above the 500 μm limit of the size range, the apparent volume concentration inverted by the LISST reduces and the number concentration increases relative to the number of particles input. The decrease in total volume of particles above the LISST size range is encouraging because the impact of large particles on the measurement of total volume concentration subsequently appears small. However, the increase in the inverted total number concentration from that of the amount input, demonstrates that the aliasing of large particles results in an increase in the number of small particles with less volume. The loss in total volume concentration outside the LISST size range is therefore due to both the loss of the primary peak in scattering (due to its position off the ring detectors), and also the gain in volume of smaller particles, produced from the inversion of the remaining scattering at larger-angles. The two peaks in volume concentration above 500 μm therefore correspond to the decreases in D_{50} shown in Figure 4.2(g).

The demonstration that particles larger than the LISST size range have the potential to cause substantial contamination across multiple size classes, in addition to the largest size class, is an important issue to consider when interpreting inverted size distributions. The percentage increase in volume concentration across all size bins due to the influence of particles larger than the LISST size range was therefore calculated for m exponents ranging from -5 to -2, typical of the range observed in-situ (Twardowski et al., 2001). This effect is demonstrated in Figure 4.3(e) for size distribution limits of up to 2000 μm, 1000 μm and 800 μm. All three size distribution limits show increasing percentage differences as the m exponent increases towards zero. With the typical Junge distribution, where $m = -4$, the percentage increase in total volume concentration was 3.1% and 4.5% for distributions limited to 800 μm and 2000 μm respectively. The increases in concentrations are substantially greater for PSDs with slopes greater than -4. For example, a slope of -3 resulted in an increase in volume concentration of 26% for particles of up to 2000 μm. This is of concern as the contamination across the wide range of LISST size classes would result in a subsequent change in gradient of the LISST-derived PSD, as well as an increase in concentration. It is interesting when comparing the LISST-derived PSDs with PSDs obtained from imaging, that there is an offset at larger sizes (Mikkelsen et al., 2005), which corresponds well to that which would be expected from the percentage increases from contamination due to large particles shown by Figure 4.3(e). The LISST-derived PSDs should therefore be treated with caution when the concentration of particles greater than the operating range of the instrument is unknown.

4.4 Conclusions

- The LISST-100 performs the inversion of a volume scattering function into a particle size distribution very well for spherical particles within the size range allowed for by the inversion matrix. For spheres greater than the instrument range of 500 μm (for the type-c instrument), the inversion produces particle volume distributions that peak at varying sizes between 250-400 μm. This is due to the principal peak in the scattering function, moving off the inside of the LISST ring detector, resulting in the remaining peaks and troughs being interpreted as the principal peak. This effect would also be apparent in the type-b configuration of the LISST-100, only occurring at the 250 μm size limit instead of the 500 μm limit of the type-c instrument.

- Refractive index becomes increasingly important as particle size increases due to its dominance in the scattering function at angles larger than the principal diffraction peak. The consequences of refraction from particles greater than 600 μm can result in sharp increases in inverted volume concentrations within the smaller size bins. This sharp increase in apparent small particles may appear to be emphasised when displaying a number concentration as opposed to a volume concentration.

- The likelihood of contamination due to large particles in *in-situ* measurements is dependant on their concentration. When extending a power-law particle size distribution with a slope of -4 up to varying particle sizes, numerical tests predicted an increase in volume concentration across multiple size classes. For gradients in the particle size distribution greater than this (i.e. more larger particles), the total volume concentration becomes increasing contaminated through aliasing of large particles.

- Care must be taken when interpreting particle size distributions from the LISST-100 when there is potential for particles outside of its range limit, and users should be aware of the emphasis that volume and number concentrations place on the PSD. In situations where large particle may be present, imaging techniques may be a preferred method for the determination of a PSD.

Chapter 5

Natural Particles

This chapter further utilises the laboratory system, presented in Chapter 3, to explore the relationship between size measurements from the LISST-100 and holographic camera when subjected to complex flocculated particles, extracted from the Menai Strait, Wales, during the summer of 2011. This is intended as a representation of the the response of the two instruments to particles typically found within the natural marine environment. The analysis of the response of the two sizing techniques to these particles of complex shapes with varying sizes and concentrations, allows for an assessment of the implications of scattering characteristics from these particles to their size measurement inferred from laser diffraction.

5.1 Sampling procedure

Near-shore surface water samples were taken from the Menai strait (Anglesey, Wales, UK), containing a variety of muddy flocs and organic particles. Confirmation of correct alignment of the LISST-100 was performed using Milli-Q water, but the background scattering data used for the correction of scattering data was taken from the filtered ($0.7\,\mu m$ GF/F filter) seawater sample immediately before each sample run. Samples of particles were introduced into the settling column of the combined LISST-100 and holographic camera system using a wide-bore pipette to reduce floc breakup. The filtrate ($0.7\,\mu m$ GF/F filter) of the seawater sample was used as the initial background water in the settling column, into which the particles were introduced. This was to reduce effects of Schlieren (Mikkelesen et al., 2008) when introducing samples of particles into the settling column of the bench system by using background water of similar temperature and salinity, in addition to the removal of scattering from very small particles (less than $\sim 0.7\,\mu m$). Despite the use of filtrate for background water, Schlieren remained a problematic issue in many samples due to slight stratification of the water sample during the time of measurement. Frames in which Schlieren was present were identified manually using the raw holographic images. The contaminated images and associated LISST-100 scans were removed

from the analysis.

After the LISST-100 scattering data were corrected the PSDs were derived through both the spherical and random-shaped matrices (Agrawal et al., 2008), with the 'sharpen' option to increase the number of possible inversion iterations for narrow size distributions. Automatic processing was used to reconstruct the holograms and produce statistics of particle geometry. Particle statistics from the holographic camera and inverted sizes from the LISST were compared using only the data from the size classes in which both instruments overlap. Information from the holographic camera was also used to inform Mie-based predictions of scattering on the LISST ring detectors, as demonstrated by Davies et al. (2011).

For each sequence of particles settling through the sample volume, frames from the holographic camera, and their associated LISST-100 scans, were grouped into clusters that contained images in which the same particle was present throughout (i.e. from the point at which a particle enters the top of the sample volume, to the point where it leaves). Data from each cluster of scans was then averaged to produce results from the LISST and holographic camera that were representative of the particles present in each cluster. These measurements are therefore as close as possible to those that represent the simultaneous responses of the two instruments from single particle populations. For each cluster of particles, the median size from the holographic camera and LISST was calculated from their inferred volume distributions. As imaging returns many length scales that represent different aspects of particle geometry, the size distribution may be a representation of the distribution of one of these scales. For example, the distribution in minor axis lengths or equivalent circular diameters.

In addition to the removal of Schlieren-contaminated data, a series of quality control measures were applied to the data before averaging into each cluster of scans (Figure 5.1 (a)). The first step was to remove all scans in which the holographic camera recorded one or more particles with an equivalent diameter greater than the size range allowed for by the LISST inversion matrix. This was to reduce the likelihood of aliasing larger particles when inverting LISST scattering (Chapter 4). The upper size limit was taken as $500\,\mu m$ for the spherical inversion and $390\,\mu m$ for the random-shape inversion. In addition to the removal of large particles, scans associated with transmission readings greater than 98% were also removed due to the poor signal-noise ratio expected. Scans which included transmission readings of less than 40% were also removed to reduce errors due to multiple scattering. The comparison between the two measurements of D_{50} for each cluster of scans, following the removal of large particles and low transmission scans, is shown Figure 5.1 (b). An analysis and examination of the results, following this quality control, are presented in the remainder of this Chapter.

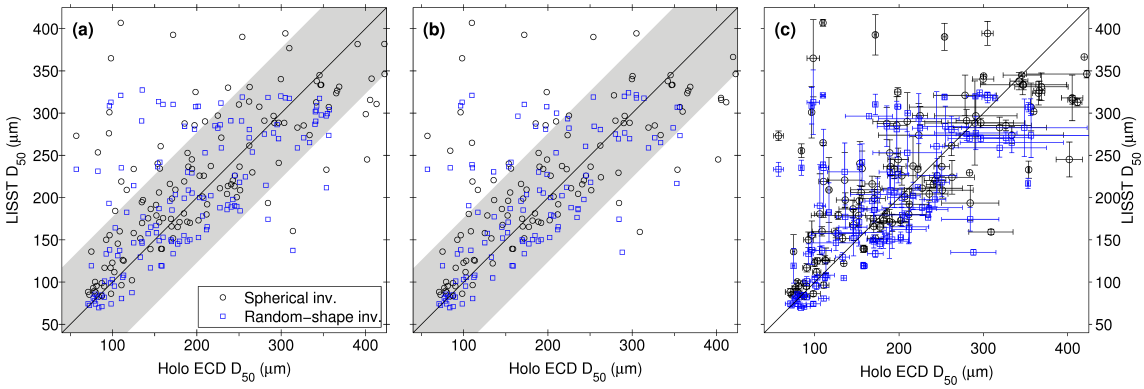

Figure 5.1: D_{50} from the LISST and holographic camera ECD before and after quality control measures were applied - a: $40\% < \tau < 100\%$; b: Removal of particles with ECDs larger than the upper LISST size, $40\% < \tau < 98\%$. The shaded area is $\pm 75\,\mu m$ either side of the 1:1 fit. These quality control measures reduce the total number of points from 134 (a) to 118 for the spherical inversion 110 for the random-shape inversion (b). Plot c is a duplicate of b, with errorbars indicating $\pm$ one standard error of the mean D_{50} for each cluster of scans.

5.2 Results and discussion

Examples of results from three clusters of scans using averaged scattering and size distribution data from the holographic camera and the LISST are shown by each column of Figure 5.2. The top row (a-c) shows scattering (normalised to its peak value) from the LISST observations (solid line) and the Mie predictions, informed by the equivalent circular diameter from the holographic camera (dashed line). Normalised volume concentrations are shown in plots (d-e), with the solid line representing the spherical inversion of LISST scattering, and the dotted line from the random-shape inversion. Again the dashed lines are from the equivalent circular diameters of the holographic camera measurements. The images in the bottom row (g-i) are one representative frame selected from within the cluster. The averaged volume concentrations inverted by the LISST have been normalized to enable comparison of the size measurements only. The conversion of LISST data to a true concentration makes use of a fixed volume calibration constant (VCC), which results in any mismatch between the concentration measurements of the camera and LISST. This mismatch is therefore constant across all size ranges in relation to the scattering intensities recorded by the LISST.

Good agreement between the positions of the principal peaks in the predicted scattering and observed scattering functions is apparent in Figure 5.2(a-c). However, all three examples of scattering show sharp oscillations in intensities on alternate rings of the LISST detectors. This is representative of azimuthal asymmetry in scattering, indicative of preferred orientations of particles during settling (Agrawal et al., 2008). The azimuthal variations in scattering intensities are emphasized when multiple LISST scans record a single collection of non-spherical particles in

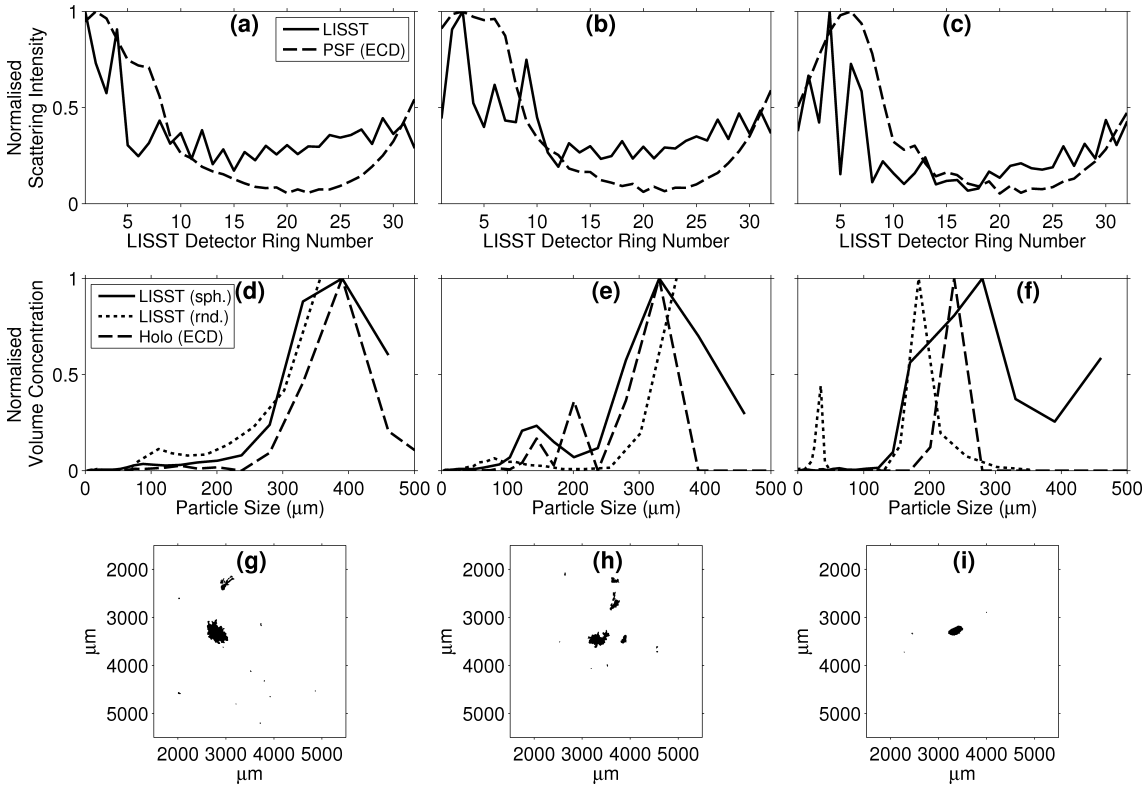

Figure 5.2: Examples of results from three clusters of scans (columns from left to right) selected from within the grey shaded region of Figure 5.1b, showing: (a-c) observed scattering (solid line) and Mie predictions of scattering informed by the camera (dashed line); (d-f) normalised volume distributions from the spherical inversion (solid line) and random shaped inversion (dotted line) of LISST scattering, and ECD from the holographic camera (dashed line); (g-i) an example binarised frame from the holographic camera from the associated cluster of scans.

a constant orientation. Despite this, the LISST inversion appears to reproduce size distributions that are remarkably close to that obtained from the holographic camera. This is likely to be due to the de-noising and smoothing performed by the LISST inversion which reduces the impact of small oscillations in scattering, and hence the magnitude of oscillations from azimuthal asymmetry in scattering at larger angles. The predicted scattering functions (PSF), informed from the holographic camera ECD distribution, were calculated using Mie Theory and are subsequently smooth in shape. With the principal diffraction lobe remaining close (± 2 detector rings) to the predictions informed by the holographic camera, and the smoothing within the inversion allowing the principal diffraction peak to play a dominant role in size distribution returned, the error in D_{50} often translates proportionally to the offset on the rings (i.e. ± 2 size classes).

Azimuthally asymmetrical scattering is likely to become smoothed when multiple non-spherical particles of varying orientations are passed through the sample volume. This will produce scattering functions without the multiple peaks and troughs associated with scattering from a sphere, as explained by Agrawal et al. (2008). This smoothed scattering function is therefore likely to be more representative of *in-situ* scattering, where particles are more randomly oriented.

5.2.1 Multiple Scattering

Multiple scattering is a potential problem for the LISST, especially in environments of high particle concentration. As a result, data containing transmissions of less than 40 % were discarded and should have reduced this problem. However, as with all the LISST measurements, transmission readings are an average for the entire incident beam during the integration time of photo-detectors ($\sim 80\,ms$). This means that multiple scattering could be problematic if, for example, a relatively low concentration of particles were to cluster around a small area within the sample volume and would not be removed through filtering of the transmission. This scenario is unlikely in a well mixed *in-situ* environment, as a homogeneous distribution of particles within the sample volume is often the norm. However, care should be taken in situations where this is not the case, such as when using a settling column.

In situations where multiple scattering is likely, the chance of particles overlapping in the images is also likely due to the reduced separation between particles. This is of concern as the consequences of these problems have the opposite effect on the two instruments. The multiple scattering recorded by the LISST is likely to increase the intensity of light at larger angles on the ring detectors, causing an increase in the number of small particles returned by the inversion process, resulting in a decrease in D_{50}. On the other hand, overlapping particles recorded by the holographic camera are likely to be interpreted as a larger particle during binarisation, leading to an increase in the D_{50}. This may therefore be a plausible explanation for

the camera reporting larger particles than the LISST when their ECD is greater than 250 μm (Figure 5.1)(b), as larger particles are more likely to overlap and increase the intensity of multiple scattering.

In an attempt to reduce these effects, the experiment runs were aimed at recording particles populations with low enough concentrations to try to avoid contamination from multiple scattering or overlapping particles. In addition, measurements of lower concentrations of particles in the settling column allowed for particles to separate more quickly due to variability in settling velocity, allowing for a more accurate analysis of varying sizes of complex particles.

5.2.2 Particle size

To represent the agreement between size estimates of the two instruments, the difference between the D_{50} measurements from the holographic camera and the LISST for each cluster of particles was counted into 25 μm intervals from $-500\,\mu m$ to 500 μm. Histograms of the differences between the D_{50} from the holographic camera and the LISST are shown in Figure 5.3. The sizes used in the holographic camera distributions were minor axis length (a), equivalent circular diameter (b) and major axis length (c). Both the standard Mie-based (spherical) inversion and the random shape inversion (Agrawal et al., 2008) were used for the inversion of LISST scattering. The effect of large particles (Chapter 4) results in the need for removal of more scans from the analysis when the random-shape inversion is used, due to the reduced maximum size (390 μm) allowed for in the inversion. The best agreement (mean difference closest to zero) between the two instruments is when the ECD distribution from the holographic camera is compared to the random-shape inversion from the LISST. There is, however, a spread either side of the best agreement in all three holographic camera dimensions shown, but 64% of the particles analysed fall within D_{50} differences of $\pm 75\,\mu m$ and 50% within $\pm 50\,\mu m$ when the ECD is used.

The use of median size (D_{50}) is a potentially misleading metric in quantifying the error between the two size measurements. For example, a large D_{50} difference could result from differences in the particle size measurements that are not close to the median size (i.e. extreme sizes). Despite this, the D_{50} difference was chosen because it is widely used for classifying particle size distributions and is often used as a proxy for settling velocity in models of sediment transport. This makes this descriptor more accessible and can be used as a comparison to other studies, as opposed to using other statistical comparisons (e.g. t-test) which produce non-dimensional descriptors that are not comparable to particle size.

Figure 5.4 shows the relationship between the size recorded by the holographic camera and the D_{50} differences between the holographic camera and the LISST. Relationships between minor-axis, ECD and major-axis are compared to both the spherical inversion and random-shape inversion of LISST scattering. In all of the

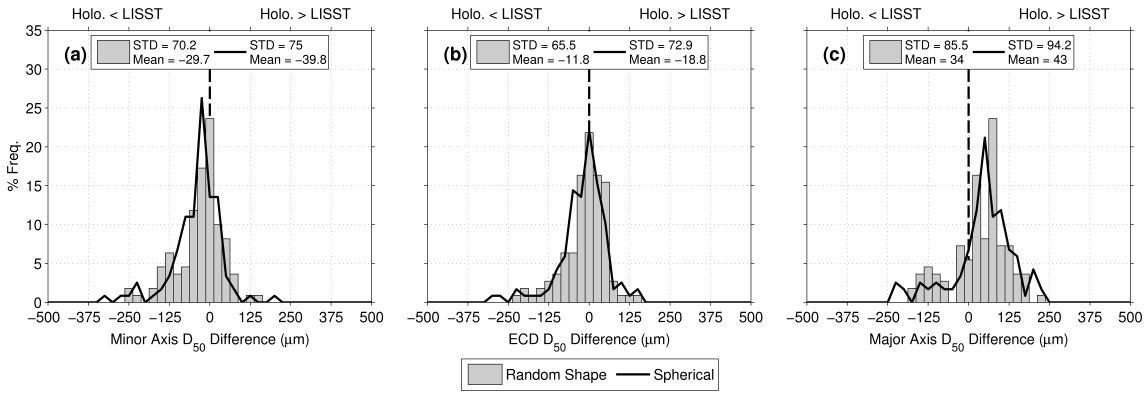

Figure 5.3: D_{50} Difference between the holographic camera and LISST. Negative D_{50} differences indicate smaller median sizes in the holographic camera than the LISST, and positive D_{50} differences indicate larger median sizes in the holographic camera than the LISST. Data clusters which contained particles greater than 500 μm (from the holographic camera) were discarded. D_{50}s were calculated using holographic camera distributions of: minor axis lengths (a), equivalent circular diameter (b) and major axis lengths (c).

size cases, when the holographic camera reports median dimensions that are smaller than approximately 250 μm, the LISST reports sizes greater than the camera. It is these small particles that form the left-hand negative tail in the histograms shown in Figure 5.3. In contrast, the right-hand positive tails in Figure 5.3 are primarily made up of larger particles, as shown in Figure 5.4, where the holographic camera D_{50} values are greater than approximately 250 μm, and the LISST measurements are reported to be smaller than the camera. The reason for the relatively large discrepancy between holographic camera and LISST at small sizes it likely to be due to the weak scattering signal produced from smaller particles, resulting in an increase in the relative amount of noise recorded on the LISST ring detectors. This is likely to flatten the shape of the scattering function on the detector rings, causing a relative increase in the number of smaller particles returned by the inversion and leading to a subsequent reduction in the reported D_{50}.

Unfortunately, due to the nature of the analysis of settling particles through a relatively narrow incident beam, increased settling velocities of large particles result in an increased error due to a smaller numbers of scans in which the particle is present within the beam. The results which show particles that appear large in the camera and smaller in the LISST could be attributed to aliasing of large particles in the inversion process. This is not the case here because particles with equivalent circular diameters larger than 500 μm (reported by the holographic camera) have been removed from the analysis. A report of large particles in the camera measurement may also be misleading in situations where particles appear overlapped in the x-y plane, but which are separated in the z plane. During the binerisation process, particles which overlap in this way will be returned as a single particle with an area equal to their apparent projected area. The LISST, on the other hand, should not

be contaminated by this effect, provided that the separation in the z plane is large enough to avoid multiple scattering. This is because the focussing lens of LISST, and its alignment with the ring detectors, produces measurements of angular scattering distribution which are independent of particle position within the incident beam. Hence, the scattering from two identical particles in separate locations within the LISST sample volume will produce the same result. A further complication, which is hard to quantify is from long, elongated particles which may have a relatively small ECD but a major axis length which exceeds that of the LISST inversion limit. In these situations the orientation of the particle in relation to the orientation of the LISST ring detectors becomes important, as the impact of the longest scale on the scattering recorded is dependant on whether the scattering from this scale propagates onto the area azimuthal cross-section covered by the ring detectors. Effects of particle shape are explored further in Section 5.2.4.

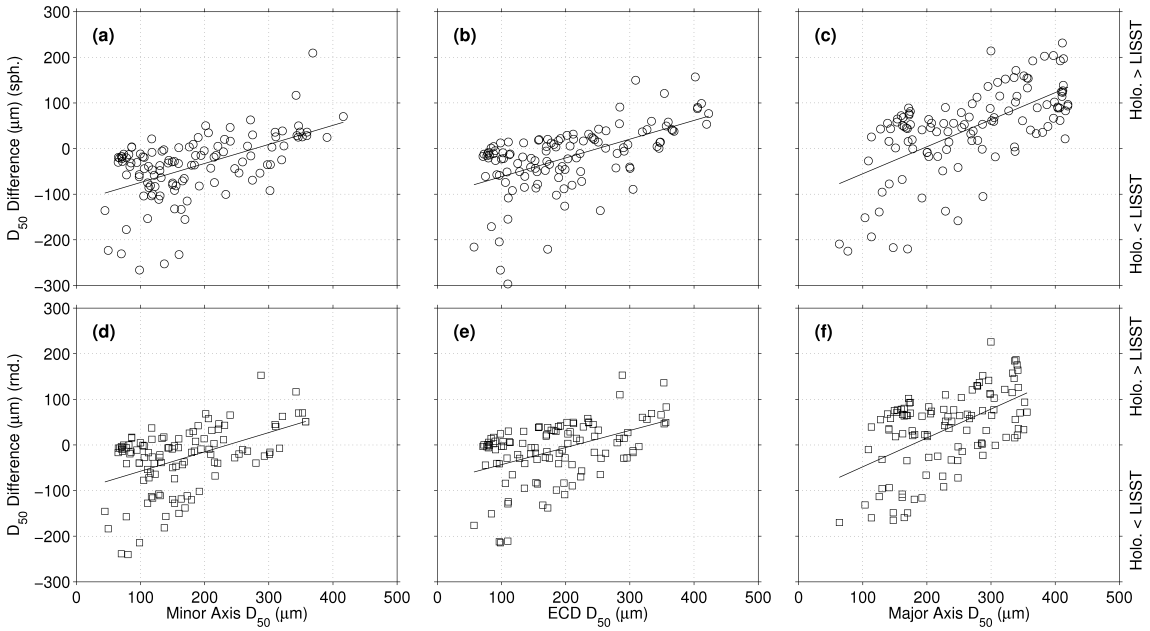

Figure 5.4: Comparison of the D_{50} differences between the holographic camera and LISST, the top row showing the spherical inversion and a: Minor Axis, b: ECD, and c: Major Axis; and the bottom row showing the random-shape inversion and d: Minor Axis, e: ECD, and f: Major Axis. Best-fit lines are shown by the thin black lines.

5.2.3 Segmentation

Segmentation is the artificial break-up of particles during the binarisation stages of the holographic data processing. Particles which appear small in the holographic camera and large in the LISST may have been distorted through segmentation, causing a decrease in the number of large particles and an increase in small particles from the broken segments of a particle (Figure 5.5). The likelihood of segmentation is greater in the combined lab system than in a standard holographic camera due

to the relatively dark edges of the Gaussian beam as particles enter and exit the sample volume.

Segmentation usually occurs when a large particle has a low signal response in the focussed reconstructed slice. This means that the area covered by a particle becomes harder to isolate from the background noise in the image, making binerisation thresholds difficult to determine. With a threshold that is too low, the binary particle will become dilated and an overestimate of area will result. A threshold too high results in gaps appearing in the particle, and for segments of the particle to break up, leading to an underestimate of particle area and an increase in the apparent number of smaller particles from the detached segments. In the combined holographic camera and LISST-100 system used here, segmentation occurs at the edges of the beam, where the intensity of incident light is lower. An example of this is shown in Figure 5.5(a-b), where the large particle in image (a) is broken up in the following frame (b) as it moves out of the middle of the Gaussian beam. The effect of segmentation on the resulting volume distribution is illustrated in (c), with the solid line representing the equivalent circular diameter from frame (a), the dashed line representing the distribution obtained from frame (c). The size distribution from frame (a), where there is no segmentation, shows a strong peak in volume concentration in the 331 μm size class and a low concentration of small particles (20-100 μm). The distribution from frame (b), where the largest particle has become segmented, shows a reduction in particle size of the large particle (right hand peak) and a reduction in the volume concentration of this peak by 15 $\mu L.L^{-1}$. In addition, this segmented distribution shows an increase in the volume concentration of smaller particles between 20-100 μm, which is the result of the smaller segments that have broken off the large particle. These changes in volume distributions do not conserve the total volume concentration in comparison to the non-segmented equivalent because some area of particle is lost through the introduction of gaps and holes in the segmented particles. In short, PSDs containing segmented particles will show overestimates of small particles and underestimates of total volume concentration.

5.2.4 Particle shape

It is demonstrated in Agrawal et al. (2008), that particle shape has a significant effect on LISST scattering measurements when simple, non-spherical particles are present. It is therefore necessary to try to account for the effects of particle geometry on the LISST measurements of naturally-occurring sedimentary and biological particles, and flocculated particles containing agglomerates of both types. A montage of reconstructed particle images from the settling column is shown in Figure 5.6. This figure is built up of randomly selected particles, which were interpreted by the reconstruction procedure as having equivalent circular diameters less than 500 μm.

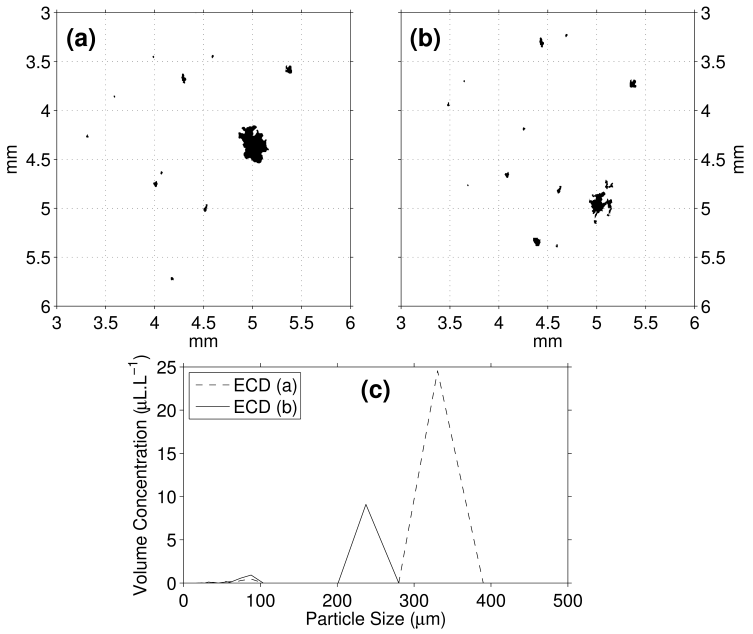

Figure 5.5: Example region of binary image showing a large, intact particle (a). The following frame is shown in (b), where the large particle has settled into an area of lower incident light intensity. The ECD distributions from the two frames is shown in (c), with the solid line representing the distribution from frame (a) and the dashed line representing the distribution from frame (b).

It demonstrates the wide variation in particle shapes that are apparent in natural suspensions, and includes small, rounded grains, large flocculated aggregates and some plankton (e.g. the long diatom chain towards the top right of the montage). Each of these particles will produce unique scattering patterns on the LISST ring detectors.

Figure 5.7 shows four examples of reconstructed and binarised particle images, overlain onto the raw hologram (corrected by subtraction from a background image). This demonstrates the variability in the holographic interference patterns associated with each particle. Simple geometrical shapes that are close to circular projected areas, such as particles 1, 2 and 4 in Figure 5.7, have smooth interference patterns that are mostly symmetrical through 360° in the azimuthal plane. More elongated particles that remain relatively simple in their complexity and perimeter roughness, have interference fringes that become less azimuthally symmetrical but maintain a smooth pattern, such as particle 3 and particle 6 (diatom). In contrast, particles 5 and 7 have much more complicated geometrical projections, resulting in the interference patterns that surround these particles being highly variable in their shape, symmetry and intensity. Both particles are surrounded by many points of constructive interference (shown by white spots in the raw image), where the intensity of the interference pattern is high. These bright spots in scattering would be recorded as flashes of light at varying angles on the LISST ring detectors. It is therefore conceivable that for randomly orientated particles, the variability in the

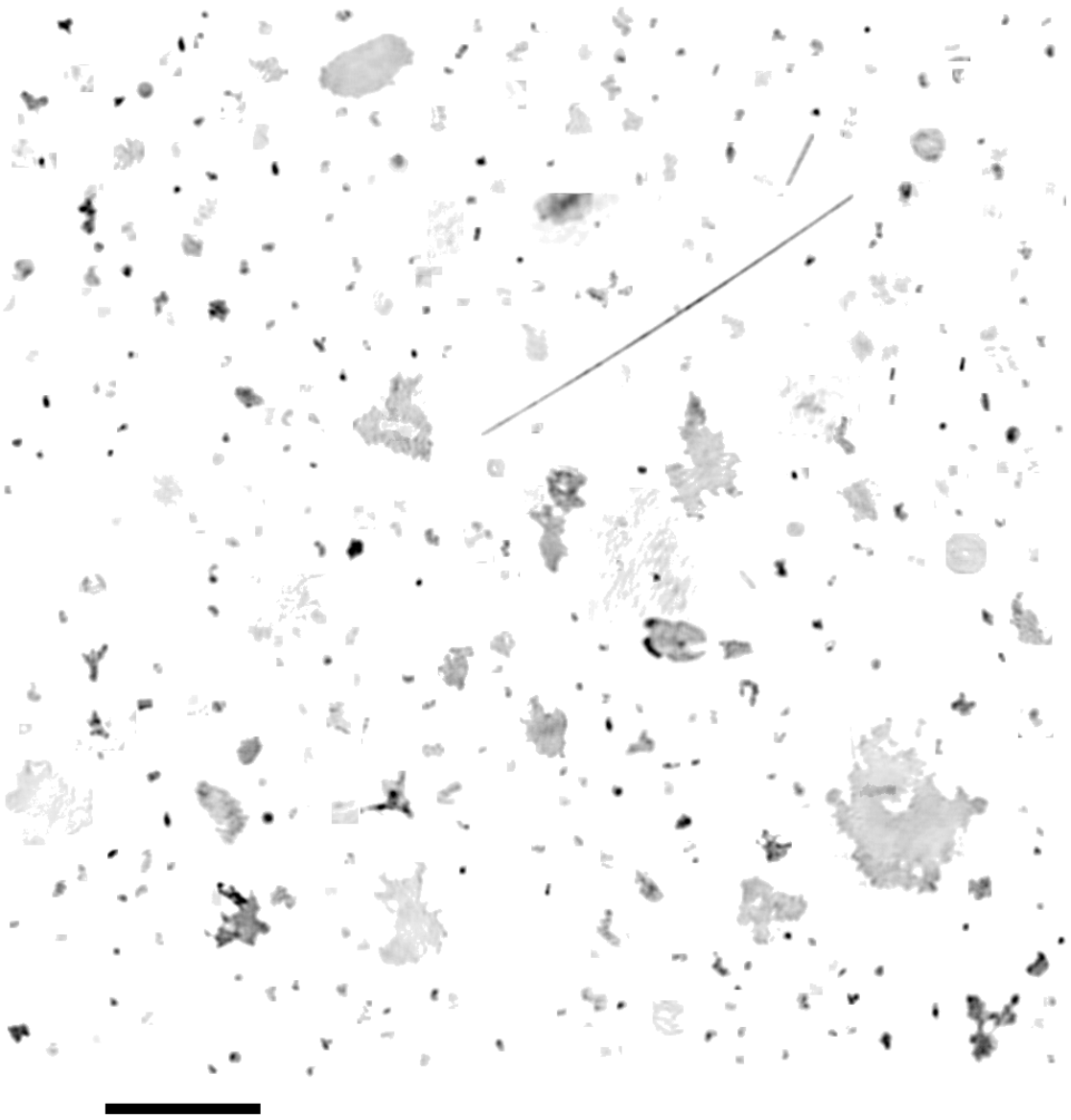

Figure 5.6: Montage of randomly selected particle images obtained from the reconstructed holograms during the sample runs. The scale-bar is $500\,\mu m$. All particles shown have ECDs less than $500\,\mu m$ after binerisation.

interference patterns produced by each of these complex particles could result in a broader angular distribution in scattering intensities than that of a sphere of equal area, as demonstrated by Agrawal et al. (2008). This wider angular distribution in scattering intensities would be interpreted by the LISST as a distribution in particle sizes that are associated with the sizes of small sub-components of the particle's geometrical structure. However, it is difficult to quantify the effects of particle shape on the scattering functions due to the strong influence of azimuthal asymmetry in the scattering recorded.

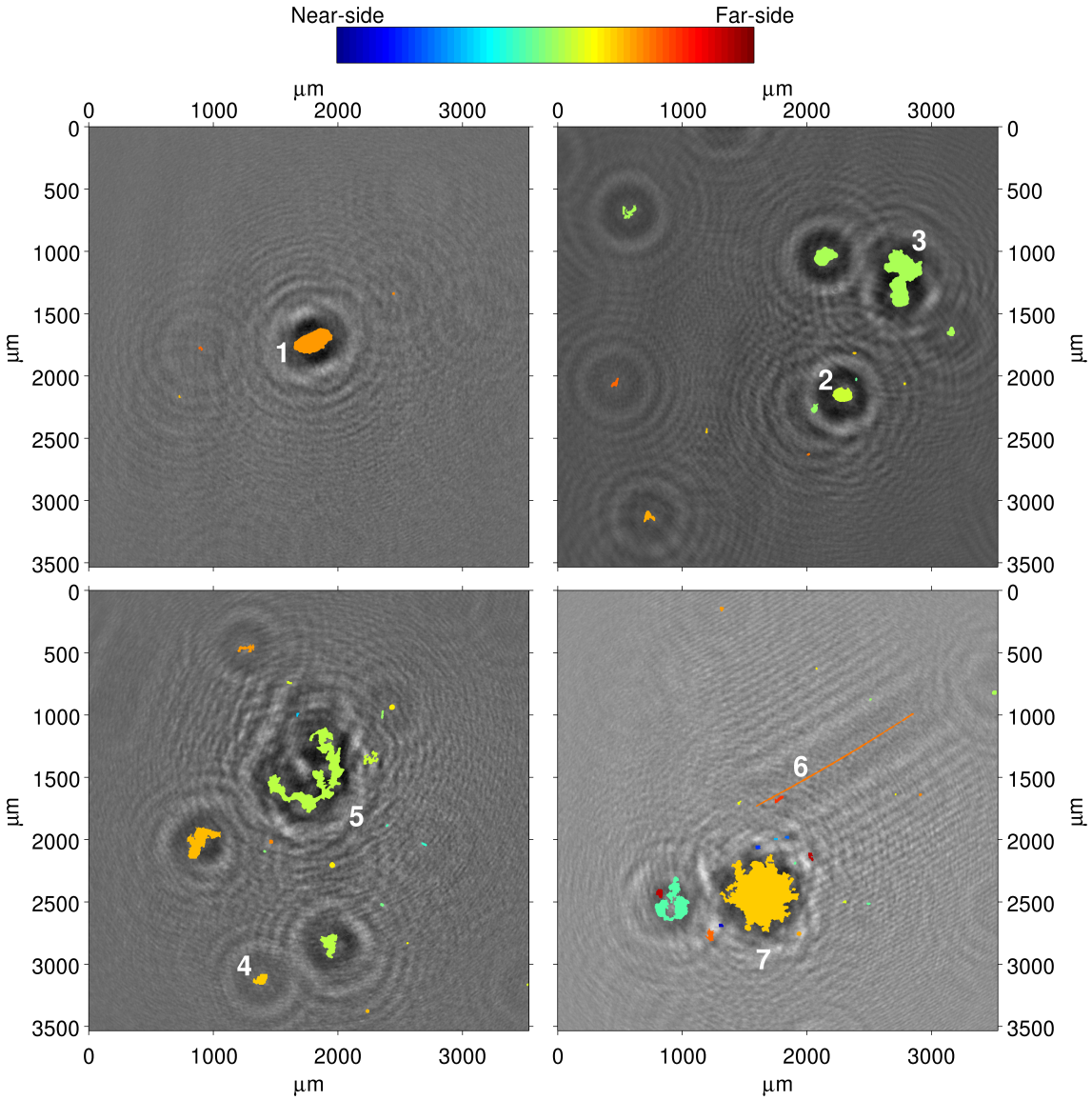

Figure 5.7: Examples of raw holograms and the associated binarised particles obtained from the reconstructed image. The colours of the binary particles correspond to an approximate location (z) through the volume.

The shape of particle projections may be derived using imagery. Circularity ($\frac{4\pi Area}{Perimeter^2}$) is a useful shape metric representing the deviation in shape from that of a perfect circle, which would most likely satisfy that of Mie Theory. However, estimations of circularity encounter a number of issues when using binary images

of a particle, as returned by the holographic reconstruction routine. Circularity cannot be accurately obtained from particle imagery due to the use of square pixels in the make-up of each image. In a binary image of a particle, the perimeter may be calculated by counting the number of pixels surrounding the edge of the particle. This is not an accurate measure of perimeter in circumstances where the particle edge deviates from a straight line. For example, the corner of a square would be counted as a single pixel, when the true perimeter consists of both edges of the pixel (i.e. twice the pixel length). In complex particles this error becomes enhanced due to the increase in occurrence of this problem. To illustrate the errors in circularity, as inferred from pixel-based images, Figure 5.8 shows computer generated circles with diameters ranging from 8 to 400 pixels, alongside the circularity and elongation (minor - major axis length ratio) derived from the pixel-based image. With circularities converging at 0.9 for large circles ($>$ 150 pixels in diameter) and a wide distribution in circularities at small sizes ($<$ 100 pixels in diameter), it is apparent that it is not a reliable metric for particle imaging when perimeters are calculated from pixel counts. Elongation, on the other hand, is not affected because a measure of particle perimeter is not needed, resulting in elongations of 1 for the entire range of circles shown in Figure 5.8.

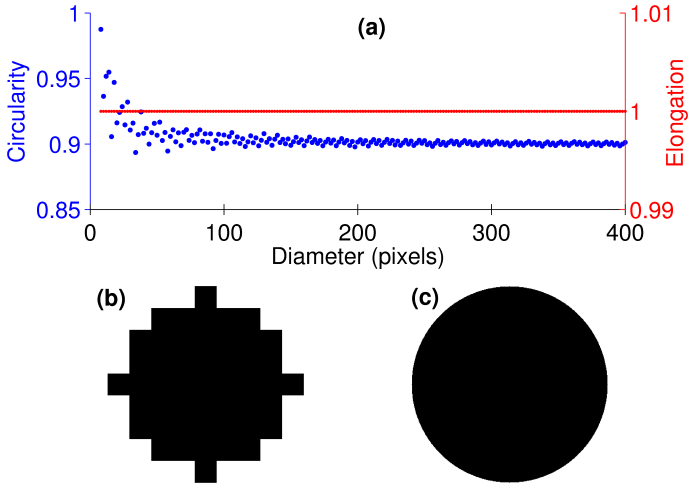

Figure 5.8: Circularity (blue) and elongation (red) for computer generated circles (a) with diameters ranging from 8 (b) to 400 (c) pixels.

Figure 5.9 shows the D_{50} values from the holographic camera and the LISST in relation to the particle elongation measured by the camera. No relationship between elongation and measurement discrepancy is apparent. This is likely to be due to the highly complex and unpredictable nature of the azimuthally asymmetric scattering from these particles, as demonstrated in Figures 5.7 and 5.2. Caution should therefore be applied to the interpretation of scattering recorded by the LISST in situations where particles are in fixed orientation or preferentially orientated, due to the effects of azimuthal asymmetry, as this results in a more variable response on the ring detectors. This would be particularly important when using the LISST-ST

variant of the LISST-100 series, which is configured to measure particles within a settling column.

Azimuthal asymmetry is a problem which is not limited to the LISST-100. Many optical sensors and numerical models adopt an assumption of symmetrical scattering, either by assuming spherical scatterers or randomly orientated scatterers. In addition, satellite remote sensing reflectance measurements are often made from one or two limited passes of a location per day, requiring that the orientation of the particles in the water is fixed over time. It is conceivable that, in a tidal environment, shear flows may preferentially orientate some particle types, such as diatoms, differently during ebb and flood conditions. In the open ocean, it may also be the case that a strongly stratified region causes settling particles to 'fall over' and preferentially orientate at the pycnocline. The lack of published articles which quantify particle orientations over different spatial and temporal scales and their relation to azimuthal scattering patterns is concerning. Subsequently there is an urgent need, in both the remote sensing and ocean optics communities, to start measurements and parametrization of the effects of particle orientations in different waters before a full quantification of the errors associated with scattering from complex particles can be achieved.

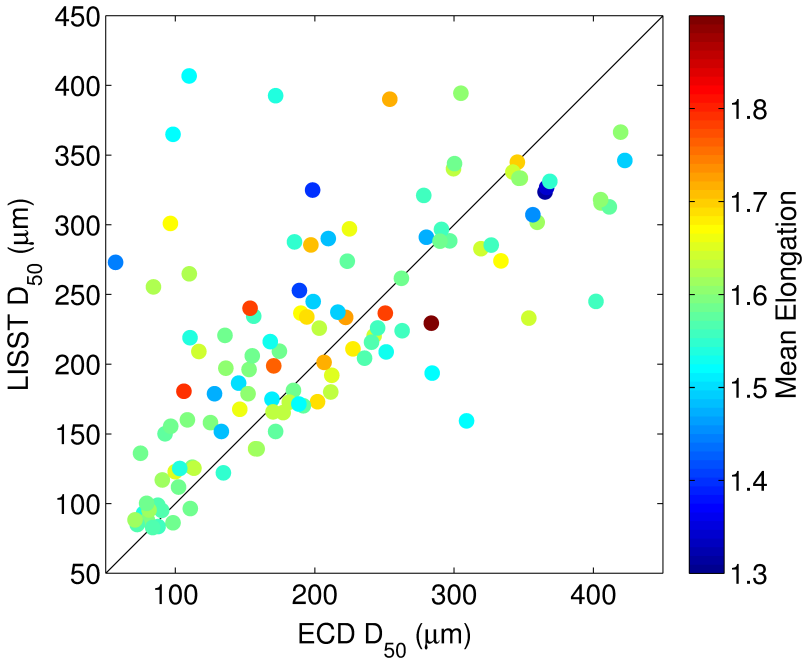

Figure 5.9: D_{50} measurements from the holographic camera and the LISST in relation to the particle elongation (Major/Minor Axis) measured by the camera.

A proper assessment of the effects of particle shape on scattering therefore requires symmetry in scattering throughout all azimuthal angles. One possible solution is to ensure that particles are recorded in all orientations during the integration time of the LISST ring detector measurement ($\sim 80ms$). To achieve this in laboratory conditions would be a challenging task if particle break-up is to be avoided. It may

therefore be the case that a more accurate assessment of the effects of particle geometry on forward scattering is only possible using *in-situ* data, where particles are more randomly oriented within their natural environment.

5.3 Summary and conclusions

- In the case of settling particles in a constant orientation, the LISST-100 is in best agreement with the holographic camera when using the equivalent circular diameter of the binary particles. Disagreement between the two instruments occurs when particle populations contain small particles in relatively low concentrations. This is due to weaker scattering intensities from smaller particles, resulting in an increase in background noise from the LISST ring detectors being inverted into an incorrect particle size. Poor agreement between the two sizing techniques is also apparent at larger sizes and may be attributed to binerisation errors during the holographic reconstruction routine. This causes a decrease in the reported number of large particles and an increase in small particles from the broken segments of a particle.

- The smoothed scattering from random-shaped particles reported by Agrawal et al. (2008) (e.g. Figure 5.10a) is not apparent in the observations of settling complex particles here. This is due to each particle being recorded in a near-constant orientation throughout the averaging period of measurement, resulting in substantial asymmetry in the scattering produced. The effects of asymmetry in scattering were noted by Agrawal et al. (2008), but appeared as only a weak signal. The effect of the alternating high and low readings on adjacent ring detectors, as illustrated in Figure 5.10b, appears to have a minimal effect on the inverted size distribution reported by the LISST. Though there is a broadening of the scatter of reported results, due to offsets in the principal peaks of between one and two rings (as inidcated in Figure 5.11).

- The observations of smoothed scattering from random-shaped particles (Agrawal et al., 2008) may be a more accurate description of an average of scattering from similar type particles. This would result in an effect similar to rotating a single non-spherical particle within the centre of the beam. This descriptor of scattering from random-shaped particles may therefore be more applicable to *in-situ* measurements, where flow speed or instrument profiling increases the number of particles per measurement, and particles are present in more random orientations.

- Segmentation of particle images during the binerisation process in holographic reconstruction results in underestimations of particle sizes reported by the camera, in relation to the LISST, and is indicated by the blue region in Figure

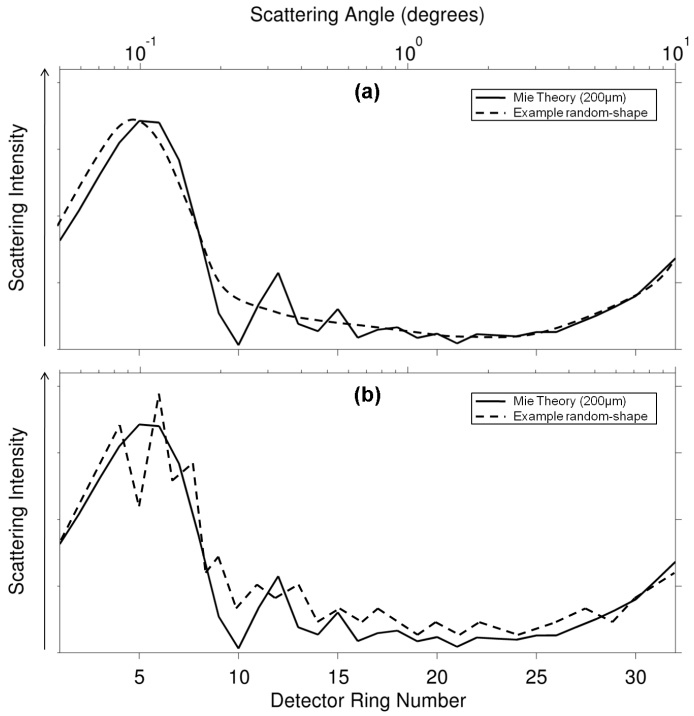

Figure 5.10: Schematic illustration of the expected scattering from: a) random-shaped particles as per Agrawal et al. (2008), and b) settling random-shaped particles presented in this Chapter.

5.11(b) and the extended example (a). The example shown in (a) demonstrates that some particles have been excluded from the binarised image in the holographic camera, and that a bright peak in scattering recorded by the LISST may have been caused by a single large particle which could be within the dark area towards the centre of the hologram. Errors due to segmentation in the laboratory system are increased relative to the standard holographic systems presented by Graham and Nimmo-Smith (2010) and Graham et al. (2012a). This is due to the camera in the laboratory system capturing the entire width of the incident beam, which causes dark regions around the edges of the image. These areas of lower incident light intensity cause the reconstructed real images of particles to have weak intensity in relation to the background, and are subsequently difficult to accurately binerise due to increased challenges in determining an accurate threshold.

- Errors in LISST measurements are increased as signal:noise ratios worsen. This occurs when the sample volume consists of weak scattering, either from very low concentrations or from weakly scattering particles. Because the weaker scattering reduces the intensity of the principal peak in the diffraction pattern recorded by the LISST, the noise at larger angles become more prominent in the inverted size distribution, causing an under-estimate in size in relation to the camera. The example shown in Figure 5.11(c), shows a combination of two negative effects on the agreement between the two instruments: the first is the

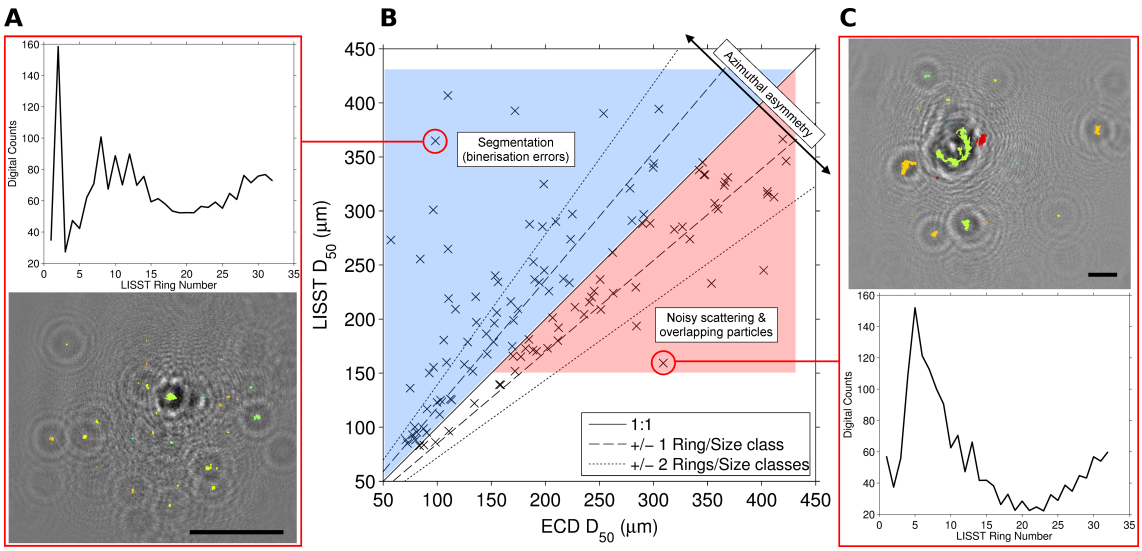

Figure 5.11: Summary of observations of median sizes recorded by the holographic camera and the LISST (b), and example scattering and holograms (a & c). Errors from scattering offsets of ± 1 and 2 LISST detectors (and subsequent size classes) are indicated by the dashed and dotted lines respectively. These offsets represent errors that could be induced from azimuthal asymmetry in scattering. Errors from segmentation of binary particles, result in smaller sizes being returned by the holographic camera, producing results that fall within the blue area. Regions where the camera returns particles much larger than the LISST could be due to noisy scattering data on the LISST detectors, and from overlapping particles in the holographic camera images (red area). The scale bars in the example holograms are 500 μm in length.

spurious and noisy scattering, indicated by the jagged pattern with low readings of digital counts on the ring detectors resulting in a decrease in reported size by the LISST; the second effect is that a region of holographic interference has been wrongly reconstructed as a relatively large particle (shown as a red particle near the centre of the image), elevating the D_{50} reported by the camera.

Chapter 6

In-situ Particles

This Chapter aims to apply knowledge gained from the laboratory studies and numerical tests, presented in the previous Chapters, to inform the analysis of particle measurements from both the LISST-100 and holographic camera in UK coastal waters. Parts of this Chapter contain content which has been adapted from the author's contributions to the following publication:

George W. Graham, Emlyn J. Davies, W. Alex M. Nimmo-Smith, David G. Bowers, and Katherine M. Braithwaite, (2012), "Interpreting LISST-100X measurements of particles with complex shape using Digital In-line Holography", Journal of Geophysical Research - Oceans, 117, C05034, pp. 20, DOI:10.1029/2011JC007613. (Appendix C)

6.1 Study site

The LISST-HOLO and LISST-100X type-c were deployed together on a bed-mounted frame for the first time in August 2011. This deployment was aimed at retrieving information on particle properties alongside measurements of the inherent optical properties of the water (from an adjacent bedframe) in the Menai Strait, Wales (Figure 6.1). The straits are dominated by strong tidal flows and an abundance of mineral grains and flocculated particles. Mean organic:inorganic ratios obtained from filtration indicated that the organic mass was approximately half that of the inorganic mass (MacDonald, 2012).

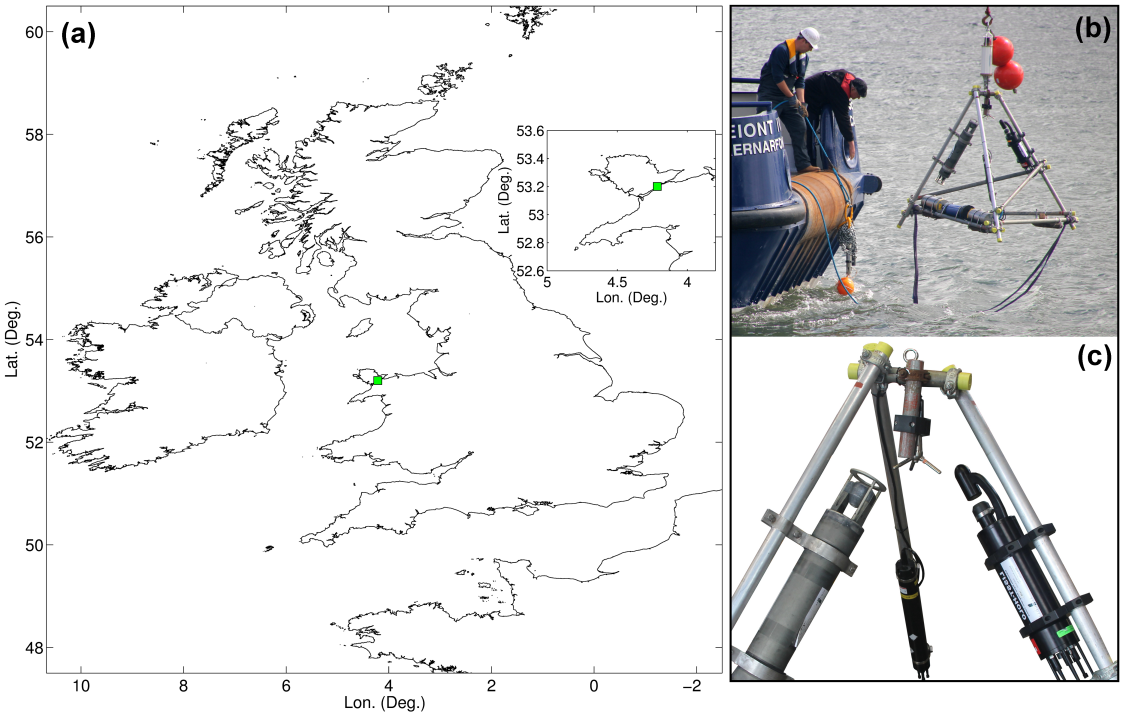

Figure 6.1: Map of the UK coast showing the location of the Menai Strait (a). Photographs of the bedframe (b-c) with the LISST-100 (left), ADV (middle) and LISST-HOLO (right).

6.2 Particle size and concentration

The LISST-HOLO is a digital in-line holographic camera produced by Sequoia Scientific Inc. It adopts the same principles as the other holographic devices used throughout this thesis, with a pixel size of $4.4\mu m$, a path length of $5\,cm$ and wavelength of $658\,nm$. Particle size distributions from the LISST-HOLO and LISST-100 are shown for a 16 hour segment of the 9 day deployment (Figure 6.2). The LISST-HOLO was sampling at 12 second intervals, and the LISST-100 at 4 second intervals. Data from the two instruments were averaged into 15 minute sections to allow the median size returned from the holographic image analysis to reach near-convergence during each averaging window. Both instruments report similar tidal modulations in particle size and concentration. High volume concentrations reported by the LISST-100 (e.g. at 17:00 and 22:30) were likely to be from temporary dirt settling onto the optical windows. Due to concerns over multiple scattering during these times, LISST data associated with transmissions less than 50% were removed from the analysis. The LISST-HOLO reported a large range in particle sizes and shapes (Figure 6.3), with some approaching $1\,mm$ in diameter, but a generally good agreement between the two size distributions within the 100-400 μm sizes is apparent throughout the time series.

When comparing the mean PSDs over the 16hr segment, the apparent number of small particles reported by the LISST is greater than the number present in reconstructed holograms. Figure 6.4 shows the average number distributions obtained

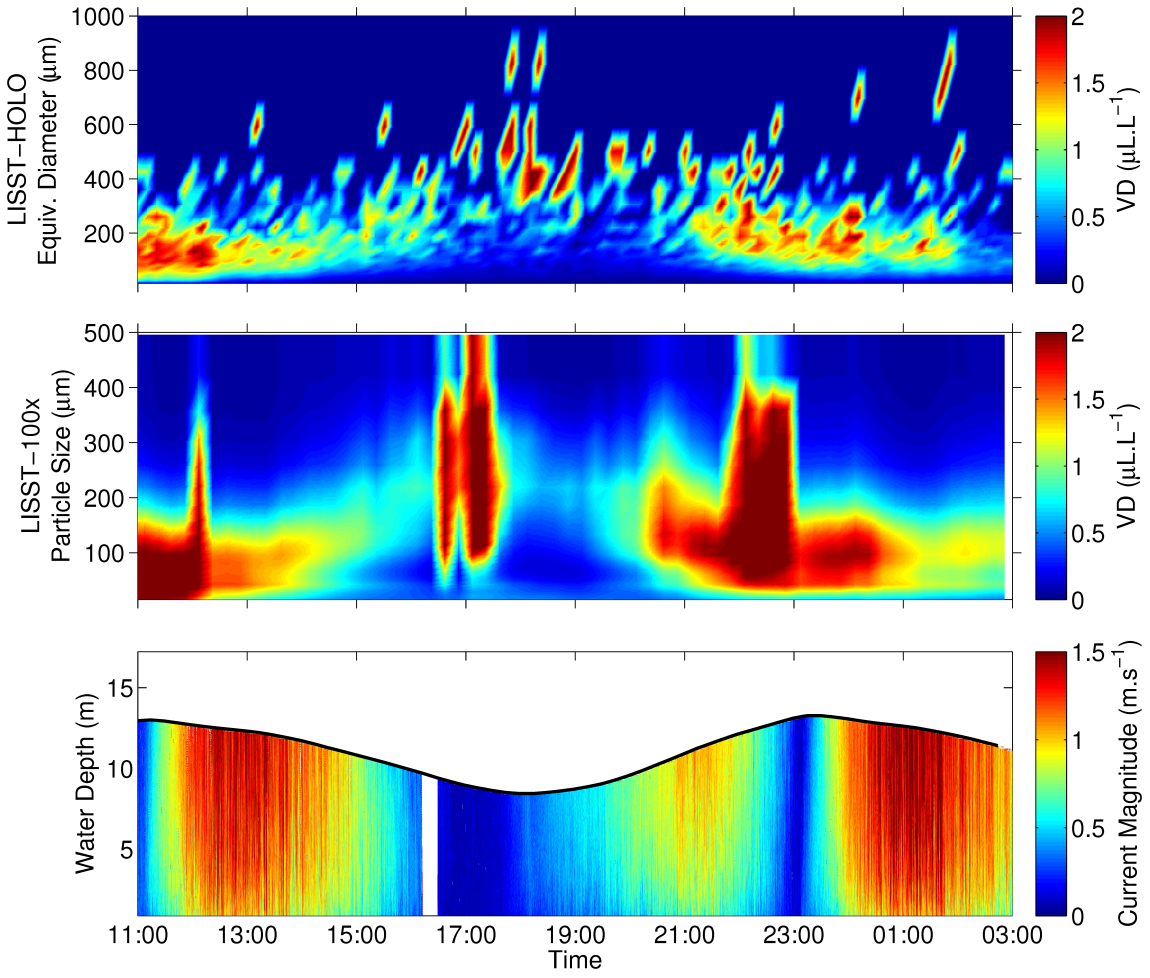

Figure 6.2: Time series of particle volume distributions from the LISST-HOLO (top) and LISST-100x type-c (middle). Water depths and current magnitudes, from a nearby bed-mounted ADCP, are shown in the bottom plot.

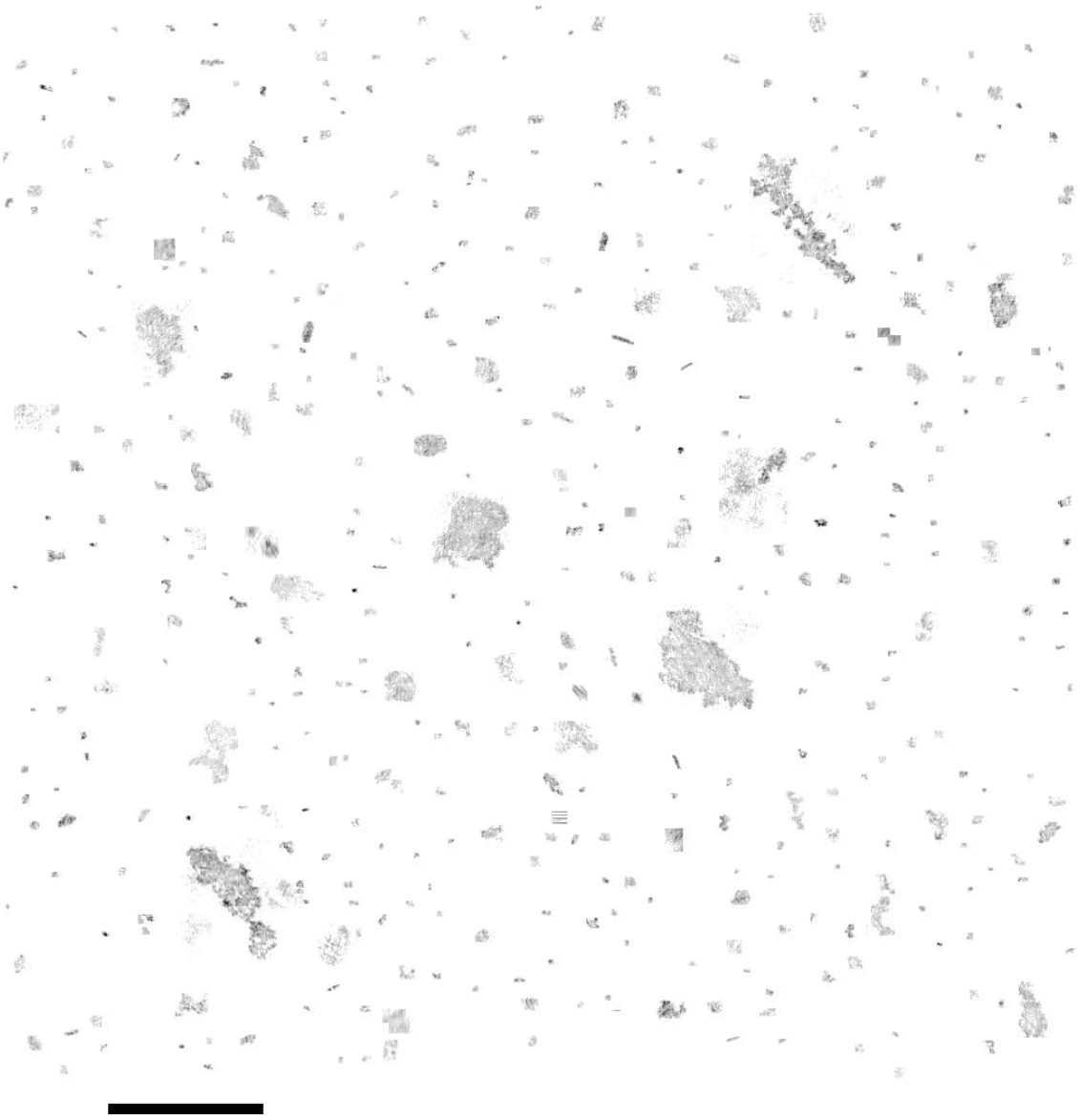

Figure 6.3: Montage of randomly selected LISST-HOLO particle images from the 16hr. segment. The scale-bar is $500\,\mu m$.

from the bed mounted frame. It would be expected for the distribution in particle Equivalent Spherical Diameters (ESD) recorded by the holographic camera to match the PSD obtained from the LISST-100, as the forward scattering is primarily controlled by particle area. However, the divergence in number concentrations within the smaller sizes of the overlapping size range of both instruments is concerning. A consideration of scattering that deviates from the restrictions of Mie Theory, and hence an assessment of particle shape, was necessary in this environment where particles are more randomly orientated. An approach to accounting for any effect of particle geometry requires a means of extracting appropriate shape information from holographic imagery. This approach is outlined in the following section.

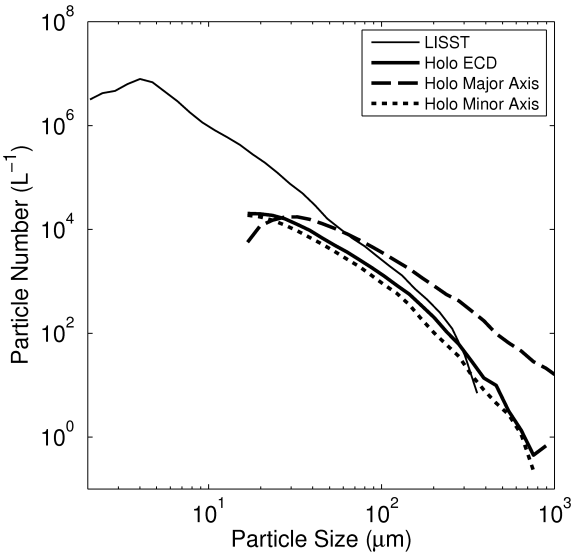

Figure 6.4: Mean Particle Size Distributions obtained from a bedframe containing the LISST-100 and holographic camera during the 16 hour segment.

6.3 Accounting for complex geometry

Measuring and classifying the wide range of particles found in the natural marine environment is challenging because multiple parameters for describing particle geometry must be used for an accurate representation of particle shape. Figure 6.5(a) shows computer generated particles of random shapes, but identical area and equivalent circular diameter. Many commonly used shape metrics, such as circularity, go some way towards describing particle shape deviations in relation to a sphere of equal area, as shown by Figure 6.5(a). A measure of circularity does not, however, consider the individual dimensions that make up the geometrical structure of the particle and, as demonstrated in Chapter 5, image analysis of perimeters becomes problematic due to square pixels. Other shape metrics, such as the Corey Shape Factor, consider a small number of dimensions but return a non-dimensional result, making it difficult to incorporate into a theoretical scattering prediction.

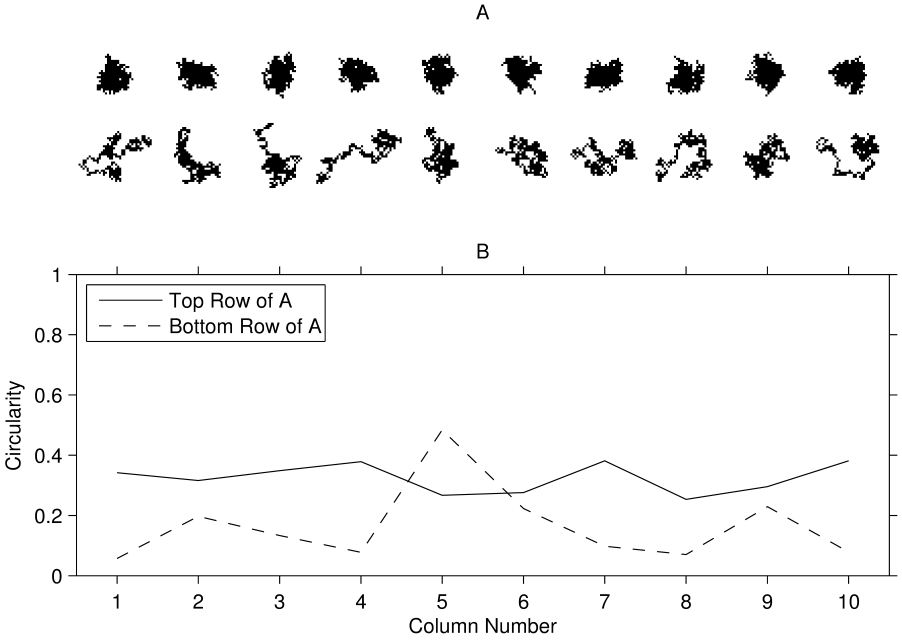

Figure 6.5: Projected area and circularity of random shapes. A shows projected areas of 20 computer generated, random-shaped particles of equal area. B shows the circularity of each of the particles in A. Circularity is taken to be: $\frac{4\pi Area}{Perimeter^2}$

The method developed here packs circles of specific configuration into the projected area of particles recorded via imagery. It provides a means of representing individual dimensions that make up any two-dimensional geometrical structure which would have the potential to approximate forward scattering based on a simple adaptation to the application of Mie Theory. It may also be used as a metric for particle complexity, and offers a possible explanation for an increase in apparent numbers of small particles that are recorded when inverting a volume scattering function into a particle size distribution. The routine is applied both to synthetic particles and to particles recorded by the holographic camera on the bed-mounted frame. Number

distributions obtained from a LISST-100, holographic camera and circle packing are then examined.

Method

The method for packing the projected area of a particle with circles requires the largest dimension of the particle to be represented by the largest circle that will fit within its projected area. The area filled by this circle can then be removed from the initial image of the particle area. The largest circle that can fit within the remaining area can then be found. These steps are applied recursively until the particle is completely filled by circles. The result is a number distribution of circle diameters that are unique to the particle shape. The position of each circle that is packed into a particle is calculated from a two-dimensional convolution of the projected area of the particle and the circle being fitted. An example is shown in Figure 6.6, where (a) is the convolution of the particle projected area and the white circle shown in (b). The peak in this convolution gives the position of the centre of the circle. Once this position has been found, the area covered by this circle is removed (Figure 6.6), and the convolution is re-applied. This routine is continued recursively until the circle diameter reaches three pixels, producing a result such as that of Figure 6.6(h). The routine is stopped at circle diameters of three pixels because of the increased error in circle area, due to pixel resolution in small circles. This error is illustrated by Figure 6.7. The number distributions of circles that are created results in simple particles being represented by a clear dominant large circle and very few small circles, and complex particles having no single dominant large diameter and many more small circles. As a result the skewness of this distribution of circles could also provide a proxy for particle complexity, although this application is not utilised here.

Optimization

The use of a two-dimensional convolution to identify the optimum location of circles has severe limitations when used with elongated shapes (Figure 6.8(a)). This is because more than one peak position will be returned by the convolution, as shown by the green crosses in the centre of Figure 6.8(b). With the method described so far, circles will be fitted as per Figure 6.8(c). However, this would provide a poor representation of the elongation, as many small circles would then be filled in the gaps between the three large circles, and a large area of open space is not covered because the length of the particle is not divisible by its width (i.e. the largest circle diameter). To better resolve these problems associated with elongation, a smearing of circles is introduced when the convolution returns multiple positions for a circle centre. In the case of Figure 6.8(b), multiple circles of equal diameter are centred on each of the possible positions returned by the convolution, as shown by the green

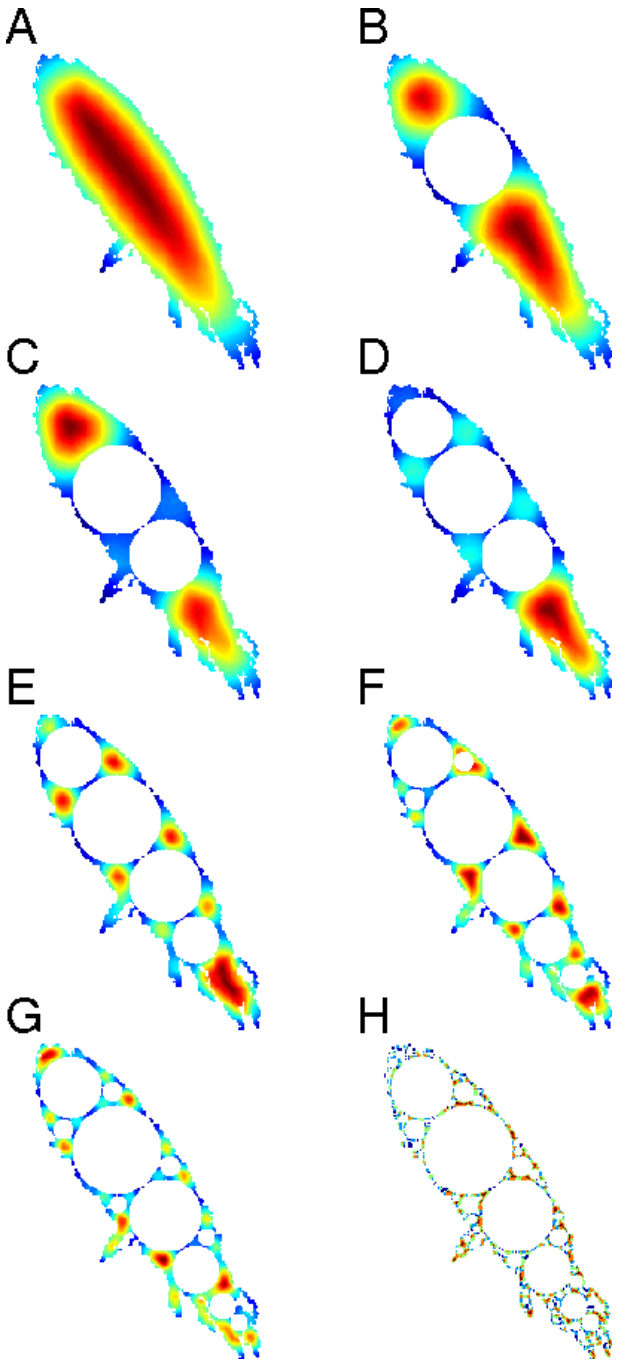

Figure 6.6: Demonstration of circle-packing convolution. (a) shows the initial convolution from a binarised particle image, obtained with the holographic camera, with the circle shown in (b). Images (b-g) show examples of the convolutions for the first six size stages of the routine. (h) shows the final convolution at the end of the routine.

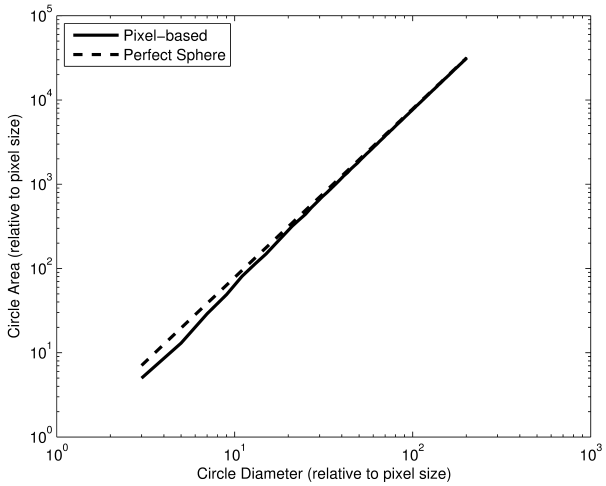

Figure 6.7: Comparison of the difference in area covered by pixel-based circles and the area of a perfect circle of equivalent diameter.

crosses. The total area covered by these overlapping circles is then calculated and removed (Figure 6.8(c)) before applying the second convolution. Subsequently, the value used to represent the equivalent number of circles (N_D) that are packed into the particle area, is given by the ratio of the total area covered by overlapping circles, to the area covered by a single circle of diameter D, as per equation 6.1.

$$N_D = \frac{A_o}{A_D} \tag{6.1}$$

where A_D is area covered by a circle of diameter D, and A_O is the area covered by the overlapping circles of diameter D.

6.4 Results

Figure 6.9 shows resultant images of the circle packing method alongside histograms of number distributions, and the area covered, for regular-shapes. It is clear that circular particles (a-b) have a dominance of a single large circle in the histogram. For angular shapes such as the square (c), rectangle (d) and parallelogram (e), the corners are represented by a distribution of small diameter circles. In addition, the branched areas of the cross and star shapes (f-h) can be seen by a peak in circle diameters closer to 50% of the largest dimension. For the 8-point star (h), this peak is found at about 25% because the points of the star are smaller in relation to the central area. Figure 6.10 shows the images of the circle packing method alongside histograms of number distributions, and the area covered, for a selection of plankton and flocculated particles obtained from the coastal waters of Plymouth (UK). When comparing histograms of number distributions shown in Figure 6.9 with those of Figure 6.10, it is clear that much larger numbers of small particles are required to fill the projected areas of the *in-situ* particles. This is due to the

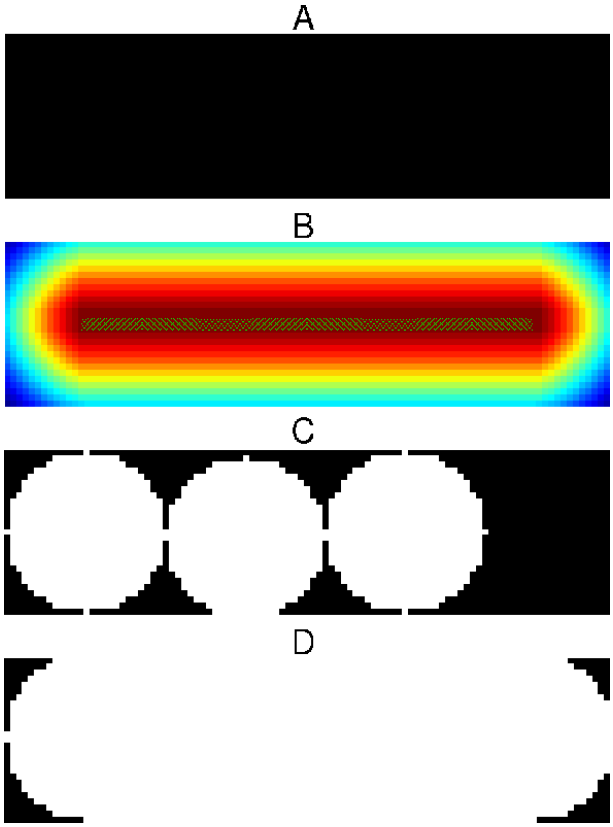

Figure 6.8: Image A represents a rectangular particle area. (b) shows the two-dimensional convolution of (a) and a circle with a diameter equal to the smallest chord of (a). The green crosses of (b) show the positions in which the circle could be placed. Image (c) shows the routine without accounting for all multiple centres. (d) shows the optimized method of smearing the circle across all centres returned by the convolution.

increased smaller dimensions that contribute to the the more complex shapes of the *in-situ* particles. The large dominant scales of particles A and B can be seen clearly in the histograms of the area covered by circles. Particle A has three dominant large scales that make up the main body of particle B. The more rounded shape of the body of the particle on the top left is represented by a single, large diameter particle that covers about 70% of the total particle area. Particles (c-d) have long, thin branch-like appendages, attached to a single bodily feature. The main bodies are represented by the large diameter circles, and the appendages are shown by a distribution of small-diameter circles. The Copepod has a more elongated body, which is resolved by two large diameter circles ($> 50\%$). The long and thin Diatom chain (f) has only four different diameter circles, with a clear peak in the area covered by a circle of about 50% relative diameter. The peak in the area covered is at a central diameter due to the overlapping of circles down the length of the particle. Without the overlapping, many more smaller diameter particles would have been produced, creating a false impression of a more branched and complex geometry.

Flocculated particles (g-h) are filled with a wide range of circle diameters, often with no clear dominance of a single sized circle. This is indicative of the complex particle structure of aggregates. When complex non-spherical particles (such as those shown in Figure 6.10) are rotated through all angles or when multiple particles are sampled in random orientations, it is conceivable that each of the small dimensions within these aggregates could contribute to additional scattering of light at relatively large angles. The scattering caused by this effect could be approximated by applying Mie Theory to each of the sub-components returned by the circle-packing routine, as opposed to the traditional scattering prediction from solely the area of the particle. This additional scattering would contribute to the increase in the number of small particles calculated by way of inversion of their volume scattering function.

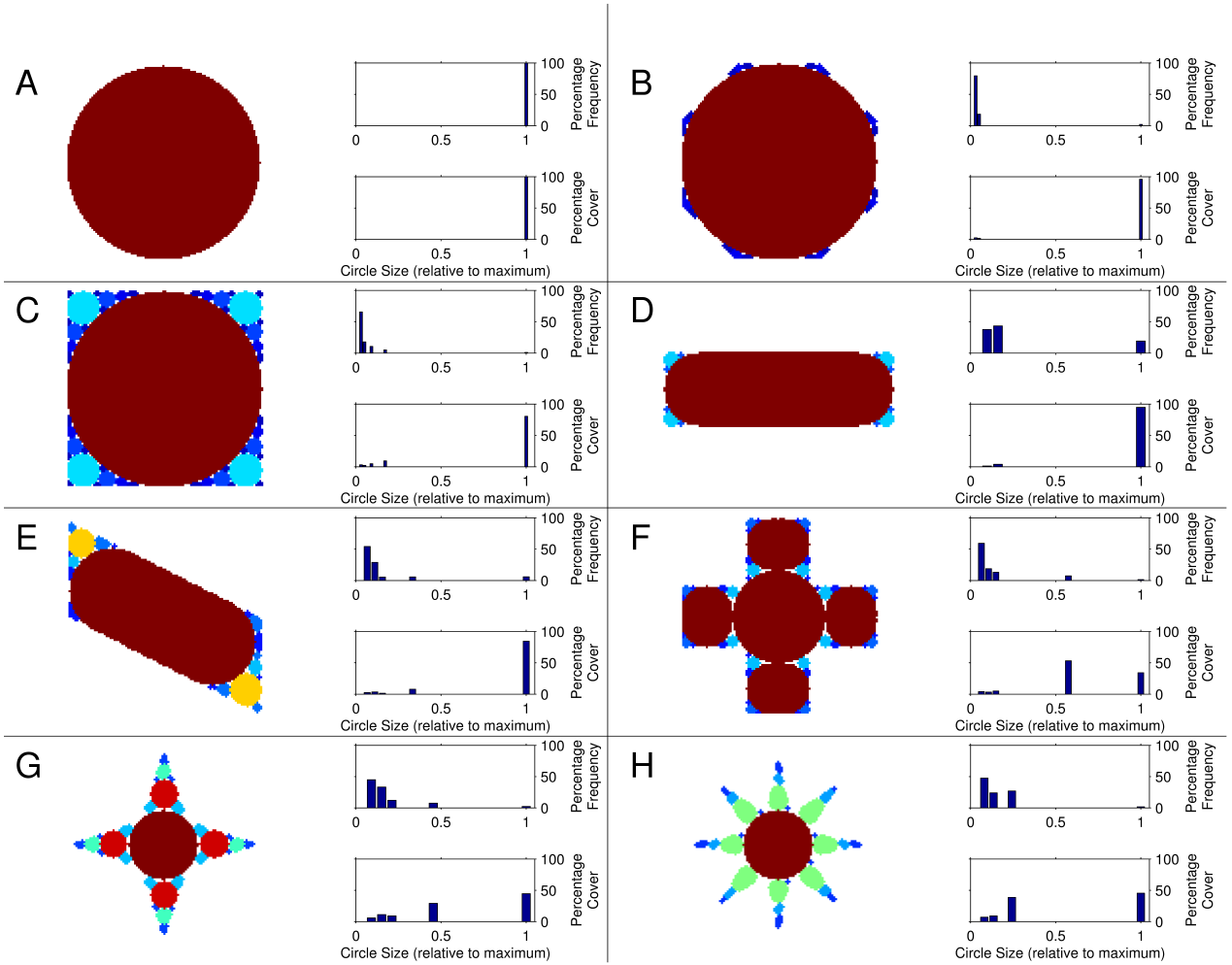

Figure 6.9: Examples of resultant circles, histograms of number distributions and histograms of area distributions, for particle projected areas of regular particles.

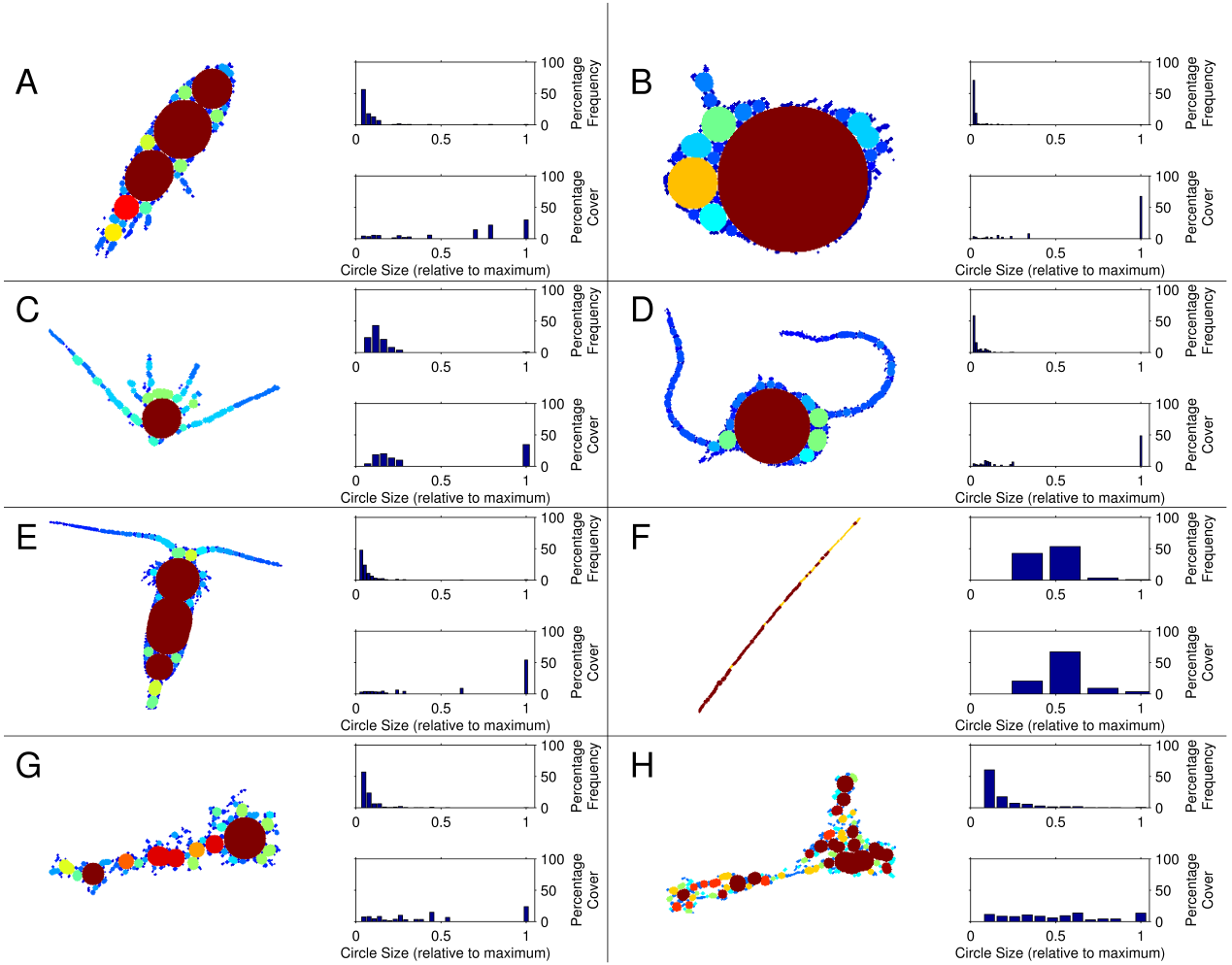

Figure 6.10: Examples of resultant circles, histograms of number distributions and histograms of area distributions, for particle projected areas obtained from *in-situ* holographic imagery in the coastal waters of Plymouth (UK).

6.5 Discussion

To quantify the effect that small sub-scales of particle geometry have on the LISST-100 measurements of particle size, the scattering functions from the distribution of equivalent circular diameters and packed circles were calculated using Mie Theory. Mobley (1994) demonstrated that it is possible to calculate the contribution of varying types of scatterers to the total scattering coefficient (b). As such, the contribution of the varying geometrical scales recorded by the holographic camera to the volume scattering function and scattering coefficients, as measured by the LISST, may be estimated. This assumes that all component scatterers conform to the requirements of Mie Theory, and that any phase relationships between the scattering components have a negligible effect in the near-forward angles.

A scattering coefficient may be derived from the integral of the associated VSF. As the LISST-100 does not record the VSF over all angles, a true scattering coefficient cannot be measured. In predicting the scattering recorded by the LISST-100, b is taken as the integral over the angle ranges covered by the LISST ring detectors, as per Agrawal (2005):

$$b = 2\pi \int_{\theta_{min}}^{\theta_{max}} \beta \sin(\theta) d\theta \tag{6.2}$$

where θ is the scattering angle, θ_{min} and θ_{max} are the minimum and maximum angles covered by the LISST ring detectors, and β is the volume scattering function recorded by the LISST. The volume scattering function (β_a) associated with the distribution of the component diameters (N_a), obtained from holography can be calculated, enabling the scattering coefficient (b_a) from these components to be derived, as per Slade and Boss (2006):

$$\beta_a = \int_{D_{min}}^{D_{max}} N_a \widetilde{\beta}_a C_{sca} dD \tag{6.3}$$

$$b_a = 2\pi \int_{\theta_{min}}^{\theta_{max}} \beta_a \sin(\theta) d\theta \tag{6.4}$$

where a is the component scale (such as the equivalent circular diameters or packed circles). D_{min} and D_{max} are the minimum and maximum observed component diameters (N_a), $\widetilde{\beta}_a$ is the phase function associated with the distribution of component diameters, and b_a is the value contributed by the a component to the scattering coefficient recorded by the LISST.

Figure 6.11 (a) shows the number distributions obtained from the LISST-100 and the equivalent circular diameter obtained from holography. The circle-packing technique, described in the previous section, was applied to projected areas of every particle reconstructed and binarised by the holographic camera during the 16-hr. segment of the bed-frame deployment, with the dashed line showing the distribution

of resultant circle-packed diameters. Figure 6.11 (b) shows the observed volume scattering function from the LISST-100 (calculated as per Agrawal (2005)) and predicted scattering functions from Mie Theory, based on the distribution of equivalent circular diameters obtained from holography and the distribution of circle-packed diameters (Equations 6.3). The circle-packed size distributions appear to match closely to that of the LISST-100 for particle diameters below approximately 20 μm. For diameters greater than 150 μm the equivalent circular diameter distribution matched closely to that of the LISST-100. These two size distributions subsequently correspond to scattering phase functions of two different shapes, as predicted by Mie Theory. The numbers of small particles ($< 20\,\mu m$) returned from the circle-packed diameter distributions, would be expected to scatter relatively more light at larger angles on the LISST-100 ring detectors. Mie predictions of the phase function that may be produced from these small sub-components of each particle, therefore return high scattering intensities in relation to the equivalent diameters at larger angles ($> 2°$), and low intensities at smaller angles ($< 0.4°$). The predicted phase function from the equivalent circular diameter corresponds to an opposite bias in the angular distribution of scattering intensities due to the apparent lack of small scatterers in relation to larger ones. The scattering coefficients from these predictions are shown for each component in Table 6.1. The combination of these scattering coefficients and phase-function shapes leads to the suggestion that the sum of both the distribution of circle-packed diameters, and area-equivalent diameters, may provide the most accurate representation of forward scattering by complex particles.

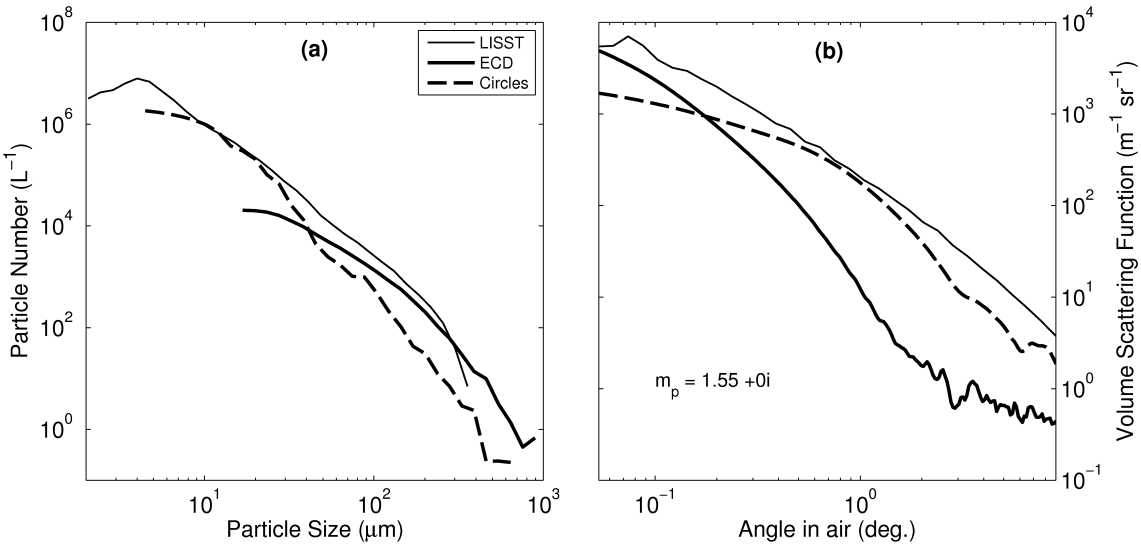

Figure 6.11: a) Average particle number distributions for each of the LISST-100 size classes using the random-shape inversion matrix, and for the holographic camera equivalent circular diameter (ECD) and circle-packed diameters; b) Average volume scattering function observed by the LISST-100 and Mie predictions of the VSF, informed by holography, for the ECD and circle-packed diameters. The refractive index used for Mie scattering predictions was 1.55 (real part) and absorption effects were considered as negligible.

Table 6.1: Scattering coefficients obtained from observations and Mie predictions (Equations 6.2 & 6.4).

Parameter	b (m^{-1})	$\%b_{LISST}$
$b_{LISST-Obs.}$	1.76	99.0
$b_{LISST-Mie}$	1.78	100 (ref.)
b_{ECD}	0.19	10.7
$b_{Circles}$	0.96	53.8
$b_{Circles+ECD}$	1.15	64.5
$b_{extr.(Circles+ECD)}$	1.88	106

The roll-off in the LISST-100 number distribution below $4\,\mu m$ and above $300\,\mu m$ is only apparent when the random-shape matrix is applied to the inversion of scattering. Interestingly, the Mie predictions of VSF using the LISST-100 PSD from the spherical inversion (and a refractive index of 1.55) produce a scattering coefficient ($b_{LISST-Mie}$) of $1.93\,m^{-1}$, much greater than the observed coefficient of $1.76\,m^{-1}$ (Table 6.1). This test, using only LISST data, appears to be a good means of determining which inversion matrix is most appropriate. With a scattering coefficient of $1.78\,m^{-1}$ from the PSD obtained via the random-shape inversion, it is clear that in this situation in the Menai Strait (Figure 6.11), the random-shape inversion is much more appropriate than the spherical alternative.

The volume scattering function, observed by the LISST-100, is shown in Figure 6.11(b) alongside predictions of the phase function from Mie Theory using the equivalent circular diameter (solid line) and circle-packed diameters (dashed line) from holography. Both Figure 6.11(a and b) show that the equivalent circular diameter alone, produces a phase function that lacks the relative scattering intensities observed by the LISST-100 at larger angles. This relates to an overestimate in the number of smaller particles returned by the inversion of the scattering. The circle-packed diameters, on the other hand, are associated with phase functions that match the observed scattering at larger angles but underestimate intensities at smaller angles. This could form a possible explanation for the overestimates of small particles returned by the inversion, leading to the suggestion that a combination of the distribution in diameters of packed circles and a primary particle dimension, such as the equivalent circular diameter, forms a good match to the number distribution interpreted by the LISST-100, as shown in Figure 6.12(a). When using this combined distribution to predict a phase function from Mie Theory, the result also matches well to the observed phase function recorded by the LISST-100, as shown in Figure 6.12(b).

Some discrepancies between the predicted and observed phase functions remain at the larger angles due to the limited smallest diameter of the packed circles, governed by the resolution of the holographic camera. A higher resolution camera

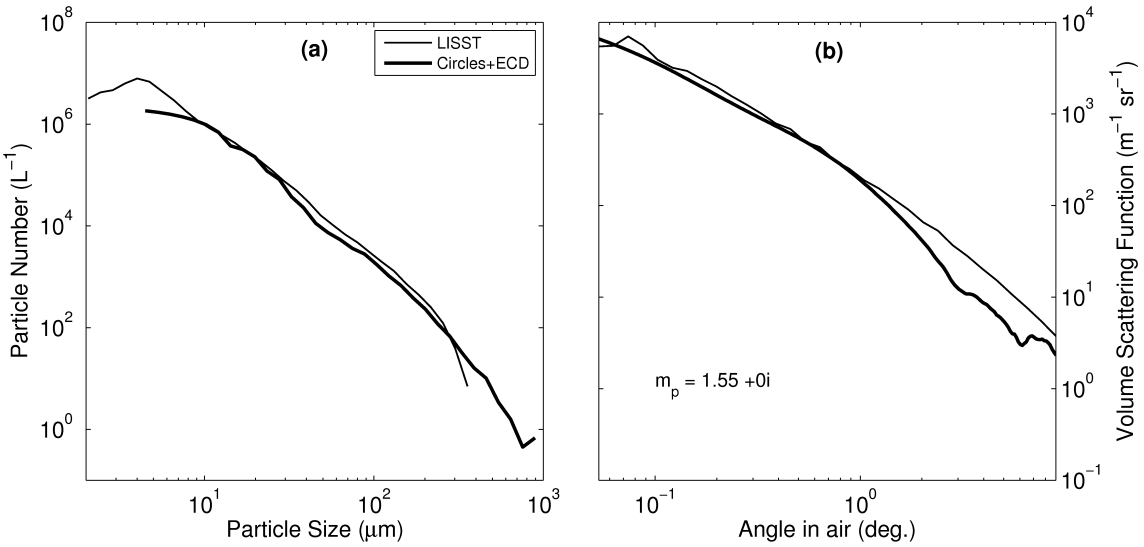

Figure 6.12: a) Average particle number distributions for each of the LISST-100 size classes using the random-shape inversion matrix, and for the combined holographic camera equivalent circular diameter (ECD) and circle-packed diameters; b) Average volume scattering observed by the LISST-100 and Mie predictions of the VSF from the combined holographic camera ECD and circle-packed diameter distributions. The refractive index used for Mie scattering predictions was 1.55 (real part) and absorption effects were considered as negligible.

system, capable of accurately resolving particles smaller than $15\,\mu m$, is therefore necessary to predict the shape of the phase function at larger angles, and to obtain accurate etimates of the scattering coefficient from within the angle range covered by the LISST-100 ring detectors. With the standard holography unable to accurately record particles smaller than about $15\,\mu m$, the contributions from particles with areas smaller than this and the associated smaller sub-components ($\lesssim 4\,\mu m$) is unable to be isolated from the possible variations in refractive index amongst the scatterers. These refractive effects would further influence scattering at larger angles, and are explored later in this Chapter.

6.6 Magnified holography

Very recent advances in the development of *in-situ* holographic imagery (Graham et al., 2012b) have allowed measurements of particle size to extend down to approximately $2\,\mu m$ (equivalent diameter). This enables particle measurements from imagery to cover the entire size range of the LISST-100 type-c. Particle size distributions from the Menai strait (obtained from a profiling system at a later date of February, 2012) using magnified holography, are presented in Figure 6.13. The figure shows decreasing particle numbers with size but with substantial deviation from that of a power-law distribution (dashed line). This is likely to be due to flocculation causing a reduction in the number of smaller particles ($< 10\,\mu m$) and an increase in larger particles ($\sim 10 - 100\,\mu m$). This curving of the size distribution

produces a distribution which is better represented by a second degree polynomial (cubic) fit rather than that of the traditional power-law (linear) fit used in the open ocean where flocculated particles are less common. It is worth noting that the counts of particles greater than approximately 100 μm are likely to be underestimated because the standard imagery was divided into four quarters for the analysis. This division reduces the likelihood of retrieving adequate particle information from larger particles. Due to potential uncertainties with these preliminary results, and for simplicity, the cubic fit shown by the solid black line in Figure 6.13 was used for the analysis presented in the remainder of this section.

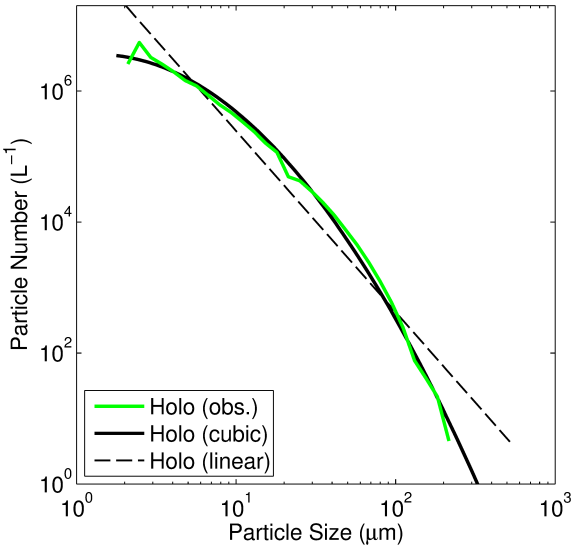

Figure 6.13: Particle size distributions from the Menai strait (Feb. 2012) using magnified holography (green line). Linear fit (dash line). Cubic fit (solid black line).

Figure 6.14a shows the particle size distribution inverted from the LISST-100 type-c, alongside the cubic fit through the size distribution from the magnified holographic cameras. A good agreement between the two size distributions is apparent within the range of 8-100 μm. As mentioned earlier, the offset in particle numbers for diameters larger than 100 μm is likely to be due to an under-estimation of particles by the holographic camera, resulting from the splitting of the standard magnification images. Offsets in the smaller size ranges ($< 8\,\mu m$) are harder to account for through comparison of the size distribution alone. To give more insight into possible reasons for this offset the original volume scattering function, observed by the LISST, is presented as the thick line in Figure 6.14b. This shows a dominance in scattering at the smaller angles with a reduction in scattering intensity towards larger angles. The thin line of Figure 6.14b is the Mie prediction of the VSF, informed by the cubic fit of the distribution of equivalent circular diameters (a), using a refractive index of 1.55 (typical of mineral grains). The scattering prediction shows good agreement with observed intensities within the angle range of ($\sim$ 0.2-0.7°). A reduction in predicted intensities, relative to the LISST observations, is observed at

angles less than $\sim 0.2^{o}$ and greater than $\sim 0.7^{o}$. The offset at the very near forward angles is due to the under-estimate of large particles by the holographic camera. However, this does not explain the offset at larger angles, where refraction plays a more dominant role in scattering (Chapter 4). A possible explanation is that the assumption of an entirely mineral refractive index (1.55) is not representative of this particle population.

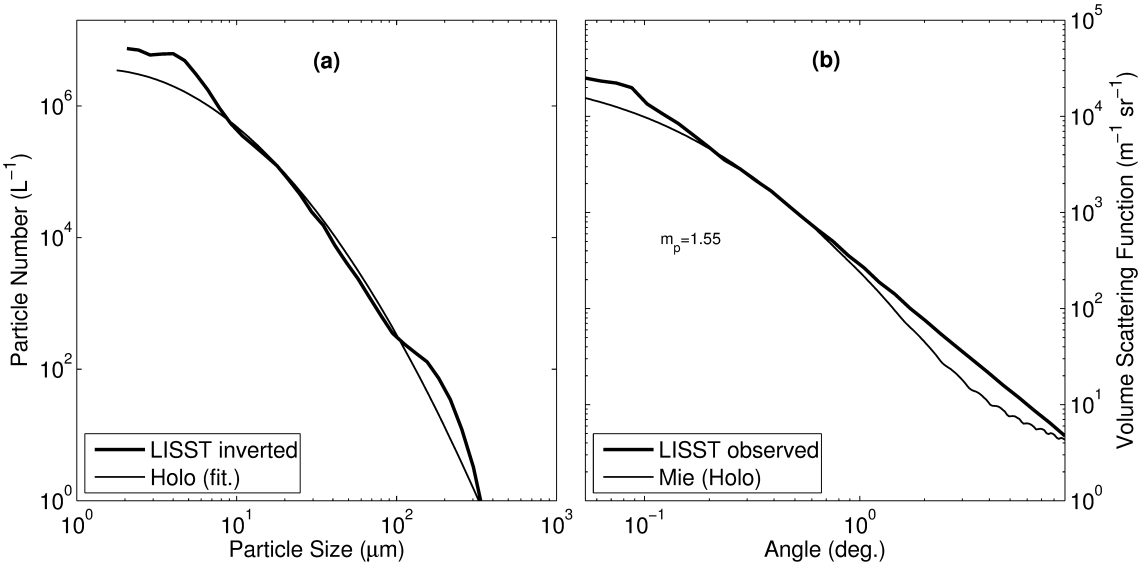

Figure 6.14: Particle number distributions from the magnified holographic camera systems and the LISST-100 type-c are shown in plot a. The thin line shows the cubic fit through the size distribution from the holographic camera, and the tick line shows the LISST-100 inverted size distribution. The observed volume scattering function from the LISST (thick line) is shown in plot b, alongside a Mie Theory prediction of the VSF from the fit of the holographic camera PSD (thin line) using a refractive index of 1.55.

To represent the variability of scattering at larger angles, caused by refraction, the Mie predictions of scattering were applied over a range of refractive indices, from 1.35 (near water) though 1.4 (typical of plankton) to 1.55 (mineral), using the same particle size distribution as in Figure 6.14. This is presented in Figure 6.15 which shows small variability at the near-forward angles and increasing variability at larger angles. The range of refractive indices shown here are representative of observed values presented by Aas (1996).

A minimisation of both the scattering coefficient from the Mie-based predictions (β_{Mie}) to the LISST observation (β_{LISST}), and the root-mean-squared error of the predicted and observed scattering functions, by way of varying the refractive index, returned an estimated refractive index (real part) of 1.414. This is within the range typical of phytoplankton (Aas, 1996). The estimation from this, however, is severely limited by the assumption of no absorption. In the forward direction absorption acts to reduce scattering intensities at angles approaching 10^{o}, the effects of which are demonstrated in Figure 6.16. Imaginary parts of the refractive index were varied

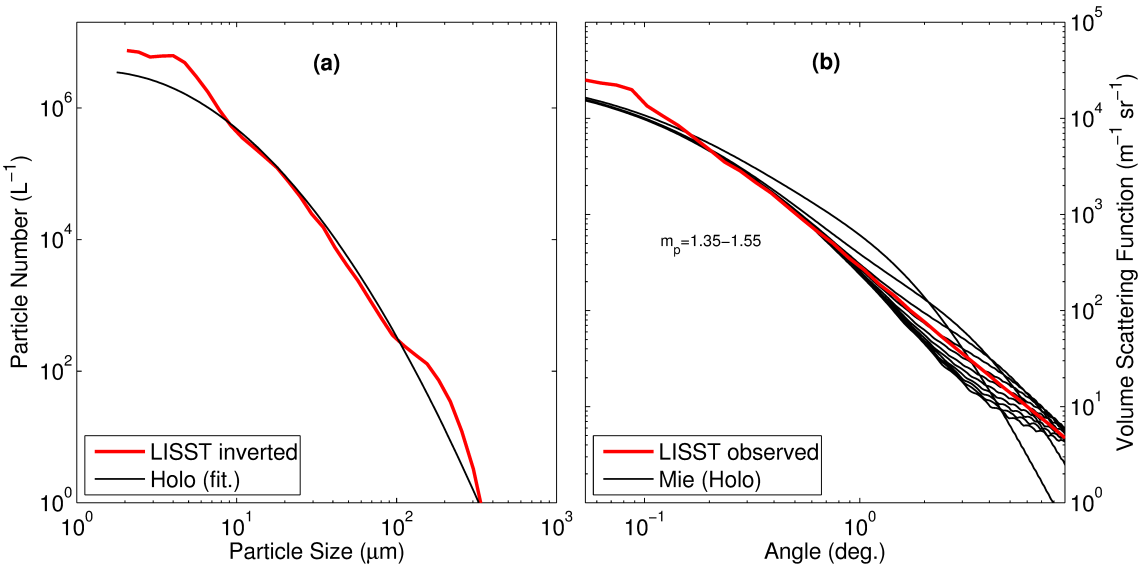

Figure 6.15: Size distributions from the LISST-100 (red) alongside the cubic fit through the magnified holographic images (black) is shown in a. The observed volume scattering function from the LISST (red) and the predicted VSFs from the cubic fit of the holography size distribution, using refractive indices ranging from 1.35-1.55 (black lines), is shown in b.

from 0-0.01 to cover the majority of ranges observed *in-situ* (Jonasz and Fournier, 2007).

A further limitation of these estimates of refractive indices is that it is highly unlikely that all particles in the population will be uniform and homogeneous in their composition throughout, and hence one bulk refractive index for the entire population is unlikely to be representative (Gillespie et al., 1978). Measurements of the backscattering coefficient, or ideally the VSF at angles larger that 10°, would provide valuable information in predicting the volume scattering function of natural marine particles, as it would allow for a more reliable estimate of refractive index. Without prior knowledge of the composition of a particle population on an individual particle basis, or variability in composition within each particle, it is very difficult to attempt to predict the accuracy of scattering properties of the population. As demonstrated in Figures 6.15 and 6.16, this uncertainty also applies to the forward angles covered by the LISST-100, leading to substantial difficulties in accurately predicting the LISST response in varying environments. The relatively good agreement between the size distributions from holography and the LISST-100 does, however, indicate that both techniques provide good estimates of the dominant features of a size distribution. The accuracy of the instruments to small-scale features is less reliable due to smoothing and possible aliasing effects in the inversion of scattering from the LISST, and binerisation errors causing particle segmentation in the analysis of holographic images. Care should therefore be taken when interpreting fine-scale features of these size distributions, as the over-analysis of these features may prove misleading.

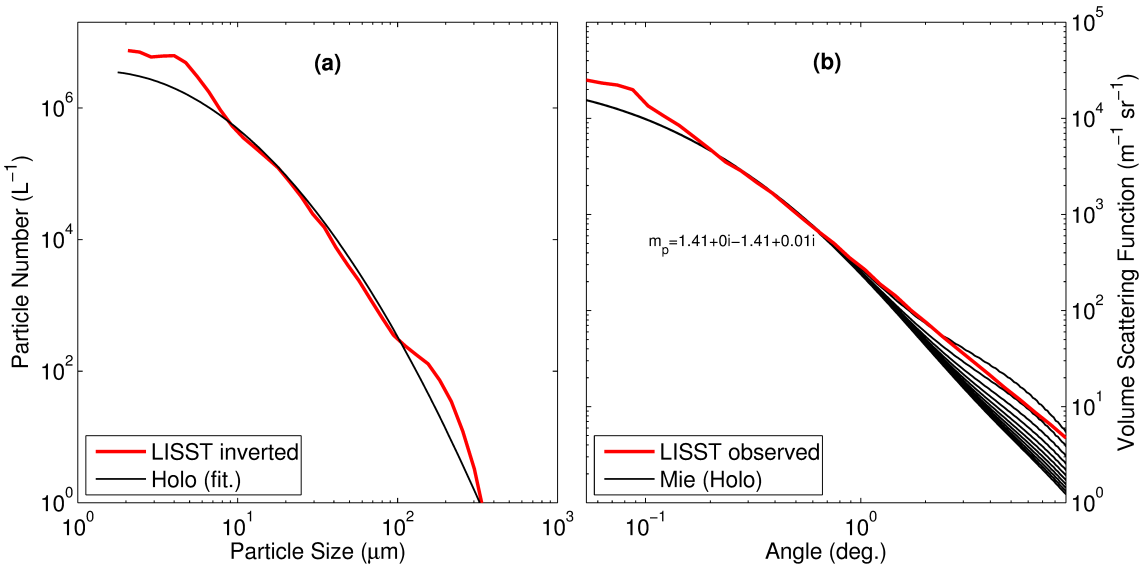

Figure 6.16: Size distributions from the LISST-100 (red) alongside the cubic fit through the magnified holographic images (black) is shown in a. The observed volume scattering function from the LISST (red) and the predicted VSFs from the cubic fit of the holography size distribution, using complex refractive indices ranging from 1.41+0i-1.41+0.01i (black lines), is shown in b.

6.7 Conclusions

- *In-situ* observations of particle size distributions of the equivalent circular diameter from holography and the LISST-100 show relatively good agreement for sizes larger than about 150 μm.

- A divergence in number concentrations between the LISST and holographic camera is observed for particles smaller than 150 μm, with the LISST reporting larger numbers of smaller particles.

- By considering both the area equivalent diameter of the particle and each of the smallest dimensions, by way of the circle packing method, it is possible to start to account for some of the differences between particle sizing through imaging and laser diffraction.

- Predictions of the scattering observed by the LISST-100 become less reliable at angles larger than approximately 2°. This is due to a lack of information on the smallest scatterers and refractive properties of the particles.

- Further information is needed on particle size, shape and composition for sizes less than 15 μm in order to account for scattering at the larger angles of LISST measurements. With imaging information spanning the 2 μm to millimetre scales it may be possible to derive refractive properties of particle populations when combined with measurements of the full volume scattering function and particle composition.

Chapter 7

Conclusions & Future Recommendations

This Chapter summarises the key findings of the work presented in this thesis. It concludes with recommendations for future directions of research that could provide further understanding of particle size measurements and optical properties within the marine environment.

Measurements of particle size in the marine environment are necessary to effectively model and monitor the oceans. Unfortunately the task of obtaining accurate measurements of these particles is complicated by the need for *in-situ* sampling, to avoid disruption of delicate aggregates and planktonic particles. This difficulty is enhanced by the complex properties of suspended particles, which vary greatly in their size, shape and composition through time and space.

The LISST-100 (Laser *in-situ* Scattering and Transmissometer) is now a commonly used instrument for obtaining measurements of suspended particles *in-situ*. It uses the principles of laser diffraction to derive particle concentration measurements in 32, logarithmically increasing size bins, from inversion of their forward-angle scattering. The disadvantages of this inversion is that it relies on the knowledge of the optical scattering properties of the particles in the sample, and as such, is reduced to simple assumptions of these scattering properties. *In-situ* imagery is becoming an increasingly used method. It has the advantage of providing greater information on the type of particles being sampled and only minimal assumptions for retrieval of particle size information. The method does, however, require increased computational demands for data collection and processing compared to that of laser diffraction.

For a detailed understanding of the reliability of the assumptions underpinning the inversion of forward scattering adopted by the LISST-100, it is necessary to understand the scattering properties of marine particles at forward-angles. In this study, this has been achieved through the development of a laboratory system which combines a LISST-100 and holographic camera, to simultaneously record in-focus

particle images and their associated forward scattering from an identical sample volume. This laboratory system was tested and validated against spherical particles, and demonstrated good agreements between the two sizing methods within the size limits of both instruments.

The size range of the LISST-100 measurement capability varies according to the instrument configuration and hence the inversion matrix. The type-b and type-c have upper limits of 270 μm and 500 μm respectively. These upper limits also vary slightly when using the empirically-derived random-shape inversion matrix provided by Sequoia Scientific Inc. When particles exceed the 500 μm limit of the standard inversion for the type-c, an aliasing of a large particle into multiple small ones was observed by the combined holographic camera and LISST-100 system. This results in the possibility for the LISST-100 to report the same median size if exposed to specific particles which exceed the intended size range.

As particle shapes deviate from the spherical assumptions of Mie Theory, their orientation becomes an important factor in determining the scattering properties. This was demonstrated by sampling natural particles with the laboratory system, which settled in fixed orientations during the period of sampling. The scattering from these effectively non-rotating particles then becomes asymmetric within the azimuthal plane. This asymmetry in scattering is problematic for the LISST-100 because the 32 scattering detectors are configured in a way that alternate detectors are offset from each other, covering a 60°azimuthal cross-section. As a result, scattering from non-rotating, or preferentially-orientated, non-spherical particles is recorded as multiple high and low intensities on the LISST-100 detectors. This is illustrated by the diagrams of Figure 7.1.

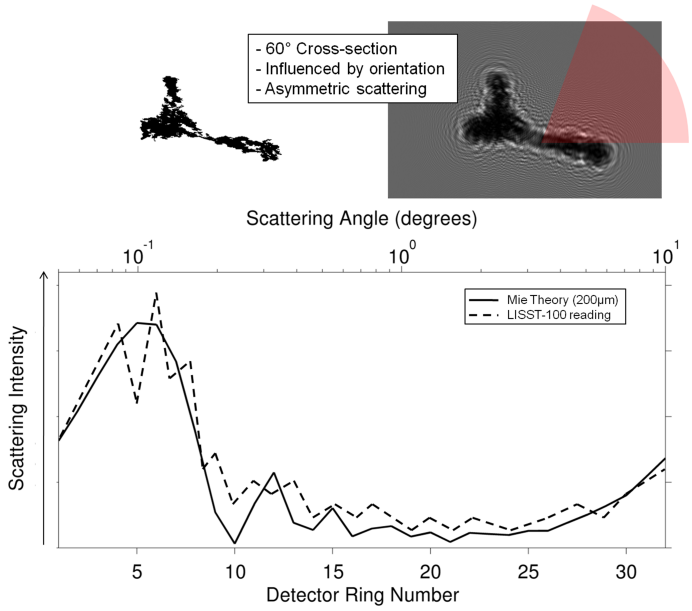

Figure 7.1: Schematic illustration of a non-spherical particle and azimuthally asymmetric scattering that results when in fixed orientations.

Particle orientation produces a different scattering effect in environments where particles are recorded in multiple orientations, such as an *in-situ* marine environment. In this situation, it is apparent that the effects of asymmetrical scattering are averaged over all angles in the azimuthal plane, resulting in a more smooth scattering pattern on the LISST-100 detectors, as illustrated in Figure 7.2. This smooth scattering is equivalent to scattering from a distribution of spheres, leading to a possibility that sub-components of particle structure may contribute to additional scattering recorded by the LISST-100, and account for the increased numbers of smaller particles reported by the LISST in relation to the holographic camera when deployed alongside each other *in-situ*.

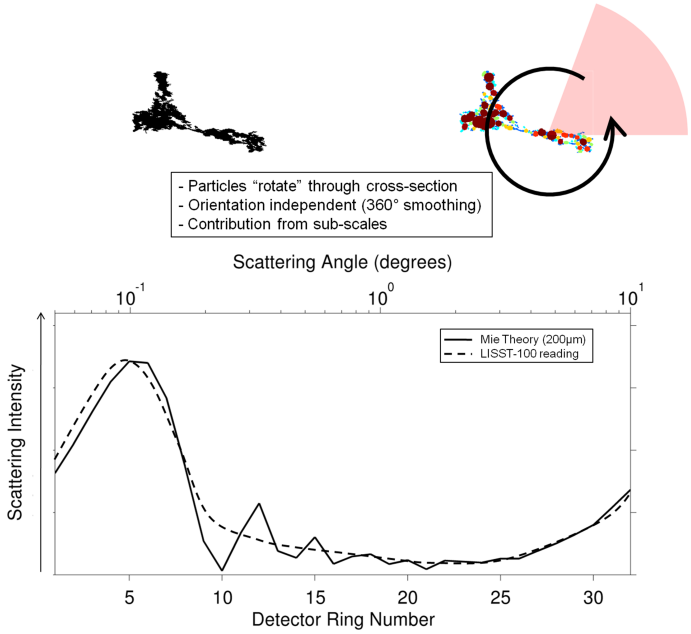

Figure 7.2: Schematic illustration of a non-spherical particle and azimuthally symmetric scattering that results when in multiple orientations, as reported by Agrawal et al. (2008).

Uncertainties remain in the reasons for some of the differences between imaging and laser diffraction. These are likely to be due to particle composition effects on refraction, which influence the larger angles of the LISST-100 detectors and control the small particle sizes which are returned by the inversion. It is therefore necessary to have very detailed information on the homogeneity of the composition of each particle to account for internal refraction. In addition, more accurate information is required from imaging small particles to better model the forward-scattering. To do this effectively it is necessary to retrieve *in-situ* measurements of the full volume scattering function, absorption and three-dimensional particle shape information, alongside particle composition. However, efforts such as this may not be necessary for reliable particle size measurements, which could be improved through better linkages with other sizing techniques, such as acoustics. The combination of optics, imaging and acoustics for obtaining particle size distribution measurements could

be optimised to correct for uncertainties associated with each technique. In each of these possibilities, and for current work which utilise particle size measurements, it is imperative for the definition of particle size to be clearly defined in every circumstance in which it is used. For example, the subtle difference between an equivalent circular diameter and an equivalent spherical diameter, implies that there is a difference in the three-dimensionality of the data used to obtain the measurements, leading to the potential for confusion when comparing the two.

The size measurements from imaging and laser diffraction do agree well, provided that appropriate quality control measures are applied to both instruments. These include, but are not limited to, the removal of contamination by Schlieren and large particles from LISST measurements, and the removal of noise from holographic image processing. Caution should be applied to avoid over-interpreting the results that are derived from either instrument. The simultaneous use of both the LISST-100 and the holographic camera has been shown as a feasible means of obtaining reliable information on concentrations, sizes and shapes of marine particles. Improvements to *in-situ* particle measurements could therefore be quickly and easily implemented through simultaneous deployments of the LISST-HOLO with a LISST-100. It may then be possible to use the LISST-100 as a means of obtaining high resolution size and concentration measurements, while periodically cross-validating with the associated measurements from the LISST-HOLO to provide information on particle shape and potential contamination from large particles. The use of the combination of these technologies, either on a profiling or bed-mounted platform, could greatly enhance the scientific understanding of particle properties across ranging temporal and spatial scale. Although this thesis has highlighted potential anomalies and limitations of the results produced by these two instruments, it has been shown that it is possible to extract valid and valuable data from them, if used correctly, to contribute to better understanding of the marine environment.

References

Aas, E., 1996. Refractive index of phytoplankton derived from its metabolite composition. Journal of Plankton Research 18, 2223–2249.

Agrawal, Y.C., 2005. The optical volume scattering function: Temporal and vertical variability in the water column off the New Jersey coast. Limnology and Oceanography 50, 1787–1794.

Agrawal, Y.C., Mikkelsen, O.A., 2009. Empirical forward scattering phase functions from 0.08 to 16 deg. for randomley shaped terrigenous $1 - 21\,\mu m$ sediment grains. Optics Express 17, 8805–8814.

Agrawal, Y.C., Pottsmith, H.C., 2000. Instruments for particle size and settling velocity observations in sediment transport. Marine Geology 168, 89–114.

Agrawal, Y.C., Whitmire, A., Mikkelsen, O.A., Pottsmith, H.C., 2008. Light Scattering by random shaped particles and consequences on measuring suspended sediments by laser diffraction. Journal of Geophysical Research 113.

Andrews, S., Nover, D., Schladow, S.G., 2010. Using laser diffraction data to obtain accurate particle size distributions: the role of particle composition. Limnology and Oceanography: Methods 8.

Asano, S., Sato, M., 1980. Light scattering by randomly oriented spheroidal particles. Applied Optics 19, 962–974.

Baker, E.T., Lavelle, J.W., 1984. The effect of particle size on the light attenuation coefficient of natural suspensions. Journal of Geophysical Research 89, 8197–8203.

Bale, A.J., 1996. *In situ* laser optical particle sizing. Journal of Sea Research 36, 31–36.

Bale, A.J., Morris, A.W., 1987. *In situ* measurements of particle size in estuarine waters. Estuarine, Coastal and Shelf Science 24, 253–263.

Benson, T., French, J.R., 2007. InSiPID: A new low-cost instrument for *in situ* particle size measurements in estuarine and coastal waters. Journal of Sea Research 58, 167–188.

Berthon, J.F., Lee, M., Shybanov, E., Zibordi, G., 2007a. Measurements of the Volume Scattering Function in a coastal environment. Proceedings of SPIE, the International Society for Optical Engineering 6615, 661506.1–661506.7.

Berthon, J.F., Shybanov, E., Lee, M.E.G., Zibordi, G., 2007b. Measurement and modelling of the volume scattering function in the coastal northern Adriatic Sea. Applied Optics 46, 5189–5203.

Bogucki, D.J., Domaradzki, J.A., Ecke, E.R., Truman, R., 2004. Light scattering on oceanic turbulence. Applied Optics 43, 5662–5668.

Bogucki, D.J., Domaradzki, J.A., Stramski, D., Zaneveld, J.R., 1998. Comparison of near-forward light scattering on oceanic trubulence and particles. Applied Optics 37, 4669–4677.

Bohren, C.F., Clothiaux, E.E., 2006. Fundamentals of Atmospheric Radiation. Wiley-VCH.

Bohren, C.F., Huffman, D.R., 1998. Absorption and Scattering of Light by Small Particles. John Wiley & Sons.

Boss, E., Slade, W.H., Hill, P., 2009. Effect of particle aggregation in quatic environments on the beam attenuation and its utility as a proxy of particulate mass. Optics Express 17, 9408–9420.

Bowers, G.G., Binding, C.E., 2006. The optical properties of mineral suspended particles: A review and synthesis. Estuarine, Coastal and Shelf Science 67, 219–230.

Bunt, J.A.C., Larcombe, P., Jago, C.F., 1999. Quantifying the response of optical backscatter devices and tranmissometers to vartiations in suspended particulated matter. Continental Shelf Research 19, 1199–1220.

Chami, M., McKee, D., Leymarie, E., Khomenko, G., 2006a. Influence of the angular shape of the volume-scattering function and multiple scattering on remote sensing. Applied Optics 45, 9210–9220.

Chami, M., Shybanov, E.B., Khomenko, G., Lee, M.E.G., Martynov, O.V., Korotaev, G.K., 2006b. spectral variation of the volume scattering function measured over the full range of scattering angles in a coastal environment. Applied Optics 45, 3605–3619.

Chiappetta, P., 1980. Multiple scattering approach to light scattering by arbitrarily shaped particles. Journal of Physics A: Mathematical and Theoretical 13, 2101–2108.

Corey, A.T., 1949. The influence of shape on the fall velocity of sand grains. Master's thesis. Colo. A & M College, Fort Collins.

Davies, E.J., Nimmo-Smith, W.A.M., Agrawal, Y.C., Souza, A.J., 2011. Scattering signatures of suspended particles: an integrated system for combining digital holography and laser diffraction. Optics Express 19, 25448–25499.

Dietrich, W.E., 1982. Settling Velocity of Natural Particles. Water Resources Research 18, 1615–1626.

Dyer, K.R., Cornelisse, J., Dearnaley, M.P., Fennessy, M.J., Jones, S.E., Kappenberg, J., McCave, I.N., Pejrup, M., Puls, W., VanLeussen, W., Wolfstein, K., 1996. A comparison of *in situ* techniques for estuarine floc setting velocity measurements. Journal of Sea Research 36, 15–29.

Dyer, K.R., Manning, A.J., 1999. Observation of the size, settling velocity and effective density of flocs, and their fractal dimensions. Journal of Sea Research 41, 87–95.

Eisma, D., 1986. Flocculation and de-floculation of suspended matter in estuaries. Netherlands Journal of Sea Research 20, 183–199.

Eisma, D., Kalf, J., 1996. *In situ* particle (floc) size measurements with the NIOZ *in situ* camera. Journal of Sea Research 36, 49–53.

Fugate, D.C., Friedrichs, C.T., 2003. Controls on suspended aggregate size in partially mixed estuaries. Estuarine, Coastal and Shelf Science 58, 389–404.

Gentien, P., Lunven, M., Lehaitre, M., Duvent, J.L., 1995. *In-situ* depth profiling of particle sizes. Deep-Sea Research I 42, 1297–1312.

Gillespie, J.B., Jennings, S.G., Lindberg, J.D., 1978. Use of an average complex refractive index in atmospheric propagation calculations. Applied Optics 17, 989–991.

Gordon, H.R., Du, T., 2001. light scattering by nonspherical particles: Application to coccoliths detatched from *Emiliania huxleyi*. Limnology and Oceanography 46, 1438–1454.

Graham, G., Nimmo-Smith, W.A.M., 2010. The application of holography to the analysis of size and settling velocity of suspended cohesive sediments. Limnology and Oceanography: Methods 8, 1–15.

Graham, G.W., Davies, E.J., Nimmo-Smith, W.A.M., Bowers, D.G., Braithwaite, K.M., 2012a. Interpreting LISST-100X measurements of particles with complex shape using digital in-line holography. Journal of Geophysical Research 117.

Graham, G.W., Nimmo-Smith, W.A.M., McKee, D., MacDonald, R., Davies, E.J., 2012b. Inconsistencies Between Theoretical Particle Abundance and In-Situ Observations in the Sea. Ocean Optics Meeting, Glasgow.

Hill, P.S., Milligan, T.G., Geyer, W.R., 2000. Controls on effective settling velocity of suspended sediment in the Eel River flood plume. Continental Shelf Research 20, 2095–2111.

Irigoien, X., Castel, J., 1997. Light Limitation and Distribution of Chlorophyll Pigments in a Highly Turbid Estuary: The Grionde (SW France). Estuarine Coastal and Shelf Science 44, 507–517.

Jackson, G.A., Maffione, R., Costello, D.K., Alldrdge, A.L., Bruce, E.L., Dam, H.G., 1997. Particle size spectra between 1μm an 1cm at Monterey Bay determined using multiple instruments. Deep-Sea Research I 44, 1739–1767.

Jonasz, M., 1987. Nonsphericity of suspended marine particles and its influence on light scattering. Limnology and Oceanography 32, 1059–1065.

Jonasz, M., Fournier, G.R., 2007. Light Scattering by Particles in Water. Elsevier.

Karp-Boss, L., Azevedo, L., Boss, E., 2007. LISST-100 measurements of phytoplankton size distribution: evaluation of the effects of cell shape. Limnology and Oceanography: Methods 5, 396–406.

Knowles, S.C., Wells, J.T., 1996. Suspended aggregate analysis using ISAAC, Elbe River, 9-10 June 1993. Journal of Sea Research 36, 69–75.

Kocifaj, M., 2009. A review of the effects of light scattering on the dynamics of irregularly shaped dust grains in the Solar System. Journal of Quantitative Spectroscopy and Radiative Transfer 110.

Kokhanovsky, A.A., Macke, A., 1997. Integral light-scattering and absorption characteristics of large, nonspherical particles. Applied Optics 36, 8785–8790.

Kokhanovsky, A.A., Zege, E.P., 1995. Local optical parameters of spherical polydispersions: simple approximations. Applied Optics 34, 5513–5519.

Konert, M., Vandenberghe, J., 1997. Comparison of laser grain size analysis with pipette and sieve analysis: a solution fo rthe underestimation of the clay fraction. Sedimentology 44, 523–535.

Kranenburg, C., 1994. The Fractal Structure Of Cohesive Sediment Aggregates. Estuarine Coastal and Shelf Science 39, 451–460.

Krone, R.B., 1963. A study of rehologic properties of estuarial sediments. Technical Bulletin No. 7. U.S. Army Engineer Committe on Tidal Hydraulics, Vicksburg.

Latimer, P., 1984. Light scattering by a homogeneous sphere with radial projections. Applied Optics 23, 442–447.

Latimer, P., 1985. Experimental tests of a theoretical method for predicting light scattering by aggregates. Applied Optics 24, 3231–3239.

Latimer, P., Wamble, F., 1982. Light scattering by aggregates of large colloidal particles. Applied Optics 21, 2447–2455.

Law., D.J., Bale, A.J., Jones, S.E., 1997. Adaptation of focused beam reflectance measurement to *in-situ* particle sizing in estuaries and coastal waters. Marine Geology 140, 47–59.

Lee, M.E., Lewis, M.R., 2003. A new method for the Optical Voume Scattering Function in the Upper Ocean. American Meteorological Society 20, 563–571.

Logan, B.E., Alldredge, A.L., 1989. The increased potential for nutrient uptake by flocculating diatoms. Marine and Freshwater Biology 101, 443–450.

Logan, B.E., Wilkinson, D.B., 1990. Fractal geometry of marine snow and other biological aggregates. Limnology and Oceanography 35, 130–136.

Lynch, J.F., Irish, J.D., Sherwood, C.R., Agrawal, Y.C., 1994. Determining suspended sediment particle size information from acoustical and optical backscatter measurements. Continental Shelf Research 14, 1139–1165.

MacDonald, R., 2012. pers. com. School of Ocean Sciences, University of Bangor, Wales.

Maldiney, M.A., Mouchel, J.M., 1996. *In situ* video recording of suspended flocs. Journal of Sea Research 36, 87–91.

Mikkelesen, O., Milligan, T., Hill, P., Chant, R., Jago, C., Jones, S., Krivtsov, V., Mitchelson-Jacob, G., 2008. The influence of schlieren on *in situ* optical measurements used for particle characterisation. Limnology and Oceanography: Methods 6, 133–143.

Mikkelsen, O.A., 2001. The use of a LISST-100 laser particle sizer for in-situ estimates of floc size, density and settling velocity. Geo-Marine Letters 20, 187–195.

Mikkelsen, O.A., Hill, P.S., Milligan, T.G., Chant, R.J., 2005. In situ particle size distributions and volume concentrations from a LISST-100 laser particle sizer and a digital floc camera. Continental Shelf Research 25, 1959–1978.

Milligan, T.G., 1996. In situ particle (floc) size measurements with the benthos 373 plankton silhouette camera. Journal of Sea Research 36, 93–100.

Mishchenko, M.I., 2009. Electromagnetic scattering by nonspherical particles: A turtorial review. Journal of Quantitative Spectroscopy and Radiative Transfer 110.

Mobley, C.D., 1994. Light and Water. Elsevier Science (USA).

Moody, J.A., Butman, B., Bothner, M.H., 1987. Near-bottom suspended matter concentration on the Continental Shelf during storms: estimates based on *in situ* observations of light transmission and a particle size dependant transmissometer calibration. Continental Shelf Research 7, 609–628.

Morel, A., Maritorena, S., 2001. Bio-optical properties of oceanic waters: A reappraisal. Journal of Geophysical Research 106, 7163–7180.

Mugnai, A., Wiscombe, W.J., 1986. Scattering from nonspherical Chebyshev particles. 1: cross sections, single-scattering albedo, asymmetry factor, and backscattered fraction. Applied Optics 25, 1235–1244.

Mugnai, A., Wiscombe, W.J., 1989. Scattering from nonspherical Chebyshev particles. 3: Variability in angular scattering patterns. Applied Optics 28, 3061–3073.

Okada, Y., Kokhanovsky, A.A., 2009. Light scattering and abosorption by densely packed groups of spherical particles. Journal of Quantitative Spectroscopy and Radiative Transfer 110.

Owen, R.B., Zozulya, A.A., 2000. In-line digital holographic sensor for monitoring and characterising marine particles. Optical Engineering 39, 2187–2197.

Perillo, G.M.E. (Ed.), 1995. Geomorphology and Sedimentology of Estuaries. Elsevier.

Petzold, T.J., 1972. Volume scattering functions for selected ocean waters. Contract No. N62269-71-C-0676, UCSC, SIO Ref. , 72–78.

Proctor, R., Holt, J.T., Allen, J.I., Blackford, J., 2003. Nutrient fluxes and budgets for the North West European Shelf from a three-dimensional model. Science of the Total Environment 312, 769–785.

Reynolds, R.A., Stramski, D., Wright, V.M., Wozniak, S.B., 2010. Measurements and characterization of particle size distributions in coastal waters. Journal of Geophysical Research 115.

Richards, S.D., Heathershaw, A.D., Thorne, P.D., 1996. The effect of suspended particulate matter on sound attenuation in seawater. Journal of the Acoustical Society of America 100, 1447–1450.

Schuerman, D.W. (Ed.), 1979. Light Scattering by Irregularly Shaped Particles. Plenum Press, New York and London.

Slade, W.H., Boss, E.S., 2006. Calibrated near-forward volumes scattering function obtained from the LISST particle sizer. Optics Express 14, 3602–3615.

Spinrad, R.W., Ronald, J., Zaneveld, V., Pak, H., 1978. Volume scattering function of suspended matter at near-forward angles: a comparison of experimental and theoretical values. Applied Optics 17, 1125–1130.

Stemmann, L., Gorsky, G., Marty, J.C., Picheral, M., Miquel, J.C., 2002. Four-year study of large-particle vertical distribution (0-1000 m) in the NW Mediterranean in relation to hydrology, phytoplankton, and vertical flux. Deep-Sea Research II 49, 2143–2162.

Stramski, D., Boss, E., Bogucki, D., Voss, K.J., 2004. The role of seawater constituents in light backscattering in the ocean. Progress in Oceanography 61, 27–56.

Syvitski, J.P.M., Hutton, E.W.H., 1996. *In situ* characteristics of suspended particles as determined by the Floc Camera Assembly FCA. Journal of Sea Research 36, 131–142.

Thorne, P.D., Agrawal, Y.C., Cacchione, D.A., 2007. A comparison of Near-Bed Acoustic Backscatter and Laser Diffraction Measurements of Suspended Sediments. IEEE Journal of Oceanic Engineering 32.

Thorne, P.D., Hanes, D.M., 2002. A review of acoustic measurement of small-scale sediment processes. Continental Shelf Research 22, 603–632.

Twardowski, M.S., Boss, E., Macdonald, J.B., Pegau, W.S., Barnard, A.H., Ronald, J., Zaneveld, V., 2001. A model for estimating bulk refractive index from the optical backscattering and the implications for understanding particle composition. Journal of Geophysical Research 106, 14129–14142.

Van-De-Hulst, H.C., 1957. Light Scattering by Small Particles. Dover Publications.

VanLeussen, W., Cornelisse, J.M., 1996. The underwater video system VIS. Journal of Sea Research 36, 77–81.

Velesco, N., Kaiser, T., Schweiger, G., 1997. Computation of the internal field of a large spherical particle by use of the geometrical-optics approximation. Applied Optics 36, 8724–8728.

Wiscombe, W.J., Mugnai, A., 1988. Scattering from nonspherical Chebyshev particles. 2: Means of angular scattering patterns. Applied Optics 27, 2405–2421.

Wriedt, T., 2009. Light scattering theories and computer codes. Journal of Quantitative Spectroscopy and Radiative Transfer 110.

Appendix A

Emlyn J. Davies, W. Alex M. Nimmo-Smith, Yogesh C. Agrawal, and Alejandro J. Souza, (2011), "Scattering signatures of suspended particles: an integrated system for combining digital holography and laser diffraction", Opt. Express 19, 25488-25499. http://www.opticsinfobase.org/oe/abstract.cfm?URI=oe-19-25-25488

The enclosed manuscript is pre-publication, but includes changes made following the reviewer comments. Please refer to the above reference for the published manuscript.

Scattering signatures of suspended particles: An integrated system for combining digital holography and laser diffraction

Davies E. J.,[1*] Nimmo-Smith W. A. M.,[1] Agrawal Y. C.,[2] and Souza A. J.[3]

[1]*Plymouth University, Devon, UK.*
[2]*Sequoia Scientific, Inc., Bellevue Washington, USA.*
[3]*National Oceanography Centre, Liverpool, UK.*
[*]*Corresponding author: emlyn.davies@plymouth.ac.uk*

Abstract: An accurate measurement of suspended particle characteristics is crucial in ensuring the effective monitoring and modelling of the marine environment. The use of laser diffraction is now common practice for the determination of an *in-situ* particle size distribution. This method relies on Mie Theory, or an alternative algorithm, to infer a particle size and concentration from a measure of scattered light. However, these predictions have a number of restrictions, for example, Mie Theory assumes spherical particles of a known refractive index, and tested alternative algorithms do not cover the full range of particle sizes or shapes found within the marine environment. Various imaging techniques have shown that particles vary greatly in their shape and composition. As a result, there is uncertainty in the response of laser diffraction instruments when subjected to this diverse range of complex particles.

Here we present a novel method for testing the response of laser diffraction when measuring suspended particles using laboratory observations from a new integrated system. This integrated system combines both digital in-line holography and a LISST-100 type C, to simultaneously record in-focus images of artificial and natural particles with their small-angle forward scattering signature. The system will allow for further development of a reliable alternative to Mie Theory when using laser diffraction for the *in-situ* measurement of complex suspended particles. A more detailed knowledge of the performance of laser diffraction when subjected to the wide variety of complex particles found in the marine environment will then be possible.

OCIS codes: (010.0010) Atmospheric and oceanic optics; (010.4458) Oceanic scattering; (120.5820) Scattering measurements; (290.2558) Forward scattering; (290.5850) Scattering, particles; (090.1995) Digital holography.

References and Links

1. C. D. Mobley, L. K. Sundman and E. Boss, "Phase function effects on oceanic light fields," Applied Opt. **41,** 1035-1050 (2002).
2. X. Irigoien and J. Castel, "Light limitation and distribution of chlorophyll pigments in a highly turbid estuary. The Grionde (SW France)," Est. Coastal and Shelf Sci. **44,** 507–517 (1997).
3. S. D. Richards, A. D. Heathershaw, and P. D. Thorne, "The effect of suspended particulate matter on sound attenuation in seawater," J. Acoustical Soc. America **100,** 1447–1450 (1996).
4. P. Gentien, M. Lunven, M. Lehaitre, J. L. and Duvent, "In-situ depth profiling of particle sizes," Deep-Sea Res. I **42,** 1297–1312 (1995).
5. G. A. Jackson, R. Maffione, D. K. Costello, A. L. Alldrdge, E. L. Bruce, and H. G. Dam, "Particle size spectra between 1µm an 1cm at Monterey Bay determined using multiple instruments," Deep-Sea Res. I **44,** 1739–1767 (1997).
6. "Geomorphology and Sedimentology of Estuaries," G. M. E. Perillo, ed. (Elsevier, 1995).
7. R. Proctor, J. T. Holt, J. I. Allen, and J. Blackford, "Nutrient fluxes and budgets for the north west European shelf from a three-dimensional model," Sci. of the Total Env. **312,** 769–785 (2003).

8. Y. C. Agrawal, and H. C. Pottsmith, "Instruments for particle size and settling velocity observations in sediment transport," Mar. Geol. **168,** 89–114 (2000).
9. Y. C. Agrawal, A. Whitmire, O. A. Mikkelsen, and H. C. Pottsmith, "Light scattering by random shaped particles and consequences on measuring suspended sediments by laser diffraction," J. of Geophys. Res. **113,** (2008).
10. O. A. Mikkelsen, P. A. Hill, T. G. Milligan, and R. J. Chant, "In situ particle size distributions and volume concentrations from a LISST-100 laser particle sizer and a digital floc camera," Cont. Shelf Res. **25,** 1959–1978 (2005).
11. R. A. Reynolds, D. Stramski, V. M. Wright, and S. B. Wozniak, "Measurements and characterization of particle size distributions in coastal waters," J. of Geophys. Res. **115,** (2010).
12. R. B. Owen, and A. A. Zozulya, "In-line digital holographic sensor for monitoring and characterising marine particles," Opt. Eng. **39,** 2187–2197 (2000).
13. G. W. Graham, and W. A. M. Nimmo Smith, "The application of holography to the analysis of size and settling velocity of suspended cohesive sediments," Limnol. and Oceanog.: Methods, **8,** (2010).

1. Introduction

Characterizing particles suspended in seawater is important for several reasons. Suspended particles affect light penetration through the water column, causing a significant impact on radiative transfer and primary productivity [1, 2]. They can also influence the way in which sound propagates through water, affecting the performance of sonar equipment [3]. Models of sediment transport require information on particle characteristics such as size, effective density and settling velocity. The distribution of pollutants can be predicted using these models because many pollutants attach to the surfaces of particles [4-6]. Understanding the distribution of organic carbon, (which may be in the form of particulate organic carbon) and how it sinks from the atmosphere to the ocean floor, is a key stage in the carbon cycle [7], and therefore has implications on large-scale climate prediction models. For all these cases it is vital to have an accurate measurement of suspended particle size and concentration.

One of the most widely used techniques for measuring the particle size distribution *in-situ* is that of laser diffraction. This technique is adopted by the LISST (Laser *In Situ* Scattering Transmissometer) series of instruments (developed by Sequoia Scientific Inc.). The method for determining a particle size distribution (PSD) in this way relies on inversion algorithms based either on scattering theory or empirical measurement, and is described later in this section. Unfortunately the available inversion algorithms perform at different accuracies, depending on the type of particles under investigation. For a thorough understanding of the response of LISST instruments to the many complex particles found in the marine environment, it is necessary to capture detailed information on both particle size and shape, which may be done using imaging. However, standard imaging techniques encounter problems associated with limited depth-of-field in large sample volumes, and as a result, in-line holography is a preferred method for obtaining in-focus and high resolution particle images, regardless of their position within the sample volume. The method of extracting particle images from digital holography is described later in this section. Here, digital in-line holography is combined with the LISST-100 to allow for both particle images and forward-angle scattering measurement to be recorded simultaneously from within an identical sample volume.

1.1. Principles of laser diffraction & the LISST-100

The LISST-100 uses 32 ring-shaped detectors that measure a VSF (Volume Scattering Function) at logarithmically increasing angle ranges from ~0.05-10° (type C instrument). Agrawal & Pottsmith (2000) describe the way in which a LISST-100 uses the principles of laser diffraction to measure particles [8]. The instrument consists of a collimated laser beam that passes through the sample volume onto a receiving lens and the 32 ring detectors are positioned at the focal plane of the receiving lens. This configuration allows scattering

intensities to be recorded at varying angles, with larger angles being focused onto the outermost rings of the detector (Fig. 1).

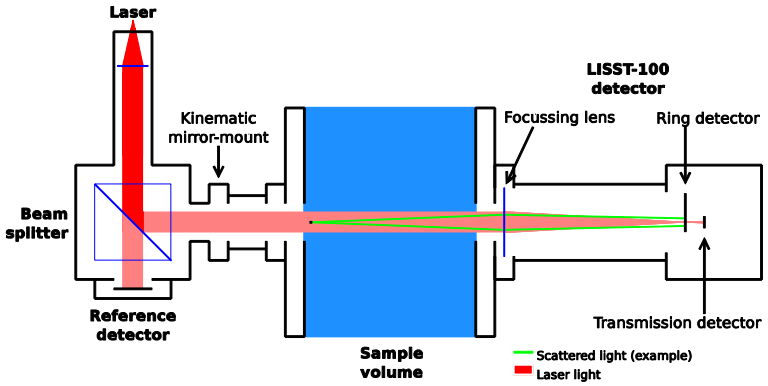

Fig. 1. Schematic illustration of the LISST-100 instrument. A light ray scattered at any angle from the laser beam is focused to a position on the ring detector, allowing for a measure of the angular distribution of scattered light. The focused beam passes through a 75 µm hole at the center of the ring detectors, behind which is a transmission detector for the calculation of beam attenuation.

The angular distribution of light scattered in the forward direction is primarily affected by the size of the particle. Using Mie Theory, it is possible to predict the intensity of light that would be recorded by each of the 32 ring detectors of the LISST-100, by integrating the theoretical VSF over the angle ranges covered by each of the rings. Figure 2 shows how the predicted intensities on each of the 32 detectors change with particle size. As particle size increases, the angle of the principal diffraction lobe (the largest peak in intensity at each size) decreases.

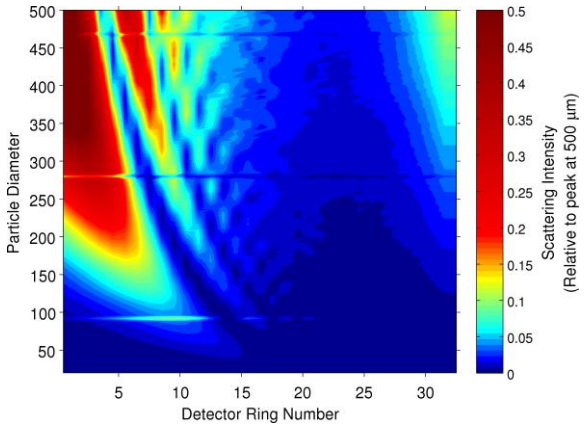

Fig. 2. Predicted scattering intensities from Mie Theory for each of the 32 ring detectors of the LISST-100 type C, for particle diameters of 20-500 µm (size range covered by both the holographic camera and the LISST-100 type C).

Substantial assumptions in the inversion of a VSF to an associated size distribution are that the particles in the sample volume are spherical and of a known refractive index. Agrawal *et al. (2008)* began to address these problems by producing an alternative kernel matrix for the inversion of scattering by random shaped particles, through empirical measurements of sand and ground coffee grains [9]. However, unknown errors remain in the inversion when the LISST-100 is exposed to the wide range of complex particles and flocs that are common in marine environments. A number of studies have compared the performance of the LISST-100

with other particle sizing techniques, for example Mikkelsen *et al.* (2005) [10] and Reynolds *et al.* (2010) [11], both of which report comparable results between the LISST and other techniques. However, in regions in which large flocs were present, problems such as an overestimation of the volume of particles in the largest size bin were highlighted.

1.2 Digital in-line holography

A digital hologram takes the form of an interference pattern recorded by a CCD (Charge-Coupled Device) of a camera. This interference pattern is produced from constructive and destructive interference between coherent background light (laser light) and the scattered light from particles within the sample volume (Fig. 3). The resulting hologram can be numerically reconstructed to produce in-focus images of every particle recorded, eliminating the problems associated with depth-of-field and focussing that occur when using conventional imaging methods. The details of holographic reconstruction are explained by Owen & Zozulya (2000) and Graham & Nimmo Smith (2010) [12, 13].

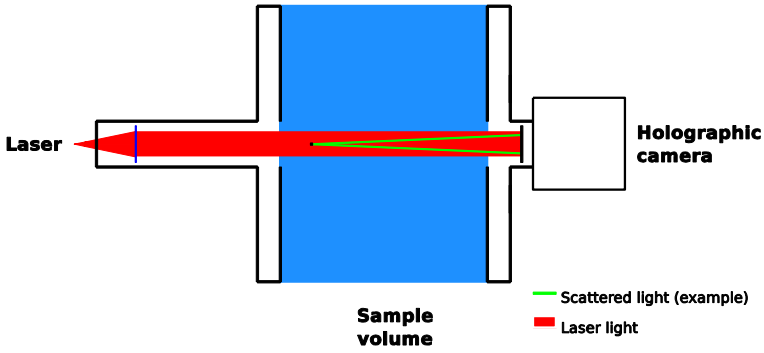

Fig. 3. Schematic illustration of the optical set-up of the holographic camera. A collimated laser beam passes through the sample volume and is recorded by the CCD of the camera, positioned on the far side of the volume. Scattering of light from within the beam interferes with the incident light of the initial beam, creating an interference pattern (hologram) on the holographic camera.

The holographic images shown in Fig. 4(A & B) show a bright centre and dark edges, created from the Gaussian beam. The reason for the chosen beam diameter, and resulting dark areas in the holograms, was to allow the holographic camera to capture the entire sample volume recorded by the LISST-100 when combining both instruments (Section 2). The background image of Fig. 4(B) was subtracted from the raw image (A) in order to remove any stationary objects and reduce noise. An example of the resulting clean image is shown in Fig. 4(C). This is a similar process to the ZScat (background scattering data) which is subtracted from LISST-100 data before analysis. Once a clean holographic image was calculated, the reconstruction procedure explained by Owen & Zozulya (2000) [12] was then implemented, producing a stack of reconstructed images. Following this, each particle within the reconstructed image stack was manually focused and binarised to allow for errors in the automatic focusing and thresholding to be reduced, and for overlapping or poorly resolved particles to be excluded from the analysis. This procedure resulted in a binary image of all in-focus particles in the sample volume. Each particle in the binarised image was then analysed independently to return their geometrical properties, such as equivalent spherical diameter, perimeter and major axis length.

An advantage of digital holography over laser diffraction for sizing particles is the ability to view a projected area for each particle in the sample, a result which is not possible without imaging technology. Unfortunately, the computational storage demands of imaging techniques greatly reduce sampling durations and increase processing times when compared with laser diffraction.

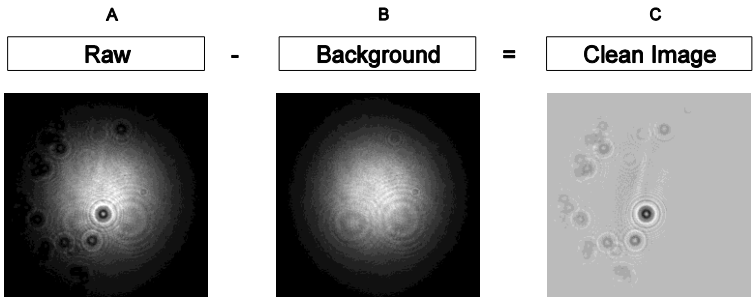

Fig. 4. A: Example of a raw hologram containing Basalt spheres. B: Example of a background image. C: Example of a clean image after background removal.

2. Combined LISST-100 and holographic camera system

The combination of digital holography and a LISST-100 should allow for a greater understanding of how forward scattering signatures are affected by various types of particle. This is because the system simultaneously records in-focus images of particles and their light scattering signature from within the same sample volume. Further development of a reliable alternative to Mie Theory when using laser diffraction for the *in-situ* measurement of complex suspended particles will then be possible.

The new laboratory-based system allows for the forward-angle VSF, recorded by the LISST-100, to be compared with an accurate measurement of particle characteristics, obtained with holographic imagery. The system consists of a purpose-built settling column that allows for a collimated laser beam (658 nm wavelength) to be passed through the sample volume, and for measurements to be taken simultaneously by the LISST-100 ring detectors and a holographic camera. This is achieved using a beam splitter positioned on the far side of the settling column, between the two instruments. A schematic illustration and photograph of the system is shown in Fig. 5 and 6 respectively. The collimated laser beam is passed through a first beam splitter to allow for a reference of laser power to be measured. A kinematic mount is positioned between this beam splitter and the sample volume to allow for precise alignment of the laser to the LISST-100 ring detector. Once light has passed through the settling column it is split again with a larger beam splitter. The purpose of this is to enable the holographic camera to record images of the interference pattern, while simultaneously allowing the LISST-100 focusing lens to receive the same light and record the VSF.

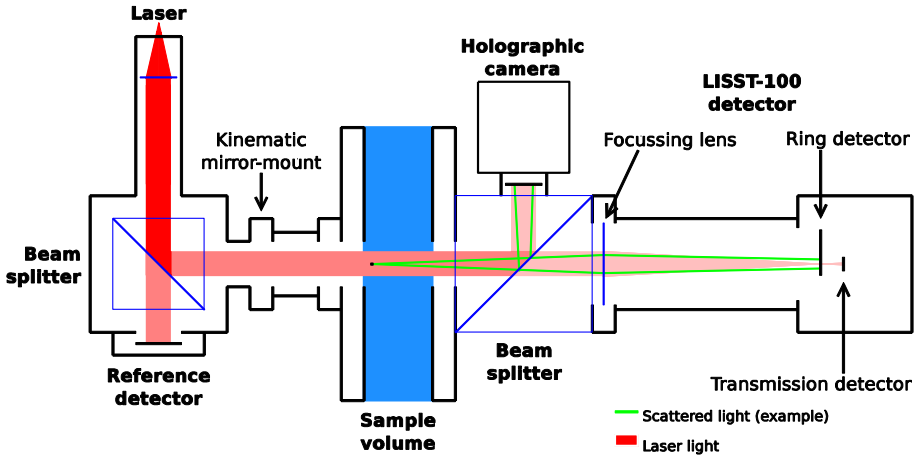

Fig. 5. Schematic illustration of the combined LISST-100 and holographic camera laboratory system.

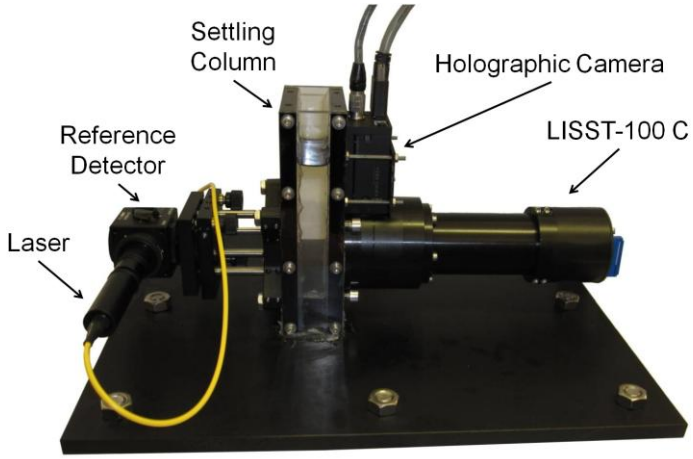

Fig. 6. Photograph of the combined LISST-100 and holographic camera laboratory system.

The use of a 35 mm beam splitter and a sample volume length of 20 mm, allowed for a gap of 3.9 mm between the 10 degree scattering angle and the outer-most edge of the focusing lens of the LISST-100. This gave reassurance that there was no vignetting whilst recording LISST-100 scattering measurements, within the angle ranges covered by the type C instrument. A schematic illustration of the triggering cycle used for the two instruments is shown in Fig. 7. The LISST-100 measurement is an average of the scattering by particles in the laser beam over a period of approximately 100ms. In contrast, the holographic camera takes a near-instantaneous snapshot of the particles in the sample. In order to accurately quantify the particles that are recorded during the period in which the LISST is recording, two holograms are recorded - one at the start of the LISST exposure (i.e. when the laser is turned on), and one at the end of the LISST averaging period (when the measurement is taken). After this period the laser is turned off until the LISST-100 ring detectors reset to zero. This ensures that each cycle obtains data restricted to the period in which that laser was switched on. The resulting sequence allows for a time series to be recorded, during which samples of particles may be introduced into the settling column and passed through the sample volume. Faster sampling is possible, but is limited by the time taken for the LISST rings to reset and the camera speed, which requires a minimum of 67 ms between consecutive holograms. A frame length of 0.2 seconds was used for this work.

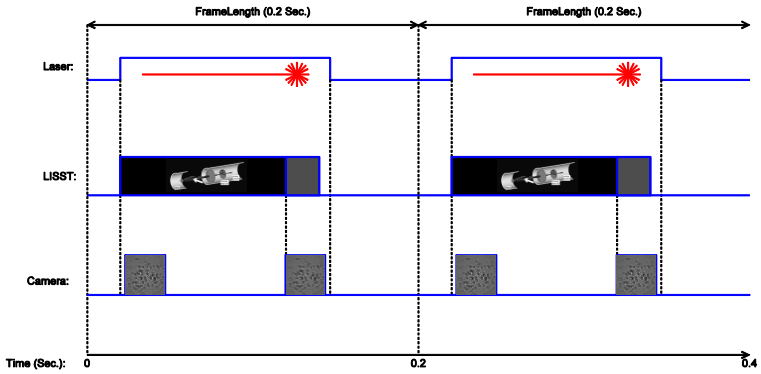

Fig. 7. Schematic illustration of the triggering sequence of the laser, LISST-100 and holographic camera. Two frames are shown in this example, which includes two LISST scans and four holograms.

2.1 Instrument validation

To validate the accuracy of measurements taken using the combined holographic camera and LISST-100, samples of Basalt spheres ranging from 90-500 µm in diameter were used. They were sieved into ¼Φ size ranges to reduce the width of the particle size distribution of each sample that was measured. The first method for validation was a cross-comparison between the adapted LISST-100 (type C) in the combined system, and a standard LISST-100 (type C). Secondly, a comparison between scattering predictions, informed through measurements of particle sizes from the holographic camera, were compared with the LISST-100 scattering.

The optical configuration of the system does not interfere with the principles of measuring the angular scattering of light that are adopted by commonly used LISST-100 instruments described in Section 1.1. However, the wavelength of the laser used for the combined holographic camera and LISST-100 system was 658 nm as opposed to 670 nm adopted by a typical LISST-100. Figure 8 demonstrates that the 12 nm difference in wavelength between the two instruments was near-indistinguishable in both the scattering predicted by Mie Theory and the associated inverted volume distribution.

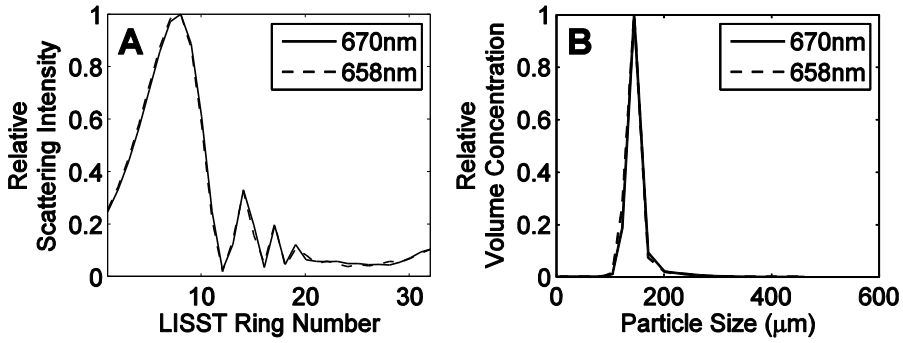

Fig. 8. A: Mie scattering, integrated over the angle ranges of the LISST-100 (type C) rings, at 670 nm (solid line) and 658 nm (dashed line). B: Inverted volume distributions from the scattering show in A. The particle diameter used for these calculations was 137.5 µm.

For reassurance that the LISST-100 scattering from the combined system was representative of a standard LISST-100, tests were carried out using the same samples of Basalt micro-spheres used in subsequent tests. An example of the agreement between the two LISST instruments is shown in Fig. 9(A). Some deviations between the two characteristic scattering functions that were recorded are present, and are as expected from slight changes in the width of the particle size distributions between the two sub-samples used. When comparing median sizes (D_{50}) from the holographic camera with the D_{50} from the inverted LISST-100 scattering, a near 1:1 fit is observed (Fig. 9(B)). It was possible to account for small deviations below the 1:1 line by comparing the observed results with inverted numerical predictions of scattering from Mie Theory, and comparing the size used in the calculation of scattering, with the D_{50} from the inverted size distribution (solid line of Fig. 9(B)). The width of each of the LISST-100 ring detectors and associated size bins resulted in slight oscillations in the predictions of D_{50}, which were amplified in the larger size classes (with larger size ranges). The observations shown in Fig. 9 illustrate the reliability of the combined laboratory system for reproducing both observations of a VSF and inverted particle sizes that are within close agreement with those of a standard LISST-100.

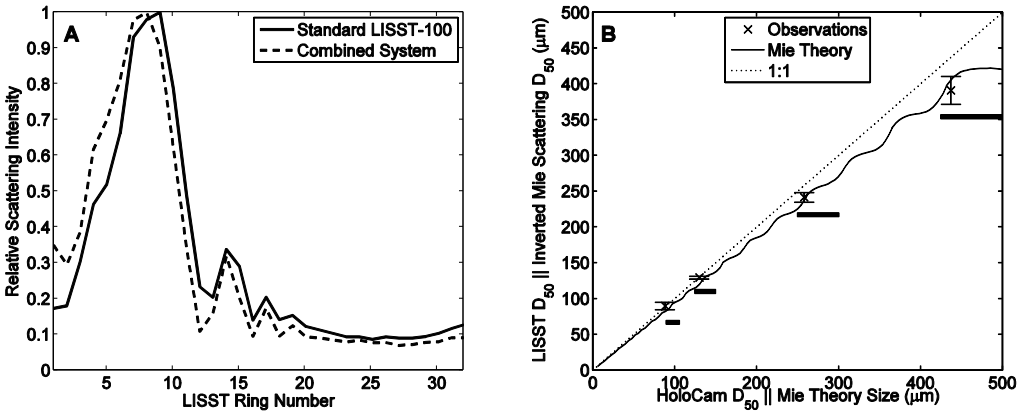

Fig. 9. A: Comparison of scattering from Basalt spheres of 125-150 μm from a standard LISST-100 type C (solid line) measurement and observation from the scattering recorded by the combined system (dashed line). B: Comparisons of calculated D_{50} (median size) values between the holographic camera and inverted LISST-100 scattering from the combined system. Observations are marked by crosses, with error-bars representing ± one standard deviation about the mean. The filled rectangles represent the limits of the sieved ranges for each sample. Numerical predictions from Mie scattering and the associated inverted PSD (calculated every 2 microns) are shown by the solid line.

3. Combined system results

The data used for background removal for both the LISST-100 and holographic camera was taken from the region at the start of each time series, before particles were introduced into the sample volume. For the LISST-100, the ZScat was taken from the frame containing the highest transmission value (i.e. the cleanest frame). The background image used for correction of the holograms was taken as the average of frames that were used to find the ZScat values. This background image was subtracted from each hologram before processing to reduce background noise, as per Fig. 4.

Data from each time series were filtered to leave only the frames that contained enough particles to produce a clear scattering response on the LISST-100 detectors, and few enough particles to allow for reliable reconstruction of holograms. This allowed for a comparison between the VSF measured by the LISST-100 and the PSD measured by the holographic camera. Multiple scattering is likely to contaminate the LISST scattering measurement with transmissions less than 40%. All data analyzed here contained transmissions greater than 80%, and is therefore unlikely to be contaminated with multiple scattering.

To predict the scattering intensities recorded by the LISST-100, it was first necessary to calculate scattering from every particle recorded by the holographic camera using Mie Theory and integrating the Mie scattering intensities across the angle ranges covered by each of the 32 ring detectors of the LISST-100. The predicted scattering intensities of each particle were then scaled relative to the average pixel intensities of the background image from the same location in which the particle was recorded. This is illustrated by Fig. 10, where the intensities of each of the particles in the binary image have been scaled according to the intensity of the background image in the same location. This scaling of scattering intensities accounted for the differences in scattering due to the particle location within the Gaussian beam. For example, particles in the centre of the beam will scatter more intensely than particles towards the edges. This was an important effect to consider due to the near-instantaneous sample time for each hologram – a problem that is removed through averaging during the LISST-100 sampling time. Predicted scattering intensities for each frame are then calculated from the sum of the predicted scattering from each particle, as predicted by Mie Theory. This "predicted scattering function" can then be compared with the recorded scattering from the LISST-100 from the same point in time.

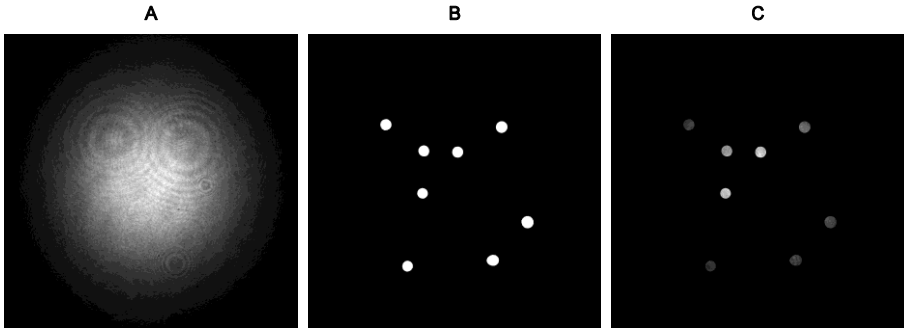

Fig. 10. A: Background image. B: Binary image of Basalt spheres. C: Binary image scaled to the background image to account for the Gaussian beam.

The progression from Fig. 11(A) to 11(D) shows that as particle size increases, the angle of the principal diffraction lobe (PDL) decreases. The relative scattering intensities recorded by the LISST-100 fit closely to intensities of the "predicted scattering function" from Mie Theory, informed by the particle size information from the digital holography. Scattering from the Basalt spheres also shows well-resolved peaks and troughs at angles larger than the PDL – a pattern that is expected from spherical particles. An examination of an electron micrograph of the Basalt spheres (Fig. 12) reveals that some of the particles have variations in their surface roughness, suggesting that many of the deviations between predictions of scattering using Mie Theory and the observed scattering is likely to be due to these slight deviations from perfect spheres. The relative amplitude of the second and third peaks and troughs in the scattering was resolved very well by the predicted scattering function described earlier in this section. A single Mie Theory prediction (integrated over the angles of each of the LISST-100 ring detectors) using only the mean particle size, consistently overestimates the amplitudes of these second and third peaks and troughs in the scattering. This is due to the slight smoothing of the scattering signature caused by the width of the particle size distribution.

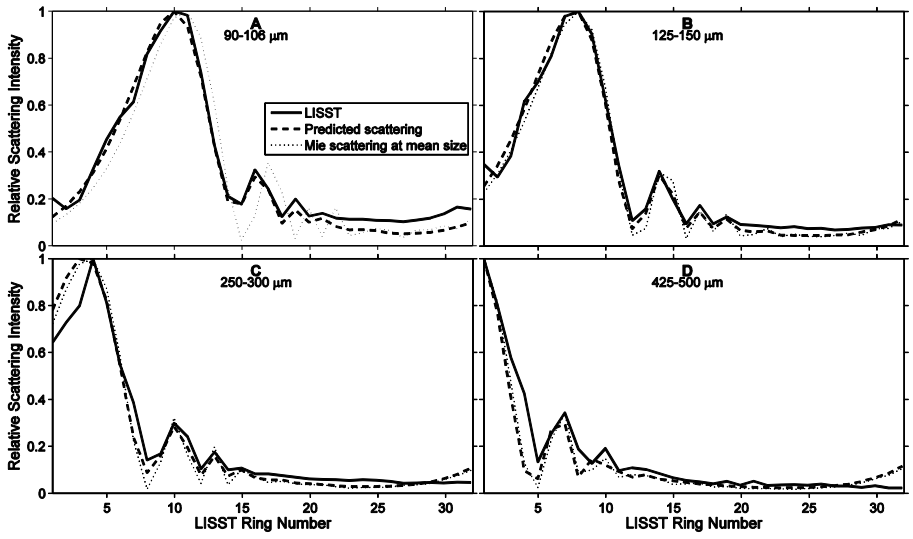

Fig. 11. Comparison of observed scattering function (solid line) from Basalt Spheres, predicted scattering function informed by the holographic camera (dashed line), and Mie theory at the mean particle size recorded by the holographic camera (dotted line). A: 90-106 µm; B: 125-150 µm; C: 250-300 µm; D: 425-500 µm.

The problem of a known particle refractive index is also clear in Fig. 12. The rising tail at larger angles of the scattering function (ring numbers greater than 22), typical of particles with refractive properties such as sand (evident in Fig. 10 of Agrawal *et al*. 2008 [9]), was not resolved with the basalt spheres. This was due to the relatively high refractive index of basalt (1.95 relative to air). Because forward angle scattering is dominated by diffraction, a variable refractive index only affects the shape of the scattering function at larger angles, and therefore the predicted position of the PDL is not affected.

Fig. 12. An example scanning electron microscope image of a Basalt particle used for the data shown in Figure 11. Scale bar is 70 µm.

Finally, the LISST-100 scattering data was inverted into a PSD and compared with the PSD obtained from the holographic camera. This allowed for a comparison between sieving, imaging and laser diffraction, as shown in Fig. 13. The "sharpen" option was used in the Sequoia Scientific Inc. inversion of scattering data because of the narrow ranges in size distributions that were used. The particle volume information from the holographic camera was binned into equivalent size classes to the LISST-100 (type C) for a reliable comparison. For each of the size ranges, the peak in volume distribution obtained from both holography and the inverted LISST-100 scattering is clearly within the sieved ranges. The shapes of the size distributions matched well from the 90-106 µm (A), 125-150 µm (B) and 180-212 µm (C) samples, although a consistent underestimation of particle volumes from the LISST-100 is observed in the coarse tails of the distributions (i.e. sizes greater than the sieved ranges) when compared to that from the holographic camera. This is possibly a result of a slight over-sharpening during the inversion of the LISST-100 scattering. While the peak in volume distribution for the sample of 425-500 µm spheres (D) is correctly placed in the correct size bin of both instruments, there is, however, a substantial increase in the number of smaller particles (< 400 µm) inverted by the LISST-100.

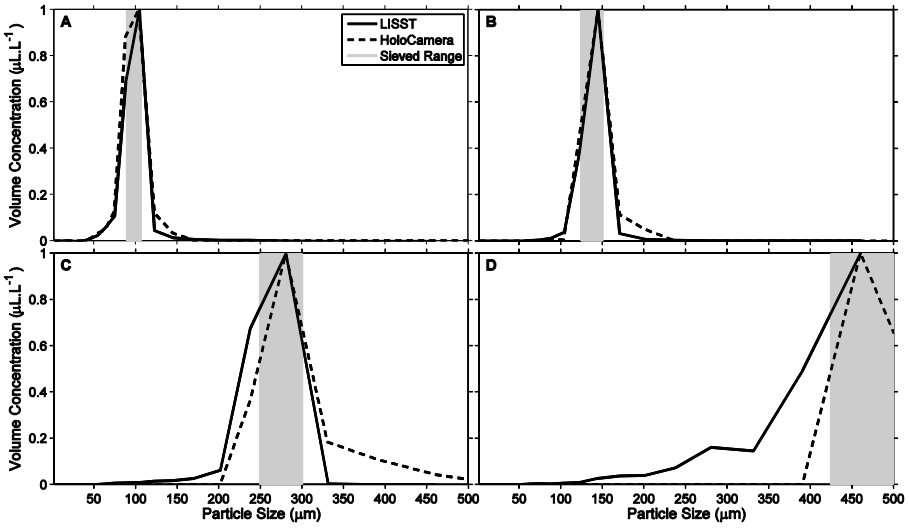

Fig. 13. Volume distributions of Basalt spheres from the inverted LISST-100 scattering data show in Fig. 11 (solid line) and holographic camera (dashed line). The shaded area represents the sieved range of each sample. A: 90-106 µm; B: 125-150 µm; C: 180-212 µm; D: 250-300 µm.

As the focus of this work is in comparing the determination of particle size measurement using a holographic camera and the LISST-100, the distributions in scattering intensities presented are relative to their peak, and are subsequently independent of total particle concentration. With a mono-disperse sample of varying numbers of particles, the intensity of scattered light recorded by the LISST is proportional to the concentration of particles present. This allows the inversion of scattering from the LISST to give an estimate of particle concentration, in addition to particle size. However, the conversion of the inverted size distribution to a true volume concentration requires calibration of the LISST-inverted distribution using a known concentration of particles. The performance of this calibration constant for determining true volume concentrations will be assessed in future publications using the system described here.

4. Summary and conclusions

The new system, comprising of a combination of digital in-line holography and a LISST-100 type C, is able to simultaneously record in-focus images of particles and their small-angle forward scattering signature. This is achieved using an additional beam splitter, positioned on the detector-side of the sample volume. The beam splitter allows for both the LISST-100 and holographic camera to simultaneously receive scattering data from particles within the sample. The combination of the LISST-100 and holographic camera, will allow for an accurate measure of particle geometry to be compared with the forward angle light scattering signature recorded by the LISST-100.

Comparison between scattering recorded by the combined system and that of a standard LISST-100 shows good agreement. It can therefore be assumed that accurate scattering measurements are possible using the adapted LISST-100 set-up described. When results from spherical particles recorded by the system are compared with Mie Theory, a very good agreement is clear between the theoretical predictions of scattering, informed by the holographic camera, and observed scattering from the LISST-100. When ranges of particle sizes are present, the use of Mie Theory at only the mean particle size is not sufficient to accurately resolve the relative amplitudes of the peaks and troughs in scattering. It is therefore

necessary for scattering to be predicted for each particle recorded in the holographic images before an accurate comparison can be made.

The combination of digital holography and a LISST-100 will allow for further development of a reliable alternative to Mie Theory when using laser diffraction for the *in-situ* measurement of more complex suspended particles. This will in turn allow for a greater understanding of the effect of particle shape and composition on the volume scattering function at forward angles. A detailed investigation of scattering from flocs and how they are interpreted by the LISST-100 will now be possible using the combined system described here.

Acknowledgments

E. Davies is funded by the Natural Environment Research Council (NERC grant number NE/H525070/1). Staff at Sequoia Scientific Inc. have provided support with instrument set-up and configuration. We would also like to thank Dr. George Graham and for his valuable feedback on improving the manuscript, and reviewer comments which were extremely helpful and gratefully received.

Appendix B

Emlyn J. Davies, W. Alex M. Nimmo-Smith, Yogesh C. Agrawal, and Alejandro J. Souza, (2012), "LISST-100 response to large particles", Marine Geology, Available online 3 April 2012, ISSN 0025-3227. http://dx.doi.org/10.1016/j.margeo.2012.03.006

The enclosed manuscript is pre-publication, but includes changes made following the reviewer comments. Please refer to the above reference for the published manuscript.

LISST-100 Response To Large Particles

Emlyn J. Davies[a,*], W. Alex M. Nimmo-Smith[a], Yogesh C. Agrawal[b], Alejandro J. Souza[c]

[a] *School of Marine Science and Engineering, Plymouth University, Drake Circus, Plymouth PL4 8AA, UK*
[b] *2700 Richards Road, Suite 107, Bellevue, WA 98005, USA*
[c] *National Oceanography Centre, Liverpool, UK*

Abstract

Particles in the marine environment vary in size from sub-micron colloids to flocculated aggregates of the order of millimetres. The LISST-100 (Laser *in-situ* Scattering and Transmissometer) range of instruments (Sequoia Scientific Inc.) determine the distribution of particle sizes *in-situ* using laser diffraction, but are limited to specific size ranges governed by the instrument configuration. Using numerical predictions of scattering and a novel observational system to combine digital holography and the LISST-100 type-c, here we examine the response of the LISST to particles larger than the intended size range of the instrument. For spheres greater than the type-c instrument limit of 500 μm, both theory and observations indicate that the inversion of the recorded scattering into particle size distributions produces volume distributions that peak at varying sizes between 250-400 μm. This is caused by

*Corresponding author. School of Marine Science and Engineering, Plymouth University, Drake Circus, Plymouth PL4 8AA, UK
Email address: emlyn.davies@plymouth.ac.uk (Emlyn J. Davies)

the principal peaks in scattering moving off the inside of the ring detectors, leading to the remaining peaks being interpreted as the principal peaks. The aliasing of larger particles as a distribution of smaller particles is also applicable to the type-b configuration of the LISST, only occurring at the 250 μm size limit instead of 500 μm. When extending the Junge particle size distribution up to varying maximum sizes, numerical tests predict an increase in volume concentration of up to 4.5 %. For power-law distributions with gradients less than that of a Junge distribution, the contamination from large particles becomes increasingly influential over the concentration and shape of the inverted size distribution.

Keywords: Particle Size Distributions; Laser Diffraction; LISST-100; Volume Concentration; Sediment Transport; Suspended Sediments.

1. Introduction

The commonly used LISST-100 instruments (Sequoia Scientific Inc.) use the principles of laser diffraction to estimate an *in-situ* particle size distribution (PSD) within the marine environment, the measurement of which is crucial to many environmental studies such as radiative transfer, sediment transport and pollution distribution. The LISST uses a custom 32-ring detector to measure the angular distribution of light scattering from particles (Agrawal and Pottsmith, 2000). Each ring detector covers scattering angles of logarithmically increasing ranges from the inner-most ring, covering angles of 0.05-10° for the type-c and 0.1-20° for the type-b. As particle

size increases, the angles of the principal peaks in the scattering function recorded by the LISST reduce and their scattering intensity increases, as illustrated in Figure 1(a). In addition, as the number of particles increases the scattering intensity also increases. Therefore the intensity distribution of the scattered light recorded by the LISST is related to both the size and concentration of particles present. This principle means that the recorded light intensities on each of the 32 rings may be inverted, using an appropriate inversion matrix, to predict the associated size distribution of the particles that produced the scattering. The concentration is then scaled according to a calibrated conversion constant, to bring the inverted size distribution to a 'true' concentration.

Restrictions apply to the inversion from a scattering function to an associated PSD. For example, an inversion matrix based on Mie Theory is restricted to spherical particles of a known refractive index and homogeneous composition, and inversions using the random shape kernel developed by Agrawal et al. (2008) are limited by the size and range of particle shapes measured in the generation of the inversion matrix. These restrictions have prompted studies into the LISST response to both varying types of particle and varying PSDs. Primarily these have been concentrated on the effect of particles smaller than the LISST size limit (e.g. Reynolds et al., 2010), and on the effect of particle shape (e.g. Karp-Boss et al., 2007). However, the LISST is often used for measurements of a PSD in estuarine and coastal waters where large flocs and biological particles are present.

These particles have been measured using imaging techniques at sizes ranging up to the order of millimetres in diameter (Eisma, 1986; Milligan, 1996; Graham and Nimmo-Smith, 2010). As the upper size limit of the LISST type-c is 500 μm, there is potential for these flocs to reach sizes outside the instrument range. Reynolds et al. (2010) reported an increased response in the smallest size bins of the LISST due to particles below the lowest limit of the instrument size range. This was in line with previous thoughts that particles outside the instrument range (either smaller than or larger than) would be contained within the outermost size bins (Agrawal and Pottsmith, 2000). Mikkelsen et al. (2005) reported that particles greater than 500 μm resulted in the LISST overestimating the volume of particles in the largest size bin. However, no studies have systematically examined the effect of these large particles on the entire LISST size distribution using both observations and numerical predictions. In an attempt to understand how scattering from these flocculated particles is interpreted by the LISST, we have first investigated the response of the instrument to spheres of diameters from 2-2000 μm, to cover the full size-range of sizes reported from *in-situ* imagery.

2. Methodology

Both numerical predictions from Mie Theory and observations from a novel system that combines digital holography and the LISST type-c were used. The observational system is described by Davies et al. (2011) and has been fully tested and validated against standard LISST instruments us-

ing spherical particles within the type-c size range. It uses a beam splitter on the detector-side of a settling column to allow scattered light from particles to be recorded simultaneously in the form of an angular intensity distribution (LISST type-c), and in the form of a digital hologram, as per Graham and Nimmo-Smith (2010). The holographic images were recorded twice per LISST measurement and manually focussed and binarised to enable high-precision particle size measurements. The background scattering for the LISST and background image for the holographic camera were taken from filtered water at the start of each sample collection run, and samples of particles were introduced to filtered water to allow for a clean background. Each sample was analysed independently, using the mean scattering from the LISST and associated particle statistics from the holographic camera. To remove uncertainties due to non-sphericity, sieved samples of basalt spheres were introduced into the combined LISST and holographic camera system. The use of basalt, as opposed to other materials such as glass, was due to difficulties in focussing images of perfect spheres with high transparency when using the holographic camera.

Numerical predictions of scattering functions from particles of single sizes were calculated using Mie Theory, and the result integrated over the angle ranges covered by each ring of the LISST type-c detectors. This gives a prediction of light intensities on each of the LISST ring detectors that matches that of spheres, as demonstrated by Agrawal et al. (2008) and Davies et al. (2011). These predictions of scattering were calculated for particle diame-

ters at the mid-points of each bin of the LISST type-c detector, as well as from 2-1000 μm in steps of 4 μm, and from 1000-2000 μm in steps of 20 μm. For each size, a refractive index of 1.95, 1.55 and 1.45 (relative to air) was used. The use of a high refractive index of 1.95 was to suit that of the basalt spheres used for observations of scattering; 1.55 was chosen to represent mineral grains; and 1.45 as an estimate of samples containing a mix of phytoplankton and mineral grains (Aas, 1996). All predictions of scattering intensities were normalised by the peak intensity at 500 μm. Both predictions and observations of scattering were inverted into a LISST (type-c) derived PSD, using the standard Mie-based inversion provided by Sequoia Scientific Inc. (Agrawal and Pottsmith, 2000). To demonstrate the applicability to the LISST type-b, the predictions of scattering were integrated over the angle ranges covered by each of the type-b detectors using a refractive index of 1.55.

3. Results & Discussion

3.1. Scattering Predictions

Results from predictions of scattering from spheres are shown in Figure 1(b-d). It is clear that as particle size increases the total intensity of scattered light increases, and the angular position (and hence ring number) of the dominant peak in scattering decreases until reaching the inner-most ring at about 500 μm. For particle sizes greater than this the principal peak moves off the inside of the inner ring detectors. This results in the secondary

peak becoming dominant and due to increasing size, becoming progressively intense. This effect is repeated again at 1400 μm, where the secondary peak moves off the detectors, leaving the third peak in scattering to be dominant on the rings. The change in refractive index across the three plots shows that the principal peak is largely unaffected by refraction. This is because the primary scattering peaks in the forward direction are dominated by diffraction, and are therefore controlled primarily by particle size. Despite this, there is a clear increase in scattering intensities on the outer rings, caused by the lower refractive index of 1.45.

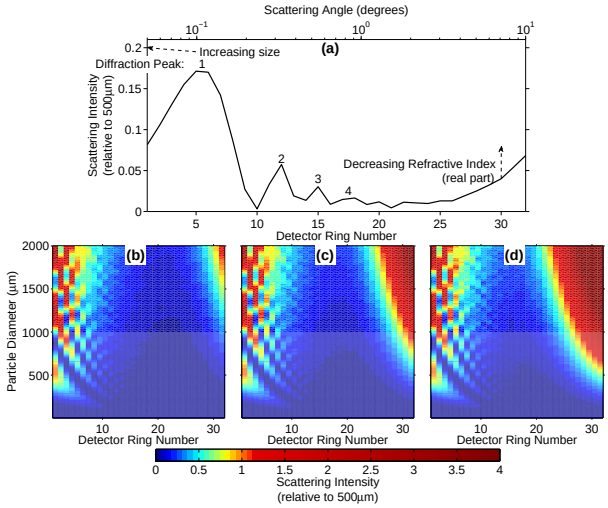

Figure 1: Schematic demonstration of Mie scattering from a 200 μm sphere as recorded by the LISST type-c (a). Mie predictions of scattering intensities on each ring of the LISST for diameters of 2-2000 μm, using a refractive index of (b) 1.95, (c) 1.55 and (d) 1.45.

3.2. Consequences For Particle Size Measurement

The inversions of predicted scattering functions (Figure 1(b-d)), applied across the entire 2-2000 μm range, are shown in Figure 2(a-b). Both volume

and number distributions are shown to illustrate the different emphasis that the each one places on the PSD. The identical number of particles used in the calculation of predicted scattering for each size results in an increase in volume for larger particles. The volume distributions of Figure 2(a) therefore show less emphasis on smaller particles than that of the number distributions (b). Within the LISST type-c size range, a good 1:1 fit is demonstrated between the sizes used in Mie predictions and the associated inverted size distributions. For particles larger than that allowed for in the LISST type-c inversion matrix, the inverted PSD is populated across multiple size classes.

Figure 2(c-d) show three examples of the predicted scattering and inverted volume distributions. The scattering from the 300 μm diameter particle was inverted into a wider distribution than that of the 150 μm particle. This is due to the angular range of the ring detectors and their associated size bins, which become increasingly wide for increasing size classes. The positions of the inner-most diffraction peaks have the most influence on the size of the inverted volume distribution. The 300 μm and 800 μm particles are therefore inverted into distributions that peak at similar sizes. The high scattering intensity of the 800 μm particle results in the secondary peak (ring 4) being similar to the intensity of the principal peak from a 500 μm particle. This results in the inverted distribution having a greater total volume concentration than that of the 300 μm particle.

Figure 2(e-f) show observed scattering and inverted volume distributions from a 250-300 μm sample of basalt spheres, compared with an 800-1000 μm

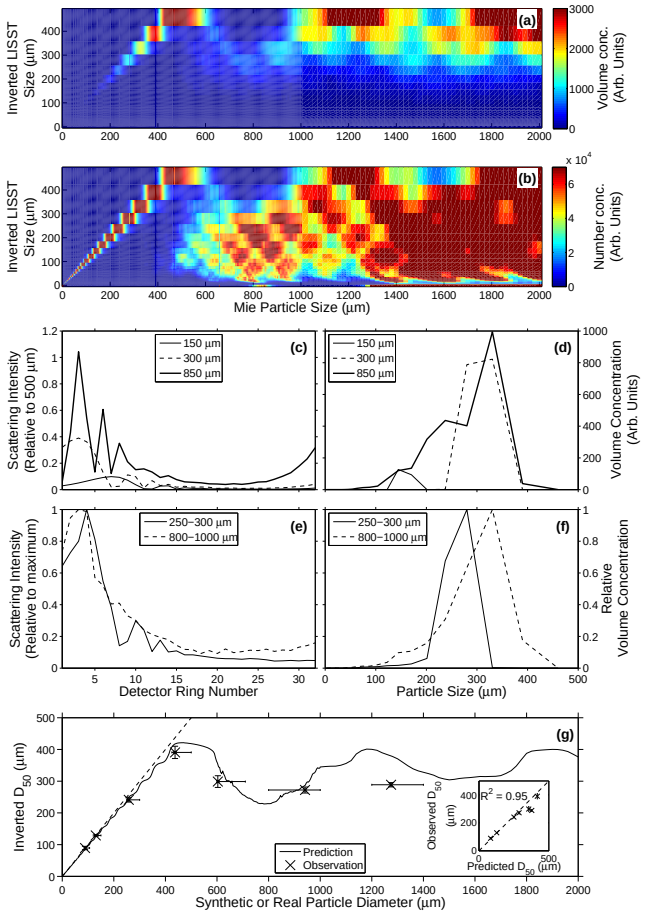

Figure 2: Inverted volume and number distributions from the scattering predictions of Figure 1(b) are shown in plots a and b respectively. Examples of predicted scattering (c) and inverted size distribution (d) are shown for 150 μm (thin line), 300 μm (dashed line), and 850 μm (thick line) particles. Examples of observed scattering (e) and inverted volume distributions (f) are shown for samples of basalt spheres of 250-300 μm (solid line) and 800-1000 μm (dashed line). A comparison of the D_{50} interpreted by the LISST type-c and the size of the scatterers is shown in g. Crosses mark the observed values from the holographic camera (x-axis) and the D_{50} from the inverted LISST scattering (y-axis). Horizontal error bars illustrate the sieved range of each sample. Vertical error bars are ± 1 standard deviation of the D_{50} measurements from the LISST. The inverted D_{50} values from observations and predictions are compared in the inserted plot, with the R^2 value from Pearson's Correlation at 0.95.

sample. The prominent second and third peaks and troughs in the scattering function of the 250-300 μm sample are as expected from distributions of spheres with a narrow size distribution. However, in distributions with a wider range of sizes, these peaks and troughs become smoothed, leaving a scattering function that has only one primary peak - a shape which appears similar to the observed scattering from the 800-1000 μm sample. The smoother shape of the recorded scattering from the 800-1000 μm sample is therefore inverted into a broader distribution of particle sizes than the 200-300 μm sample.

The D_{50} (median size) from the inverted LISST distribution was compared with the particle sizes used for the calculation of scattering. This comparison was performed across the 2-2000 μm size range, and compared with the observations of scattering from basalt spheres (Figure 2(g)). Observations compliment the numerical prediction of a good 1:1 fit within the size range covered by the instrument. At 425 μm, the D_{50} of the LISST plateaus, before reducing again as particle size increases. The reduction in inverted D_{50} reaches a trough at 750 μm, where the reported median size from the LISST is 230 μm. This is caused by the primary peak in the scattering pattern moving off the inside of the inner-most ring of the detector, leaving the second peak in the scattering to be interpreted as the first during the inversion process, as shown in Figure 2(a-f).

The observations of scattering from samples above the LISST type-c range match closely with the predictions from Mie Theory, with the exception of

the largest size sampled (1200-1400 μm). This deviation from the numerical prediction is likely to be due to the increased sensitivity of the LISST ring detectors to the alignment of the laser to the detectors. Accurate observations of scattering were therefore extremely difficult for particles so far outside the intended range of the instrument, and as a consequence, no observations were made for spheres larger than those contained within the 1200-1400 μm sample. The holographic images, on the other hand, remained largely unaffected by the increase in particle size, and an accurate measurement was possible, showing a good match with the sieved ranges for each sample. This highlights the importance of an appropriate measurement technique based on the nature of the particle population under investigation.

The high correlation coefficient ($R^2 = 0.95$) from the predicted and observed D_{50} values over a wide range of particle sizes, gives reassurance that the numerical predictions were an accurate representation (insert of Figure 2(g)). The second oscillation in D_{50} from the numerical predictions between 1200 and 1900 μm does not return such a large trough when compared to the second reduction in median size between 700 and 900 μm. This is due to the primary diffraction peak being much larger in amplitude than the subsequent peaks and troughs. It would be expected for the oscillations to continue to reduce in amplitude as size increases beyond 2000 μm due to a reduction in amplitude of adjacent peaks and troughs at angles larger than the primary diffraction peaks.

The contamination of the LISST size distribution due to the effects of

particles larger than the intended size range is applicable to both the type-c and type-b instruments. This is because both detector configurations and inversion matrices rely on the primary diffraction peak of the scattering function falling within the angle range covered by the detectors. Predictions show that the same misinterpretation of the second and third scattering peaks is apparent on the LISST type-b, only occurring at the 250 μm size limit as opposed to 500 μm.

3.3. Refractive Index Effects

It is shown in van de Hulst (1957) (page 71) that at small angles, Mie Theory is dominated by diffraction, while at large angles, it transitions to geometrical optics, causing refractive effects to be more apparent. As particle size increases, this transition from diffraction to geometrical optics occurs at increasingly smaller angles. As a result, the effects of refraction become increasingly important as size increases, because diffraction dominates a reducing angle range over which the LISST scattering is recorded. The rising tail at angles greater than these primary peaks typically becomes brighter and covers a larger proportion of the LISST angle range as size increases. Figure 3(a) shows three examples of predicted scattering from Mie Theory for spheres of identical size but different refractive index. When using a refractive index of 1.55, spheres above 800 μm produce scattering with a rising tail that is brighter than the primary diffraction lobes at smaller angles, and is apparent across a wider range of angles (rings 22-32) than the rising

tail from the same size particle with a refractive index of 1.95. Figure 3(b) shows that this is interpreted as many small particles by the LISST when the inversion is applied - a problem which would be highlighted if using a number distribution. A sharp increase in apparent volume concentration in the smallest 5 size classes is initiated as soon as particle size exceeds the LISST range. The results from a refractive index of 1.45 show an increase in reported volume concentration in the smallest 5 size classes that is apparent over all sizes above $100\,\mu m$. This is of concern if using the LISST in environments where large flocculated particles are present, as their complex composition and low effective density (Graham and Nimmo-Smith, 2010) leads to an unpredictable refractive index. This would cause the rising tail at large angles of the scattering function to play a greater role in the inverted size distribution, resulting in greater uncertainty in the volume and number concentration of small particles returned by the inversion.

3.4. Application To Particle Size Distributions

The importance of the spurious results from large spheres reported so far is dependent on the shape of the size distribution in question. For example, a Junge-like power-law distribution (where $n(D) \propto D^m$ when n is the number of particles of diameter D, and $m = -4$ (Morel and Maritorena, 2001)) would result in very few large particles, and a dominance in small sizes, leaving a reduced likelihood of contamination by large scatterers. However, as the exponent m increases towards zero, the chance of contamination by large

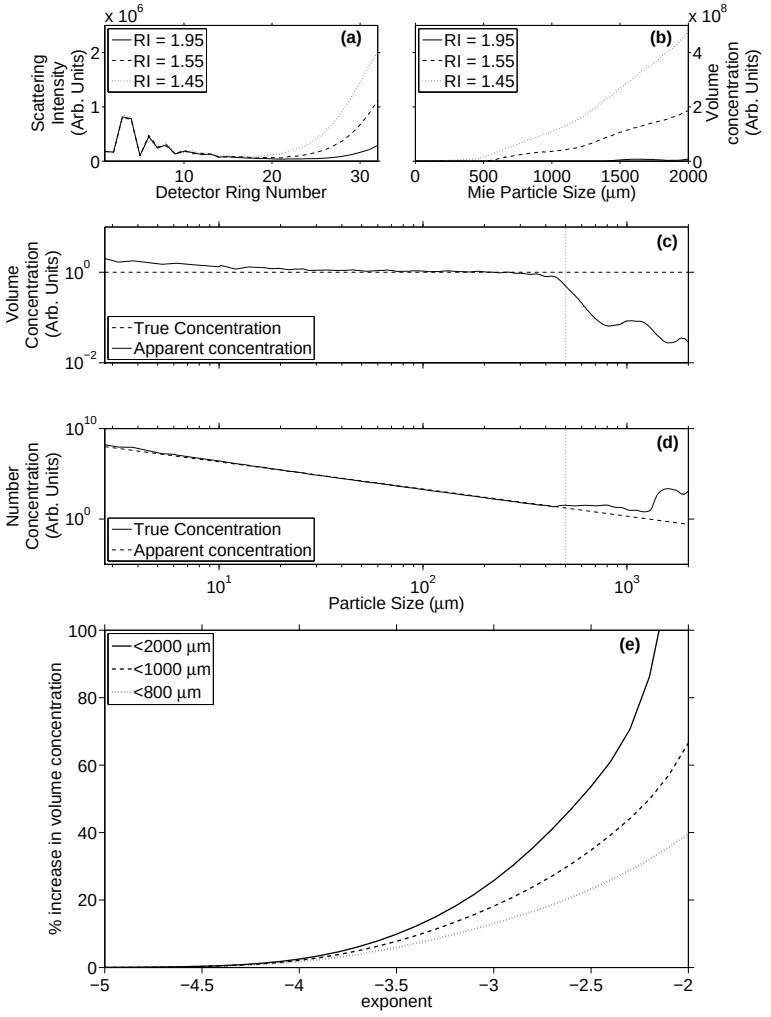

Figure 3: (a): Scattering functions from $800\,\mu m$ spheres with a refractive index of 1.95 (solid line), 1.55 (dashed line) and 1.45 (dotted line). (b): Total volume concentration from the smallest 5 size classes ($< 6\,\mu m$) inverted from Mie scattering of $2 - 2000\,\mu m$ spheres using a refractive index of 1.95 (solid line), 1.55 (dashed line) and 1.45 (dotted line). (c): LISST volume concentration response (solid line) to particle sizes ranging from 2-2000 μm with equal volume concentration (dotted line) and a refractive index of 1.95. The associated number concentrations are shown in d. Percentage increase in total volume concentration due to particles larger than this LISST size range with varying m exponents of the power-law distribution is shown by e. The solid line shows the percentage increase when the size distribution is extended up to $2000\,\mu m$, the dashed line up to $1000\,\mu m$, and the dotted line up to $800\,\mu m$. The refractive index used for scattering calculations was 1.55.

particles increases. Using the same numerical predictions validated in Figure 2(g), tests of different power-law size distributions were conducted to establish the impact of contamination from large scatterers. The use of power-law distributions is to represent a simple size distribution, similar to that which would be expected from a typical *in-situ* LISST-derived PSD. These tests were not able to be performed using *in-situ* samples due to uncertainties in refractive index and particle shape effects on the inversion. For simplicity, these numerical simulations are therefore an illustration of a 'best-case' scenario if all particles match the conditions of Mie Theory.

We start with a constant volume of particles across all sizes, represented by the dashed lines in Figure 3(c-d), and demonstrate the apparent volume and number concentrations inverted by the LISST type-c, represented by the solid lines. The response of the LISST to particles within the operating range produces volume and number concentrations that match closely to those which would be expected with a constant volume concentration. Above the $500\,\mu m$ limit of the size range, the apparent volume concentration inverted by the LISST reduces and the number concentration increases relative to the number of particles input. This decrease in total volume of particles above the LISST size range is encouraging because the impact of large particles on the measurement of total volume concentration subsequently appears small. However, the increase in the inverted total number concentration from that of the amount input, demonstrates that the aliasing of large particles results in an increase in the number of small particles with less volume. The loss in

total volume concentration outside the LISST size range is therefore due to both the loss of the primary peak in scattering (due to its position off the ring detectors), and also the gain in volume of smaller particles, produced from the inversion of the remaining scattering at larger-angles. The two peaks in volume concentration above 500 μm therefore correspond to the decreases in D_{50} shown in Figure 2(g).

The demonstration that particles larger than the LISST size range have the potential to cause substantial contamination across multiple size classes, in addition to the largest size class is an important issue to consider when interpreting inverted size distributions. The percentage increase in volume concentration across all size bins due to the influence of particles larger than the LISST size range was therefore calculated for m exponents ranging from -5 to -2, typical of the range observed in-situ (Twardowski et al., 2001). This effect is demonstrated in Figure 3(e) for size distribution limits of up to 2000 μm, 1000 μm and 800 μm. All three size distribution limits show increasing percentage differences as the m exponent increases towards zero. With the typical Junge distribution, where $m = -4$, the percentage increase in total volume concentration was 3.1% and 4.5% for distributions limited to 800 μm and 2000 μm respectively. The increases in concentrations are substantially greater for PSDs with slopes greater than -4. For example, a slope of -3 resulted in an increase in volume concentration of 26% for particles of up to 2000 μm. This is of concern as the contamination across the wide range of LISST size classes would result in a subsequent change in

gradient of the LISST-derived PSD, as well as an increase in concentration. It is interesting when comparing the LISST-derived PSDs with PSDs obtained from imaging, that there is an offset at larger sizes (Mikkelsen et al., 2005), which corresponds well to that which would be expected from the percentage increases from contamination due to large particles shown by Figure 3(e). The LISST-derived PSDs should therefore be treated with caution when the concentration of particles greater than the operating range of the instrument is unknown.

4. Conclusions

The LISST-100 performs the inversion of a volume scattering function into a particle size distribution very well for spherical particles within the size range allowed for by the inversion matrix. For spheres greater than the instrument range of 500 μm (for the type-c instrument), the inversion produces particle volume distributions that peak at varying sizes between 250-400 μm. This is due to the principal peak in the scattering function, moving off the inside of the LISST ring detector, resulting in the remaining peaks and troughs being interpreted as the principal peak. This effect would also be apparent in the type-b configuration of the LISST-100, only occurring at the 250 μm size limit instead of the 500 μm limit of the type-c instrument.

Refractive index becomes increasingly important as particle size increases due to its dominance in the scattering function at angles larger than the principal diffraction peak. The consequences of refraction from particles greater

than 600 μm can result in sharp increases in inverted volume concentrations within the smaller size bins. This sharp increase in apparent small particles may appear to be emphasised when displaying a number concentration as opposed to a volume concentration.

The likelihood of contamination due to large particles in *in-situ* measurements is dependant on their concentration. When extending a power-law particle size distribution with a slope of -4 up to varying particle sizes, numerical tests predicted an increase in volume concentration across multiple size classes. For gradients in the particle size distribution greater than this (i.e. more larger particles), the total volume concentration becomes increasing contaminated through aliasing of large particles.

Care must be take when interpreting particle size distributions from the LISST-100 when there is potential for particles outside of its range limit, and users should be aware of the emphasis that volume and number concentrations place on the PSD. In situations where large particle may be present, imaging techniques may be a preferred method for the determination of a PSD.

5. Acknowledgements

E. Davies is funded by NERC grant number NE/H525070/1. The authors would like to thank George Graham, Wayne Slade and Jaimie Cross for their help in improving this manuscript. Two reviewers provided helpful comments which were gratefully recieved and incorporated in the revised text.

316 Aas, E. (1996), Refractive index of phytoplankton derived from its metabolite
317 composition, *Journal of Plankton Research,* 12 (18), 2223-2249.

318 Agrawal, Y. C., and Pottsmith, H. C. (2000), Instruments for particle size
319 and settling velocity observations in sediment transport, *Marine Geology,*
320 (168), 89-114.

321 Agrawal, Y., Whitmire, A., Mikkelsen, O., Pottsmith, H. (2008), Light scat-
322 tering by random shaped particles and consequences on measuring sus-
323 pended sediments by laser diffraction. *Journal of Geophysical Research,*
324 C4 (113), C04023.

325 Davies, E. J., Nimmo-Smith, W. A. M., Agrawal, Y. C., Souza, A. J. (2011),
326 Scattering signatures of suspended particles: an integrated system for com-
327 bining digital holography and laser diffraction, *Optics Express,* (19), 25488-
328 25499.

329 Eisma, D. (1986), Flocculation and de-floculation of suspended matter in
330 estuaries, *Netherlands Journal of Sea Research,* (20), 183-199.

331 Graham, G., and Nimmo-Smith, W. A. M. (2010), The application of holog-
332 raphy to the analysis of size and settling velocity of suspended cohesive
333 sediments, *Limnology and Oceanography: Methods,* (8), 1-15.

334 Karp-Boss, L., Azevedo, L., and Boss, E. (2007), LISST-100 measurements
335 of phytoplankton size distribution: evaluation of the effects of cell shape,
336 *Limnology and Oceanography: Methods,* (5), 396406.

337 Mikkelsen, O. A., Hill, P. A., Milligan, T. G., and Chant, R. J. (2005), In
338 situ particle size distributions and volume concentrations from a LISST-
339 100 laser particle sizer and a digital floc camera, *Continental Shelf Research*
340 (25), 1959-1978.

341 Milligan, T. G. (1996), In situ particle (floc) size measurements with the
342 benthos 373 plankton silhouette camera, *Journal of Sea Research,* 1 (36),
343 93-100.

344 Morel, A., and Maritorena, S. (2001), Bio-optical properties of oceanic wa-
345 ters: A reappraisal , *Journal of Geophysical Research* C4 (106), 7163-7180.

346 Reynolds, R. A., Stramski, D., Wright, V. M., and Wozniak, S. B. (2010),
347 Measurements and characterization of particle size distributions in coastal
348 waters, *Journal of Geophysical Research*, C8 (115), C08024.

349 Twardowski, M. S., Boss, E., Macdonald, J. B., Pegau, W. S., Barnard,
350 A. H., Ronald, J., and Zaneveld, V. (2001), A model for estimating bulk
351 refractive index from the optical backscattering and the implications for
352 understanding particle composition, *Journal of Geophysical Research* C7
353 (106), 14129-14142.

354 van de Hulst, H. C. (1957), *Light scattering by small particles*, Dover, New
355 York

Appendix C

George W. Graham, **Emlyn J. Davies**, W. Alex M. Nimmo-Smith, David G. Bowers, and Katherine M. Braithwaite, (2012), "Interpreting LISST-100X measurements of particles with complex shape using Digital In-line Holography", Journal of Geophysical Research - Oceans. http://dx.doi.org/10.1029/2011JC007613

The enclosed manuscript is pre-publication, but includes changes made following the reviewer comments. Please refer to the above reference for the published manuscript.

Interpreting LISST-100X measurements of particles with complex shape using Digital In-line Holography.

G.W. Graham,[1] E.J. Davies,[1] W.A.M. Nimmo-Smith,[1] D.G. Bowers,[2] and K.M. Braithwaite[2]

G.W. Graham, School of Marine Science & Engineering, Portland Square, Drake Circus, Plymouth, Devon, PL4 8AA, UK. george.graham@plymouth.ac.uk

E.J. Davies, School of Marine Science & Engineering, Portland Square, Drake Circus, Plymouth, Devon, PL4 8AA, UK.

W.A.M. Nimmo-Smith, School of Marine Science & Engineering, Portland Square, Drake Circus, Plymouth, Devon, PL4 8AA, UK.

D.G. Bowers, School of Ocean Sciences, Craig Mair, Bangor University, Menai Bridge,Anglesey, LL59 5AB, UK.

K.M. Braithwaite, School of Ocean Sciences, Craig Mair, Bangor University, Menai Bridge,Anglesey, LL59 5AB, UK.

[1]Plymouth University, UK.

[2]Bangor University, UK.

Abstract. Measurements of suspended sediment volume concentrations, particle size and number density are routinely collected in marine and freshwater environments with LISST-100X instruments to understand sediment transport, biological processes and fundamental opto-acoustic problems. A LISST-100X was simultaneously deployed with a novel holographic camera (holocam) in UK coastal waters to assess the performance of the laser diffraction technique when measuring natural suspensions. Volume distributions from the LISST-100X, truncated to exclude non-overlapping size bins with the holocam, exhibit an increase in small particles and median particle size is elevated in comparison to the holocam by 20 – 40%. We observe positive offsets between LISST-100X and holocam number distributions of up to 2 orders of magnitude for particle sizes between 58 – 218 μm, with discrepancies rising to 4 orders of magnitude for finer and coarser sizes. To explain these differences, a novel multi-scale representation of particle size is used. The method quantifies individual dimensions that make up any two-dimensional geometrical structure, it can be used as a metric for particle complexity, and offers a plausible explanation for an apparent increase in small particles (<58 μm) reported by the LISST-100X. The results suggest that for non-spherical natural suspensions the LISST-100X may be sensitive to optical scattering from sub-scales within larger particles, reporting them as individual particles regardless of the way in which they may be packaged into particles of larger overall size. We urge caution in over interpretation of LISST size distribu-

tions obtained in natural suspensions without verification with independent particle imaging.

1. Introduction

Measurements of particle size in coastal and oceanic waters are routinely made in an effort to understand the propagation of light and sound; the transport of suspended particulates and adsorbed contaminants; and the distributions and concentrations of biological organisms. Small angle laser diffraction is a popular method for particle size measurement, both *in-situ* and in the laboratory. Sequoia Scientific's LISST family of instruments [Agrawal and Pottsmith, 2000] are increasingly becoming the industry standard for *in-situ* measurement since they are robust, easy to deploy and return estimates of the particle size distribution (PSD) with minimal computational effort. The inversion from LISST recorded angular distribution of forward-scattered laser light to a particle size distribution utilises Mie theory of scattering from spherical particles. The system works well for simple suspensions, for example Traykovski et al [1999] have shown that the LISST is capable of resolving peaks in uni-modal distributions and bimodal distributions as long as modes are separated by 1 ϕ (where $\phi = -log_2 D/D_0$ with D defined as particle size in mm and D_0 equal to 1 mm). Reynolds et al [2010] have shown good agreements between Coulter counter and LISST measurements for uni-modal suspensions of known standard, with multiple modes adequately distinguished given sufficient size-separation of the modes. We have shown previously, using well-abraded sands, that the general shape of the size distributions and the location of modes in uni-modal populations, agree well between imaging and laser diffraction systems [Graham and Nimmo-Smith, 2010]. For biological particles of high sphericity, laser diffraction can also perform well. Anglès et al [2008] show a 1:1 relation between particle number concentrations from LISST and optical microscopy

counts for *Alexandrium taylori* phytoplankton. As particle morphology becomes increasingly complicated, the size distributions generated by laser diffraction become increasingly difficult to interpret without independent verification. Ahn and Grant [2007] have shown that LISST PSDs compare well to optical micrographs for dinoflagellates (approximately spherical) but noted that discrepancies (including a rising fine tail in the size distribution) developed when analysing inorganic natural particles. Increasing error in laser diffraction measurements has also been noted by Reynolds et al [2010] for particle populations with poor sorting. Interestingly Ahn and Grant [2007] observed that chemical and mechanical disaggregation of samples prior to analysis improved the agreement between LISST and optical microscopy and both Reynolds et al [2010] and Uitz et al [2010] have show almost 1:1 agreement in particle concentration and size between LISST and Coulter counter measurements for fine particles.

Natural sediments are far from spherical; suspended particulates in the marine environment often form complex aggregations (see images in Manning 2001 and Graham and Nimmo-Smith 2010), the optical response and scattering efficiency of which is poorly understood, yet laser diffraction instruments are often deployed in such environments and their results interpreted without considering the reliability of the derived PSDs. Recently there have been a number of studies that have begun to question the accuracy of laser diffraction instrumentation for suspensions that do not meet the strict assumptions of Mie theory. Gabas et al [1994] speculated that the interpretation of the diffraction events occurring from each of the chords that can be drawn across the cross-sectional area projection of a non-spherical particle leads to a distribution of particle sizes. Inhomogeneities in aggregate composition and packaging have led van Wijngaarden and Roberti [2002]

and Thonon et al [2005] to speculate that PSDs from laser diffraction instrumentation may contain modes associated with the small component parts and pore spaces within aggregates. Sensitivity to the multiple scales contained within non-spherical natural aggregates could increase the number of small particles measured, which would contribute to a low bias in reported mean size estimates. Karp-Boss et al [2007] illustrated this phenomena by comparing LISST-derived PSDs of homogeneous suspensions of the phytoplankton *Ceratium longipes* with manual optical microscopy measurements, and were able to identify modes in the LISST PSD that correspond to clearly identifiable plankton scales such as length, width and projected area. Karp-Boss et al [2007] provide the first convincing evidence that laser diffraction systems are sensitive to multiple scales present in the measurement volume and this suggests that extreme caution ought to be exercised when interpreting LISST PSDs from suspended particle populations of irregular shape.

In an effort to validate the LISST-100X response to natural suspended sediments, Mikkelsen et al [2005] compared *in-situ* volume distributions with those from a Digital Floc Camera. The two instruments overlapped by 8 LISST-100X size bins in the region 132-500 μm and offsets of between factors of -0.3 to 8.5 were reported. The authors speculated that particle shape might contribute to the inter-instrument offset and assumed that the inter-instrument discrepancy was constant over the full dynamic range of the LISST-100X data. Mikkelsen et al [2005] suggested that the LISST-100X data sets could be corrected by multiplying the total volume concentration by a fixed factor to bring them in line with those reported by the Digital Floc Camera. Most recently, Reynolds et al [2010] have shown that uni-modal suspensions of particles with simple geometry

(i.e. approximately spherical) are well resolved by the LISST-100X instrumentation, but significant ambiguities arise once distributions with multiple length-scales are considered.

In order to account for shape effects Agrawal et al [2008] measured the characteristic scattering functions of size-sorted sand grains, and sand grain analogues, then used these empirical measurements to develop a kernel matrix, which can be used to invert LISST scattering data without recourse to Mie theory. Although the modified inversion kernels of Agrawal et al [2008] are an excellent first step in interpreting LISST response to the forward scattering signatures of such sediments, the alternative algorithms do not cover the full range of particle sizes or shapes found within the marine environment. Further work is still required to fully resolve remaining ambiguities and develop inversions for particles that have a representative morphology of suspended particulates commonly found in fluvial, lacustrine, coastal and open-ocean locations. To do this requires some knowledge of the actual size and shape of particles in suspension. Measuring and classifying this wide range of particles is challenging because multiple parameters describing particle geometry must be used for an accurate representation of particles shape and size. A simple circularity metric, for example, does not consider the individual dimensions that make up the geometrical structure of a particle and is clearly unsatisfactory in describing complex geometry.

To examine the size and shape of natural particles, and elucidate their effect on LISST-100X measurements, we have simultaneously deployed a LISST-100X and a holographic camera system (holocam) to image suspended particles at a range of locations along the Western coastline of the British Isles between June 2008 and July 2009. In this paper, we utilise the holocam to ground-truth the number distributions and volume concentrations

reported by the LISST-100X and examine discrepancies between the two particle sizing instruments which emerge as a consequence of the natural shape complexity exhibited by suspended particulates. We demonstrate how multiple dimensions that make up the geometrical structure of particles could be the cause of this discrepancy. This is achieved using a novel method for the representation of each of these individual dimensions.

We recognise that naturally occurring cohesive sediments have shapes that are stochastically generated and extremely irregular so that the term 'particle size' is ambiguous. Size depends upon the method of measurement and, because particles can be composed of multiple sub-particles bound together into a larger composite structure, what appears to be an individual particle may contain multiple size scales. In this article we utilise 'particle' to refer to the collection of sub-components that contribute to an object's total projected area. 'Flocculated particle' or 'aggregate' is used when referring to particles composed of biotic and abiotic material fused together by inter-grain forces or mucal gels and 'biological particle' refers to biological organisms such as plankton. We use the term 'particle size' to indicate Equivalent Circular Diameter, which by definition is the diameter of a circle with equivalent projected area to a measured particle, unless otherwise qualified.

2. Methodology

2.1. Instrumentation and Deployment

A LISST-100X (type C, size range 2.5 - 500 μm) and a holographic camera, described by Graham and Nimmo-Smith [2010] and illustrated in Figure 1, were co-located on a frame with a CTD in either a vertically lowered (Figure 1 D) or horizontally lowered configuration (Figure 1 B) to enable deployment of the instrumentation from survey vessels.

The significant advantage of holography over other high-magnification imaging systems is that it is not limited by a shallow depth of field so that a comparatively larger volume can be analysed. In addition, suspended particles are focused during post-processing of the imagery so that sharp images of individual particles can be obtained over the full depth of the sampling volume. The holographic camera system uses two distinct configurations, the first is the nose-to-nose system, described by Graham and Nimmo-Smith [2010], where the imaging volume is located between the laser (532 nm) and Charge Coupled Device (CCD) housings and separated from them by short extension tubes (Figure 1 A–B). We refer to this as system 1 and it has a pixel size of 7.4 μm. The second is an adaptation of system 1 for vertical profiling with minimal disruption to the sampled volume. Figure 1 C–D illustrates the camera system equipped with long, vertical extension tubes and 90° prisms to distance the sampling volume (between the prisms) from the camera and laser housings. We refer to this adapted holocam as system 2, and it has been deployed with two different resolution CCDs with pixel sizes of 3.45 and 4.4 μm respectively.

Figure 2 illustrates the locations of deployments of system 1 from SV Catfish (University of Plymouth) in Plymouth Sound and Tamar Estuary (S.W. England, UK) and system 2 from the RV Prince Madog (Bangor University) in the Irish Sea and along the Western UK coastline. Additional information about the deployments and instrument configurations is given in Table 1.

2.2. Data Processing

For inter-comparison of the LISST-100X and holocam systems, we have utilised data from a transect of Plymouth Sound and Tamar Estuary in June 2008 and the Irish Sea cruises in April and July 2009. Information from the two systems has been restricted

to surface water data (depth $\leq$10m) and, assuming a homogeneous distribution of particle properties in this layer, depth averaged to produce mean particle properties for inter-comparison. The LISST-100X sampled at approximately 1 Hz and data were post-processed according to manufacturer recommendations using the standard spherical inversion [Agrawal and Pottsmith, 2000], resulting in total volume concentrations within 32 logarithmically spaced size classes from 2.5 μm to 500 μm. The holocam sampled at 2 Hz. A vertical profile can contain a few hundred to over 1000 holograms, depending on cast depth (image quantities for each location are given in Table 1). Imagery from each profile was reconstructed and analysed for suspended particles using a similar methodology to that outlined by Graham and Nimmo-Smith [2010]. A sub-domain measuring 1000x1000 pixels and centered on each raw 2D image was digitally reconstructed at 0.6 mm depth intervals over a configuration dependant path-length (see Table 1) centered within the holocam's sample volume. This generates a 3D stack from within which in-focus particles can be identified and accurately measured. Reconstruction of the volume at smaller intervals had no significant impact on the resultant particle concentrations or sizes. Image resolution is inversely proportional to reconstruction depth, for spherical objects the minimum resolution can be determined using the empirical relation [Vikram, 1992]:

$$d_s = \sqrt{\frac{z\lambda}{100}} \tag{1}$$

where z is the distance from the CCD plane and λ the laser wavelength. For the systems presented in this paper, the minimum resolution of a sphere occurring at the rear of the sample volume is 28.2 μm and 19.3 μm for system 1 and 2 respectively. We refer to this as the minimum spherical resolution. Malkiel et al [1999] and Katz et al [1999] demonstrate the the detection resolution for linear objects is significantly smaller than that of a sphere,

consequently we are able to resolve objects down to the system pixel size. However, we impose an arbitrary minimum particle area criterion of 9 interconnected pixels as the minimum object area for which to return information as we are confident that this is the smallest collection of pixels for which shape can be inferred. This equates to Equivalent Circular Diameters of 25 μm for system 1 and 11.7 – 14.9 μm for system 2. Projected Area, Equivalent Circular Diameter, Equivalent Spherical Volume, Major and Minor Axis Lengths are calculated for each individually identified particle in the reconstructed volume that exceeds our minimum area criterion.

The maximum linear dimension that we can reconstruct with the current holocam configuration is approximately 10 mm and the reporting interval user selectable. For instrument comparison, distributions of individual particle statistics from the holocam are generated in 50 log-spaced bins, the first 1 – 32 being identical to those of the LISST-100X (Figure 3). Since the holographic camera has an imposed minimum resolution limit which is coarser than the LISST-100X (2.5 μm), only bins in the interval 10 – 32 are populated. We are confident that we can accurately size particles which have sizes greater than the minimum spherical resolution defined above, we are less certain about particles that occur between the minimum area criterion resolution and the minimum spherical resolution limit. Therefore, for comparison between the two instruments their particle size distributions are truncated to the bin ranges above the minimum spherical resolution. Inter-comparison with the LISST-100X is conducted over bins 16 – 32 for system 1 and bins 14 – 32 for system 2 as indicated in Figure 3, unless explicitly stated in the text. Particle size properties are presented in the following section, either averaged

per profile or, where there are multiple profiles per location, double averaged by profile and location as indicated in Table 1 and Figure 2.

2.3. Quantifying Particle Structure

We have developed a new method for representing the individual dimensions that make up the geometrical structure of a particle by packing its projected area with circles. The procedure adopted by this method is described as follows: First, the largest dimension of the particle is represented by the largest circle that will fit within its projected area; The area filled by this circle is subsequently removed from the initial image of the particle area; The largest circle that can fit within the remaining area is then found. These steps are applied recursively until the particle is completely filled by circles - a process we refer to as circle-packing. The result is a number distribution of circle diameters that can be packed into the original particle image. This distribution of circle diameters can be used to represent particle shape.

The position of every circle within each particle is calculated from the two-dimensional convolution of the projected area of the particle and the circle being fitted. Figure 4 A illustrates the 2D convolution of a particle's projected area with the white circle shown in Figure 4 B. The peak in this convolution gives the position for the centre of the circle. Once this position has been found, the area covered by this circle is removed, and the convolution re-applied. This routine continues recursively until the circle diameter reaches three pixels, producing a result such as that of Figure 4 H. The packing routine terminates at circle diameters of three pixels because of the increased error in circle area, due to pixelation.

The resultant number distributions of circle sizes that are created by this packing procedure show that simple particles are represented by a dominant large circle and a few smaller circles. More complex particle shapes are packed with a broader distribution of circles, often with no singular dominant size. As a result, the skewness of the distribution of packed circle diameters may be used as a proxy for particle complexity.

2.3.1. Optimization

Elongated shapes (Figure 5 A) have more than one peak position returned by the convolution, as illustrated by the green crosses in the centre of Figure 5 B. With the packing method described so far, circles will be fitted as per Figure 5 C. However, this provides a poor representation of the elongation, as many small circles are required to fill the gaps between the three large circles, and a large proportion of the particle area is not covered because the length of the particle is not wholly divisible by its width (i.e. the largest circle diameter).

To better resolve problems associated with elongation, a smearing of circles is introduced when the convolution returns multiple positions for a circle centre. In the case of Figure 5 B, multiple circles of equal diameter are centred on each of the green crosses shown. The total area covered by these overlapping circles is calculated and removed (Figure 5 D) before iterating the convolution with a smaller circle. Subsequently, the value used to represent the equivalent number of circles of diameter D (N_D) that can be packed into the particle area, is given by the ratio of the total area covered by overlapping circles of diameter D, to the area covered by a single circle of diameter D:

$$N_D = \frac{A_O}{A_D} \tag{2}$$

where A_O is the area covered by the overlapping circles of diameter D and A_D is the area covered by a circle of diameter D.

Figure 6 shows resultant images of the circle-packing method for regular shapes, alongside histograms of number distributions and the area covered by each circle. It is clear that circular particles (A) are dominated by a single large circle. For angular shapes such as the square (B) and rectangle (C), the corners are represented by a distribution of small diameter circles. In addition, the branched areas of the 8-point star (D) are represented by a peak in particle diameters at about 25% of the largest dimension.

In the following section we will examine the initial differences between particle size distributions derived from the LISST-100X and holocam, then use our circle-packing methodology to develop a plausible explanation for the observed differences.

3. Results

3.1. Population Averaged Characteristics

The average size of a particle population is typically characterised by a median particle size and information on particle volume is routinely used to evaluate mass fluxes of suspended material. Figure 7 A contrasts the reported median size by volume (d_{50}) from the holocam with that of the LISST-100X. Clearly, central estimates of d_{50} from the LISST-100X vary over a smaller range, but are consistently coarser, than those of the holocam. Data from the Isle of Man, Conway Bay, the Solway Firth and Plymouth Sound and Estuary exhibit an almost 1:1 agreement, whilst for stations surrounding the Isle of Arran holocam d_{50} values are less than half those of the LISST-100X.

A comparison of the volume distribution skewness (Figure 7 B) suggests that the LISST-100X has a bias towards smaller particle sizes for half the survey locations. Anglesey,

Conway Bay, the open Irish Sea and Plymouth stations exhibit a small positive skewness. Median particle size from the holocam is positively skewed in 8 of the 9 locations indicating enhanced observation frequency of larger particles.

Figure 8 contrasts both the reported total volume and total number concentrations from the holocam with those obtained from the LISST-100X. LISST-100X total number concentrations are between 2.5 - 4 orders of magnitude larger, and total volume concentrations can be almost 2 orders of magnitude larger, than those reported by the holocam. The largest discrepancies are observed at the Isle of Arran and the open Irish Sea, while the smallest discrepancies are observed around Angelsey and the Isle of Man.

These population mean observations suggest that the LISST-100X reports an elevated number of small particles in comparison to the holocam. To examine this in more detail, we next consider the detailed variation between particle size distributions.

3.2. Comparison of Particle Distributions

Size distributions of Equivalent Circular Diameter (ECD, the diameter of a circle with identical projected area to the measured particle) are presented as volume and number concentration form in Figure 9 and Figure 10. In these figures the coloured portions of the distributions indicate the truncated data used for direct inter-comparison (i.e. from the minimum spherical resolution of the holocam to the maximum size range of the LISST-100X, as indicated in Figure 3) while the grayed portions indicate the full extent of the measurements. Direct comparison of LISST-100X and holocam size distributions from Plymouth Sound show a similar shape over bins 20 - 27 (58.10 – 218.49 μm) but with the LISST-100X positively offset from the holocam by at most 1 order of magnitude. For particle sizes less than 58.10 μm, agreement between volume or number of particles

observed by the two instruments diverges and, in the worst case, the LISST-100X can be offset by 2 orders of magnitude above the holocam. The number distributions of the LISST-100X indicate a large quantity of particles from the lower resolution limit of the instrument to approximately 200 - 300 μm in size. The concentration of these particles appears inversely related to size and can be well described by a power-law of the form $N = mD^j$. The values of the exponent j for the LISST-100X number distributions, calculated over bins 1 – 23 (2.5 - 112.67 μm), are indicated on Figure 9 B (and in subsequent number distributions presented in Figures 9 and 10). For bins below 20, holocam number, and consequently volume, concentrations (Figure 9 A – D) fall steeply in comparison to LISST-100X estimates, a trend that is not associated with holocam resolution limits since the decline is initiated 10 full bins (78 μm between bin centres) before the resolution limit of the camera. There is also divergence between the two systems for particle sizes larger than 257.83 μm (in bins 29 and up).

In the April Irish Sea data set (Figure 9 C – H) volume and number distributions from the LISST-100X are similar in shape for bins greater than 17 (41.72 μm) and with best agreement shown between the data sets from the Isle of Man. In all the data sets there is a consistent offset in volume and number concentration which is at its worst for Anglesey and the open Irish Sea, becoming just over an order of magnitude in the latter case. There is considerable variability between the holocam data sets that contribute to the averaged representations plotted in Figures 9 (and 10) to which the LISST-100X appears non-responsive. Below size bin 17 (particle size $<$ 35.36 μm) in the holocam data sets there is a sharp decline in number, and consequently volume. Notice that in Figures 9 E and F, the holocam does not report particles in-excess of bin 27 (218.49 μm) yet the

LISST-100X reports particles in all bins up to 500 μm. The holocam reports particles above the LISST-100X range in Figures 9 C,D,G and H.

A similar pattern is observed in the Irish Sea deployment during July 2008 (Figure 10) with the exception of the data set from Arran (Figure 10 A and B) in which the holocam reports particle concentrations (and volume) slightly above those of the LISST-100X over bins 15 – 24 (25.39 – 132.96 μm) while LISST-100X concentration and volume are above those of the holocam by 2 – 3 orders of magnitude in the coarse ($\geq$112.67 μm) and fine ($\leq$21.52 μm) tails. Agreement between the two instruments in bins 15 – 24 is improved in Figure 10 C and D, decreasing to 1 – 1.5 orders of magnitude offset in Figure 10 E–H.

The data obtained around the Isle of Man, Galloway and Angelsey exhibit the smallest offset between the two instruments (less than 1 order of magnitude across bins 17 – 29, increasing to 3 orders of magnitude for the smallest sized particles in bins below 17). The largest discrepancies between instruments, at least 1 order of magnitude across bins 17 – 29, are observed in the data set from Plymouth Sound, open Irish Sea, Solway Firth and Conway Bay with differences in small particle concentrations of almost 4 orders of magnitude.

90% of our observations show that the LISST-100X reports both particle numbers and volumes which are in excess of those from the holocam over the overlapping size range. The exception is the data set from Arran (Figure 10 A and B) in which the holocam reports marginally more particles over bins 15 – 24. In all data sets, the holocam reports a decay in both number and volume concentrations for particle sizes less than 58.10 μm (bin 20) - 35.36 μm (bin 17). The consequent divergence between the two instruments in this particle size range is consistent between deployment locations. To demonstrate that the reduction

in particle volume (and inferred number concentration) is not an artefact of the holocam the insert between Figure 10 G and H demonstrates the accurate determination of the size distribution and volume concentration of fine sand (sieved range 38<45 μm) imaged in our laboratory at a concentration of 20 mg L^{-1}. The mode of the PSD accurately characterises the suspended sand (given the errors inherent in wet-sieving and imaging of a randomly orientated suspension of non-spherical particles) and the sieved volume concentration matches that calculated before imaging for grains with an assumed density of 2650 kg m^{-3}.

3.3. Particle Shape Variations

Montages of randomly selected in-focus particles from four sampling locations are presented in Figure 11 and illustrate the diversity of particle shapes and sizes encountered during deployment. The Plymouth deployment comprises compact flocculated aggregates and the occasional biological organism such as a diatom chain or zoo plankton. The Irish Sea cruises are principally composed of biological material. The April Irish Sea deployment is dominated by high aspect ratio ('stick-like') diatom chains. The July Irish Sea Deployment has the largest diversity of particle shapes, from a relatively small number of compact flocculated particulates to near spherical objects (which we believe to be diatoms of the *Coscinodiscaceae* family) and highly irregular spiny particles (probably *Chaetoceros* spp).

It is clear from the particle montages that the suspended populations are heterogeneous in composition, size and shape. Consequently, there is a wide variation in the range of characteristic length scales that could be used to describe the size of the observed particle populations. Since there is not a unique metric for particle size characterisation,

it might be the case that some of the discrepancy between LISST-100X and holocam PSDs reported in section 3.2 arises because the LISST-100X responds to and reports length scales which are different to the Equivalent Circular Diameter which we have used in Figures 9 to 10 to relate projected area to size. Karp-Boss et al [2007] have demonstrated that for homogeneous suspensions of irregularly shaped plankton, laser diffraction returns multiple modes in a distribution which correspond to specific length scales of the particles in suspension. Using the circle-packing method described in Section 2.3, we are able to characterise the geometrical structure of each particle recorded by the holocam and estimate the characteristic length scales in suspension. Examples of the results of this method using a selection of *in-situ* particles are shown in Figure 12. Images after circle-packing are shown alongside histograms of number distributions and the area covered by each circle.

When comparing histograms of number distribution shown in Figure 6 with those of Figure 12, it is clear that much larger numbers of small particles are required to fill the projected areas of the *in-situ* particles. This is due to the increased shape complexity of the *in-situ* particles which results in a greater diversity in packed size scales. The dominant large scales of particles A and B in Figure 12 can be seen clearly in the histograms of the area covered by circles. Particle A has three dominant large scales making up the main body. The more rounded shape of the body of the particle B is represented by a single, large diameter circle that covers about 70% of the total particle area. Particles C, D and E have long, thin branch-like appendages, attached to a single bodily feature. The main bodies are represented by the large diameter circles, and the appendages are shown by a distribution of small diameter circles. The Copepod (E) has a more elongated body,

which is resolved by two large diameter circles ($> 50\%$ of the projected area covered). The long, thin diatom chain (F) has only four different diameter circles, with a clear peak in the area covered by a circle of about 50% relative diameter. The peak in the area covered is at a central diameter due to the overlapping of circles down the length of the particle. Without the use of the optimised overlapping circle-packing, many more smaller diameter particles would have been produced, creating a false impression of a more branched and complex geometry. Flocculated particles (G and H) are filled with a wide range of circle diameters, often with no clear dominance of a single sized circle. This is indicative of the complex multi-scale particle structure, typical of flocculated aggregates.

To determine whether multiple scale reporting is significant in our LISST-100X data sets we combine alternative size metrics, for example Major or Minor axes length, with the size distributions of circles packed into the projected areas of all particles imaged during a deployment, and compare the distribution of these metrics with LISST-100X PSDs. Figure 13 A schematically illustrates the Major axis, Minor axis and ECD length metrics for a particle, and Figure 13 B illustrates the PSDs derived using these length scales in comparison to a LISST-100X PSD from our deployment in Plymouth Sound. From the imagery collected in Plymouth Sound there is little difference between holocam PSD's of Equivalent Circular Diameter or Minor Axis, so only the former is illustrated in Figure 13 B, but both show negative offset from the distributions reported by the LISST-100X by 0.5 - 2 orders of magnitude. Utilising a Major Axis measure coarsens the PSDs principal mode by 40-50 μm and raises the coarse tail of the distribution (D$\geq$200 μm) so that both number and volume concentrations are elevated marginally above those reported by the LISST-100X. The use of simple size metrics such as Equivalent Circular Diameter

or Major Axis length have little or no impact on the discrepancy between the holocam and LISST-100X for particle sizes less than 70 μm.

The number distribution derived from applying the circle-packing methodology to the data set from the Plymouth Sound deployment is illustrated in Figure 13 B. There is a marked improvement in agreement with number distributions reported by the LISST-100X for particles less than 100 μm in comparison to distributions of Equivalent Circular Diameter or Major Axis. The agreement is not perfect since the circle-packing methodology does not quite generate sufficient particle diameters to match the number that the LISST-100X reports for particles in the range 10 – 70 μm, but it represents a significant improvement over using an Equivalent Circular Diameter distribution. Interestingly, if we combine the number distributions derived from Major Axis length (over size bins greater than 100 μm) with those from circle-packing (over size bins less than 100 μm) we have a reasonable approximation to the number distribution reported by the LISST-100X, although there is still a positive vertical offset between the LISST-100X and holocam of maximum 1 order of magnitude. Figure 13 D-E illustrate this combined PSD (i.e. the summation of a circle-packed PSD and a Major Axis length PSD) with LISST-100X number distributions for the open Irish Sea (April 2009 cruise) and the Isle of Arran (July 2009 Cruise). For the open Irish Sea the combined PSD has similarity in slope and general shape to the LISST-100X distribution but does not match the number concentration exactly. A variable offset in the magnitude between the number distributions is observed for the Isle of Man (Figure 13 E). The fact that we can approximate the shape and slope of LISST-100X PSDs by combining both the Major Axis sizes and an estimate of the diversity of size scales contained within a particle imaged by the holocam, suggest that the

LISST-100X is sensitive to scattering from numerous scales in suspension (from the small internal structure of particles, estimated by the circle-packing methodology, through to the maximum dimension of a suspended particle, represented by the Major Axis length) and that the reported number and volume distributions of the LISST-100X are some composite of these scales.

In an effort to evaluate whether the inclusion of the variety of scales in suspension improves the agreement between the two instruments we have taken the combined PSDs (circle-packed scales plus Major Axis scales) calculated from the holocam imagery (extending from 2.5 – 500 μm to exactly match the LISST-100X range) and re-calculated d_{50}, total particle numbers and total particle volumes (Figure 14). As expected, Figure 14 A shows that holocam median particle sizes are increased in comparison to initial estimates (Figure 7 A) by the inclusion of the estimated scales contained within each suspended particle. d_{50} data are clustered within $\pm$100 - 150 μm about the 1:1 line in Figure 14 A, which is a marked improvement on the initial clustering in Figure 7 A. Total number concentrations of the holocam (Figure 14 B) are substantially increased above those estimated using an Equivalent Circular Diameter distribution alone, although we still cannot match the exact number distributions generated by the LISST-100X. Consequently, the total volume concentrations for the holocam (Figure 14 C) are increased such that estimates from the two instruments are within 1.5 orders of magnitude.

4. Discussion

Since our submersible digital holographic camera has a greater resolution than previous imaging systems, we obtain a substantially increased overlap with LISST-100X PSDs (21-26 size bins, depending on camera resolution) than have previously been reported.

In line with Mikkelsen et al [2005], our observations indicate that the shape of the PSD in bins 20–32 (58-500 μm) can be similar to those of the LISST-100X but that there is a variable offset between both the number and volume concentrations reported by the two instruments. Number and volume concentrations reported by the LISST-100X over this range of size bins are consistently at least 1 order of magnitude greater than those reported by the holocam. Interestingly, for bin numbers less than 17 ($\leq$35.36 μm) - 20 ($\leq$58.10 μm) the holocam consistently reports a decrease, by up to 5 orders of magnitude, in both number and volume concentration of suspended particles in comparison with the LISST-100X. The discrepancy between the LISST-100X, which consistently reports increasing numbers of particles in the same size range, and the holocam is intriguing. The decrease in small particle observations is initiated at least 8 size bins above the resolution limits of the holocam, and we have shown that we can, under controlled conditions, accurately measure the size distribution and volume concentration of quartz sand in the range 38$<$45 μm (covering LISST-100X size bins 17 - 18). We are confident, therefore, that the reduction in small particles we observe *in-situ* is not an artefact of the imaging technique. Since aggregation is one of the key processes that affects the suspended size distribution in coastal waters containing both minerogenic and biological particles, it seems counter-intuitive to expect small particles (such as individual grains, phytoplankton cells, bacteria and viruses) to exist as isolated individuals in large numbers. Given the efficiency with which small particles at high concentrations undergo electro-chemical aggregation and then further binding by biological glues, these particles might be expected to exist as component parts of larger flocculated particles rather than free floating, discrete entities. Aggregation and disaggregation are dynamically active processes which generate a contin-

ually varying population of particles with proportions of individual grain through to large aggregates fluctuating in responsive to environmental forcing. We interpret our *in-situ* holocam observations as indicative that the majority of the suspended particulates do not exist as isolated entities but are bound up into larger flocculated particles. It seems even more counter-intuitive, therefore, that during our deployments the LISST-100X reported a consistent fine tail, especially given the dynamism of *in-situ* size distributions. Given the discrepancy between *in-situ* imaging and LISST-100X size distributions, and the similarity between LISST-100X and distributions derived in the laboratory [e.g. Reynolds et al, 2010; Uitz et al, 2010], it seems that sample handling, preparation and the choice of analysis method itself (e.g. flow cytometery, optical microscope) cause significant discrepancies between instrumentation in most inter-comparisons (see for example Serra et al [2001]). Caution against over-interpretation of laboratory-derived size distributions ought to be exercised. *Ex-situ* analysis of water samples necessarily means some disruption to suspended particles and consequently laboratory size distributions are unlikely to reflect the size distribution of particles suspended *in-situ*. The disruption of fragile flocculated particles, and consequently the liberation of their component parts, during laboratory particle sizing with instrumentation such as flow-through cytometery or flow field fractionation may artificially elevate number concentrations at small sizes. In fact, such disruption may explain why such techniques report large numbers of small particles in comparison to *in-situ* imaging measurements when analysing natural suspensions. Intriguingly, these laboratory observations agree well with the rising fine tail of *in-situ* laser diffraction measurements and have led us to question what the LISST-100X instruments are responding to when measuring natural suspensions. We observe a consistent decay (or roll-off) in the

number concentrations reported by the holocam for particle sizes below the range 41.72 - 50.1 μm, yet the LISST-100X reports increasing numbers of small particles. Since this roll-off occurs well above the resolution limit of the camera, and we have demonstrated that we can accurately resolve the volume concentration of particles in the range 38 - 45 μm ECD, we hypothesise that the LISST-100X may be sensitive to scattering from the multiple scales contained within suspended particles. Such scales would be the size of the individual component parts that make up the objects in suspension and contribute to the particle's total projected area (illustrated in Figure 13 A as the sub-components with linear size smaller than the particle's Minor Axis length). It is these scales that we are able to estimate with our circle-packing methodology.

In this paper, we have attempted to minimize the discrepancies between the two systems by modifying the holocam size distributions using the circle-packing method to match those of the LISST-100X in order to understand the size scales in suspension which the LISST-100X might be responsive to. It seems unlikely that the scattering pattern of a flocculated particle or complex structure (e.g. a biological assemblage) is a simple superposition of scattering from its component parts, but rather some variable mixture of scattering from all of the scales present within the particle weighted by the efficiency with which each scale scatters light. Flocculated particles are by definition composed of multiple sub-components. The microscopy images of Droppo et al [1997] and Droppo [2001] show mineral and biological particles held together by a matrix of extra-cellular polymeric 'glues' so that the structure and refractive index of such a package is non-uniform. Particle packaging influences the space filling properties and thus the effective density of aggregates which is also likely to influence the particle's scattering signature.

Since populations of suspended, natural particles are heterogeneous in shape and size they contain a multitude of scales that can be used to measure size or shape. Previous research has indicated that LISST instruments respond to a range of scales in homogeneous suspension of phytoplankton which exhibit readily identifiable component parts [Karp-Boss et al, 2007]. We have shown that distributions of a single size metric, for example an Equivalent Circular Diameter, do not agree with number distributions generated by the LISST-100X since there is a disparity in total number of particles, especially for particles greater than 100 μm and less than 70 μm. Using a distribution of the Major Axis lengths in suspension, holocam number distributions can be increased to a similar magnitude as those reported by the LISST-100X for particles larger than 150 μm. Crucially, there remains a strong disparity between instruments for particle sizes less than 60 μm. The LISST-100X reports an increasing number of small particles, while the holocam indicates a decay in number concentration. Both van Wijngaarden and Roberti [2002] and Thonon et al [2005] have suggested that PSDs from laser diffraction instrumentation may contain information related to the small component parts and pore spaces within flocculated particles. Sensitivity to the multiple scales contained within non-spherical natural particles could increase the number of small particles measured if the LISST-100X responds to flocculated particles as individual components rather than as a single particle with a projected area which is the sum of the component part areas. Such sensitivity would contribute to the low bias in reported median size estimates and negatively skewed LISST-100X distributions we have observed during all our deployments. Number distributions derived using our circle-packing method show a rising fine tail which mimics those reported by the LISST-100X. It is conceivable that each of these small dimensions within a particle, could

519 contribute to the inverted volume distribution, elevating the number of small particles
520 reported. Using number distributions of the Major Axis metric (which corrects best for
521 particles greater than 100 μm) and from the circle-packing methodology (correcting best
522 for particles less than 100 μm) we are able to recreate a number distribution that has
523 both similar shape and slope to that reported by the LISST-100X using holocam imagery
524 from Plymouth Sound and Tamar Estuary and the Irish Sea. This methodology does not
525 exactly capture the total number of particles, the LISST-100X still reports 1 - 2 orders
526 of magnitude more particles than can be derived by manipulating the holocam data sets
527 in this way. These offsets in magnitude are intriguing, and we think the variable accu-
528 racy with which we can mimic the LISST-100X distributions is closely linked to particle
529 structure (e.g. complex refractive index, variation in particle shape, surface roughness
530 and orientation) that is likely to modify the particles' characteristic scattering function.
531 Deploying the holographic system in a range of coastal shelf-sea locations we have en-
532 countered a diversity in particle size, shape and composition. The montages of in-focus
533 particles generated for each of the deployment locations indicate an apparent continuity of
534 particle form between high aspect ratio particles ('stick-like' diatom chains that dominate
535 the April Irish Sea cruise), through compact but irregular flocculated particles and sand
536 grains (Plymouth Sound) to approximately spherical biological particles (July Irish Sea
537 cruise). Of course, there are other particle properties, in addition to shape, that affect the
538 system inter-comparison and which we have yet to account for. Indeed, we speculate that
539 significant variability between the two systems arises due to variability in composition
540 and thus refractive index and scattering efficiency of natural particles in suspension. In
541 our digital holograms, particles that generate strong interference patterns (for example

sand grains and other objects which have high refractive index) can be reconstructed and sharply focused. Biological particles with a more jelly-like consistency, and thus a lower refractive index, can be observed but prove more difficult to focus since the imaged interference patterns are weaker from these objects. Particles that comprise both types of material, for example marine flocs which are typically inorganic mineral particles and biological components bound together, have very variable interference patterns. The optical properties of marine particles such as these are not well understood, and while the LISST-100X is well designed to measure the small angle forward scattering, there remain interesting questions about the errors that derive from inversion of laser diffraction patterns from particles of complex structure, since scattering characteristics may vary with changes in morphology, packing, composition and non-uniform refractive index. However, inter-station mineral:biological ratios, derived from loss on ashing of gravimetric filter samples, exhibit negligible variation and appear un-related to instrument response, so are not presented here. The exact mechanism by which multiple scales may impact laser diffraction measurement technology requires further research and there are likely to be other mechanisms that also contribute to offsets between the instruments. For example, the number of particles that occur above the LISST-100X's upper size limit may lead to errors since they might be aliased to smaller sizes by the LISST-100X inversion algorithm [Davies et al, submitted]. The detailed scattering properties of inhomogeneous suspensions of complex particles are currently being explored to further understand the difference between LISST-100X and holocam PSDs [Davies et al, 2011].

We suggest that the LISST-100X is highly sensitive to scattering from multiple scales in suspension. It appears from our observations that the LISST-100X reports the largest

dimension of a particle as well as the dimensions of sub-components that occur within each particle. In effect, this is similar to the size distribution one might expect from the sum of the size distribution of aggregated particles and the size distribution of the component parts from within the aggregated particles (if the aggregates were to be fully disaggregated). This leads us to hypothesize that the LISST-100X reports the distribution of optical scatter sizes, i.e. the distribution of particle sizes that contribute to the measured angular distribution of forward scatter, regardless of the way in which these particles may be packaged into larger assemblages. These distributions have elevated numbers of small particles in comparison to the actual size distribution in suspension since these small optical scatterers can be bound up within flocculated particles or are internal scales of particles with complex geometry. In contrast, holography (and other particle imaging systems) report the size distribution of suspended particles based on a total projected area. This distribution has a sedimentological significance since the total size and volume of a particle control effective density, settling velocity and thus mass fluxes of the suspended material. The holocam is capable of sizing particles whether they occur as single grains or aggregated together and, as we have shown, distributions of sedimentologically significant particle sizes can be related to the distribution of optical scatterer sizes by using the circle-packing methodology developed in this paper. However, without some knowledge of the way in which the optical scatterers are packaged into larger particles *in-situ* it is, at present, impossible to take the distribution of optical scatterers reported by the LISST-100X and estimate the sedimentologically significant size distribution without co-incident, independent imaging. Figure 15 A – C graphically illustrates the concept of differences between optical scatterer distributions and sedimentologically significant distributions of

particle sizes, in a simplified form. In the simplest case (Figure 15 A), a hypothetical LISST size distribution reports a single circular particle characterised by a diameter of length a from an unknown object. Using the holocam we generate three size metrics for this unknown object, the Major Axis length, an Equivalent Circular Diameter and the diameter of small scale components contained within the object's projected area by circle-packing. For a single spherical particle, these three metrics are identical and agree well with the LISST-100X's spherical equivalent size. In Figure 15 B, a hypothetical LISST response to an unknown object results in 6 discrete particles: a single particle of diameter b and 5 of diameter c. The holocam reports a single diameter of size b (or the Equivalent Circular Diameter) or, by circle-packing the imaged object, 5 diameters (c) of the smallest components. Consequently each size metric has a different magnitude and number of occurrences. The discrepancy in metrics suggests that the unknown particle consists of 5 circles of diameter c chained together with a major axis of b. The 'particle shape' of the unknown object is represented in the final column of Figure 15 B. Our interpretation of the discrepancy is that the LISST-100X is sensitive to scattering from each length scale and consequently reports the distribution of optically significant particle sizes as discrete entities, i.e. 1 particle of size a and 5 particles of size b. Using the holocam we have the option of reporting a sedimentologically significant size, using the Major Axis length (or Equivalent Circular Diameter), or can approximate the inverted PSD from the LISST by using the circle-packing methodology to estimate the distribution of scales contained within a particle's projected area. Finally, Fig 15 C illustrates an example in which the LISST reports 8 discrete particles of size $c - f$ after measuring an unknown object. With the holocam we return a single sedimentologically significant particle of size

611 d or a collection of sub-particles (1 of size e, 2 of size f and 4 of size c). Again, we suggest
612 that the discrepancy between size metrics indicates the unknown object is packaged as
613 illustrated in the final column of Figure 15 C.

614 The discrepancies which we have identified between the holocam and the LISST-100X,
615 and the mechanisms we have invoked to explain these inter-instrument differences, lead
616 us to consider the accuracy with which *in-situ* particle size distributions are empirically
617 represented by the ocean optics community. Size distributions of suspended particulate
618 matter in the oceans, measured with Coulter counter or LISST technology, are commonly
619 observed to follow an inverse power-law distributions which, in a log-log representation
620 when reported as dN/dD, results in a straight line with negative slope. This power
621 function is commonly described as a "Junge" distribution. The exponent j typically takes
622 a central value of -4 for oceanic particles in oligotrophic waters [Morel and Maritorena,
623 2001], which suggests that in ocean water there are 10^4 times more freely floating particles
624 as size is decreased by a factor of 10, i.e. a continuous background of ever smaller particles.
625 The Junge distribution is used routinely in oceanographic optics calculations for scattering
626 and absorption coefficients, or in radiative transfer modelling and applications to remote
627 sensing, as a simplified approximation to the continuous size distribution in the sea [e.g.
628 Forget et al, 1999; Stramski and Kiefer, 1991; Boss et al , 2001]. Since LISST-100X and
629 holocam number distributions are $d(N)/d(log(D))$ the widths of the particle size bins
630 must be taken into account before the slopes presented in Figures 9 – 10 are comparable
631 to those of the Junge distribution. The exponent of the Junge distribution that describes
632 the number distributions in Figures 9 – 10 consequently becomes -1 power smaller than
633 those presented, i.e. ranging from -3.37 to -4.94. The Junge exponent j from our LISST-

100X observations generally have a shallower slope than -4, which is not unexpected since large particles in the form of flocculated particles are more prevalent in coastal waters. It is also clear that there are significant departures from an inverse power-law when using the holocam, particularly for particles smaller than 58 μm. The divergence between LISST-100X and holocam distributions, and our hypothesis that the LISST-100X responds to sub-scales within suspended assemblages, raises questions about the universal applicability of an inverse power function (the Junge distribution) as an adequate representation of *in-situ* particle size spectra in coastal shelf-seas. The use of a Junge distribution for marine particles has been criticised as too simplistic [Chami et al , 2006; Risovic, 2002; Stavn et al, 2004] and there is a distinct lack of *in-situ* information regarding the concentrations of finest particles ($<$1 μm) which are thought to contribute significantly to light scattering [e.g. Babin et al , 2003] and which would verify the validity of the Junge distribution. In addition, the theoretical distribution does not take into account any processes that might bind such small, freely floating particles into larger assemblages causing deviation from the power function. Jonaz and Fournier [2007, Chap.5, p.269] state that the parametric model 'is a convenient "first-order-of magnitude" approximation that reflects the major feature of size distributions: a rapid decline in the particle size concentration with increasing particle size. ... frequent references to the power-law size distribution ... should not be understood as our desire to impress on the reader a particular fitness of this approximation.' From our observations in coastal shelf-seas, we would suggest that the Junge distribution appears to be an inappropriate model. We urge caution in the literal interpretation of the empirical distribution as evidence that large numbers of free-floating small particles exist in coastal

shelf-sea waters since the distribution may be an artefact of the measurement technology employed.

We suggest that the LISST-100X's sensitivity to all scales of particle size explains why we observe that the LISST-100X consistently reports several orders of magnitude more particles than the holocam, particularly in the fine tail of the size distribution. In suspensions of non-spherical particles, or in environments where aggregation forms assemblages that contain sub-components with multiple sizes (e.g. the particle sketched in Figure15 C) we urge caution in the interpretation of reported particle size and number concentrations from LISST-100X instrumentation if the user is interested in the sedimentologically significant *in-situ* size distribution. Without an imaging system to verify the LISST-100X PSDs, it is impossible to determine whether the reported sizes are individual objects in suspension or variably sized objects packaged-up into a larger entity. In other words, laser diffraction measurement systems appear to respond to multiple length scales when non-spherical particles are analysed. There are a number of metrics that can be used to estimate particle size using imaging systems and it appears that some combination of a particle's projected area, Major Axis length and the scales of a particle's component parts are combined within PSDs reported by laser diffraction systems. Without independent verification of the size-scales present, it is impossible to de-convolve the resulting PSD to determine discrete populations in suspension. A hypothetical example of over interpretation of a LISST-100X PSD might be the attribution of distinct particle populations to discrete modes in a multi-modal PSD. Verification with an imaging system, as has been done by Karp-Boss et al [2007] and in this publication, might show that the discrete modes in the LISST-100X PSD can be related to sub-scales within the large particles in

679 suspension and are not separate particles in their own right. Such erroneous interpreta-
680 tion of the LISST-100X size distribution has consequent impacts on the understanding of
681 particle dynamics, mass fluxes, pollution transport or the calculation of optical properties.

5. Conclusions

682 We have presented comparative data sets for a LISST-100X and a submersible digital
683 holographic camera, in variably overlapping size bins over a range of 6.75 - 500 μm, in
684 order to assess the operational ability of laser diffraction systems in natural suspensions.
685 The LISST-100X appears sensitive to the smallest size-scales in suspension, and reports
686 larger sized particles than are imaged with the holocam such that median particle size by
687 volume is between 20 and 40% greater than those of the holocam. Number and volume
688 concentrations reported by the LISST-100X are positively offset from the holocam by up
689 to 2 orders of magnitude for particles in the range 58 – 218.49 μm, with discrepancies
690 rising to almost 4 orders of magnitude at finer and coarser sizes. In contrast to previous
691 studies, the large overlap in particle size range between systems enables us to show that
692 this offset is not uniform across the LISST-100X's measurement range and that a simple
693 offset correction is not appropriate.

694 Our LISST-100X number distributions exhibit an inverse power relation with particle
695 size, with slopes of -3.37 to -4.94. These slopes are similar to a range of previous observa-
696 tions which have utilised the Junge distribution to describe particle size distributions in
697 coastal and ocean waters. Holocam volume and number distributions exhibit a distinct
698 decay for particles smaller than 41.72 – 58.1 μm and do not support the Junge distribu-
699 tion. This decay in number concentration is not associated with resolution limitations and
700 we hypothesise that the discrepancy between instruments is related to the way in which

the LISST-100X inversion algorithm responds to scattering from suspended particles with complex shape. Complex particles in the marine environment have multiple dimensions that make up their geometrical structure and these dimensions are likely to cause scattering in-addition to that related to a particle's cross-sectional area. Utilising measurements of the largest dimensions of suspended particles, we can approximate the number densities reported by the LISST-100X for particles $\geq 100\,\mu$m. The inclusion of multiple size scales derived from the holocam imagery is required to reduce the discrepancies in reported number distributions between the two systems for smaller particle sizes. Using an novel, multi-dimensional spherical representation of particle geometry we are able to provide a way of quantitatively representing individual dimensions that make up the geometrical structures of particles. This method of circle-packing can provide both a proxy for geometrical complexity and a representation of multiple particle dimensions. Using circle-packed holocam imagery we can approximate the distribution of small scales that may occur within suspended particles of complex morphology, and can replicate both the shape and slope of the fine rising tail that is consistently reported in all our LISST-100X measurements.

We conclude that the reasonable agreement we obtain between circle-packed holocam distributions and those of the LISST-100X indicate that laser diffraction measurements respond to a multiplicity of scales in suspension, rather than a single size scale which might be related to projected area. Reported particle size distributions from the LISST-100X are thus a combination of the different optical scattering scales contained within suspended particles, regardless of how they may be packaged into larger aggregates. We question whether the Junge power-law is an appropriate approximation of suspended particle size in

coastal shelf-seas where aggregation processes can strongly modify particle size, shape and structural packaging. Further, we suggest that observations of size distributions which do conform to power-law distributions in these environments may be a measurement technology artefact.

It is not yet possible to take LISST-100X optically significant number distributions and match them to sedimentologically significant distribution from the holocam. Therefore, without independent verification of the packaging, shape, size and concentration of particles in suspension, interpretation of the volume or number distributions derived by laser diffraction should not be made when such systems are deployed in natural suspensions that contain non-spherical particles. Equally, inferences about the characteristics of sedimentologically significant particle sub-populations should only be drawn from LISST-100X measurements if their existence has been independently corroborated.

The complexity in form and composition exhibited by natural suspended sediments means that users of *in-situ* particle sizing systems, who have no *a-priori* information on the particle properties, should be extremely cautious in the use and literal interpretation of PSDs generated by laser diffraction. The optical properties of complex suspended aggregates in the marine environment are so poorly understood that it is, at present, only possible to speculate about how a laser diffraction system might respond to them. If such systems are deployed in environments which violate the strict assumptions governing the Mie theory inversions, namely sphericity and uniform refractive index, it would be prudent to verify the reported size distributions with an imaging system that is capable of characterising distributions of both shape and size without such limiting assumptions.

746 **Acknowledgments.** This work was supported by the National Environment Re-
747 search Council (NE/E015247/1) and E. Davies was in receipt of a NERC studentship
748 (NE/H525070/1). We would like to thank Paul Hill and Robert MacDonald for insightful
749 discussions on a draft version of this manuscript and express our gratitude to two anony-
750 mous referees who provided insightful comments which have improved the clarity of this
751 manuscript.

References

752 Agrawal, Y., and Pottsmith, H., 2000. Instruments for particle size and settling velocity
753 observations in sediment transport. Marine Geology 168, 89 – 114.

754 Agrawal, Y., Whitmire, A., Mikkelsen, O., and Pottsmith, H., 2008. Light scattering by
755 random shaped particles and consequences on measuring suspended sediments by laser
756 diffraction. Journal of Geophysical Research 113, C04023.

757 Ahn, J., and Grant, S., 2007. Size distribution, sources, and seasonality of suspended
758 particles in Southern California marine bathing waters. Environmental Science and
759 Technology 41(3), 695 –702.

760 Anglès, S., Jordi, A., Garcès, E., Masó, M., and Basterretxea, G., 2008. High-resolution
761 spatio-temporal distribution of a coastal phytoplankton bloom using Laser In Situ Scat-
762 tering and Transmissometry (LISST). Harmful Algae 7, 808 – 816.

763 Babin, M., Morel, A., Fournier-Sicre, V., Fell, F., and Stramski, D. 2003. Light scattering
764 properties of marine particles in coastal and oceanic waters as related to the particle
765 mass concentration. Limnology and Oceanogrphy. 48: 843859.

766 Boss, E., Pegau, W.S., Gardner, W.D., Zaneveld, J.R.V., Barnard, A.H., Twardowski,
767 M.S., Chang, G.C., and Dickey, T.D. 2001. Spectral particulate attenuation and par-
768 ticle size distribution in the bottom boundary layer of a continental shelf. Journal of
769 Geophysical Research. 106: 9509-9516

770 Chami, M., Shybanov, E.B., Khomenko, G. Lee, M., Martynov, O.V., and Korotaev,G.
771 2006. Spectral variation of the volume scattering function measured over the full range
772 of scattering angles in a coastal environment. Applied Optics 45, 36053619.

773 Davies, E.J., Nimmo-Smith, W.A.M., Agrawal, Y.C., and Souza, A.J. Submitted. LISST-
774 100X response to large particles. Marine Geology.

775 Davies, E.J., Nimmo-Smith, W.A.M., Agrawal, Y.C., and Souza, A.J. 2011. Scattering
776 signatures of suspended particles: an integrated system for combining digital holography
777 and laser diffraction. Optics Express, 19, 25488-25499.

778 Droppo, I., 2001. Rethinking what constitues suspended sediment. Hydrological Processes
779 15, 1551 – 1564.

780 Droppo, I., Leppard, G., Flannigan, D., and Liss, S., 1997. The fresh water floc: A
781 functional relationship of water and organic and inorganic floc constituents affecting
782 suspended sediment properties. Water, Air and Soil Pollution 99, 43 – 54.

783 Forget, P., Ouillon, S., Lahet, F., and Broche, P. 1999. Inversion of reflectance spectra
784 of nonchlorophyllous turbid coastal waters. Remote Sensing of the Environment 68,
785 264272.

786 Gabas, N., Hiquily, L., and Laguuerie, C., 1994. Response of laser diffraction particle sizer
787 to anisometric particles. Particle and Particle Systems Characterisation 11, 121 – 126.

Graham, G., and Nimmo-Smith, W., 2010. The application of holography to the analysis of size and settling velocity of suspended cohesive sediments. Limnology and Oceanography: Methods 8, 1 – 15.

Jonaz, M., and Fournier, G.R. 2007. Light scattering by particles in water: Theoretical and experimental foundations. Elsevier Academic Press. Amsterdam

Karp-Boss, L., ZAzavedo, L., and Boss, E., 2007. LISST-100 measurements of phytoplankton size distribution: Evaluation of the effects of cell shape. Limnology and Oceanography: Methods 5, 396 – 406.

Katz, J., Donaghay, P.L., Zhang, J., King, S., and Russel, K. 1999. Submersible holocamera for detection of particle characteristics and motions in the ocean. Deep Sea Research, 46, 1455–1481.

Malkiel, E., Alquaddoomi, O., and Katz, J. 1999. Measurements of plankton distribution in the ocean using submersible holography. Measurement Science and Technology, 10, 1142 – 1152.

Manning, A., 2001. A study of the effect of turbulence on the properties of flocculated mud. Ph.D. thesis, University of Plymouth, Plymouth.

Mikkelsen, O., Hill, P., and Milligan, T., 2006. Single grain, microfloc and macrofloc volume variations observed with a LISST-100 and a digital floc camera. Journal of Sea Research, 55, 87 – 102.

Mikkelsen, O., Hill, P. S., Milligan, T., and Chant, R., 2005. In situ particle size distributions and volume concentrations from a LISST-100 laser particle sizer and a digital floc camera. Continental Shelf Research, 25, 1959 – 1978.

Morel, A., and Maritorena, S. 2001. Bio-optical properties of oceanic waters: A reappraisal. Journal of Geophysical Research, 106,C4,7163 – 7180.

Reynolds, R., Stramski, D., Wright, V., and Woźniak, S., 2010. Measurements and characterization of particle size distributions in coastal waters. Journal of Geophysical Research, 115, C08024.

Risovic, D. 2002. Effect of suspended particulate-size distribution on the backscattering ratio in remote sensing of seawater. Applied Optics, 41, 70927101.

Serra, T., Fernando, H., and Rodríguez, R., 2001. The role of the emergent vegetation on lateral diffusion in wetlands. In: Casamitjana, X. (Ed.), The 6^{th} Workshop on Physical Processes in Natural Waters. University of Girona, IMA, pp. 190 – 194.

Stavn, R. H., and Keen, T.R. 2004. Suspended minerogenic particle distributions in high-energy coastal environments: Optical implications. Journal of Geophysical Research, 109, doi:10.1029/ 2003JC002098.

Stramski, D. and Kiefer, D.A. 1991. Light scattering by microorganisms in the open ocean. Progress in Oceanography 28, 343-383.

Thonon, I., Roberti, J., Middelkoop, H., van der Perk, M., and Burrough, P., 2005. *In situ* measurements of sediment settling characteristics in floodplains using a LISST-ST. Earth Surface Processes and Landforms 30, 1327 – 1343.

Traykovski, P., Latter, R., and Irish, J., 1999. A laboratory evaluation of the laser in situ scattering and transmissometery instrument using natural sediments. Marine Geology 159, 355 – 367.

Uitz, J., Stramski, D., Baudoux, A., Reynolds, R., Wright, V., Dubranna, J., and Azamb, A., 2010. Variations in the optical properties of a particle suspension associated with

viral infection of marine bacteria. Limnology and Oceanography 55, 2317–2330.

van Wijngaarden, M., and Roberti, J., 2002. *In situ* measurement of settling velocity and particle size distribution with the LISST-ST. In: Winterwerp, J. C., Kranenburg, C. (Eds.), Fine Sediment Dynamics in the Marine Environment. Elsevier Science, pp. 295 – 312.

Vikram, C.S. 1992. Particle Field Holography. Cambridge University Press. Cambridge.

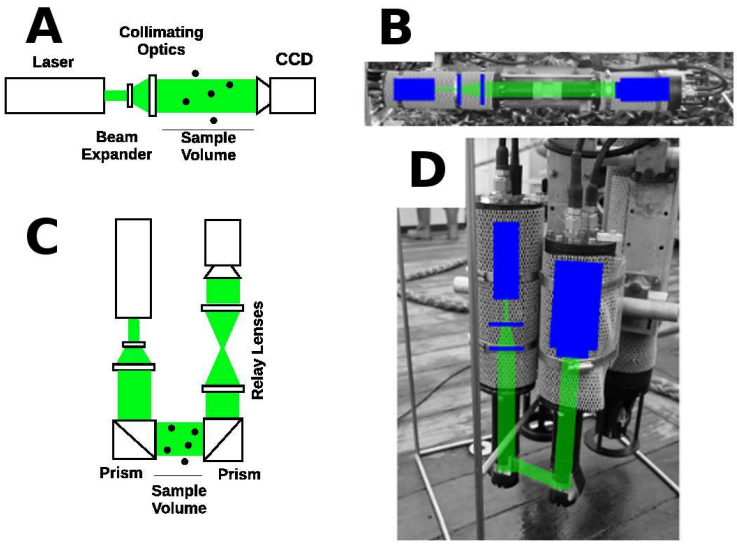

Figure 1. Conceptual diagram of in-line digital holographic system.

A-**B** the original nose-to-nose configuration described in Graham and Nimmo-Smith [2010]. **C**-**D** a modified system using 90° prisms in a compact, profiling configuration. Diffraction patterns from scatterers in expanded and collimated laser beam are recorded on CCD for later digital reconstruction.

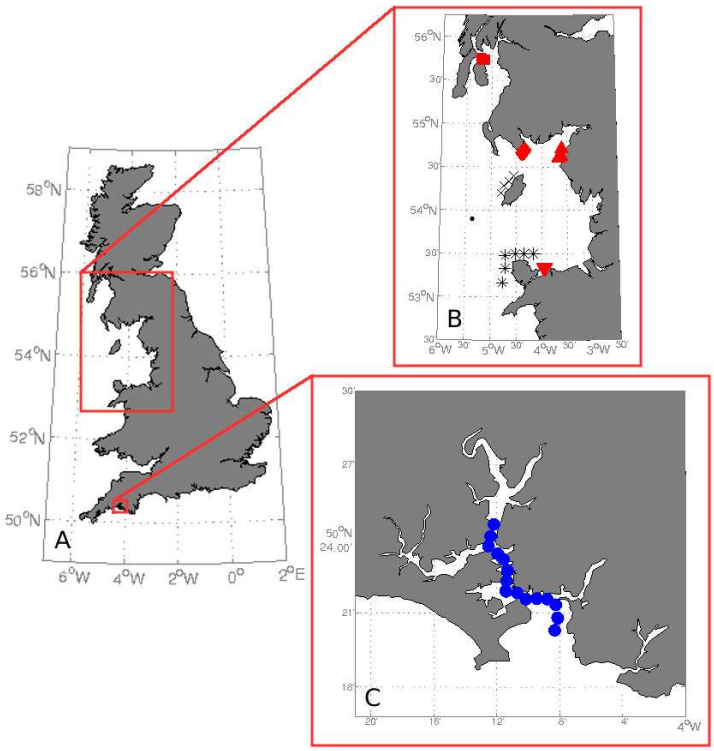

Figure 2. Map of UK Deployment Locations

A UK context, **B** in the Irish Sea and **C** Plymouth Sound and Tamar Estuary. In the Irish Sea, stations marked in black indicate measurements during April 2009 (system 2, CCD pixel size of 3.45 μm) and those in red indicate measurements in July 2009 (system 2, CCD pixel size of 4.4 μm). Blue markers in Plymouth Sound and Estuary indicate position of stations during a transect using system 1 (CCD pixel size of 7.4 μm).

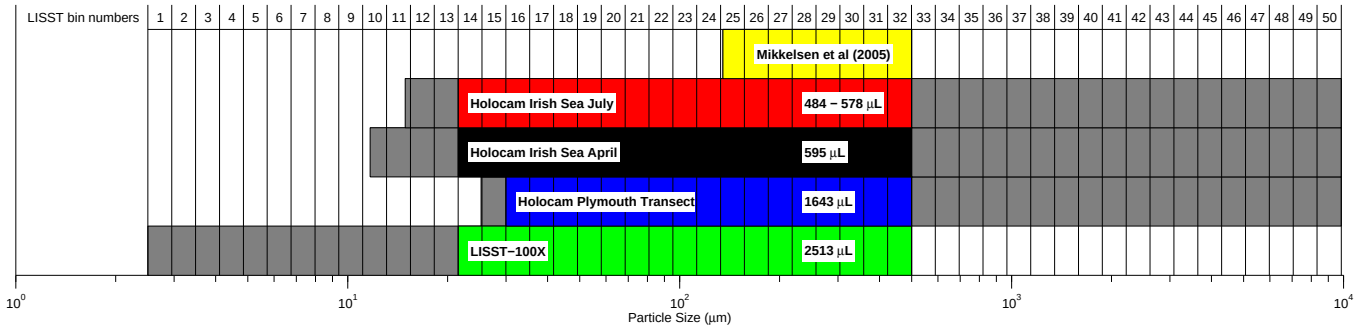

Figure 3. LISST-100X and holocam size bins.

Graphical illustration of log-spaced size bins for LISST-100X (type C), holocam and the Digital Floc Camera deployed by Mikkelsen et al [2005]. Overlap between instruments is indicated by coloured bars, whilst full extent of instrument measurement capability is indicated by gray shaded areas. Although the holocam identifies individual objects from 9 connected pixels (14.9,11.7,25μm Equivalent Circular Diameter for the systems identified in red, black and blue) up to about 9 mm in maximum linear dimension, for analysis we impose a minimum particle diameter of 19.3μm (corresponding to bin 14 of the LISST-100X) on the Irish Sea datasets, 28.3 μm for the Plymouth Sound and Tamar Estuary dataset and a maximum of 500μm corresponding to an overlap of 16–19 full size bins. Sample volumes are also indicated (per reconstruction, for holocam; approximate static volume, for LISST-100X).

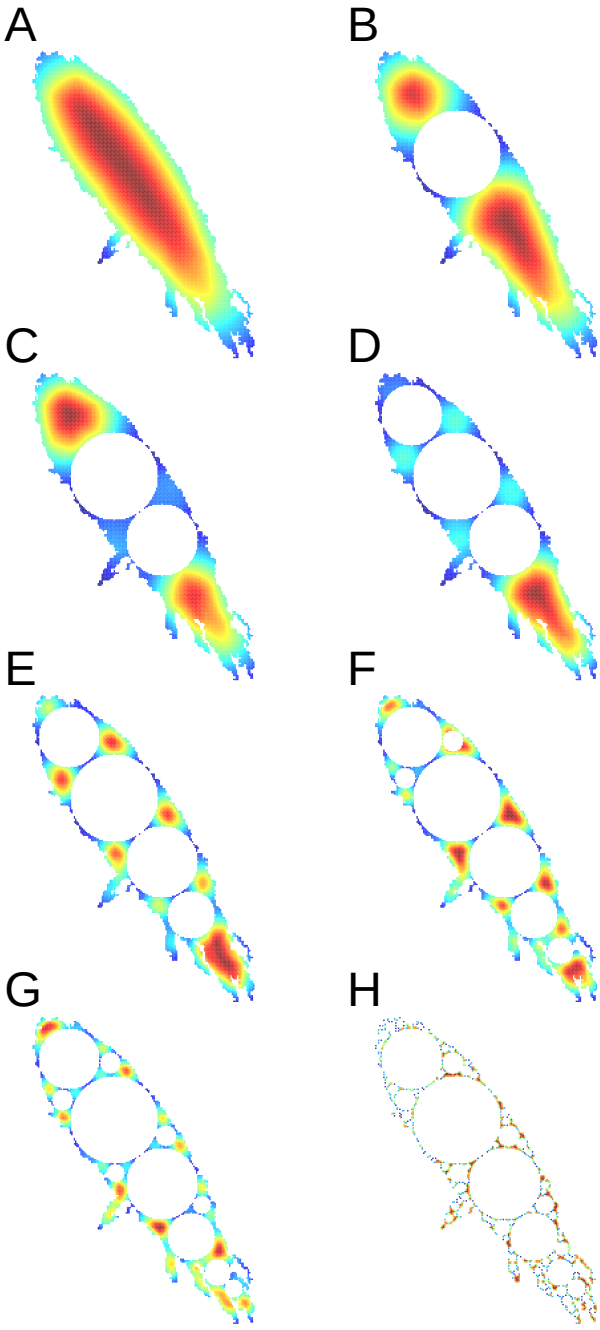

Figure 4. Demonstration of circle-packing convolution.

A shows the initial convolution from a binarised particle image, obtained with the holocam, with the circle shown in **B**. Images **B** – **G** show examples of the convolutions for the first six size stages of the routine. **H** shows the final convolution at the end of the routine.

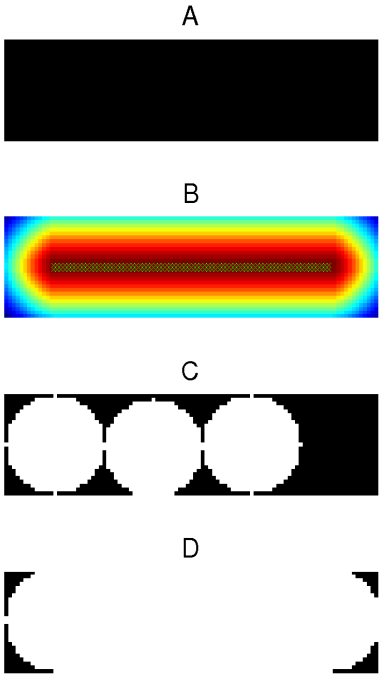

Figure 5. Demonstration of optimised circle-packing

Image **A** represents a rectangular particle area. **B** shows the two-dimensional convolution of **A** and a circle with a diameter equal to the smallest chord of **A**. The green crosses of **B** show the positions in which the circle could be placed. Image **D** shows the routine without accounting for all multiple centres. **C** shows the optimized method of smearing the circle across all centres returned by the convolution.

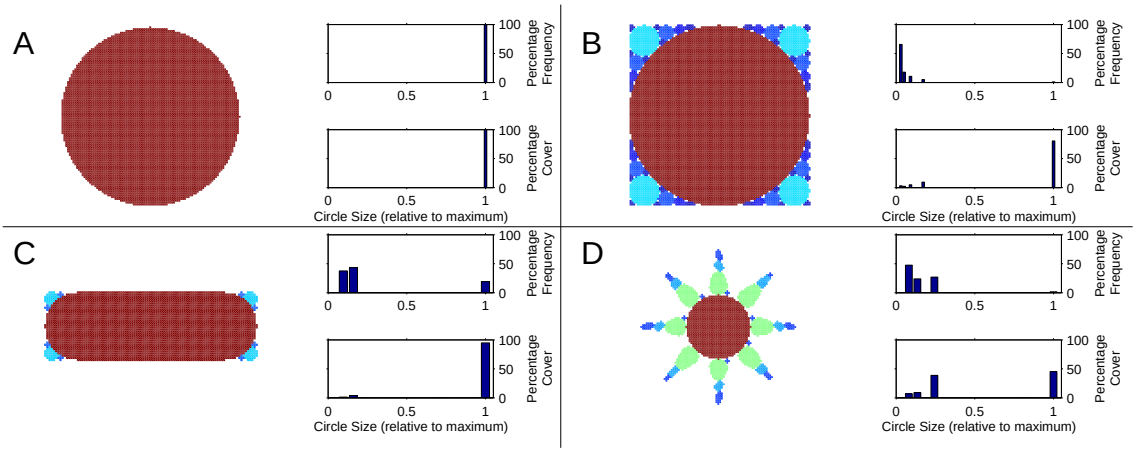

Figure 6. Circle-packing regular shapes

Examples of resultant circles, histograms of number distributions and histograms of area distributions, for regular shapes.

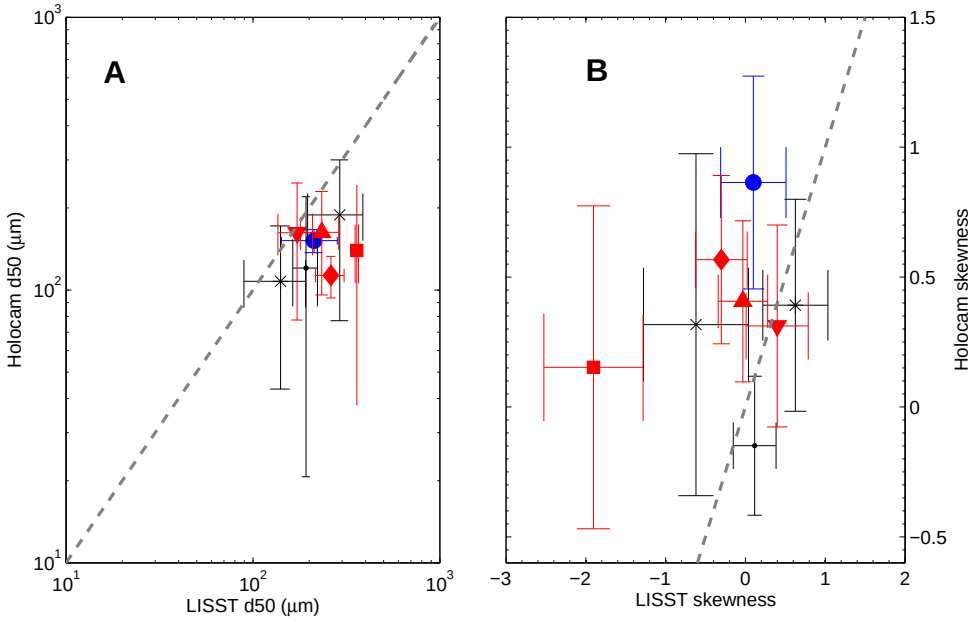

Figure 7. LISST-100X and holocam d_{50} and skewness comparison.

A Comparison of LISST-100X and holocam median particle size by volume (d_{50}) within size range of 29.96 – 500 μm for Plymouth Sound and Tamar Estuary datasets and 21.52 – 500 μm for the Irish Sea datasets. **B** Skewness of particle volume distributions. Data points are averages of all profiles at each of the locations in Table 1 and coloured according to Figure 2. Dashed line indicates 1:1 relation, error bars are ± 1 standard deviation.

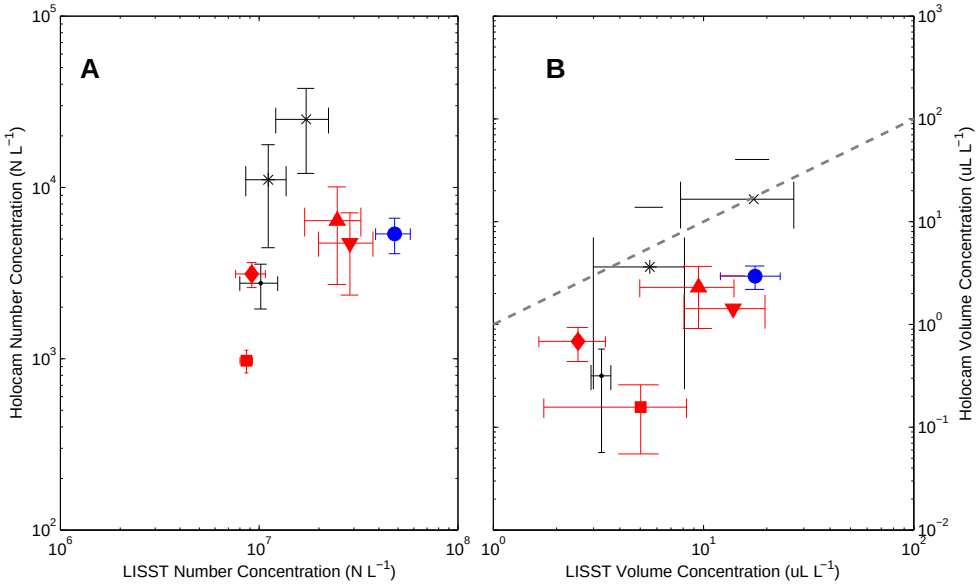

Figure 8. LISST-100X and holocam total number and volume comparisons. **A** Comparison of LISST-100X and holocam total number concentrations. **B** Total particle volume concentrations. Data points are averages of all profiles at each of the locations in Table 1 and coloured according to Figure 2. Dashed line indicates 1:1 relation. Error bars are ± 1 standard deviation about the mean.

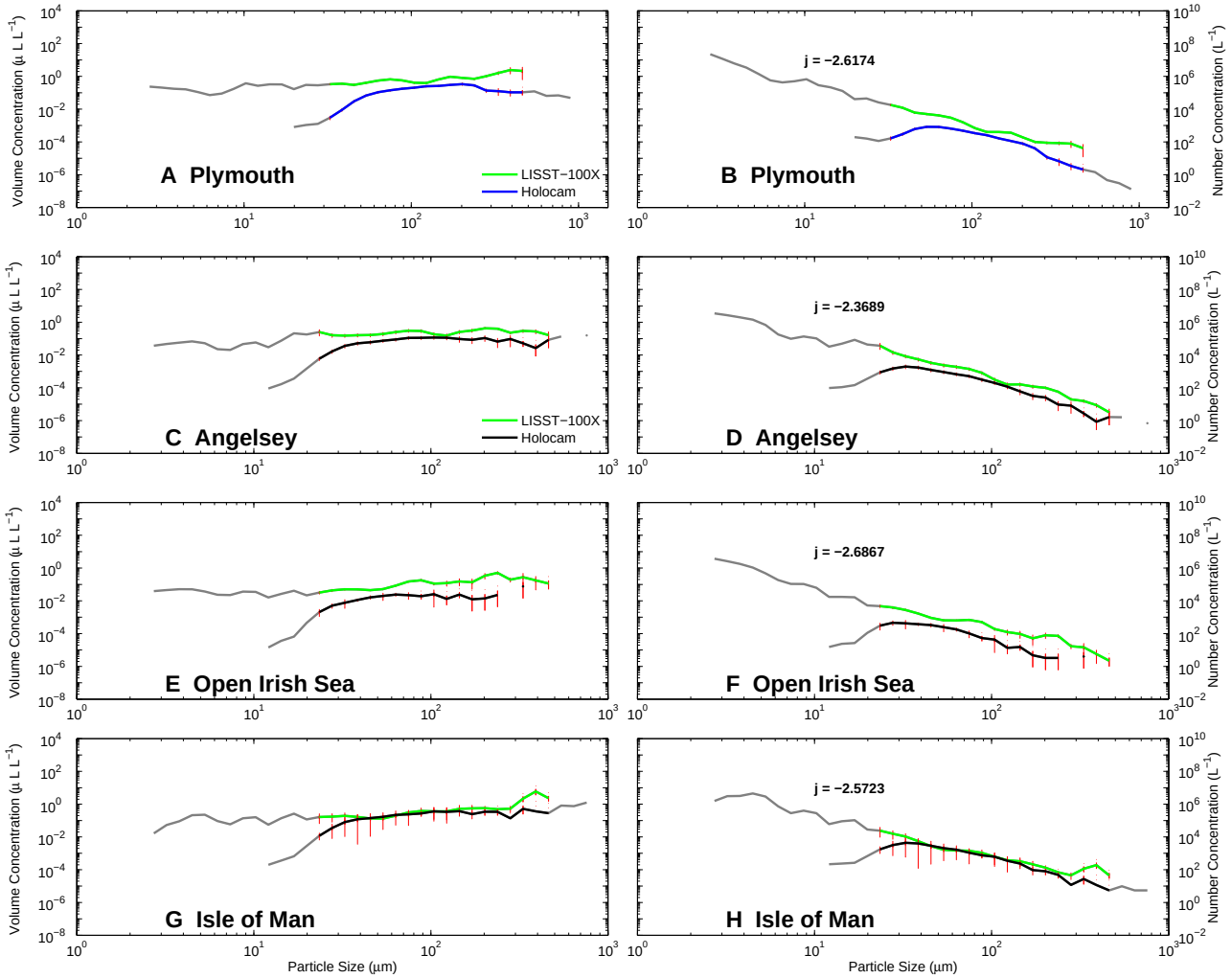

Figure 9. PSD comparison - Plymouth (June 2008) and Irish Sea (April 2009). Comparison of LISST-100X and holocam average particle size distributions in volume and number concentration for Plymouth Sound and Tamar Estuary in June 2008 (**A**–**B**) and the Irish Sea in April 2009 (**C**–**D** ;**E**–**F** ;**G**–**H**). Line colours for the holocam refer to locations identified in Figure 2. Distributions are averaged over all profiles from each transect with error bars indicating the confidence interval about the mean at α=0.05. Coloured portions of the distributions refer to the size interval used for inter-comparison (29.96 – 500 μm for **A**–**B** and 21.52 – 500 μm for **C** – **H**). The grayed portions indicate the entire dataset.

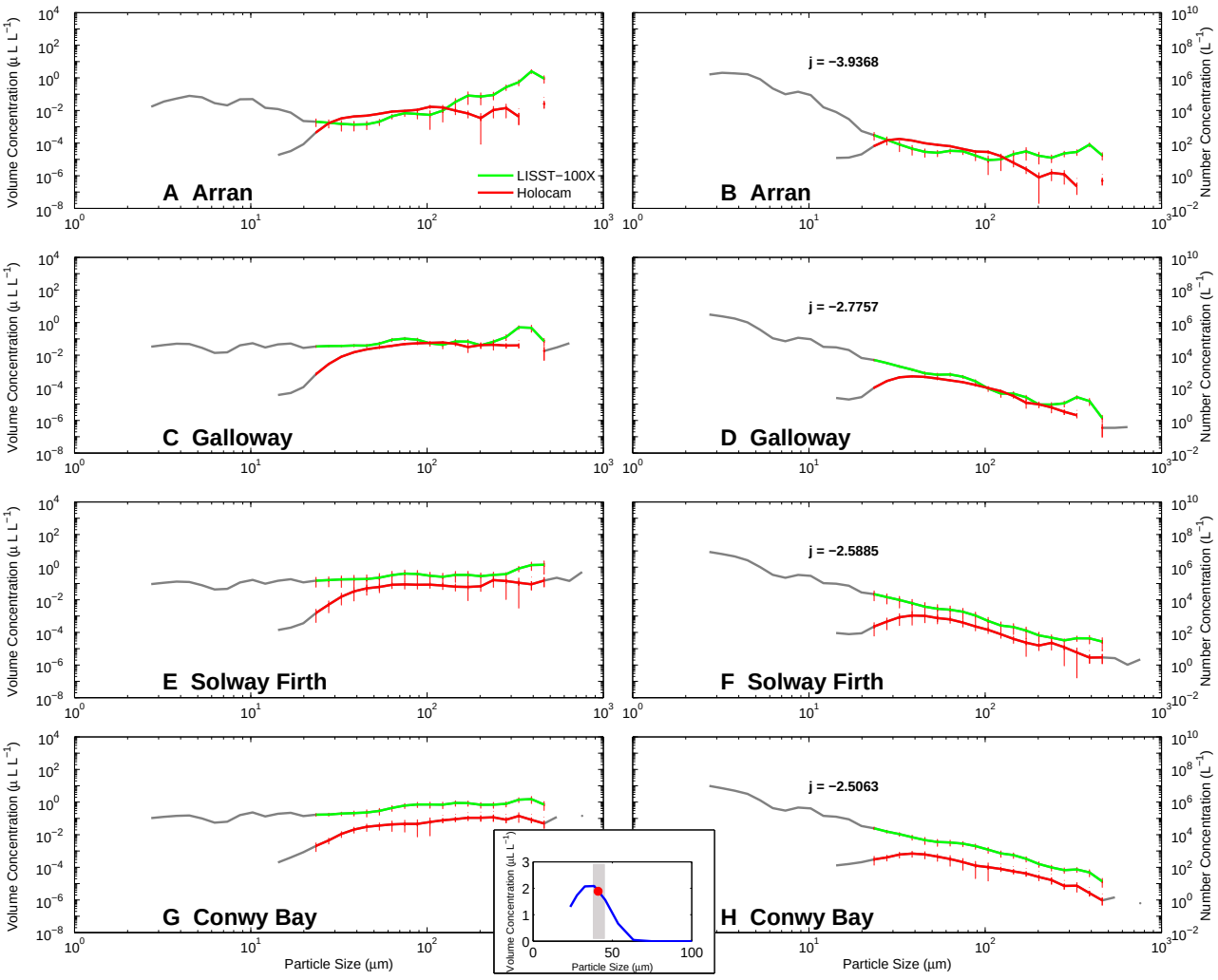

Figure 10. PSD comparison - Irish Sea July 2009.

Comparison of LISST-100X and holocam average particle size distributions in volume and number concentration for locations sampled in the Irish Sea in July 2008. Distributions are averaged over all profiles from each location with error bars indicating the confidence interval about the mean at α=0.05. Line colours for the holocam refer to locations identified in Figure 2. The insert between **G** and **H** is a laboratory derived volume distribution generated by the holocam (blue line) for fine quartz sand. The shaded rectangle indicates the wet-sieved range (38<45 μm) and the red dot an *a-priori* estimate of the volume concentration for the sieved range mid-point.

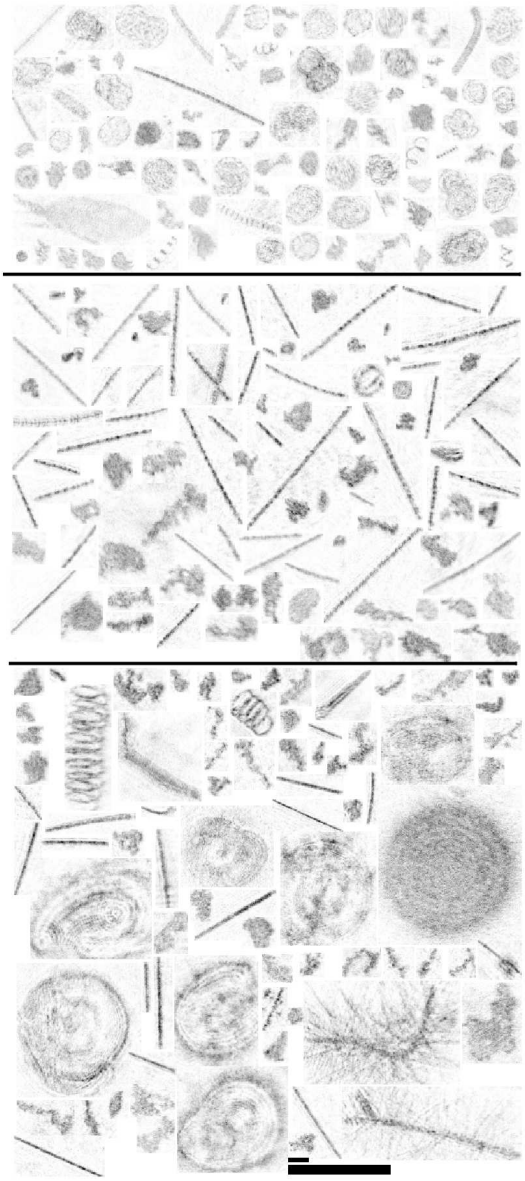

Figure 11. Holocam particle montages

Montage of particles from sample sites in Plymouth Sound (top panel) and the Irish Sea April (mid panel) and July (bottom panel) deployments. These montages are generated by random selection of in-focus imagery from all sampling stations within a deployment location. They give a graphical indication of the frequency of occurrence of particular particle shapes and sizes. Scale bar in bottom panel is 500 μm in length, with 100 μm subdivision indicated.

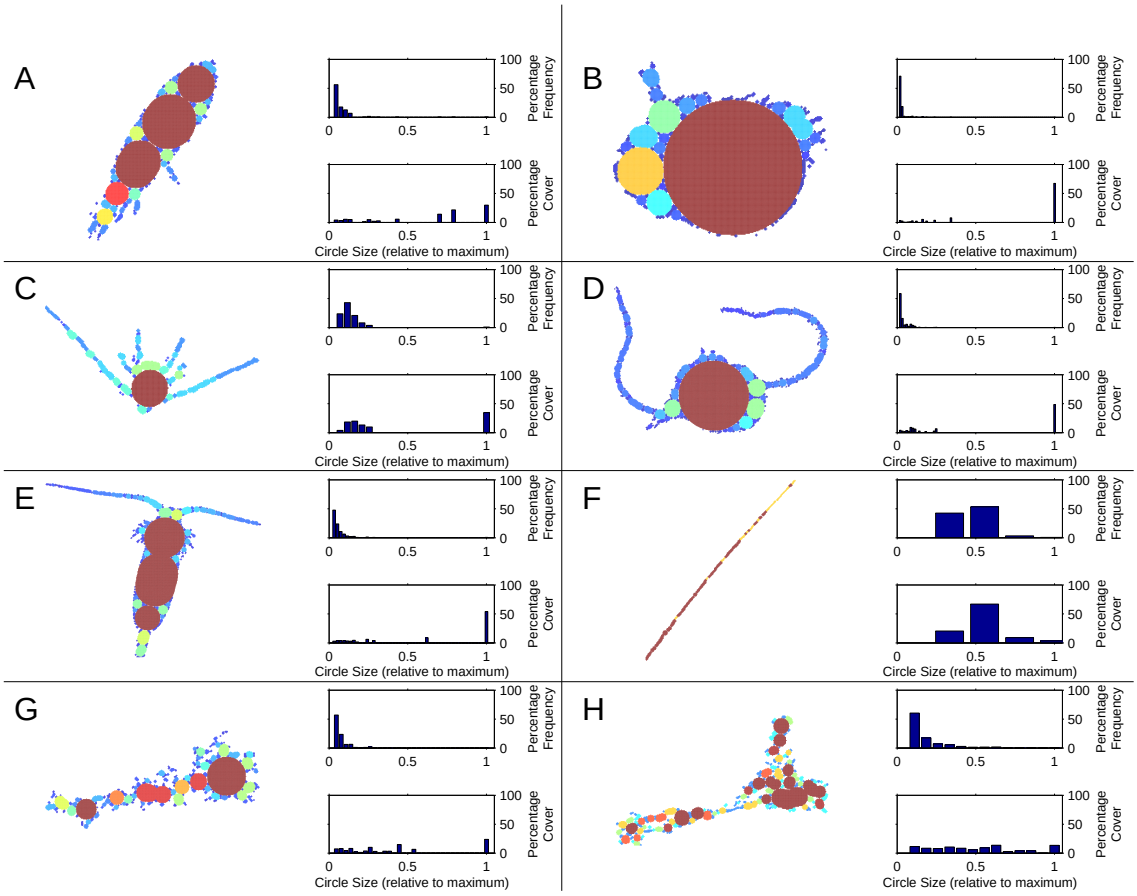

Figure 12. Circle packing natural particles.

Examples of resultant circles, histograms of number distributions and histograms of area distributions, for particle projected areas obtained from *in-situ* holographic imagery in the coastal waters of Plymouth.

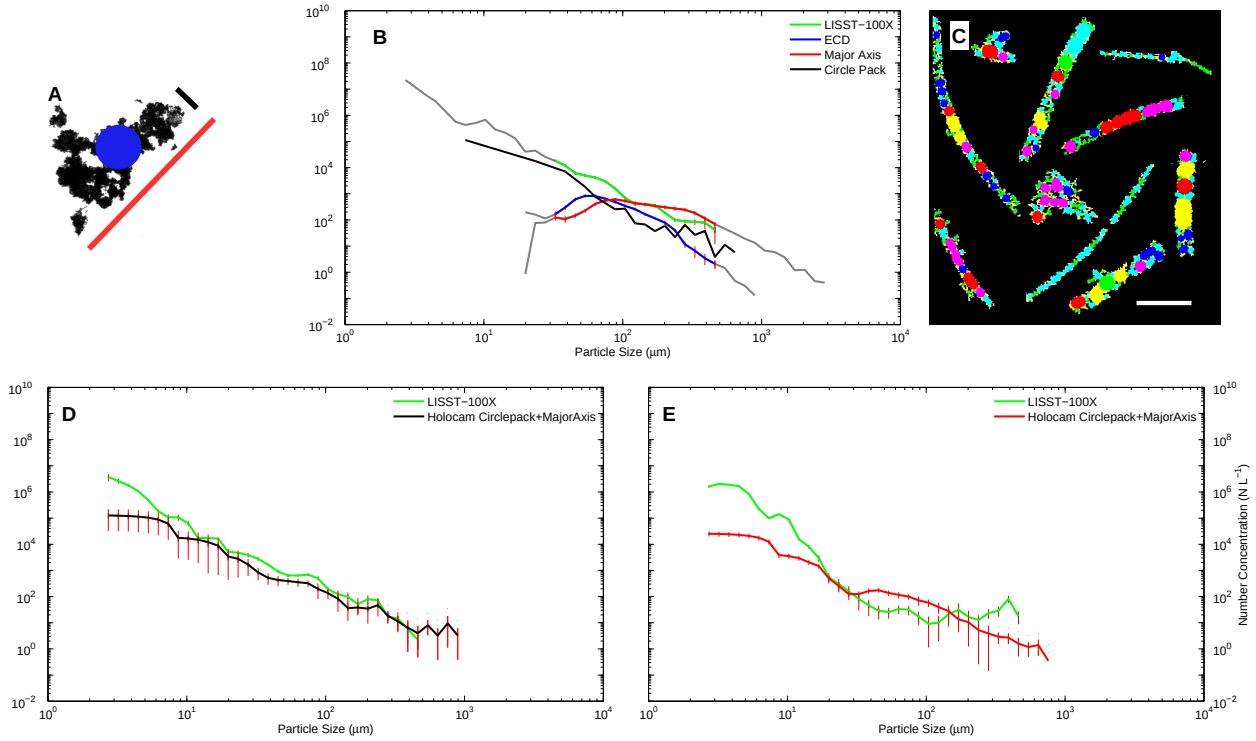

Figure 13. Characteristic length scale distributions.

Influence of characteristic length scales for a complex particle on size distribution. **A** illustrates length scales of Major Axis (Red), Minor Axis (Black) and Equivalent Circular Diameter (Blue). **B** illustrates number distributions for Major Axis and Equivalent Circular Diameter length scales for particle populations from Plymouth Sound. In addition the size distribution from smaller, internal scales is illustrated (Black line) after application of a circle-packing methodology to each imaged particle. A montage of circle-packed particles are illustrated in **C** with packed circles of different radii differentiated by colour). Panels **D** and **E** compare LISST-100X number distributions with PSDs derived from summation of the Major Axis length distribution with a circle packed distribution for the Open Irish Sea (April Cruise) and the Isle of Man (July Cruise).

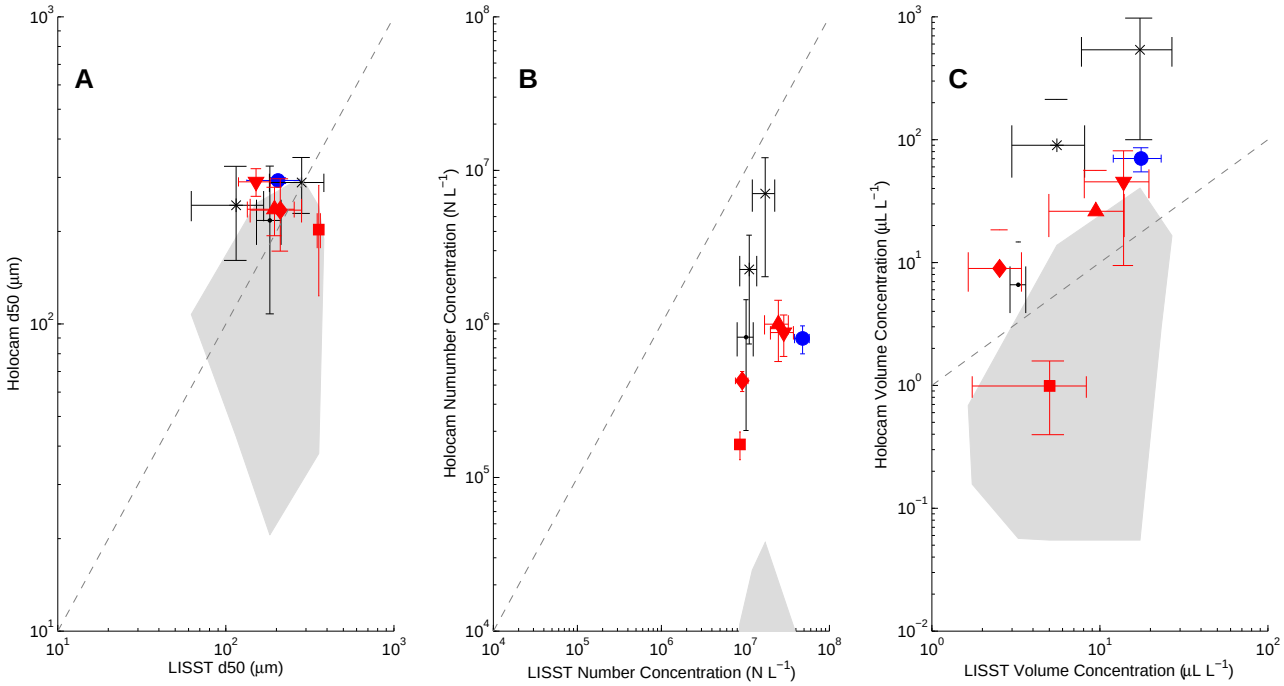

Figure 14. Combined PSDs comparison

Comparison between LISST-100X and holocam using the combined holocam PSD (summation of circle-packed distribution and Major Axis distribution over the LISST-100X range of 2.5-500μm) to calculate d_{50} (**A**), total particle number concentration (**B**) and total particle volume concentration (**C**). Grayed patches indicate envelope of data-point positions, from Figure 7 A and Figure 8 A-B, prior to circle-packing.

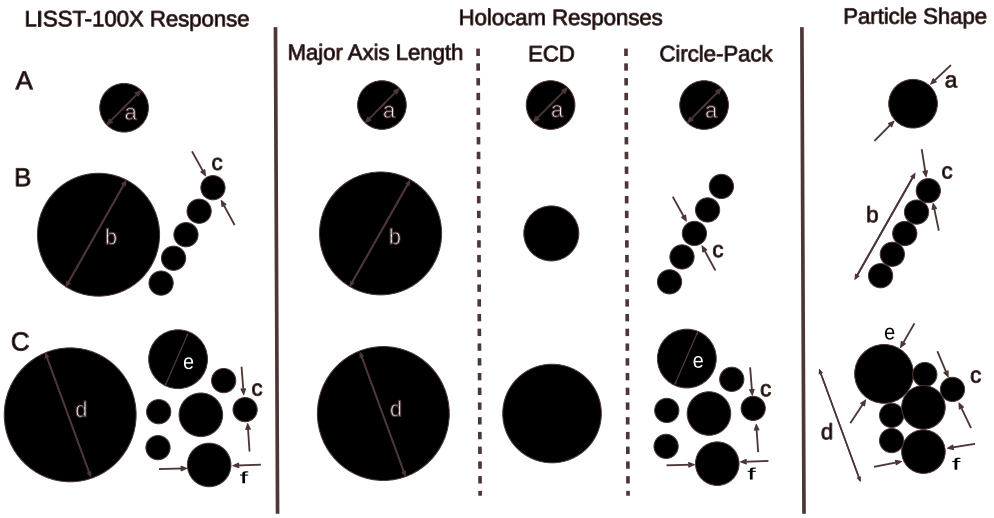

Figure 15. Particle packing schematic.

Representation of three (A,B,C) hypothetical LISST-100X responses to objects of unknown shape (Column 1), discrete particles are reported with scales indicated by arrows and letters (a – f). The three methods of representing these particles using the holocam (Major Axis length, Equivalent Circular Diameter or diameter of component parts after non-optimised circle-packing) are illustrated in columns 2 to 4. The discrepancy between size metrics provides information about particle packaging and suggests the shape of the unknown object is to be inferred as illustrated in column 5. The use of optimised circle-packing would reduce the number of circles of size c in example B and include a fractional component as indicated by Equation 2.

Table 1. Deployment information, holocam configuration and number of LISST-100X scans used for analysis.
The number of holocam images and LISST-100X scans included in the analyses are the sum over all casts per station. The number of particles (reported by the holocam) are similarly the sum over all casts per station, with the numbers in parentheses corresponding to particles within truncated limits (see Figure 3 for specification of size limits) which are utilised in the inter-comparison with the LISST-100X (type C).

Location	Date	Station ID	Pixel size (μm)	ROI width and height (pixels)	Path-length (mm)	No. of profiles	No. of images	No. of particles	No. of LISST scans
Plymouth Sound	19/06/08	Plymouth	7.4	1000	30	15	2664	38301 (34864)	496
Irish Sea 1	20/04/09-	Angelsey	3.4	1000	50	27	1941	14090 (12962)	914
	23/04/09	Open Irish Sea	⋮	⋮	⋮	7	301	738 (685)	207
		Isle of Man	⋮	⋮	⋮	4	276	4430 (4133)	142
Irish Sea 2	17/07/09-	Arran	4.4	1000	50	22	3204	5004 (4712)	955
	21/07/09	Galloway	⋮	⋮	⋮	11	2292	7486 (7254)	402
		Solway Firth	⋮	⋮	⋮	6	997	6354 (5991)	170
		Conwy Bay	⋮	⋮	25	9	1334	8459 (7443)	355